Failure Mechanics of Nonlinear, Heterogeneous, Anisotropic Cardiovascular Tissues: Implications for Ascending Thoracic Aortic Aneurysms

A THESIS
SUBMITTED TO THE FACULTY OF THE
UNIVERSITY OF MINNESOTA
BY

Christopher E. Korenczuk

IN PARTIAL FULFILLMENT OF THE REQUIREMENTS
FOR THE DEGREE OF
DOCTOR OF PHILOSOPHY

Victor H. Barocas, Adviser

June 2019

Acknowledgments

First, I'd like to thank my adviser, Victor Barocas. Victor, you have been an exceptional mentor and friend throughout my graduate tenure. Thank you for constantly showing me how exciting and rewarding academic research can be. I can truly say that both the quality of my PhD research, and my entire graduate school experience, would not be the same without you. You have instilled formative scientific practices, and have helped me develop a framework for research that I will carry with me for the rest of my life. You have always tried to "do what is best for the student", and I can honestly say that you have been unwavering in this tenant for my entire tenure. Thank you for helping me process both scientific and personal topics, and for always having an open mind to engage in other thoughts and worldviews outside of research. Know that I am forever grateful to have worked with you on this PhD thesis, and I look forward to any future collaborations we might have.

To all of the Barocas Lab members, past and present, thank you for being a welcoming family to share graduate school with. Vic Lai - you were the first lab member I was able to work with, thank you for helping me grow accustomed to the changes graduate life presented and for introducing me to Hope Community Church. I will always appreciate your mentorship and friendship. Thank you for always being a great sounding board and strong encouragement. Colleen - thank you for passing along this project and mentoring me in the short time that we were able to work with each other. Your aptitude and hard work ethic have been particularly motivational for me in my career. Amy, Inka, and Sarah - thank you for the example you set as senior lab members. You were all instrumental in helping me choose the Barocas Lab and welcoming me in. Julia, Rohit, and Vahab - the experiences we shared hold some of my most fond memories during this season. Thank you all for making the lab

(and office) truly an enjoyable place to work every day, I can't thank you all enough for your help. Whether it was related to classwork, research, or a personal topic, you three were always there to process anything that arose, and you were always supportive. I'm grateful to have shared this experience with you, and I value our friendships. Shannen, Lauren, Emily, Ryan, Hernan, Liz, Tiffany, David, and Jae - I can't thank you all enough for helping me throughout these last few years. We have shared countless, memorable discussions and experiences, all of which I will carry with me. Thank you all for your support, our friendships have played a significant role in my growth and experience throughout graduate school. Continue to make the Barocas Lab a welcoming place, where ideas and challenges are always approached as a collective team.

To the community at Anselm House (Andrew, Erin, Matt, Cheri, Danica, Bryan, and the rest of AH staff) - thank you all for work you do pouring into students at the University of Minnesota. My time in the MacLaurin Fellows Program was one of the most formative experiences during my graduate tenure, and I will leave graduate school equipped with not only scientific training, but also with a more comprehensive worldview. I cannot stress enough how pivotal AH was in guiding my personal development during graduate school, allowing me to carry these principles into my future career and life. Thank you for showing me how intertwined faith and work are, and for always living out the Gospel in your words and actions.

To my Small Group and friends at Hope Community Church - thank you all for making Minnesota home. You have all been the exception to the idea that finding community in a new location is never easy. It would be impossible for me to state all the ways you have helped throughout my time in graduate school. I'm so grateful to walk through life with all of you, thank you for your continued love and support.

To my family and friends - Kevin, thank you for being a great example and role

model, taking time and effort to show a new college student how interesting academic research can be. Without you, I would have never considered the field of Biomedical Engineering, and consequently would have never pursued this research. Thank you for your mentorship during my undergraduate years. Jordan, thank you for your advice and support throughout graduate school, especially during these final months. I know our undergraduate selves looked forward to the day our theses would finally be complete, and that day has arrived. Thank you for journeying with me throughout undergraduate and graduate work. Mom and Dad, thank you for always being a great example of hard work and determination. Your guidance has equipped me with so much, and without it I would never have finished - or even started - this work. Thank you for your constant love and encouragement, I know it was not easy to watch me move halfway across the country (to somewhere cold, nonetheless). You have given me unwavering support in every possible way, and the quality of character you both lead with has been imprinted on me. This work is the culmination of all the effort you put into my education throughout the years, for which I am eternally grateful.

Lastly, to my wife. Mal - meeting you was the highlight of my entire graduate school tenure. We've shared all of the ups and downs of my grad school experience together. You have journeyed with me through the stresses and joys of qualifying exams, conferences, publications, and finally, my thesis and defense. Most of these required late nights and early mornings, resulting in time away from you, especially during this final year. Thank you not only for your understanding, but your constant and unchanging support. Thank you for listening to me, helping me process, making me laugh, and, most importantly, challenging me to pursue excellence in all areas, especially my work. I cannot express what you mean to me, and I could not be more grateful to have you by my side during this season. This work would not be what it is without you.

Credo ut intelligam.

"For I do not seek to understand in order that I may believe, but I believe in order to understand. For this also I believe - that unless I believe I shall not understand."

St. Anselm of Canterbury

Colossians 1:9-14

Philippians 2:12-14

Philippians 4:11-12

Contents

List of Tables

List of Figures

3.5 Plots analyzing the differences between each of the network cases for all the samples. **A)** A representative plot for one sample is shown to illustrate how the plots work. The y-axis displays the average Ω_{11} for the sample, while the x-axis displays the standard deviation of Ω_{11} over all elements within the sample. Thus, the y-axis represents how strongly aligned the sample is on average (0.5 = isotropic, 1 = perfectly aligned), and the x-axis represents how strongly the sample deviates from its average alignment (0 = no deviation (homogeneous), 0.5 = strong deviation (heterogeneity)). Each sample has the 3 network cases plotted for the given variable. The isotropic case always corresponds to (0, 0.5), as there is no degree of alignment, or deviation from the average. The homogeneous and heterogeneous cases lie on a horizontal line, as they have the same average degree of alignment, but differing variation from the alignment in the heterogeneous case. The dotted line shows the range of possible ($< \Omega_{11} >$, $std(\Omega_{11})$) pairs. The gray box contains all of the samples that were studied and sets the zoomed-in plot area shown for **B)**, **C)**, and **D)**. **B)** The ratio of P_{11} to P_{22} is shown at 20% strain for each of the samples, as a measure of anisotropy. As degree of alignment increases, so does the degree of anisotropy. The effect is slightly more pronounced in the homogeneous case. **C)** Peak P_{11} stresses are consistently higher in the heterogeneous case compared to homogeneous and isotropic cases but do not show any obvious trend within the heterogeneous model results. **D)** The % strain required to fail 0.5% of the fibers in the sample is shown for each case. For the isotropic and homogeneous

Chapter 1

Introduction

> "It is the first, and in a way the most important task of science to enable us to predict future experience, so that we may direct our present activities accordingly."
>
> *H.R. Hertz, 1857-1894*

I open with the same quote Jay Humphrey does in his book titled, *Cardiovascular Solid Mechanics* [Humphrey, 2002], as it provides a fitting mindset for the work to follow. The work herein seeks to understand and predict the complex phenomenon that is soft tissue failure, particularly as it relates to pathological cardiovascular tissue. Each of the following chapters looks to grapple with both the *mechanism* and *characterization* of tissue failure in various scenarios, with the hope of improving our understanding of these situations. Tissue failure, after all, is an event easy to identify once it occurs, but challenging to predict *a priori*. Yet, nearly all human beings will experience some form of soft tissue failure within their lifetime. In some cases, failure is non-debilitating and addressed naturally by the body's healing processes. In others, however, such as myocardial infarctions and aortic aneurysms, predicting and understanding tissue failure is crucial, as failure of these tissues can be harmful

at best and fatal at worst. By understanding how and when these tissues fail, we create a strong foundation of knowledge that informs diagnoses, and in turn affects patient outcomes. The work contained here is certainly not exhaustive, but rather an addition to the growing field of cardiovascular soft tissue mechanics and failure.

1.1 Cardiovascular System

1.1.1 Healthy Cardiac Function and Anatomy

The cardiovascular system exists as a vital component within the human body, providing a closed loop for blood transport to and from all major organs and tissues. During normal functioning, a highly organized network of arteries and veins coherently works to allow for oxygen and nutrient delivery, as well as waste and CO_2 removal. The heart sits centrally, both physically and functionally, within the cardiovascular system as the driving pump, contracting upwards of 2.5 billion times within an average human life [Humphrey, 2002]. The contraction of the heart is constantly regulated, adapting to demands made necessary by the rest of the body. Each component of the cardiovascular system is uniquely fit to accomplish the unified goal of transporting blood throughout the body.

In the healthy heart (Fig. 1.1), deoxygenated blood enters the right atrium via the super and inferior vena cava during ventricular systole. As the conduction system of the heart initiates, atrial myocytes contract and increase atrial pressure, causing the tricuspid valve to open and allow blood to fill the right ventricle. Once conduction reaches the ventricles, causing them to contract, blood is pumped through the pulmonary valve into the pulmonary arteries. Deoxygenated blood then travels through the pulmonary arteries to the lungs, where CO_2 is exchanged for oxygen during simple diffusion. Now oxygenated blood returns to the left atrium via the pulmonary veins,

filling the left atrium during ventricular systole. The conduction process mentioned previously causes atrial contraction once again, allowing blood in the left atrium to fill the left ventricle, flowing through the mitral valve. Once full, the left ventricle contracts, pumping blood out through the aortic valve into the ascending aorta, allowing it to travel to the rest of the body.

Throughout the cardiac cycle, both the heart and aorta experience complex loading, acting as both passive and active tissues at different times. The heart experiences both contractile and torsional loading, along with rotation, due to the contraction of myocytes and their orientation [Nakatani, 2011, Omar et al., 2015] while the aorta experiences significant expansion ($\sim$11% area change [Mao et al., 2008]) due to the blood pressure, followed by active contraction to pump blood to the extremities. The ability of both these essential tissues to bear repetitive stress and strain relies entirely on their underlying tissue composition.

The myocardium of the heart is comprised of myocytes, fibroblasts, and an extracellular matrix (ECM) [Humphrey, 2002]. Myofibrils reside within the cytoplasm of the myocytes, providing the mechanism by which the myocardium can contract. The myocytes are oriented in a helical manner, allowing for counterclockwise apical rotation and twisting during ventricular systole, and clockwise rotation during diastole [Omar et al., 2015]. Fibroblasts, the must abundant cell type in the heart, aid in healing and remodelling, laying down collagen in response to changes in mechanical loading or damage. Collagen (type I) makes up a majority of the ECM composition, providing structural support for the loading experienced during the cardiac cycle.

Arteries (particularly the ascending aorta, which is of primary focus in this work) are comprised of 3 layers (Fig. 1.2). The innermost layer, known as the tunica intima, contains a lumen lined with endothelial cells in constant contact with blood flow, anchored to an internal elastic lamina composed of connective elements and

collagen fibers [Wagenseil and Mecham, 2009]. The middle layer, known as the tunica media, contains concentric lamellar layers of collagen and elastin, held together by vascular smooth muscle cells (VSMCs) and other ECM components (such as fibrillin-1 and proteoglycans). The outermost layer, known as the tunic adventitia, is comprised primarily of collagen fibers, along with myofibroblasts [Wagenseil and Mecham, 2009]. The unique ECM composition of arteries allows them to expand during diastole and to recoil elastically during systole, shifting significant blood pressure load away from the heart, and helping to pump blood throughout the body. The primary load-bearing layer within the vascular wall is the media, due to its high collagen and elastin fiber concentration and highly-aligned fiber architecture. Collagen fibers exhibit a preferred alignment in the circumferential direction, providing structural integrity to the vessel during expansion and contraction. Elastin is primarily isotropic, having a lower stiffness and higher failure stretch than collagen, yielding an elastic response in the vessel and stability during large deformations. VSMCs help to give the lamellar layers support, along with providing the active contractility of the vessel. In a healthy state, the ascending aorta bears significant and repetitive loading during the cardiac cycle, playing a crucial role in the overall functionality of the cardiovascular system.

The inherent behavior of these underlying components gives rise to the overall macroscale behavior of the tissues, and consequently, the title given to this work. Each one of these attributes: nonlinearity, heterogeneity, and anisotropy, plays an essential role in the overall tissue behavior, and understanding how these contribute is crucial to understanding both the mechanical response and the mechanisms of tissue failure. Nonlinearity, common to all soft tissues, is specified by the nonlinear relationship between stress and strain. In contrast to materials such as metals, which typically reside in low strain regimes, biological tissues undergo a significant amount of strain during normal use. The inherent response of load-bearing fibers such as

collagen and elastin is particularly nonlinear, resulting in a nonlinear tissue response. Heterogeneity is the unique characteristic of soft tissues, particularly the heart and aorta, to have a spatially varying microstructure throughout. The difference in cell and fiber density, along with alignment, yields spatially varying mechanical behavior in the tissue. Anisotropy is the characteristic of the heart and aorta to exhibit a preferred fiber alignment, usually in a load bearing direction. By orienting fibers in a different manner, tissue loaded in different situations will respond based on the underlying fiber directions, producing higher stress in preferred fiber directions. Each of these aspects is unique, and varying, within soft tissues, and must be considering when attempting to understand tissue mechanics.

So far, we have observed how the cardiovascular system, namely the heart and aorta, operate in a healthy, idealized manner. This, however, is not always the case. A variety of trauma events and pathologies can negatively impact the tissue, causing subsequent remodeling and change in response. These situations are of primary concern in the work to follow, specifically, myocardial infarctions and ascending thoracic aortic aneurysms. Most importantly, *when and how does failure occur in these situations?* What factors contribute to failure? What is the threshold, or location of failure? These questions are of utmost importance as we consider the impact detrimental remodeling has on native tissues.

1.1.2 Myocardial Infarctions

A myocardial infarction (MI) occurs when an ischemic event causes cardiac myocyte death, affecting upwards of 1 million Americans every year [Benjamin et al., 2018]. As cardiac musculature is a nondividing tissue, trauma response depends on fibroblasts laying down collagen fibers to replace necrotic areas, resulting in scar tissue. The subsequent outcome of native tissue replacement with stiff collagen fibers, is altered

cardiac behavior. Scar formation can impede normal cardiac function, and cause future complications such as cardiac rupture or heart failure [Richardson et al., 2015]. As such, the orientation and density of new collagen fiber deposition plays a large role in the resulting mechanics of the surrounding cardiac tissue. Factors such as fiber heterogeneity and anisotropy can affect stress and strain redistribution under normal cardiac loading, creating locations at a higher risk of failure. Much is still unknown about the risks scar healing creates in the case of MI, as well as how to improve post-MI tissue mechanics. Consequently, a fundamental understanding of the effect scar mechanics have on native tissue due to their underlying microstructure is needed.

1.1.3 Ascending Thoracic Aortic Aneurysms

The healthy ascending aorta of an average adult is 2-3 cm in diameter and experiences pressures of 100-140 mmHg during systole and 60-90 mmHg during diastole [Iaizzo, 2009], undergoing large deformation during the cardiac cycle. Ascending thoracic aortic aneurysms (ATAAs) occur when the aorta abnormally enlarges in diameter between the aortic root and aortic arch (Fig. 1.3) [Cruz et al., 2007]. ATAAs pose a significant risk as the vessel can 1) rupture, causing likely mortality, or 2) dissect, allowing blood to enter the vessel wall, causing further expansion and the possible formation of intraluminal thrombus. ATAAs occur in over 15,000 people throughout the United States each year [Cleveland Clinic, 2014], with 60% of thoracic aneurysms occurring in the ascending region [Isselbacher, 2005]. If not surgically corrected, ATAAs have a high rate of rupture (21% to 74%), with a mortality rate of $\sim$100% in those with ruptured ATAAs [Davies et al., 2002, Olsson et al., 2006]. Surgical repair also presents a relatively high mortality rate of 5-9%, with emergency operations reaching as high as 57% [Davies et al., 2002]. ATAAs present a unique situation,

as aberrant remodeling and disease progression typically happen slowly over time, allowing for careful diagnostic assessment prior to surgical recommendations.

Enlargement of the ascending aorta negatively impacts the vessel's mechanical integrity. Though mechanical differences in pathological aortic tissue are evident and well-known [Isselbacher, 2005, García-Herrera et al., 2012, Vorp et al., 2003, Okamoto et al., 2002], current diagnostic methods for surgical treatment are based solely on morphology (diameter size or growth rate), neglecting mechanical considerations. The current threshold for surgical intervention is a diameter larger than 5-6 cm [Davies et al., 2002, Elefteriades, 2002, Coady et al., 1999], or a growth rate greater than 1 cm/year [Saliba and Sia, 2015]. Diagnosis based on diameter measurements, however, is prone to subjectivity and discrepancies, shown by inconsistencies among common imaging techniques [12]. More importantly, the current diameter-based diagnostic threshold proves to be inefficient in predicting aneurysm failure, as mortality is prevalent on both sides of the threshold. Vorp *et. al* [Vorp et al., 2003] have shown a 5-year mortality rate of 39% for ATAAs smaller than 6 cm, and 62% for those greater than 6 cm, along with no correlation between aneurysm diameter and mechanical strength [Vorp et al., 2003]. Their study emphasizes the fact that failure is complex process, unique to each individual, that involves many key factors which may not be captured by morphology. Taken collectively, this information highlights the critical need to better understand the mechanical behavior and failure of ATAAs, in order to appropriately predict risk of failure in the ATAA pathology.

Recent Studies

Remodeling during aneurysm development causes nonuniform expansion and thinning of the vessel wall, imposing local heterogeneity and altered stiffness. Though some studies have reported no significant difference in vessel wall thickness between

diseased and healthy tissue [Vorp et al., 2003], typical progression of the pathology results in a thinner vessel wall lacking elastin and smooth muscle cells [Humphrey, 2002]. Previous studies have quantified non-aneurysmal and aneurysmal aortic tissue mechanical response through various loading configurations including bulge inflation [Trabelsi et al., 2015,Romo et al., 2014], uniaxial extension [García-Herrera et al., 2012, Vorp et al., 2003, Okamoto et al., 2002, Iliopoulos et al., 2009a, Duprey et al., 2010,Khanafer et al., 2011], biaxial extension [Okamoto et al., 2002,Choudhury et al., 2009, Matsumoto et al., 2009, Azadani et al., 2013, Geest et al., 2004, Duprey et al., 2016], peel [Pasta et al., 2012,Noble et al., 2016], and shear [Sommer et al., 2016] testing regimes. Results have shown an anisotropic response, producing higher stresses in the circumferential direction compared to axial [Okamoto et al., 2002, Humphrey, 2002,Duprey et al., 2016]. Studies have also highlighted the decreased tensile strength of pathological tissue compared to healthy tissue [Vorp et al., 2003, Phillippi et al., 2011a, Duprey et al., 2016] in both circumferential and axial directions, making the tissue more susceptible to rupture or dissection [Phillippi et al., 2011a]. It has also been reported that ATAA wall stiffness is higher compared to control tissue [Vorp et al., 2003, Phillippi et al., 2011a], which may be caused by elastin degradation in the aneurysm pathology [Campa et al., 1987]. Regional heterogeneity of healthy and diseased tissue has also been reported, with variation between the lesser and greater curvature of the aortic arch being observed [Duprey et al., 2016, Gao et al., 2006, Thubrikar et al., 1999, Poullis et al., 2008]. The anterior region of the ATAA has been shown to be weaker and less stiff in the axial direction, which may be related to clinical data that reports preferential aneurysm bulging in the anterior location [Iliopoulos et al., 2009b].

Peel testing, in which layers of the vessel wall are peeled apart, has been performed to quantify delamination between wall layers as a method of ATAA dissection [Pasta

et al., 2012], while shear testing has been used to quantify strength between the lamellar layers of the arterial wall [Sommer et al., 2016]. Inflation testing has been used to investigate factors that contribute to aortic dissection [Tiessen and Roach, 1993, Mohan and Melvin, 1983, Groenink et al., 1999]. Factors such as age did not affect dissection initiation or propagation, but sex, location, and atherosclerotic plaque formation caused significant changes in medial strength of the vessel wall, and thus dissection behavior [Tiessen and Roach, 1993]. Other factors, such as genetic defects and overall cardiovascular health, have been found to contribute to ATAA prevalence and wall strength. Patients with Marfan syndrome, Ehlers-Danlos syndrome, or bicuspid aortic valves are more prone to experiencing ATAAs [Humphrey, 2002, Nataatmadja et al., 2003], and patients with bicuspid aortic valves have stiffer ATAA tissue compared to patients with a tricuspid aortic valves [Duprey et al., 2010]. Other ATAA risk factors include cigarette smoking, diastolic hypertension, and chronic obstructive pulmonary disease [Humphrey, 2002]. Although much work has been done to characterize both mechanical behavior and possible risk factors, it is still unclear which contributors play a significant role in ATAA failure, and how to quantify the risk of ATAA failure.

Along with experimental testing, computational modeling has been investigated to provide predictive models. Models regarding the ATAA pathology have historically been given less attention compared to abdominal aortic aneurysms (AAAs), most likely due to the more complex, curved geometry in the ascending aorta. Some initial work has sought to predict local wall stress and strength noninvasively in AAAs, in hopes of properly characterizing tissue properties in vivo for better diagnostic considerations [Phillippi et al., 2011b, Doyle et al., 2009, Doyle et al., 2010, Vorp et al., 1996, Wang et al., 2001, Maier et al., 2010], but these techniques are still limited. Various constitutive strain energy density functions have been used to capture

ascending and abdominal aortic bulk tissue behavior from a phenomenological standpoint [Okamoto et al., 2002, Chuong and Fung, 1983, Roccabianca et al., 2014], and have been integrated into growth [Volokh, 2008, Watton et al., 2004, Alford and Taber, 2008], remodeling [Volokh, 2008, Watton et al., 2004, Alford and Taber, 2008], and failure [Volokh, 2008, Balakhovsky et al., 2014, Pal et al., 2014] simulations. These models have become increasingly more accurate, incorporating more structural components such as fiber composition, density, and orientation. Finite element simulations of reconstructed aneurysm geometries allow for the prediction of locations at higher wall stresses, indicating possible rupture or dissection locations [Phillippi et al., 2011b, Nathan et al., 2011, Raghavan et al., 2000]. A rupture potential index (RPI) has also been incorporated in finite element analysis (FEA) for AAAs [Phillippi et al., 2011b, Maier et al., 2010, Vande Geest et al., 2006], which is taken as a ratio of wall stress to wall strength in order to consider regional heterogeneity. Limited work has been done, however, to validate the accuracy of FEA with an RPI in correctly predicting locations of aneurysm rupture or dissection. Current FEA models of ATAAs are also simplistic in nature, often assuming a material that is homogenous, incompressible, isotropic, linearly elastic, and of uniform thickness [Nathan et al., 2011, Beller et al., 2004]. Though some of these models are now patient-specific [Nathan et al., 2011], the simplifications used limit the accuracy and efficacy of such models as new diagnostic resources.

1.2 Motivation for Current Work

1.2.1 Previous Work

The studies performed in this thesis are motivated by a collective of previous work. Stylianopoulos *et. al* [Stylianopoulos and Barocas, 2007b] and Chandran *et. al*

[Chandran et al., 2008] began by studying the mechanical behavior of collagen-based fiber networks using a novel multiscale modeling approach. By creating a custom multiscale finite-element model, constitutive relationships were defined on the fiber level, rather than using bulk constitutive equations seen in common FEA softwares. Creating physiologically-relevant microstructural networks for the multiscale model with considerations such as fiber density, orientation, and heterogeneity allowed for the microscale behavior to give rise to the macroscopic tissue mechanics. Furthermore, due to the nature of modeling capabilities, aspects of tissue mechanics which cannot be observed experimentally, such as complex network reorganization and fiber failure, could be interrogated. Once developed, the multiscale model was expanded to study image-based tissue equivalents [Sander et al., 2009b, Sander et al., 2009a], single-element fiber networks [Lake et al., 2012, Lai et al., 2012], and structure-based models of the arterial wall [Stylianopoulos and Barocas, 2007a]. These studies laid a strong foundation for expansion into other fiber-based soft tissues such as the facet-capsular ligament [Zarei et al., 2017a, Zarei et al., 2017b], the Pacinian corpuscle [Quindlen et al., 2015], and the aorta [Shah et al., 2014, Witzenburg et al., 2017]. By combining experimental testing with multiscale modeling, model parameters could be specified to match experimental behavior, giving rise to appropriate model behavior. The coalescence of experimental testing and computational modeling provides a unique characterizing of tissue allows for more in depth analysis of components that cannot typically be explored experimentally. Failure was also incorporated into the multiscale model for single network fatigue studies [Dhume et al., 2018] as well as macroscale arterial mechanics [Witzenburg et al., 2017]. The natural progression of this work led us to begin thinking about how pathological tissue can alter mechanical behavior, and in particular, how failure could be analyzed within the context of a multiscale model for situations such as myocardial infarctions and aortic aneurysms.

1.2.2 Outline of Current Work

The first step in addressing cardiovascular tissue failure was understanding commonly used techniques for predicting failure in anisotropic tissues. The idea of failure prediction, however, is not easily handled within computational modeling, as soft tissues have an exceptionally complex microstructure. As a result, failure criteria are often simplified to using isotropic methods, which inherently cannot predict failure in anisotropic tissues. This led us to study the efficacy of a commonly-used anisotropic failure criteria in fibrous laminates, the Tsai-Hill failure criteria (chapter 2, [Korenczuk et al., 2017]). We found that the Tsai-Hill failure criteria outperformed other isotropic criteria when attempting to predict failure in porcine abdominal aortic tissue, which is inherently anisotropic. Though our conclusions from this work were valuable, our model used a bulk constitutive description defined by simplified fiber families, and did not incorporate failure on the fiber-level.

Next, to observe how fiber failure could be studied with our multiscale model, we explored the effect of fiber alignment on myocardial infarcted tissue (chapter 3). Myocardial infarctions present a unique fiber-based tissue scenario, as collagen fibers are deposited in various configurations throughout the scar tissue, creating a collagen-dominated, heterogeneous area of tissue. We created three different fibrous networks based on previously imaged rat myocardial infarcted tissue; an isotropic network, a homogeneous network, and a heterogeneous network. Multiscale simulations were performed on macroscale geometries based on tissue morphology using each of the three network types, providing an opportunity to explore how altering fiber heterogeneity and anisotropy could affect failure mechanics of a highly-collagenous cardiac tissue. Our results showed that heterogeneity and strength of alignment had an effect on the overall tissue mechanics, particularly failure. Simulations with heterogeneous fiber networks exhibited a higher amount of fiber failure when compared to

the isotropic and homogeneous networks. This work confirmed the importance of accurate microstructural considerations when assessing tissue failure, motivating us to study other cardiovascular pathologies.

Expanding on work done previously on the aorta [Shah et al., 2014, Witzenburg et al., 2017], we explored the mechanics and failure of ATAAs (chapter 4), a complex pathology in the cardiovascular system. We collected a comprehensive data set of experimental data from multiple tissue loading configurations, and paired the data with a complex multiscale model to specify model parameters and interrogate tissue failure. Experimentally, we found that ATAA tissue was weaker than healthy porcine tissue, and exhibited the lowest strength in shear loading conditions. Computationally, we found that interlamellar connective fibers experience higher failure in shear loading, and display the highest amount of failure from any fiber type in inflation simulations. Shear stresses during inflation simulations were also relatively high, suggesting that intramural shear plays a role in the failure risk of ATAAs. To our knowledge, this work is the first to present a comprehensive experimental data set on ATAA tissue paired with a patient-specific multiscale finite-element model interrogating tissue failure.

Guided by the results in chapter 4, we wanted to identify the role of each microstructural constituent in the overall mechanics of arterial tissue to better understand failure. We performed uniaxial and shear testing on healthy porcine abdominal aortic tissue, and compared results to tissue treated with collagenase, elastase, and SDS. These treatments sought to remove microstructural components, and thus their contribution to overall mechanics, namely: collagen, elastin, and smooth muscle cells, respectively. We found that removal of collagen and elastin led to weaker mechanical strength in uniaxial loading, emphasizing the the mechanical role of the lamellar layer in planar configurations. Removal of smooth muscle cells did not affect the

mechanical strength in uniaxial loading, but did play a role in shear loading conditions, weakening the vessel's strength and increasing the failure stretch. The results substantiate similar conclusions found in chapter 4, namely, that VSMCs and other interlamellar components play a role in shear mechanical strength.

These chapters, taken collectively, provide a versatile foundation for further work in the space of cardiovascular tissue failure.

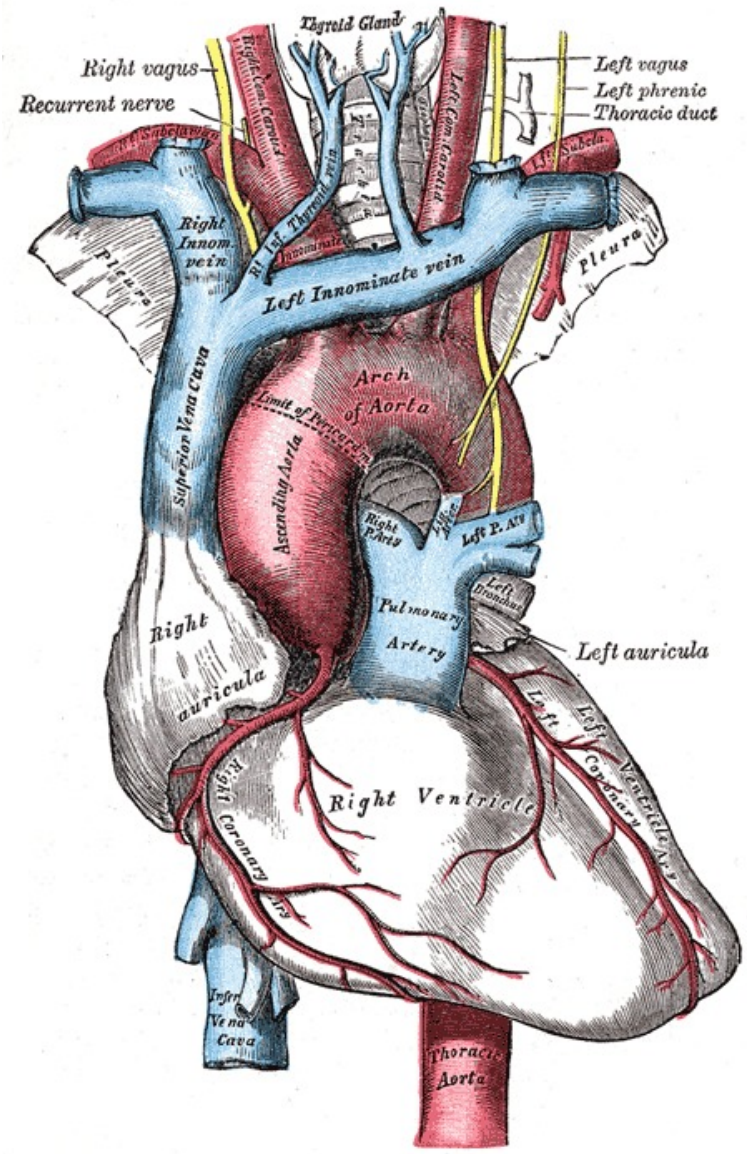

Figure 1.1: Anatomy of the heart [Gray, 1918].

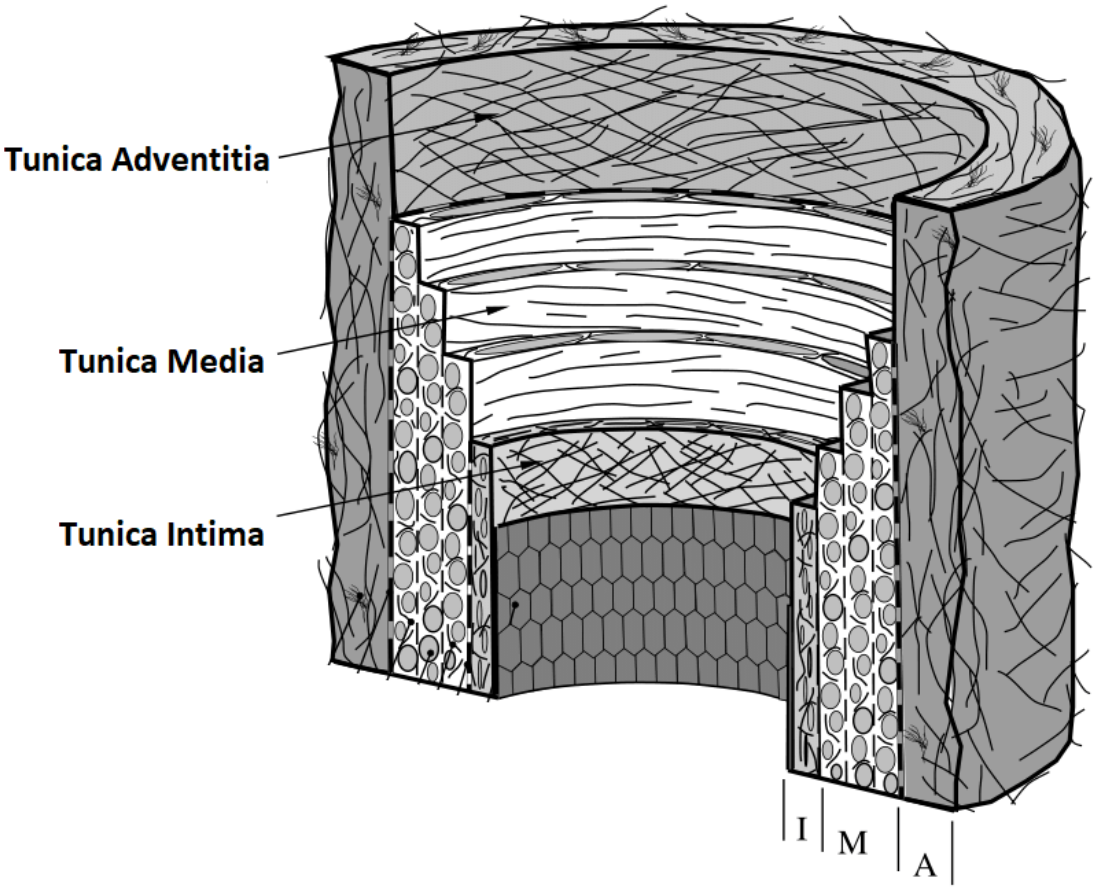

Figure 1.2: Arterial structure, adapted from [Gasser et al., 2006].

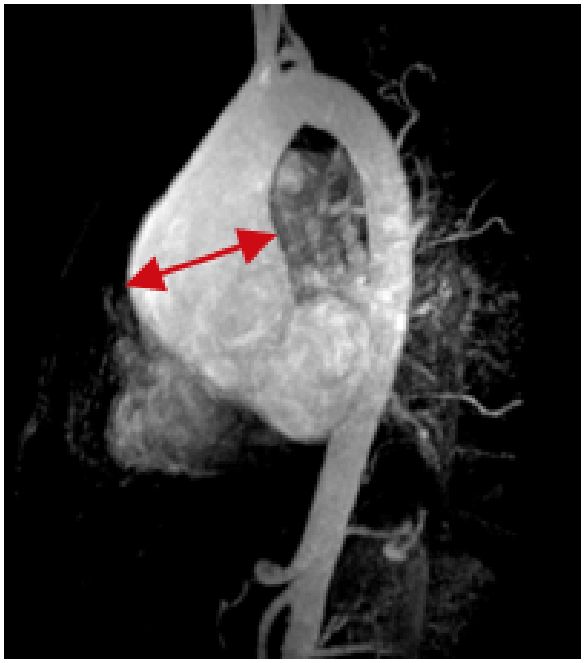

Figure 1.3: A magnetic resonance angiogram of an ATAA [Cruz et al., 2007]. Arrows indicate enlarged diameter.

Chapter 2

Isotropic Failure Criteria are not Appropriate for Anisotropic Fibrous Biological Tissues

The content of this chapter was published as a research article in the *Journal of Biomechanical Engineering* by Korenczuk, Votava, Dhume, Kizilski, Brown, Narain, and Barocas [Korenczuk et al., 2017]. My contribution to the work was performing experimental testing on aortic tissue, data processing, computational modeling, and a majority of the writing.

2.1 Introduction

Accurate failure prediction techniques are essential to assess and understand biological tissues at risk of failure. In the case of adverse physiological conditions (i.e. traumatic injury, repetitive use, pathological states, etc.), tissue failure is often unprecedented and always unfavorable. When tissue function is compromised, preventive actions

such as surgical resection, replacement, or repair can be used to correct and/or fortify the damaged tissue. Without the ability to assess tissues at risk of failure properly, however, corrective action may be misguided or incomplete. As a result, failure analysis and modeling have become increasingly active research areas [Grosse et al., 2014, Sanyal et al., 2014, Zwahlen et al., 2015, Clouthier et al., 2015].

Many fibrous soft tissues exhibit anisotropic mechanical behavior, including arteries [Holzapfel et al., 2005, Vorp et al., 2003, Duprey et al., 2016, Luo et al., 2016], ligaments [Woo et al., 1983, Woo et al., 1991, Little and Khalsa, 2005, Claeson and Barocas, 2017], tendons [Nicholls et al., 1983, Natali et al., 2005], and skeletal muscle [Takaza et al., 2012, Gennisson et al., 2010]. Directionally-dependent material strength is central to tissue function, allowing for proper load bearing during the complex loading situations brought on by bodily processes and movement. For example, the anterior cruciate ligament (ACL) is composed of elastin, extracellular proteins, and highly aligned collagen (type I) fibers in the longitudinal direction, which gives rise to a strong connection between the femur and tibia, providing resistance of anterior-tibial translation and rotation during various loading schemes [Duthon et al., 2006]. As collagen fibers are highly aligned in the direction of tensile loading, large forces are permitted during such movements, allowing the ACL to function as a vital mechanical stabilizer in the knee.

Showing the von Mises stress in computer simulations of a fibrous tissue at risk of failure has become a routine practice (e.g., [Volokh, 2011, Karimi et al., 2014, Wood et al., 2011, Phillippi et al., 2011a, Nathan et al., 2011, Humphrey and Holzapfel, 2012]). The von Mises stress incorporates the 6 components of the Cauchy stress tensor into a single, easily visualized, scalar value. While its ease of calculation and its availability as a standard output in most finite-element software packages make the von Mises stress attractive, its use is accompanied by the implicit assumption

that the von Mises failure criterion is applicable to the tissue in question. The von Mises criterion, however, is isotropic, in that the von Mises stress depends equally on stresses in all directions. By showing the von Mises stress within a tissue, one implicitly treats it as isotropic.

The maximum principal stress (MPS) is also commonly reported in finite element simulations of biological tissue [Hwang et al., 2015, Quental et al., 2016]. Like the von Mises stress, the MPS depends equally on stresses in all directions, thus making it inherently isotropic as well. The MPS may also be a poor stress metric to use when considering anisotropic tissues because the tissue is generally designed to bear the largest loads in the strongest direction. Another direction, however, may experience stress smaller than the MPS but greater than the material strength in that direction.

For many fibrous tissues (e.g. Achilles tendon), loading most often occurs along the direction of highest material strength, so considerations of an anisotropic failure criterion may not be necessary. For tissues that undergo complex loading situations, where failure may occur in multiple directions and ways, directional strength must be accounted for. As anisotropy plays a significant role in the proper mechanical functioning of these tissues, it is imperative that directional strength be considered when predicting failure of anisotropic tissues.

Typically, isotropic failure criteria have been used when assessing soft biological tissues. Volokh et al. [Volokh, 2011] explored the use of isotropic failure criteria, including the von Mises failure criterion, when assessing arteries using various constitutive models. They found that the von Mises failure criterion was incapable of accurately predicting failure in the case of biaxial loading situations, as expected, and suggested that anisotropic alternatives must be used. Nathan et al. [Nathan et al., 2011] assessed thoracic aorta wall stress in patients using the von Mises stress, without any failure considerations. Their conclusions focused on identifying locations

of high wall stress, however, all results were based solely on the von Mises stress, assuming that it is a meaningful measure of stress in the aortic wall. These studies, among others [Karimi et al., 2014, Wood et al., 2011, Phillippi et al., 2011a, Humphrey and Holzapfel, 2012], exemplify how common it has become to use the isotropic von Mises stress and failure criterion when tissues well known to be anisotropic.

Extensive work has been done to analyze the failure behavior of non-biological anisotropic fiber composites [Agarwal et al., 2006, Matzenmiller et al., 1995, Derrien et al., 2000, Nuismer and Whitney, 1975, Fuchs et al., 2006, Aktas and Karakuzu, 1999]. For example, the Tsai-Hill theory [Tsai, 1968, Hill, 1950] is a popular maximum-work theory to characterize the in-plane failure of orthotropic lamina. For a given stress state, the theory provides a single scalar failure criterion based on the principal material direction strengths and the shear strength. The Tsai-Hill theory has been used to study reinforced polymer-polymer composites [Fuchs et al., 2006], carbon-epoxy composites [Aktas and Karakuzu, 1999], and simulations of fiber composites [Arola and Ramulu, 1997], along with other fibrous materials [Liu, 2007, Woo and Whitcomb, 1996], and has proven effective as a failure criterion for such materials.

Thus, unlike the von Mises failure criterion, the Tsai-Hill failure criterion provides a potential platform to analyze how off-axis loading affects an anisotropic fibrous material. This advantage, however, is not without cost. The Tsai-Hill criterion requires three parameters for full model specification, in contrast to the single parameter of the von Mises criterion, so additional testing is needed. An additional advantage of the von Mises stress is that it can be calculated without foreknowledge of the failure behavior of the tissue.

Clearly, the choice of failure model depends on the specific system under study and the question(s) to be answered, but the validity of the von Mises stress as a metric of the stress state in an anisotropic tissue must be challenged. In the present

work, we conducted a series of failure experiments on a representative anisotropic tissue (porcine aorta) and analyzed the results using both an isotropic (von Mises) and an anisotropic (Tsai-Hill) failure criterion.

2.2 Methods

The porcine abdominal aorta is an anisotropic tissue that contains an underlying fiber laminate structure comprised mainly of collagen and elastin. The primary load-bearing layer, the tunica media, consists of lamellar sheets of elastin and collagen connected by vascular smooth muscle cells and extracellular proteins such as fibrillin-1 [Wagenseil and Mecham, 2009]. The collagen fibers exhibit a strong preferential alignment in the circumferential direction, along with a weaker, but still significant preference for the axial over the radial direction [Gasser et al., 2006], making these two fiber alignments the assumed principal material directions. Thus, the porcine arterial wall provided an excellent representative system on which to study the efficacy of different failure criteria.

2.2.1 Experiment

Uniaxial Dog-Bones

Porcine abdominal aortas (11.35 ± 1.67 cm in length, mean ± SD) were obtained from 6-9 month old pigs (n=7, 83.6 ± 10.0kg in weight) following an unrelated study and stored in a 1x phosphate-buffer saline (PBS) solution at 4° C. The aorta was cleaned of excess connective tissue on the adventitial surface, and in some cases a small amount of adventitia was inadvertently removed during the dissection process. Each aorta was cut open axially along the posterior region where it was anchored to the vertebral column. Uniaxial dog-bone samples (approximately 5 mm in width

and 10 mm in length with a 3 mm wide neck region) were cut from the opened aorta with sample angles ranging from 0° (circumferential) to 90° (axial) with respect to the vessel circumference in increments of 15° (Fig. 2.1A, n > 9 for each angle). Sample orientation was randomized along the length of the vessel to minimize error due to any regional heterogeneity. Each sample was photographed prior to testing, and the undeformed sample width and thickness were measured using ImageJ. Samples were speckled with powdered, dry Verhoeff's stain in order to produce a distinct surface texture for full-field displacement tracking analysis via digital image correlation (DIC) [Raghupathy et al., 2011]. Samples were loaded into custom grips and subjected to uniaxial tensile loading tests (Instron 8800 Microtester) at 10 mm/min until failure (Fig. 2.1B) in a 1x PBS bath at room temperature. Loads were recorded by a 500N load cell. All experiments were performed within 48 hours of harvest.

The measured force was divided by the undeformed cross-sectional area to calculate the 1st Piola-Kirchhoff stress. Due to speckle adherence issues in the PBS bath, a significant number of uniaxial samples (> 40) did not have a usable, distinct speckle pattern for DIC. Strain tracking of selected dogbones (n=5) showed a maximum error of 10% between the grip stretch and the neck region stretch, so grip stretch was used to convert 1st Piola-Kirchhoff stresses into Cauchy stresses under the assumption of tissue incompressibility. To validate this method, Cauchy stresses for 6 samples with usable speckle patterns from one sample angle were calculated based on neck stretch obtained via DIC as well as grip stretch. Cauchy stresses calculated with the grip stretch were within 10% of the stresses calculated with the neck stretch throughout the entire loading curve, and some samples exhibited even as low as 1-2% error throughout the entire loading curve. Statistical analyses (one-way ANOVA and Tukey's multiple comparisons) of failure stresses were performed using GraphPad Prism 6.

Uniaxial Shear Lap Samples

Shear lap samples were prepared (n=7 from 2 porcine aortas) with sample arms oriented in the circumferential direction (Fig. 2.1C). Samples were approximately 35 mm long with an arm width of 3 mm. The overlap region was approximately 5 mm wide at the largest point. The sample geometry was selected due to the large amount of shear that would be imposed in the overlap region of the sample during mechanical testing (c.f. [Witzenburg et al., 2017, Gregory et al., 2011]), yielding a challenging problem for failure predictors.

Samples underwent the same procedure as specified for the uniaxial dog-bones regarding tissue dissection, storage, photographing, and speckling. Shear lap samples were clamped in custom grips, submerged in a 1x PBS bath at room temperature, and pulled in strain-to-failure experiments on a uniaxial testing machine (MTS, Eden Prairie, MN) at a rate of 3 mm/min. Forces were recorded by a static 10N load cell. The displacement at the onset of failure was determined by correlating the sample video time with the recorded data.

Area fraction of the smaller remaining piece post-failure was calculated using an image of the sample immediately prior to total failure. A crack propagation line was selected for each experimental sample by connecting the start and end points of the crack. Samples were then manually outlined, and the pixel area was calculated for the entire sample and the two pieces on both sides of the crack propagation line. A pixel area average from 5 manual outlines was used for each piece. Area fraction was calculated as the pixel area of the smaller torn piece divided by the total pixel area of the sample.

The crack propagation angle was calculated in the undeformed domain for each shear lap sample. The line of crack propagation on the image prior to total failure was projected back to the undeformed domain using the deformation gradient (obtained by

strain tracking methods described earlier) for an element along the crack propagation line. The crack propagation angle was then calculated between the crack propagation line in the undeformed domain and the horizontal direction.

2.2.2 Failure Criteria

The von Mises failure criterion takes the form

$$\left[\frac{(\sigma_1-\sigma_2)^2+(\sigma_2-\sigma_3)^2+(\sigma_3-\sigma_1)^2+6(\tau_{12}^2+\tau_{23}^2+\tau_{31}^2)}{2}\right]^{1/2} \leq \sigma_{yield} \tag{2.1}$$

where σ_i are the normal Cauchy stresses with respect to the coordinate directions. In the case of uniaxial extension (in the 11 direction),

$$\sigma_2 = \sigma_3 = 0 \tag{2.2}$$

$$\tau_{12} = \tau_{23} = \tau_{31} = 0 \tag{2.3}$$

which reduces the von Mises failure criterion to the form

$$\sigma_1 \leq \sigma_{yield} \tag{2.4}$$

When σ_1 reaches the failure threshold, σ_{yield}, failure is predicted. As the choice of uniaxial yield stress for the von Mises failure criterion is ambiguous, three cases were explored, where the yield stress was equal to 1) the overall average uniaxial failure stress, 2) the average uniaxial circumferential failure stress, and 3) the average uniaxial axial failure stress.

The Tsai-Hill model for a uniaxial test takes the form [Agarwal et al., 2006]

$$\frac{\cos^4\theta}{\sigma_{1U}^2} - \frac{\cos^2\theta\sin^2\theta}{\sigma_{1U}^2} + \frac{\sin^4\theta}{\sigma_{2U}^2} + \frac{\sin^2\theta\cos^2\theta}{\tau_{12U}^2} < \frac{1}{\sigma_x^2} \tag{2.5}$$

where σ_{1U}, σ_{2U}, τ_{12U} are constants representing the material behavior. Specifically, σ_{1U} ultimate strength of the material in the principal material direction (direction of highest material strength, typically that of fiber orientation), σ_{2U} is the ultimate strength of the material in the transverse direction, and τ_{12U} accounts for the shear strength of the material. For in-plane artery tests, the preferred principal material direction was assumed to be the circumferential, and the transverse direction was taken to be the axial, since uniaxial testing shows higher circumferential failure stresses compared to axial [García-Herrera et al., 2012, Iliopoulos et al., 2009a, Sokolis et al., 2012]. Therefore, in eqn. (5), θ was defined to be the counterclockwise sample angle relative to the circumferential direction, σ_{1U} was the circumferential (0°) failure stress, σ_{2U} was the axial (90°) failure stress, τ_{12U} was the shear stress, and σ_x was the failure stress in uniaxial extension at a given sample angle. When $\theta = 0°$, the condition reduces to $\sigma_x > \sigma_{1U}$, and when $\theta = 90°$, the condition reduces to $\sigma_x > \sigma_{2U}$. The three constants σ_{1U}, σ_{2U}, τ_{12U} were fit to the experimental data.

2.2.3 Finite Element Modeling

Finite element models were constructed in FEBio [Maas et al., 2012] to simulate the shear lap experiments. Each undeformed shear lap sample geometry (n=7) was reconstructed based on the image taken during experimental testing. A uniform thickness was applied to each sample to match its measured thickness (2.07 ± 0.28 mm, mean ± SD). Geometries were meshed in Abaqus with approximately 6,000 brick elements.

Sample meshes were imported into FEBio for finite element analysis. The tissue was specified as a volume-conserving uncoupled solid mixture consisting of a Neo-Hookean component given by the strain-energy density function

$$\tilde{\Psi} = C_1(\tilde{I}_1 - 3) + \frac{1}{2}K(\ln J)^2 \tag{2.6}$$

where C_1 is the Neo-Hookean material coefficient, $\tilde{I}_1$ is the first strain invariant of the deviatoric right Cauchy-Green tensor, K is the bulk modulus, and J is the determinant of the deformation gradient tensor. There was also one fiber family, oriented in the circumferential direction, specified by the strain-energy density function

$$\tilde{\Psi} = \frac{\xi}{\alpha\beta}(\exp\left[\alpha(\tilde{I}_4 - 1)^\beta\right] - 1) \tag{2.7}$$

where ξ is the fiber modulus, α is the exponential coefficient, β is the power of the exponential, and $\tilde{I}_4$ is the square of the fiber stretch. β was set to 2, and C_1, ξ, and α were left as fitting parameters based on the pre-failure behavior of the tissue during the experiment.

The bulk modulus, K, was set to one thousand times the Neo-Hookean material coefficient (C_1) to ensure that the model was nearly incompressible. The fiber family also had a bulk modulus, which was set to one thousand time the fiber modulus (ξ) to ensure incompressibility. Incompressibility was satisfied within 1-7% when the stress reached its maximum. One fiber family, as opposed to multiple, was used to create a constitutive model that captured the experimental behavior with minimal fitting parameters.

To perform each simulation, boundary conditions were applied to the fixed and moving faces of the sample mesh to match the experiment. The nodes on the fixed face were given a zero-displacement boundary condition in all directions, while the

nodes on the moving face were given a zero-displacement boundary condition in the vertical and out of plane directions (Fig. 2.2). Prescribed nodal displacements, based on experimental displacements, were applied to the moving face.

The material fitting parameters (C_1, ξ, and α) were optimized to fit the experimental loads for each sample by a customized routine utilizing a modified version of the Matlab *fminsearch* function to minimize the squared error between the simulation and experimental loads (described fully in [Claeson and Barocas, 2017]). The reaction forces on the moving face were output from the simulation and compared to the experimental loads at 10 specified displacements. Comparing the force output from the simulation to the pre-failure experimental forces ensured a proper material description. On average, $R^2 = 0.99$ for the 7 shear lap samples, with the worst fit having $R^2 = 0.97$. Optimization was performed on one core at the University of Minnesota Supercomputing Institute.

2.2.4 2D Failure Propagation Simulations

To compare the predictive capabilities of the von Mises and Tsai-Hill criteria, 2-D failure calculations for the shear lap samples were performed in a modified version of the ArcSim thin sheet dynamics simulator [Narain et al., 2014]. The deforming sample geometry was modeled as a triangle mesh in two dimensions, with elastic forces computed using linear finite elements. The constitutive model (same as above) was adapted to triangular elements by treating them as constant strain prisms with zero out-of-plane shear. Imposing the assumptions of incompressibility and zero out-of-plane normal stress then determined the deformed thickness and the in-plane stress. Rayleigh damping proportional to the tangential stiffness matrix was added.

In order to resolve regions undergoing failure, the finite element mesh was dynamically refined during the course of the simulation using the algorithm of Narain

et al. [Narain et al., 2012]. Refinement was driven solely by the value of the failure criterion, so that regions close to failure were refined to maximum resolution (a target edge length of 0.05 mm). Failure propagation was computed using the substepping algorithm described by Pfaff et al. [Pfaff et al., 2014], that alternated between two steps: (i) splitting elements that reached the failure threshold, and (ii) recomputing stresses in the neighborhood using a virtual time step. The substepping algorithm was modified to delete elements undergoing failure, as computing accurate split directions for arbitrary failure criteria proved difficult. The mass loss caused by element deletion was negligible because adaptive refinement ensured extremely small elements near the failure location.

Area fraction was determined for each failure criterion by calculating the mesh area on both sides of the fully failed sample. As in the experimental shear lap samples, area fraction was taken as the area of the smaller torn side over the total area of the sample. Crack propagation angle was calculated for both failure criteria on each sample in the undeformed domain (Fig. 2.8C,D). A line of crack propagation was created by connecting the two points of crack initiation and total crack failure, and the angle between that line and the horizontal direction determined the crack propagation angle.

2.2.5 Failure Calculations in 2-D Simulations

The von Mises stress was calculated for each element and normalized by the von Mises yield stress, σ_{yield}, based on the values obtained from experimental testing. Three σ_{yield} values were considered when assessing failure with the von Mises failure criterion

- $\sigma_{yield} = \sigma_C$, the mean failure stress in the circumferential direction

- $\sigma_{yield} = \sigma_A$, the mean failure stress in the axial direction
- $\sigma_{yield} = \sigma_{avg}$, the overall average failure stress based on the mean failure stresses at each sample angle

By normalizing the von Mises stress to each one of these σ_{yield} values, failure was considered when the normalized stress in any element reached 1.

In order to evaluate the Tsai-Hill failure criterion, a modified form of (5) was used [Agarwal et al., 2006], in which a failure metric Φ was defined,

$$\Phi = \left(\frac{\sigma_1}{\sigma_{1U}}\right)^2 - \left(\frac{\sigma_1}{\sigma_{1U}}\right)\left(\frac{\sigma_2}{\sigma_{1U}}\right) + \left(\frac{\sigma_2}{\sigma_{2U}}\right)^2 + \left(\frac{\tau_{12}}{\tau_{12U}}\right)^2 \tag{2.8}$$

where σ_{1U}, σ_{2U}, and τ_{12U} are the same as previously stated, and σ_1, σ_2, and τ_{12} are the stresses in the primary fiber, transverse, and shear directions, respectively. When Φ reached 1, failure was predicted. The model fiber family was oriented in the 1 direction (circumferential) in the undeformed tissue (i.e., the unit fiber vector $N^{(1)}$ points in the horizontal direction). Based on the deformation of each element during the simulation, however, the fiber direction changed. Thus, to calculate the Tsai-Hill failure metric, the Cauchy stress tensor was double-contracted with the affinely rotated unit vectors to calculate σ_1, σ_2, and τ_{12}. Specifically,

$$n_i^{(1)} = \frac{F_{ij}N_j^{(1)}}{\|F_{ij}N_j^{(1)}\|} \tag{2.9}$$

$$n_i^{(2)} = \frac{F_{ij}N_j^{(2)}}{\|F_{ij}N_j^{(2)}\|} \tag{2.10}$$

where $N_j^{(1)}$ is the primary fiber direction in the undeformed domain, $N_j^{(2)}$ is the transverse direction in the undeformed domain, F_{ij} is the deformation gradient of the

element, and $n_i^{(1)}$, $n_i^{(2)}$ are the primary fiber and transverse directions in the deformed domain, respectively. Therefore, the stress calculations were as follows,

$$\sigma_1 = \sigma_{ij} n_i^{(1)} n_j^{(1)} \tag{2.11}$$

$$\sigma_2 = \sigma_{ij} n_i^{(2)} n_j^{(2)} \tag{2.12}$$

$$\tau_{12} = \sigma_{ij} n_i^{(1)} n_j^{(2)} \tag{2.13}$$

where σ_{ij} is the Cauchy stress for each element, calculated by ArcSim. Based on (8), failure was predicted when the value of Φ in any element reached 1.

2.3 Results

Experimental testing (n $>$ 9 for each dogbone orientation angle) showed that the largest failure stress occurred in the circumferentially aligned tests (0°) at 2.67 ± 0.67 MPa (mean ± 95% CI), as expected based on previous studies [Witzenburg et al., 2017, García-Herrera et al., 2012]. A decrease in failure stress was seen with increasing sample angle to the fully axially aligned case (90°) at 1.46 ± 0.59 MPa (Fig. 2.3). The smallest failure stress was seen in the 75° case at 1.41 ± 0.51 MPa, but that value was not significantly lower than the failure stress at 90°. A one-way ANOVA showed that the effect of sample angle change on the failure stress was highly significant (p = 0.0003), and a Tukey-HSD comparison showed a significant difference between the 0° and 90° alignment cases (p = 0.01).

The von Mises failure criterion did not fit the experimental data well, as the von Mises stress reduces to a single value in the uniaxial case (eqn. 4). Although the

95% confidence interval range encompassed most of the failure stresses when using $\sigma_{yield} = \sigma_{avg} = 1.87$ MPa (Fig. 2.4A), the von Mises criterion could not capture the anisotropic response of the tissue. The data were also not fit when using both $\sigma_{yield} = \sigma_C = 2.67$ MPa and $\sigma_{yield} = \sigma_A = 1.46$ MPa. The Tsai-Hill model (eqn. 5), in contrast, showed an excellent fit to the experimental data ($R^2 = 0.986$, Fig. 2.4B). Fitting the model provided $\sigma_{1U} = 2.71 \pm 0.19$ MPa (mean ± 95% CI) , $\sigma_{2U} = 1.40 \pm 0.14$ MPa, and $\tau_{12U} = 1.04 \pm 0.12$ MPa.

The shear lap samples (n = 7) all exhibited nonlinear behavior until failure (Fig. 2.1D). Digital image correlation showed a large amount of shear strain (∼40%) in the overlap region of the sample (Fig. 2.5). The onset of tissue failure was calculated to occur at an average displacement of 19.73 ± 1.03 mm (mean ± 95% CI) and load of 3.14 ± 0.22 N, and the total failure of the tissue occurred at an average displacement of 21.53 ± 0.89 mm and load of 3.77 ± 0.33 N. Experimental shear lap samples failed in two different manners: 1) failure began on the arm near the overlap region and propagated into the overlap region of the sample until the sample failed (deemed "lap across" failure, Fig. 2.6B) and 2) failure began on the arm near the overlap region of the sample and propagated towards the overlap region, but ultimately the arm ripped off and failure did not occur in the overlap region ("lap arm" failure, Fig. 2.8A). 4 experimental samples experienced lap across failure, while 3 samples experienced lap arm failure. The crack propagation angle was calculated to be 28.13° ± 9.13° (mean ± 95%CI) relative to horizontal (Fig. 2.9), and the area fraction was calculated as 0.33 ± 0.52 (mean ± 95%CI, Fig. 2.7).

Failure simulations exhibited both types of failure (lap across and lap arm) seen experimentally, along with another, where failure began in the sample arm far away from the overlap region and propagated vertically, only in the arm region ("arm" failure, Fig. 2.6D, Fig. 2.8D). The von Mises failure propagation simulations (σ_{yield}

$= \sigma_{avg}$) predicted arm failure for all 7 samples. The crack propagation angle was calculated as $80.50^\circ \pm 6.52^\circ$ (mean $\pm$ 95%CI, Fig. 2.9) and the area fraction was calculated as 0.09 ± 0.06 (Fig. 2.7). The Tsai-Hill failure propagation simulations predicted 1 lap across failure, 4 lap arm failures, and 2 arm failures. The crack propagation angle was $59.86^\circ \pm 14.57^\circ$ (mean $\pm$ 95%CI, Fig. 9) and the area fraction was 0.16 ± 0.06 (Fig. 2.7).

Both the von Mises and Tsai-Hill failure criteria severely underpredicted the amount of displacement needed to produce initial failure in the samples. The von Mises failure criterion ($\sigma_{yield} = \sigma_{avg}$) predicted the onset of failure at 11.97 ± 0.94 mm (mean $\pm$ 95%CI) of displacement, and the Tsai-Hill failure criterion predicted the onset of failure at 11.86 ± 0.85 mm.

2.4 Discussion

Our results indicate that an isotropic failure criterion, such as the von Mises criterion, is not acceptable when assessing anisotropic tissues. Although the von Mises stress is convenient for visualization of finite element results, one must recognize that the anisotropy of the tissue is not addressed by the von Mises stress. Furthermore, tissues undergo complex loading situations that are unknown *a priori*, so it is unclear which von Mises yield stress to select for a given tissue. As a result, reporting the von Mises stress risks leading to conclusions that are at best quantitatively inaccurate and at worst misleading or outright wrong when tissue failure is being considered.

The degree of anisotropy in failure mechanics of the aortic wall is highly variable across studies, with different results arising for abdominal vs. thoracic aorta and for healthy vs. aneurysmal tissue [Vorp et al., 2003, Witzenburg et al., 2017, García-Herrera et al., 2012, Mohan and Melvin, 1983, Kim et al., 2012, Teng et al., 2015,

Shah et al., 2014]. We found a moderate anisotropy (factor of two in the uniaxial failure stress between directions) in our healthy porcine abdominal aortic samples. An increase in sample angle from the circumferential resulted in decreased failure stress.

The Tsai-Hill maximum-work theory provides a single scalar function that considers two perpendicular principal material directions, making it generally applicable to orthotropic lamina [Agarwal et al., 2006] such as the porcine abdominal aorta. It is a more robust and potentially a more relevant failure criterion, considering that many tissues, such as arteries, contain anisotropic fibrous networks. Our results show its potential as a tool to predict failure in anisotropic tissues, including the porcine abdominal aorta studied here. Over a range of loading conditions, the Tsai-Hill theory better predicted failure when compared to the von Mises failure criterion. It was able to capture the anisotropic behavior of porcine tissue in uniaxial experiments at different angles and more accurately predict failure type, propagation, and area fraction in 2-D failure simulations. Of course, the Tsai-Hill theory is only one simple model that accounts for material anisotropy, and it is likely that a different criterion may work better. For example, many bone (femoral) failure studies have accounted for directional strength by using an anisotropic failure criterion [Gómez-Benito et al., 2005, Pietruszczak et al., 1999, Cezayirlioglu et al., 1985, Feerick et al., 2013], namely, the Cowin Fracture Criterion [Cowin, 1986] based on the Tsai-Wu model [Tsai and Wu, 1971]. Furthermore, the Tsai-Wu model accounts for material strength in multiple directions, which may be more applicable to fibrous tissues with several fiber families, such as arteries.

Other tissues may exhibit regional heterogeneity and fiber anisotropy, in which case a modified approach would be needed. In addition, the Tsai-Hill theory only accounts for two principal directions, but arteries and other fibrous tissues have been

characterized by four or more fiber families [Humphrey and Yin, 1987] and/or a continuous fiber distribution [Gasser et al., 2006, Cortes et al., 2010, Sacks, 2003], so a more extensive model could be explored. Furthermore, the Tsai-Hill theory is 2-dimensional, and would require significant experimental effort to expand to 3 dimensions, as extensive material characterization in 3 dimensions would be required. 2-dimensional restrictions currently limit the potential application of the Tsai-Hill theory to complex 3-dimensional failure problems, such as aortic aneurysms, in which failure mechanisms are clearly 3-dimensional [Witzenburg et al., 2017,Pal et al., 2014, Sommer et al., 2008].

In our uniaxial experiments, the minimum failure stress occurred at an angle of 75° from the preferred direction, but that failure stress was not significantly different from the failure stress at 90° ($p > 0.5$). The Tsai-Hill criterion can support a non-monotonic failure-angle relation, as is often seen in synthetic fiber composites [Agarwal et al., 2006]. Whether the minimum at 75° was real or noise, and whether other tissues do or do not exhibit a local minimum in failure stress, are questions that merit further exploration.

The assumption of constant failure through the thickness of the shear lap samples and the use of a 2-dimensional failure code are questionable and likely incorrect. Furthermore, the constitutive equation is rather simplistic, the optimization only fit the forces on the moving face of the experimental sample, and no strain field data were used to help optimize constitutive parameters [Nagel et al., 2014]. An inadequate constitutive model most likely resulted in an inaccurate stress field, which may have contributed to the incorrect failure prediction results. The use of alternative constitutive models (i.e. the Holzapfel-Gasser-Ogden model [Gasser et al., 2006] or the four-fiber family model [Baek et al., 2007]) may prove more effective. The underprediction of displacement may be due to the extreme non-linearity of the exponentials,

leading to artificially high stresses as the strains increase, and a constitutive model which incorporates plasticity could potentially address this issue. The material was also treated as perfectly elastic, resulting in brittle failure. Furthermore, the von Mises and Tsai-Hill failure criteria do not address the idea of crack initiation and propagation in their formulation, which may be the main factor contributing to inadequate model predictions. These assumptions are the most likely causes for the limited ability of the models to accurately predict the displacement at the onset of failure, crack initiation, and crack propagation for all experimental samples.

It should also be noted that the use of a particular stress or failure criterion is dependent upon the objectives of a given study. Often, there is sufficient reasoning for using the von Mises stress when analyzing anisotropic tissues, such as comparing different tissue types, where the importance of comparison outweighs the need for accuracy; the von Mises failure criterion captures the failure behavior of porcine abdominal aorta with relatively mild error (Fig. 2.4A), which may meet the needs of a specific study. It is also often the case that extensive material strength data for anisotropic tissues are not readily available. Furthermore, available resources and the complexity of certain problems require computational simplifications, as in the case of large geometries comprised of multiple types of materials, in which case the von Mises stress would be better suited. Even in those cases, however, it is essential to recognize that if the tissue is anisotropic, its failure behavior will surely be anisotropic, and an isotropic failure criterion may be misleading.

Tissue failure is a very complex process, as demonstrated by experimental work [Vorp et al., 2003, Tong et al., 2016] and microstructural theory [Witzenburg et al., 2017, Pal et al., 2014, Balakhovsky et al., 2014]. Accurately characterizing tissue failure requires an adequate understanding of tissue behavior, particularly in relation to directional material strength and failure methods. Ignoring well-known tissue prop-

erties that contribute to failure (e.g., the mechanical anisotropy explored here) yields incorrect assessments, and ultimately limits the potential use of failure-predicting tools in applications such as patient diagnosis.

2.5 Acknowledgment

This material is based upon work supported by the National Science Foundation Graduate Research Fellowship Program under Grant No. 00039202 (CEK). Any opinions, findings, and conclusions or recommendations expressed in this material are those of the author(s) and do not necessarily reflect the views of the National Science Foundation. This work was supported by the National Institutes of Health (R01EB005813), and CEK is a recipient of the Richard Pyle Scholar Award from the ARCS Foundation. Tissue was provided by the Visible Heart Laboratory at the University of Minnesota. The authors acknowledge the Minnesota Supercomputing Institute (MSI) at the University of Minnesota for providing resources that contributed to the research results reported within this paper. We also gratefully acknowledge the assistance of Vahhab Zarei and Jacob Solinksy.

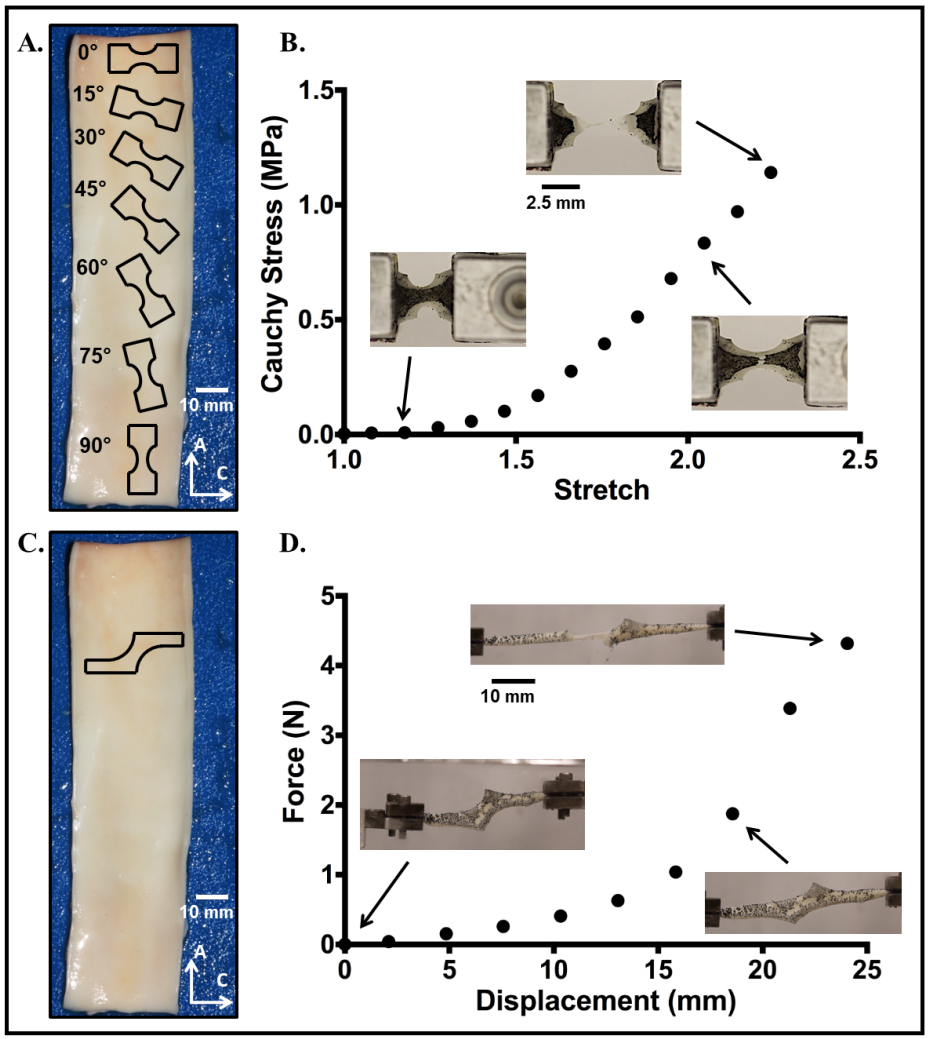

Figure 2.1: **A.** Outlines of dogbone sample geometries are shown along the axial length of the vessel (not drawn to scale). Angles were taken to be relative to the circumferential orientation (0^o). Scale bar shown in white. **B.** A representative stress-stretch curve for one uniaxial sample, with corresponding tissue images during testing. **C.** Outline of the shear lap sample geometry (not drawn to scale). **D.** A representative force-displacement curve for one shear lap sample. Failure initiated near the overlap region of the sample and propagated across the overlap region (lap across failure).

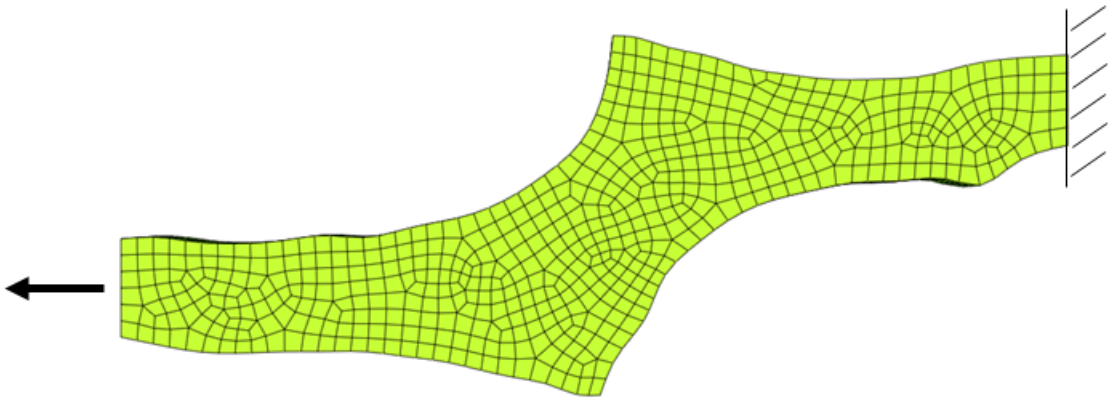

Figure 2.2: Finite element mesh for one shear lap sample with applied boundary conditions. The nodes on the right face were fixed in all directions, while the nodes on the left face were fixed in the vertical and out of plane directions, and given prescribed displacements based on the experiment.

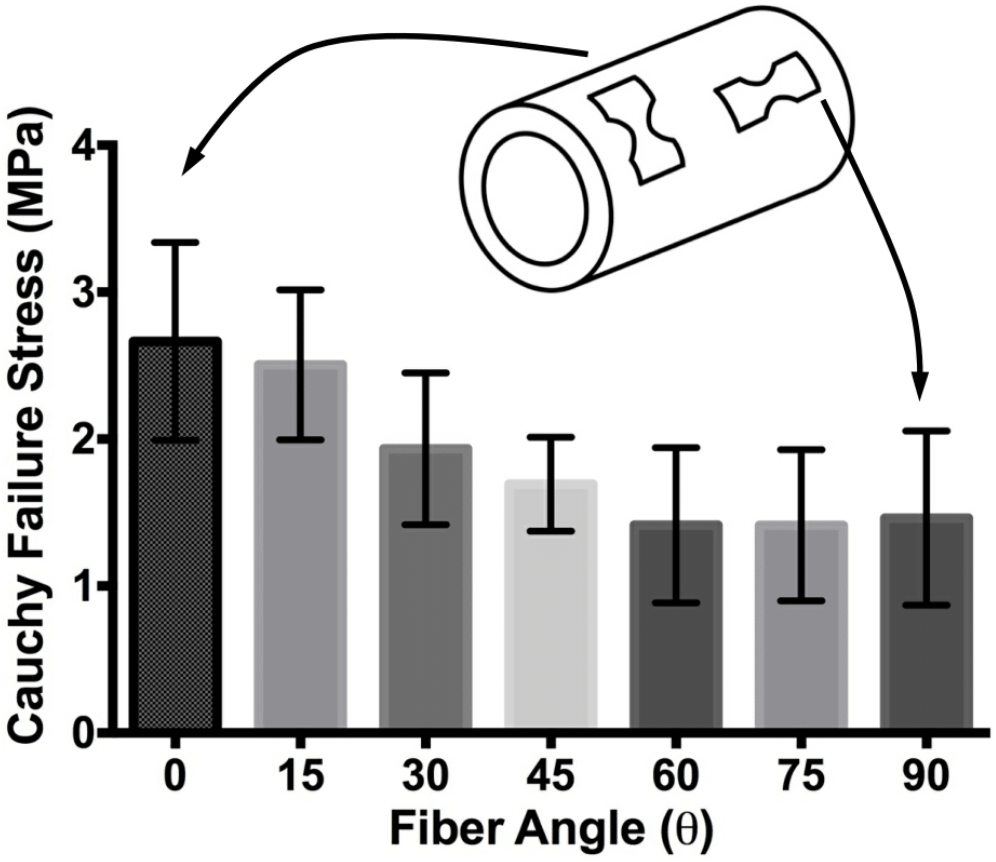

Figure 2.3: Failure stresses at each sample angle (n > 9 for each angle). ANOVA showed that change in sample angle had a statistically significant effect on failure stress (p = 0.0003). Error bars show 95% CI's.

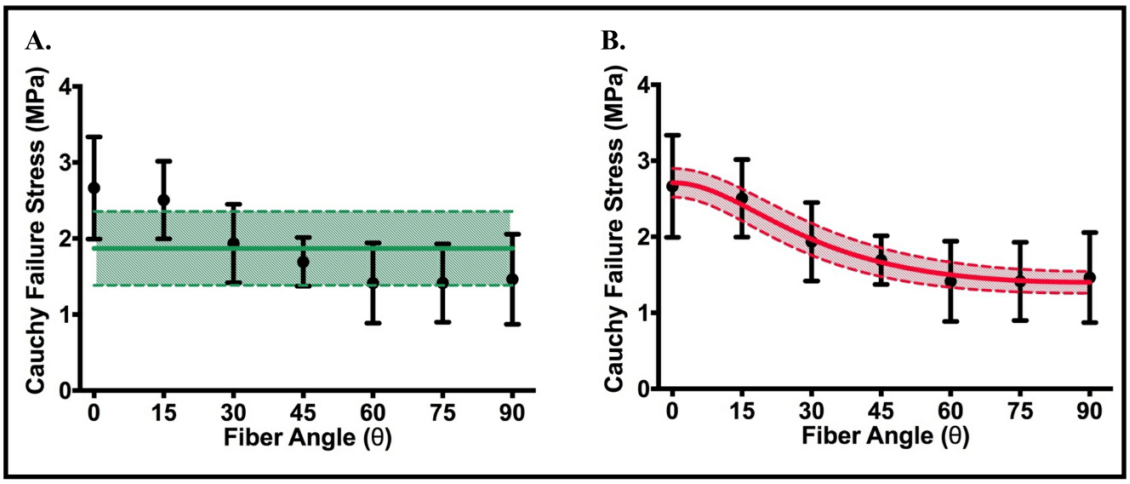

Figure 2.4: Experiment (points) and failure criteria fits. **A.** The von Mises failure criterion (solid green line, 95% CI shaded) fit to the mean peak stresses does not capture the anisotropic response of the tissue. **B.** Tsai-Hill maximum-work theory model (solid line, 95% CI shaded). Black error bars indicate 95% CI's on experimental points.

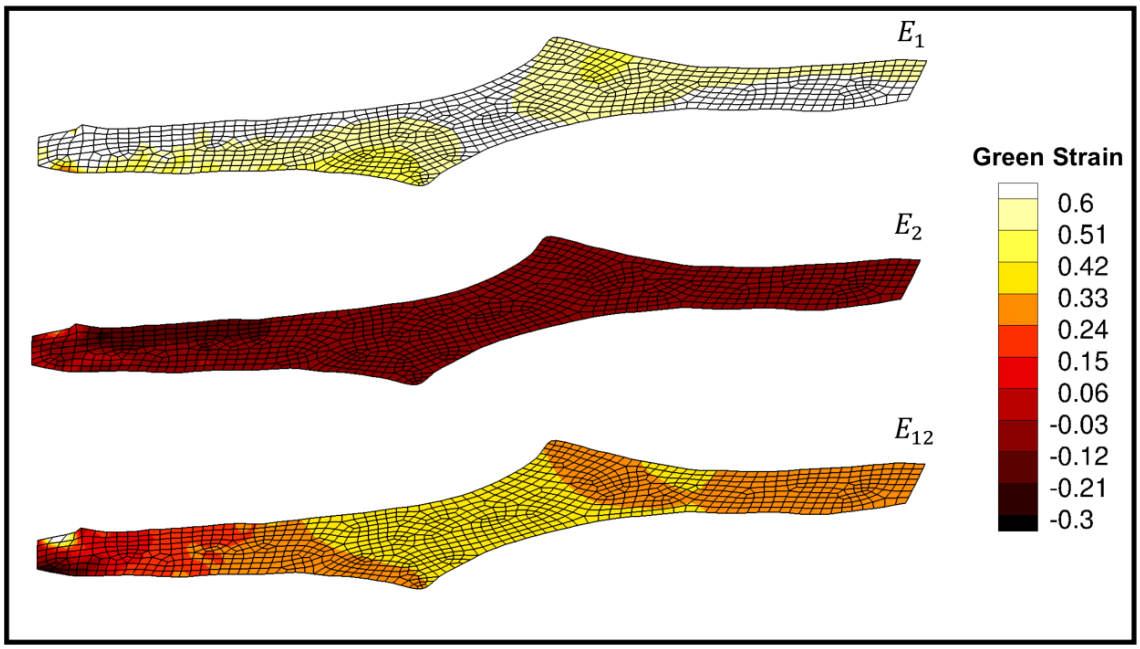

Figure 2.5: Strain tracking results from one shear lap sample. Large shear strains (∼40%) were exhibited in the overlap region of the sample.

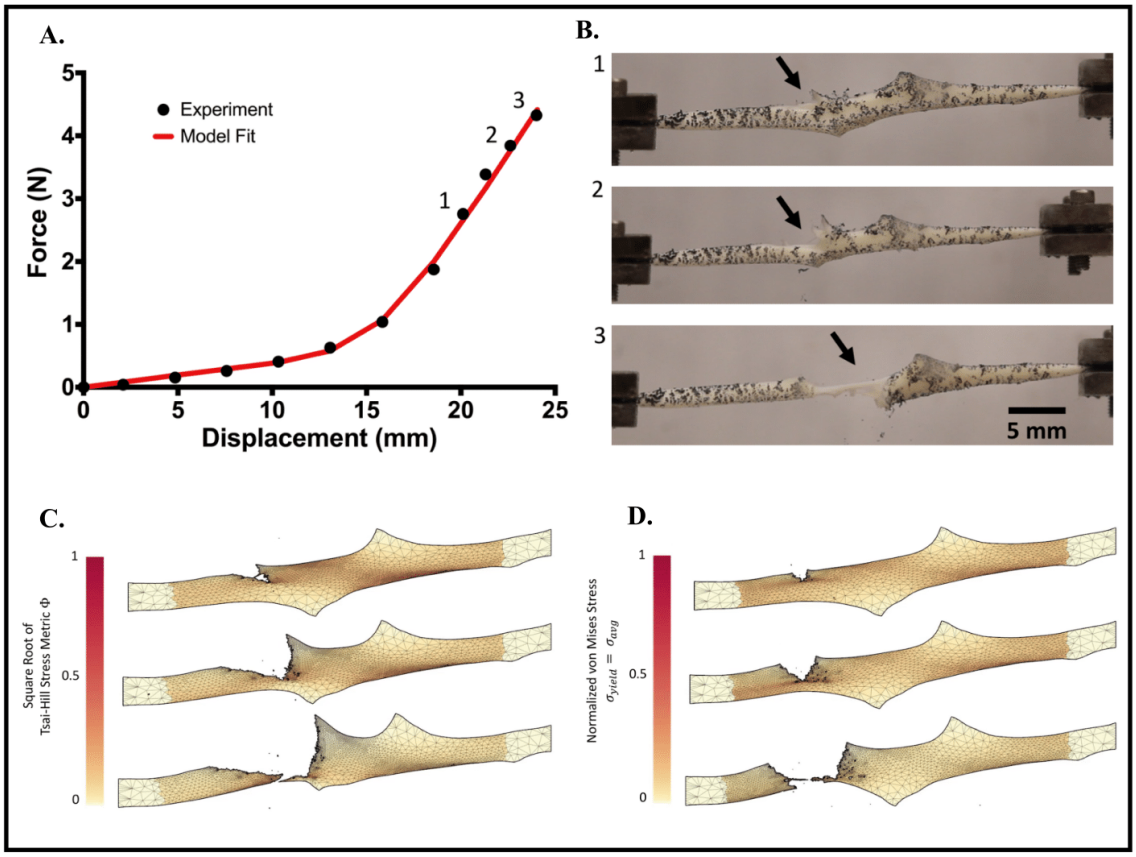

Figure 2.6: **A.** Representative force-displacement curve for one shear lap sample (black dots), with a simulation force-displacement curve (red line) using optimized parameters. **B.** Failure propagation for one shear lap sample, shown at three different displacements. The onset of failure began near the overlap region of the sample (indicated by the arrow), and propagated across the center (lap across failure). **C.** Failure simulation using the Tsai-Hill criterion. Propagation occurred through the overlap region of the sample, and eventually tore in the overlap region (lap across failure). **D.** Failure simulation using the von Mises criterion, where $\sigma_{yield} = \sigma_{avg}$. Failure propagated across the sample arm, and tore the arm off (arm failure). Failure simulations are shown at similar failure points to the experiment, but not at the same displacement as the experiment.

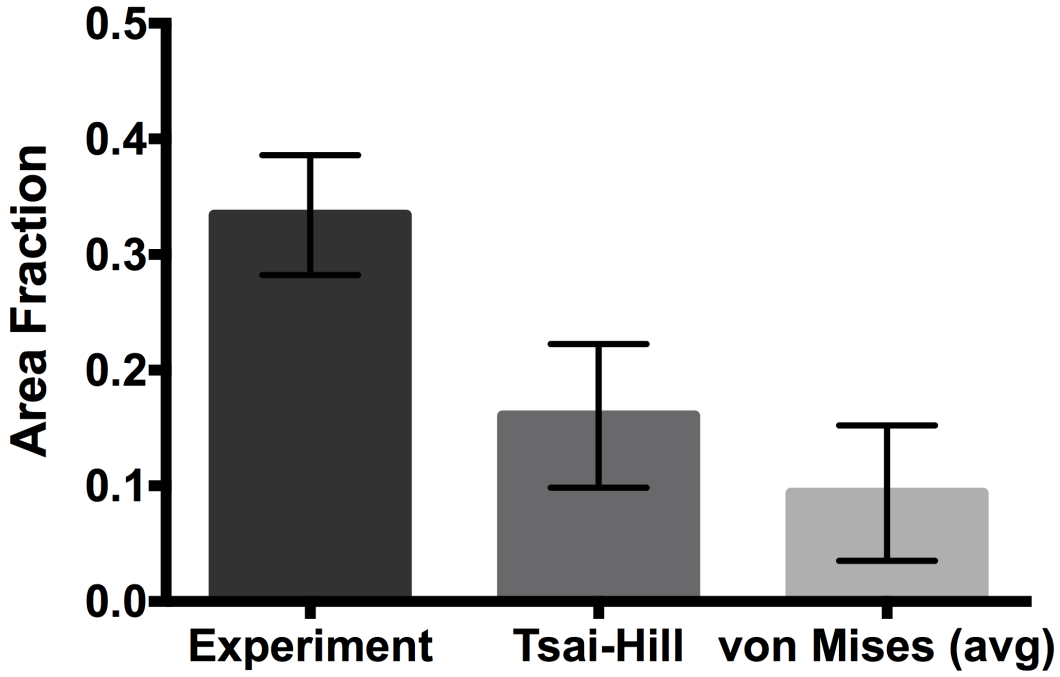

Figure 2.7: Area fraction for the experimental shear lap samples, along with the Tsai-Hill and von Mises (avg) failure cases. Averages shown with 95% CI bars.

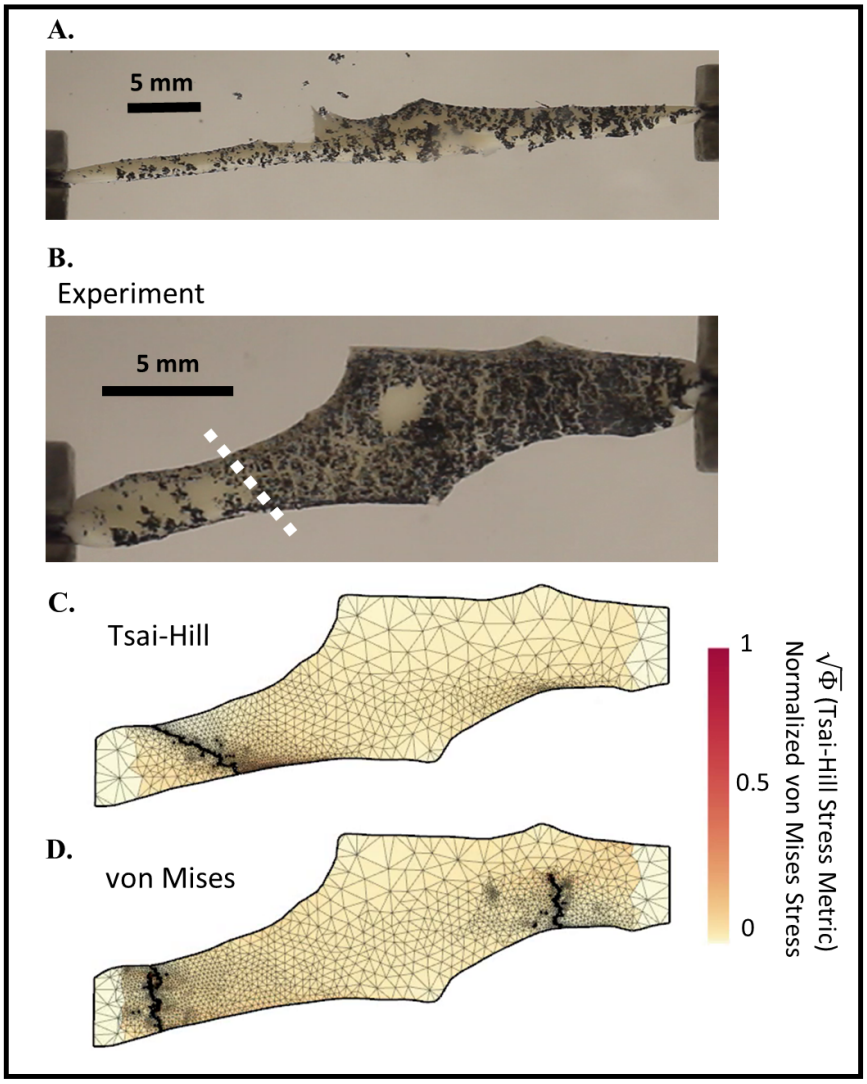

Figure 2.8: **A.** One experimental sample immediately prior to total failure. **B.** Sample in the undeformed domain. White dotted line indicates calculated crack propagation location and direction in undeformed domain. Lap arm failure occurred in the experimental sample. **C, D.** Typical failure comparison between the Tsai-Hill and von Mises failure criteria in the undeformed domain. The Tsai-Hill failure criterion predicted lap arm failure, while the von Mises failure criterion predicted arm failure.

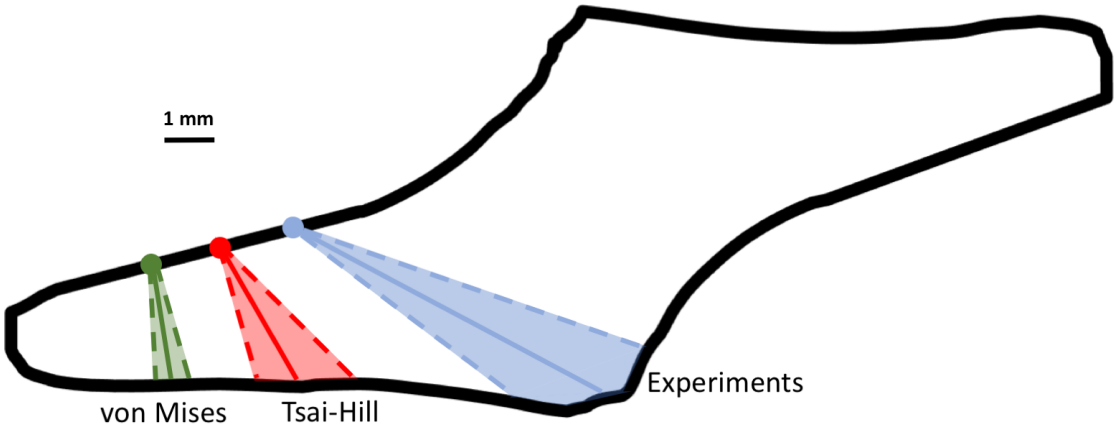

Figure 2.9: Average failure location (dots) and crack propagation angle (solid line) with 95%CI (dotted lines and shaded region) for experimental samples, Tsai-Hill, and von Mises (avg) failure simulations. Shown in black is the average shear lap sample geometry calculated using radius-based averaging from sample outlines (linear approximation was used for noisy regions of the average sample outline). Samples were rotated (if needed) so that failure occurred in the left arm for comparison purposes.

Chapter 3

Effects of Collagen Heterogeneity on Myocardial Infarct Mechanics in a Multiscale Fiber Network Model

The content of this chapter was submitted as a research article to the *Journal of Biomechanical Engineering* by Korenczuk, Barocas, and Richardson [Korenczuk, Christopher et al., 2019], and is currently under review. My contribution to the work related to image processing to extract fiber orientations and generate fiber networks, along with completing the multiscale modeling simulations, data processing, and writing.

3.1 Introduction

Each year, nearly 1 million Americans experience a myocardial infarction (MI), wherein a region of myocardial ischemia results in cardiomyocyte death and subsequent replacement by collagenous scar tissue [Benjamin et al., 2018]. Past work

has shown that the mechanical properties of the resulting scar are important for determining long-term cardiac function and risk for post-MI complications such as cardiac rupture and heart failure [Clarke et al., 2016, Richardson et al., 2015]. As is the case for many collagenous tissues, the particular mechanical properties of MI scar are largely determined by the underlying structure of its primary matrix component - collagen fibers. Therefore, many studies have extensively measured healing infarcts for global properties such as bulk collagen density, cross-linking, orientation, and alignment [Jugdutt et al., 1996, McCormick et al., 2017, Zimmerman et al., 2001, Holmes et al., 1997, Fomovsky et al., 2012b, Fomovsky et al., 2012a, Fomovsky and Holmes, 2009]. Recently, we also assessed localized variations in collagen structures and found stark spatial heterogeneities of fiber orientations [Richardson and Holmes, 2016]. Specifically, collagen fibers from rat infarct scar samples displayed high alignment within small sub-regions ($\sim$250 x 250 μm), but the orientation of those fibers varied greatly from sub-region to sub-region such that the global alignment for the bulk scar appeared more random.

Structural heterogeneity has been observed in a variety of tissues including heart valves, facet capsular ligaments, aortic aneurysms, and tendon-to-bone insertion points [Joyce et al., 2009, Ban et al., 2017, Thomopoulos et al., 2003, Hurks et al., 2012]. Aneurysms, for example, exhibit significant variation in matrix and cellular compositions around the circumferential direction, which is consistent with similar spatial variation in matrix protease activity and spatial variation in the tensile moduli and strengths of aneurysm samples taken from different regions [Hurks et al., 2012, Gilling-Smith et al., 2005]. From a mechanical perspective, fiber heterogeneity could likely alter how infarct scar material redistributes stress and strain under loading, potentially giving rise to stress/strain concentrations, failure points, altered apparent stiffness, and/or altered degrees of anisotropy. Thus, the objective of the

current study was to test the effects of collagen fiber orientation heterogeneity on both local and global mechanical responses of infarct scar tissue. Herein, we applied a previously-published, computational model of multiscale fiber network mechanics to explore the mechanical responses of subject-specific scar orientation maps obtained from rat MI tissue sections.

3.2 Methods

3.2.1 Fiber Map Generation from Scar Samples

In a previously reported study, Fomovsky and Holmes obtained scar samples from healing rats at 1, 2, 3, and 6 weeks after permanent coronary artery ligation [Fomovsky and Holmes, 2009]. Upon sacrifice of each animal, they arrested and excised the rat hearts, then sectioned samples (7μm thick) in parallel to the epicardial plane, and stained collagen fibers with picrosirius red. In a follow-up study, we previously imaged a selection of those mid-wall sections under 20X magnification with automated stitching (Aperio ScanScope), and used a gradient-based image processing method (MatFiber, code freely available at http://bme.virginia.edu/holmes, and implemented in MATLAB) to generate collagen orientation maps for each sample (Fig. 3.1A) [Richardson and Holmes, 2016].

Due to sectioning artifacts in the samples, tissue was not present in some areas, leading to gaps in the raw fiber maps (Fig. 3.1B). To fill the entirety of the tissue geometry and prepare the sample for our finite-element simulations, the 2D outline of each tissue piece was traced, extruded into 3D, and then meshed with roughly 600 hexahedral elements to create a finite-element mesh of the tissue sample (Fig. 3.1C). Each sample had an extruded thickness of 0.25mm, to represent a myocardial tissue slab of uniform thickness. A linear interpolation was performed on the 2D fiber

orientation scatter data to produce a full fiber orientation map for the entire sample within the finite-element mesh (Fig. 3.1C). After the image analysis, a fiber-based multiscale finite element model was generated and solved (Fig. 3.1D) as described in the next section.

3.2.2 Fiber Network Model Generation

Three different types of networks (Fig. 3.2) were created to compare the effects of network orientation:

1. The same isotropic network used for every element (the *isotropic* case, Fig. 3.2A)

2. The same aligned network used for every element, where the network was aligned in the average fiber direction (θ) for the whole sample with the average degree of alignment (α) (the *homogeneous* case, Fig. 3.2B)

3. Differently aligned networks for each finite element (the *heterogeneous* case, Fig. 3.2C).

Networks were comprised of collagen fibers defined by the constitutive relation

$$F = \frac{EA}{B}(e^{(B*\epsilon_G)} - 1) \tag{3.1}$$

where F was fiber force, E was fiber modulus, A was fiber cross-sectional area, B was fiber nonlinearity, and ϵ_G was the fiber green strain. Each fiber also had a critical failure stretch, λ_f, where the fiber failed if it exceeded the critical stretch, and was removed from the network by reducing its modulus 10 orders of magnitude. A neo-Hookean component was also included in parallel to collagen fibers, resembling nonfibrous material. Collagen fiber parameters were based on previous values used

for aortic tissue [Witzenburg et al., 2017] and collagen gels [Dhume et al., 2018], where $E = 10$ MPa, $A = 0.0314$ mm^2, $B = 2.5$, and $\lambda_f = 1.42$. The volume fraction of collagen fibers was 10% for all of the networks, based on [Fomovsky and Holmes, 2009].

For the isotropic case, the same Delaunay isotropic network was used for each of the 15 samples, and was created with the orientation tensor (Ω)

$$\Omega = \begin{bmatrix} 0.495 & 0.004 \\ 0.004 & 0.505 \end{bmatrix} \tag{3.2}$$

producing no preferred fiber direction or degree of alignment. The network for each homogeneous case was an aligned Delaunay network, created according to the overall sample orientation tensor,

$$< \Omega >= \frac{1}{N} \sum_{i=1}^{N} \begin{bmatrix} \Omega_{11}^{(i)} & \Omega_{12}^{(i)} \\ \Omega_{21}^{(i)} & \Omega_{22}^{(i)} \end{bmatrix} \tag{3.3}$$

where i is the element number and N is the number of elements. The average fiber direction (θ) and degree of alignment (α) were calculated as

$$\theta = \tan^{-1}(\frac{v_y}{v_x}) \tag{3.4}$$

$$\alpha = \Lambda_1 - \Lambda_2 \tag{3.5}$$

where v_y and v_x are the components of the eigenvector corresponding to the largest eigenvalue, Λ_1 is the largest eigenvalue, and Λ_2 is the smallest eigenvalue. θ is taken as the angle relative to the circumferential direction (horizontal), and ranges from -90^o to 90^o, while α ranges from 0 to 1, where 0 = no alignment, and 1 = fully aligned. Average angle and degree of alignment for each sample are shown in Table

3.1. The heterogenous networks were created according to the orientation tensor and degree of alignment for each element, $\Omega^{(i)}$ and $\alpha^{(i)}$, where Ω is of the same form as the homogeneous case, created by averaging over the space of each individual finite element instead of the entire sample. Thus, the heterogeneous case contains differing local angles and degrees of alignment for each element, but on average has the same overall preferred fiber direction and degree of alignment as the homogeneous case.

3.2.3 Model Simulations

A custom multiscale finite-element model [Witzenburg et al., 2017,Dhume et al., 2018] was used to simulate each sample (n = 15) in uniform biaxial extension by displacing the boundary nodes of the mesh outward (Fig. 3.1D), with no shear stress on the boundaries. Results were considered at 20% strain to allow for comparison among all samples, as this was the maximum strain reached prior to failure in one sample. Simulations were run on 256-core parallel processors at the University of Minnesota Supercomputing Institute.

3.2.4 Statistics

Paired t-tests were performed (Graphpad, Prism 6) on the homogeneous and heterogeneous data to compare results, as the differences between these two groups is of primary concern. A linear regression was performed on the homogeneous and heterogeneous data to determine the strength of trends for the anisotropy ratio and peak stress in the sample.

3.3 Results

Following biaxial extension to 20% strain, samples were analyzed for each of the 3 network cases. The stress and strain for each sample was calculated in the direction of the overall average fiber direction for the sample, n_{11}, and the perpendicular direction, n_{22} (Fig. 3.3A, 3.4A). A representative sample with strong alignment (Fig. 3.3) demonstrates a few trends present in the highly-aligned samples: **1)** the macroscale stresses for the homogeneous case exhibit a higher degree of anisotropy compared to the heterogeneous and isotropic case (Fig. 3.3B), **2)** homogeneous and isotropic strains, stresses, and fiber failure are homogeneous throughout the sample, while the heterogeneous case displays localized hotspots of strain, stress, and fiber failure (Fig. 3.3C), and **3)** the peak strain, stress, and percentage of failed fibers is significantly higher in the heterogeneous case (Fig. 3.3C). These trends are similar, but less pronounced in samples with weaker alignment, as shown in Fig. 3.4 for a representative weakly-aligned sample. Mechanical anisotropy for the homogeneous and heterogeneous cases is weaker (Fig. 3.4B), accompanied by lower strains, stresses, and percentage of failed fibers (Fig. 3.4C) in the heterogeneous case.

The interactions between anisotropy and heterogeneity can be seen in the plots of Fig. 3.5. For these plots, the location of a point indicates a sample's degree of alignment (y axis) and heterogeneity (quantified as the standard deviation of orientation over the finite elements and measured on the x axis), and the color of the point shows the degree of the resulting effect. Throughout all the samples, there is a trend of increasing anisotropy linked to increasing degree of alignment (Fig. 3.5B). As the degree of alignment rises, the anisotropy ratio (P_{11}/P_{22}) increases in both the homogeneous ($R^2 = 0.97$) and heterogeneous ($R^2 = 0.86$) conditions. The maximum stress in the sample also has an increasing trend with increasing degree of alignment for

the homogeneous case ($R^2 = 0.96$, Fig. 3.5C). There was no trend, however, related to the peak stress experienced in the sample with increasing degree of alignment for the heterogeneous case ($R^2 = 0.03$, Fig. 3.5C). When considering fiber failure, the heterogeneous case consistently required less strain ($22.2\% \pm 0.79\%$, mean $\pm$ 95% CI) to initiate failure in the sample compared to homogeneous ($31.4\% \pm 1.27\%$) and isotropic ($32\% \pm 0\%$) cases (Fig. 3.5D).

When pooling all samples and comparing differences between the network cases, the heterogeneous condition exhibited a significant difference in maximum strain (Fig. 3.6A) and stress (Fig. 3.6B) compared to the isotropic and homogeneous conditions. The isotropic and homogeneous cases showed a similar maximum strain, but the homogeneous case displayed higher peak stress than the isotropic case. As seen above, the homogeneous and heterogeneous cases present higher anisotropy compared to the isotropic case, with the homogeneous case showing a trend of higher anisotropy compared to the heterogeneous case (Fig. 3.6C). Furthermore, fiber failure is overwhelmingly more present in the heterogeneous case, exhibiting higher total fibers failed (Fig. 3.6D), percentage of elements with failed fibers (Fig. 3.6E), and percentage of fibers failed within the worst element (Fig. 3.6F) compared to the homogeneous case which has limited fiber failure at 20% strain. The isotropic case experienced no fiber failure in any elements at 20% strain.

Overall, the results show that fiber heterogeneity vastly affects the mechanical behavior of the tissue on the macroscopic level. Despite the same average fiber direction and degree of alignment in the homogeneous and heterogeneous cases, the results show a decrease in anisotropy for the heterogeneous case, joined by an increase in local peak strains, stress, and fiber failure. These localized events of high strain, stress, and fiber failure within the heterogeneous samples emphasize the notion that overall tissue behavior (and thus, tissue failure), is highly dependent on the underlying

fibrous structure.

3.4 Discussion

3.4.1 Heterogeneous Collagen Structure Produces Heterogeneous Stresses and Strains

After an MI, ischemic myocardium is infiltrated by a swift and large inflammatory wave that serves to degrade necrotic myocytes and recruit cardiac fibroblasts into the wound site for collagen production [Jugdutt, 2003, Dewald et al., 2004]. The resulting fiber network structure within the collagenous scar is a key determinant of infarct mechanical properties and critically affects cardiac performance. Prior studies have observed a range of scar structures with variable collagen densities and alignments across infarcts from different cardiac locations and different experimental models, but these reported structures typically represented bulk measurements of the global, aggregate scar [Holmes et al., 1997, Fomovsky et al., 2012b, Fomovsky et al., 2012a, Fomovsky and Holmes, 2009]. Recently, we observed and quantified regional heterogeneity of collagen fiber orientations within individual scar samples [Richardson and Holmes, 2016]. We specifically found that both collagen fibers and cells demonstrated strong alignment in small sub-regions of rat scars from 1-6 weeks post-MI, but fiber and cell orientations varied greatly from sub-region to sub-region resulting in clearly observable spatial heterogeneities.

From an electrical perspective, previous work has shown that spatial variations in scar geometry can lead to dangerous arrhythmias in the heart as tortuous paths can produce nonuniform and reentrant currents [Richardson et al., 2015]. But, no other study (to our knowledge) has examined the effects of heterogeneity on mechanical

properties of the scar, so our current objective was to test mechanical behaviors of subject-specific infarct orientation maps. In the current fiber network simulations, heterogeneous fiber orientations resulted in corresponding heterogeneous stress and strain fields. While homogeneous scars exhibited uniformly low stresses/strains, heterogeneous scars led to high regional variations with some sub-regions under very low stress/strain and other sub-regions under very high stress/strain likely due to the redistribution of loads (e.g., stress shielding).

It is currently unknown how fiber heterogeneity emerges and evolves in healing scars. Collagen is deposited and arranged by fibroblasts that infiltrate the wound during the healing cascade, and it is of course possible that the wound environment presents heterogeneous chemical gradients or heterogeneous pre-existing structural cues that direct fibroblasts into a heterogeneous arrangement, which the collagen network then follows. However, we previously used an agent-based computational model to support an alternative hypothesis that structural heterogeneity can emerge even from an initially homogeneous environment due to cell-cell and cell-matrix interactions within the system [Richardson and Holmes, 2016]. Specifically, long-range cell sensing and long-range remodeling were predicted to produce local self-reinforcing pockets of cell and matrix alignment. Perturbing these interactions, therefore, may offer a therapeutic approach for controlling the degree of fiber heterogeneity. To guide potential therapeutic modulation of this heterogeneity, we sought to test the mechanical implications of fiber orientation heterogeneity on tissue anisotropy and failure.

3.4.2 Effect of Heterogeneity on Scar Tissue Anisotropy

Isotropic samples displayed isotropic material properties (i.e. same stress-strain behavior in all directions) whereas the homogeneous samples displayed anisotropic prop-

erties with stiffer behavior parallel to the direction of global fiber alignment (i.e., higher P_{11} vs. P_{22} at the same levels of strain). Not surprisingly, the samples with higher degrees of alignment demonstrated higher degrees of anisotropy. Scar anisotropy is clinically interesting as a potential therapeutic target - both computational and experimental reports have indicated that highly anisotropic scars oriented in the longitudinal direction may benefit left ventricular function much more than isotropic scars [Fomovsky et al., 2012a, Fomovsky et al., 2011].

Heterogeneity within sample orientations usually dampened anisotropy. In other words, the anisotropic stress ratio P_{11}/P_{22} was lower in the majority (11/15) of heterogeneous samples compared to their corresponding homogeneous counterparts, even though both samples across each pair demonstrated identical global fiber alignment. This finding is consistent with previous results and presumably due to the ability for stiff and compliant regions to redistribute loads/displacements [Picu, 2011, Hatami-Marbini and Picu, 2009]. Given that a high degree of anisotropy may provide a therapeutic benefit for improving MI properties, our current results suggest that orientation heterogeneity in the infarct may act as a deterrent to achieving this benefit.

3.4.3 Effect of Heterogeneity on Scar Tissue Failure

Infarct rupture is a rare but catastrophic event occurring when the infarct is too weak to support the ventricle's cavity pressure, leading to mechanical failure of the tissue. Though it only afflicts <3% of infarct patients, left ventricle free wall rupture carries a 60-90% mortality rate, and typically occurs very early in the healing time-course within the first few days [Gao et al., 2012]. The early occurrence is thought to coincide with a narrow window when inflammation and protease-mediated degradation of the necrotic myocardium has peaked but prior to the influx of fibroblasts and newly generated matrix material [Clarke et al., 2016].

While the imbalance in infarct mass turnover is likely to contribute to scar tissue vulnerability, our current results suggest that fiber orientation heterogeneity might also lead to infarct rupture. Heterogeneous samples exhibited substantially higher failure rates compared to their homogeneous counterparts, measured by total percentage of failed fibers across the sample, percentage of elements with failed fibers, and percentage of failed fibers in the weakest element. Such failure rates were not surprising given the elevated peak stresses in heterogeneous vs. homogeneous samples. The fiber failure rate was very high in just a few elements that corresponded to the locations of peak stresses and strains (i.e., failure was a localized event). However, we should note that the degree of stretch subjected in our simulations ($\sim$20%) is considerably higher than most *in vivo* strains measured in these healing rat infarcts, which averaged $\sim$5% (though some infarcts did reach up to 16% *in vivo*) [Fomovsky and Holmes, 2009]. Also, since the earliest obtained samples were acquired at 1 week post-MI, it is unknown whether fiber heterogeneity actually emerged during the rupture-prone window around 2-3 days.

3.4.4 Limitations of Current Study

There are a few important limitations to our model predictions. First, since the goal of this study was to explore the effects of orientation heterogeneity on scar mechanics, we chose to ignore other structural heterogeneities like spatial variations in collagen density and other coronary blood vessels. These other heterogeneous inclusions may also contribute interesting and important roles in scar mechanics. We also assumed each sample had identical collagen densities, which we know is not true, but enabled us to isolate the role of fiber orientation heterogeneity alone. Now that we have isolated the effects of orientation heterogeneity, future work can combine other sources of heterogeneous mechanics for improved predictions.

A second limitation is that our current simulations focused on single 'slabs' of scar tissue with uniform collagen structure throughout the 0.25mm thickness of the material. The free wall thickness of an unloaded, healthy left ventricle in rats is approximately 1-2mm, and thickness of unloaded, infarct scar tissue drops as low as 0.4mm [Richardson et al., 2015]. Across the full thickness of healthy myocardium, average myocyte orientation varies from around -60° at the epicardium to around +60° at the endocardium; this transmural variation is also present in scar collagen structure but the variation is reduced to approximately -30° to +30° [Rouillard and Holmes, 2012]. We have not yet analyzed how localized heterogeneities vary through the full thickness of the infarct scar (i.e., variation in the radial direction); the samples used herein were sections taken near the mid-wall so our current simulations describe the planar heterogeneous behavior within a scar slab representing a partial thickness (i.e., variation in the circumferential-longitudinal plane). Future work with 3D orientation maps of the full thickness (capturing heterogeneity in all 3 directions) will enable predictions of the full scar behavior.

As a third limitation, we are simulating acute mechanical responses as a single snapshot of scar behavior vs. structure. Of course, scar tissue in vivo is dynamically remodeling as cells continue to deposit, degrade, and rearrange collagen fibers in response to chemical, structural, and mechanical signals. Here we show that heterogeneous structure gives rise to heterogeneous stress and strain fields with increased peak stresses and increased failure rates. However, long-term implications of this structure will also depend on how cells continue to remodel their local matrix across the spatially varying mechanics. In our previous agent-based simulations of scar heterogeneity, we showed that cell-matrix interactions over long ranges could give rise to heterogeneous structures, but those simulations assumed homogeneous mechanical cues for the entire tissue over the remodeling time course [Richardson and Holmes,

2016]. Future modeling work that couples cell behaviors with heterogeneous mechanics will help predict the evolving interplay of scar structure and properties over the chronic, healing time course.

3.4.5 Conclusions

In summary, this work highlights the importance of microenvironment considerations within the larger scope of macroscopic infarct tissue mechanics. Our results show a striking dependence on local fiber orientation and degree of alignment, where samples with heterogeneous networks exhibit significantly different deformation patterns and overall mechanics when compared to samples with homogeneous and isotropic networks. Most notably, while homogeneous and heterogeneous cases share the same average fiber direction and degree of alignment for the entire sample, several factors, such as anisotropy, peak strain, peak stress, and fiber failure differ between the two cases. These results support the conclusion that infarct mechanics depend on the underlying fiber orientation and degree of alignment, which affect the tissue behavior and tissue failure on a whole.

3.5 Acknowledgment

We gratefully acknowledge Jeff Holmes (Department of Biomedical Engineering at the University of Virginia) for originally sharing infarct histology images, and the following funding sources: NIH COBRE 1P20GM130451 (WJR), NIH R01 EB005813 (VHB, CEK), and U01 HL139471 (VHB, CEK). This material is based upon work supported by the National Science Foundation Graduate Research Fellowship Program under Grant No. 00039202 (CEK). Any opinions, findings, and conclusions or recommendations expressed in this material are those of the author(s) and do not

necessarily reflect the views of the National Science Foundation. CEK is a recipient of the Richard Pyle Scholar Award from the ARCS Foundation. The authors also acknowledge the technical support of Shannen Kizilski, and computational resources provided by the University of Minnesota Supercomputing Institute.

Angle (θ)	**Degree of Alignment (α)**
25.8º	0.22
75.6º	0.04
-7.5º	0.20
45.0º	0.35
8.9º	0.43
-0.56º	0.33
65.9º	0.11
23.3º	0.25
-7.6º	0.44
34.2º	0.41
24.0º	0.25
15.7º	0.25
58.2º	0.15
16.6º	0.16
5.0º	0.16

Table 3.1: The average angle and degree of alignment for each of the 15 samples.

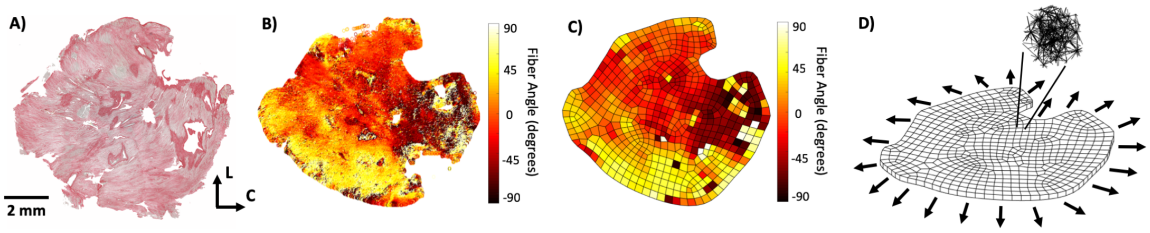

Figure 3.1: **A)** Excised rat scar samples stained with picrosirius red to show collagen fiber orientations in the circumferential (C) - longitudinal (L) plane. **B)** Collagen fiber orientation extracted from the tissue sample using gradient-based image processing. Each pixel was assigned an angle from -90° to 90°, representing the angle deviation from the circumferential direction (C = 0°, L = -90° or 90°). **C)** A 2D finite-element mesh was created to encompass the entire tissue area, and a nearest-neighbor linear interpolation was performed to complete the data set where fiber angle data was previously missing in B). **D)** The 2D mesh was extruded into the 3rd dimension to create a tissue slab of uniform thickness. Aligned networks were created for each of the elements based on the fiber angle data, and each sample was subjected to uniform biaxial extension, indicated by the arrows.

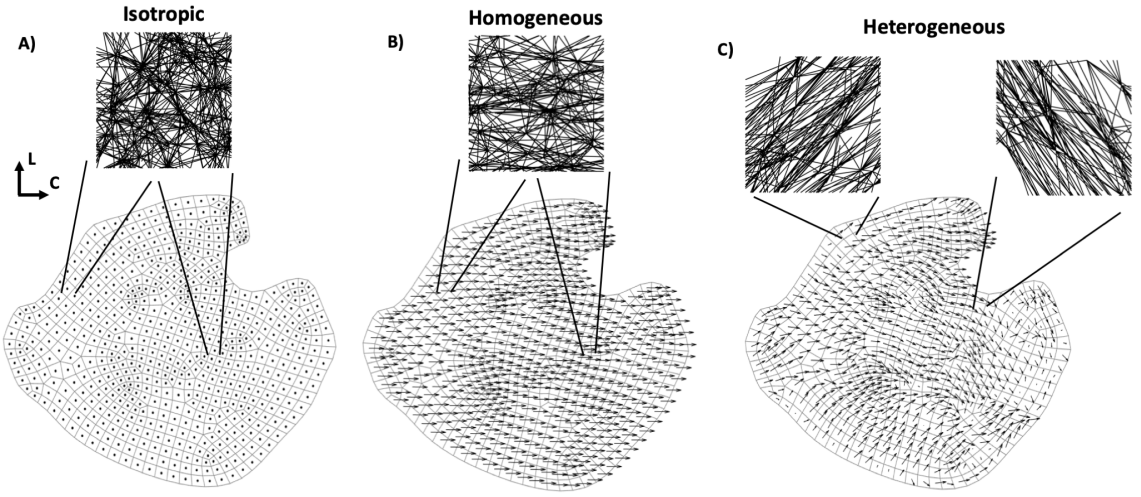

Figure 3.2: An example of the 3 different network cases used for each sample. The 2D finite-element mesh is shown, with a quiver plot of fiber orientation overlaid on each element. Quiver plot arrows indicate the fiber direction, and the arrow length corresponds to degree of alignment (i.e. dots indicate no degree of alignment (isotropic), while longer arrows indicate higher degree of alignment (homogeneous and heterogeneous)). **A)** The same isotropic network was used for every element in the isotropic case, where the network had no degree of alignment. **B)** Likewise, the same network was used for every element in the homogeneous case, where the network was now aligned in the average fiber direction, with the average degree of alignment in that direction. In the example shown here, the average fiber direction is close to the circumferential direction. **C)** Different networks were used for each element in the heterogeneous case, where networks were constructed based on local fiber orientations and degrees of alignment for each element.

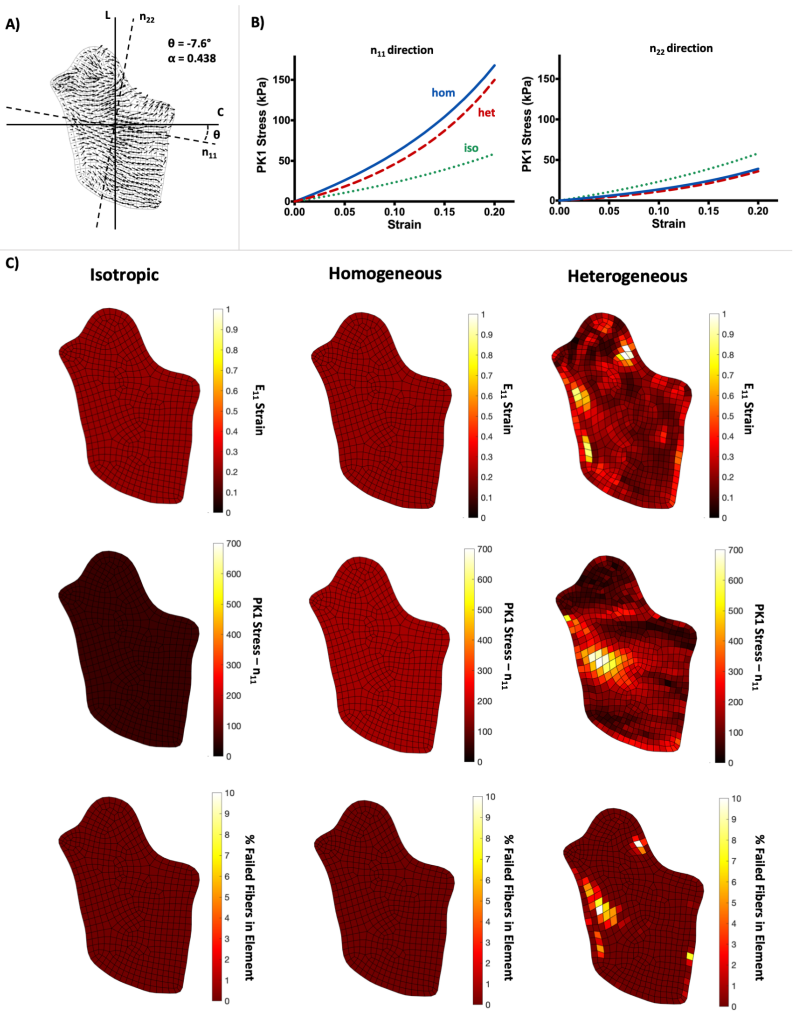

Figure 3.3: A representative, comprehensive analysis of the data, shown for an image with a high degree of alignment. **A)** The 2D mesh and quiver plot is shown for the sample, where the n_{11} direction indicates the average fiber orientation for the sample, and the n_{22} direction is perpendicular to n_{11}. The angle relative to circumferential (θ) and the degree of alignment (α) are shown. **B)** Averaged macroscale stress plots shown in the n_{11} (left) and n_{22} (right) directions for each of the 3 cases, isotropic (green, dotted line), homogeneous (blue, solid line), and heterogeneous (red, dashed line). For highly aligned samples, the homogeneous case was more anisotropic on average, displaying higher stresses than the heterogeneous or isotropic stress for the n_{11} direction, but lower stresses in the n_{22} direction. **C)** Heatmaps shown on the sample for the isotropic (left column), homogeneous (middle column), and heterogeneous (right column) cases, displaying the E_{11} strain (top row), PK1 stress in the n_{11} direction (P_{11}, middle row), and % of fibers failed in each element (bottom row). Isotropic and homogeneous cases displayed homogeneous strain, stress, and fiber failure throughout all of the samples, while the heterogeneous case experienced localized areas of high strain, stress, and fiber failure.

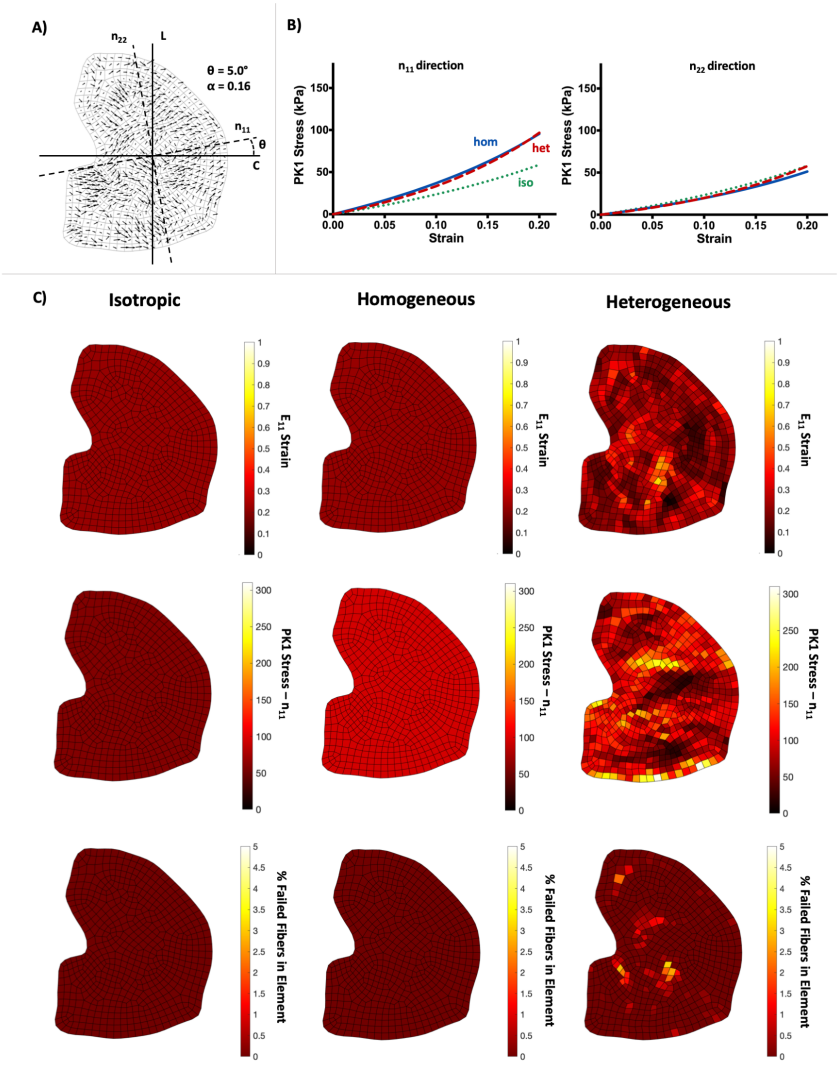

Figure 3.4: A representative analysis of the same from as Fig. 3.3, shown for a sample with low degree of alignment ($\alpha = 0.16$). **A)** The quiver plot shows a lesser degree of preferred fiber angle and degree of alignment. **B)** Averaged macroscale stresses are very similar between the 3 network cases for both the n_{11} and n_{22} directions. The amount of anisotropy is similar between the homogeneous and heterogeneous samples, on average. **C)** Heatmaps shown again for each of the network cases. As in the highly aligned images, the isotropic and homogeneous cases display homogeneous strains, stresses, and fiber failure. The heterogeneous case shows the same trend as the highly aligned case, to a lesser degree. The maximum strain, stress, and % of failed fibers are lower in cases with low degree of alignment.

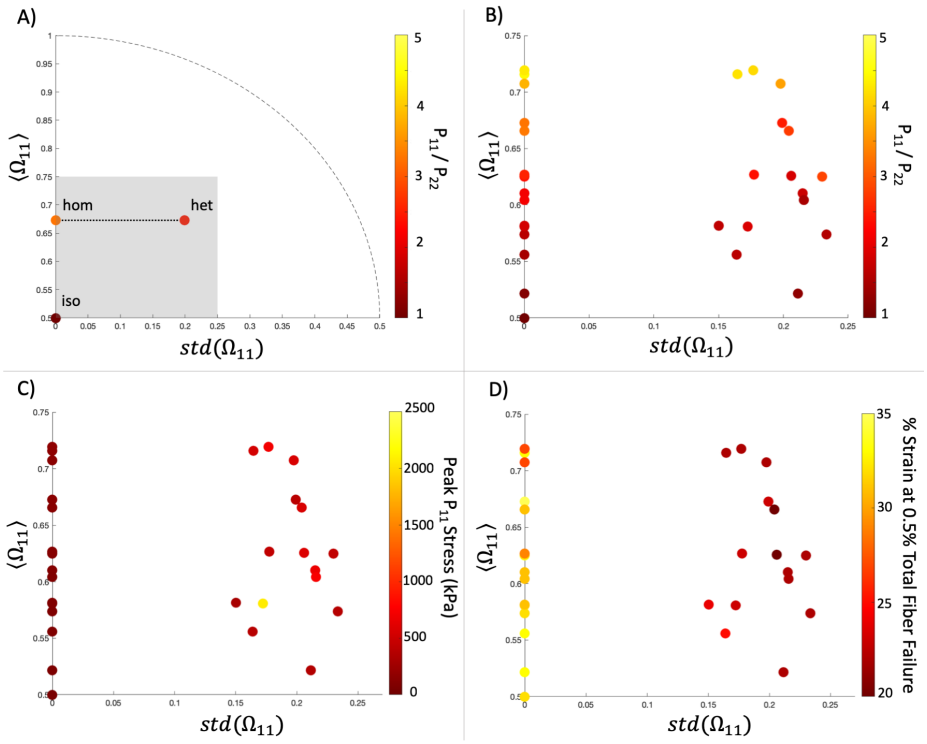

Figure 3.5: Plots analyzing the differences between each of the network cases for all the samples. **A)** A representative plot for one sample is shown to illustrate how the plots work. The y-axis displays the average Ω_{11} for the sample, while the x-axis displays the standard deviation of Ω_{11} over all elements within the sample. Thus, the y-axis represents how strongly aligned the sample is on average (0.5 = isotropic, 1 = perfectly aligned), and the x-axis represents how strongly the sample deviates from its average alignment (0 = no deviation (homogeneous), 0.5 = strong deviation (heterogeneity)). Each sample has the 3 network cases plotted for the given variable. The isotropic case always corresponds to (0, 0.5), as there is no degree of alignment, or deviation from the average. The homogeneous and heterogeneous cases lie on a horizontal line, as they have the same average degree of alignment, but differing variation from the alignment in the heterogeneous case. The dotted line shows the range of possible ($< \Omega_{11} >$, $std(\Omega_{11})$) pairs. The gray box contains all of the samples that were studied and sets the zoomed-in plot area shown for **B)**, **C)**, and **D)**. **B)** The ratio of P_{11} to P_{22} is shown at 20% strain for each of the samples, as a measure of anisotropy. As degree of alignment increases, so does the degree of anisotropy. The effect is slightly more pronounced in the homogeneous case. **C)** Peak P_{11} stresses are consistently higher in the heterogeneous case compared to homogeneous and isotropic cases but do not show any obvious trend within the heterogeneous model results. **D)** The % strain required to fail 0.5% of the fibers in the sample is shown for each case. For the isotropic and homogeneous cases, a much higher strain must be reached in order to initiate failure in the sample. In the heterogeneous cases, the strain to initiate failure is much lower.

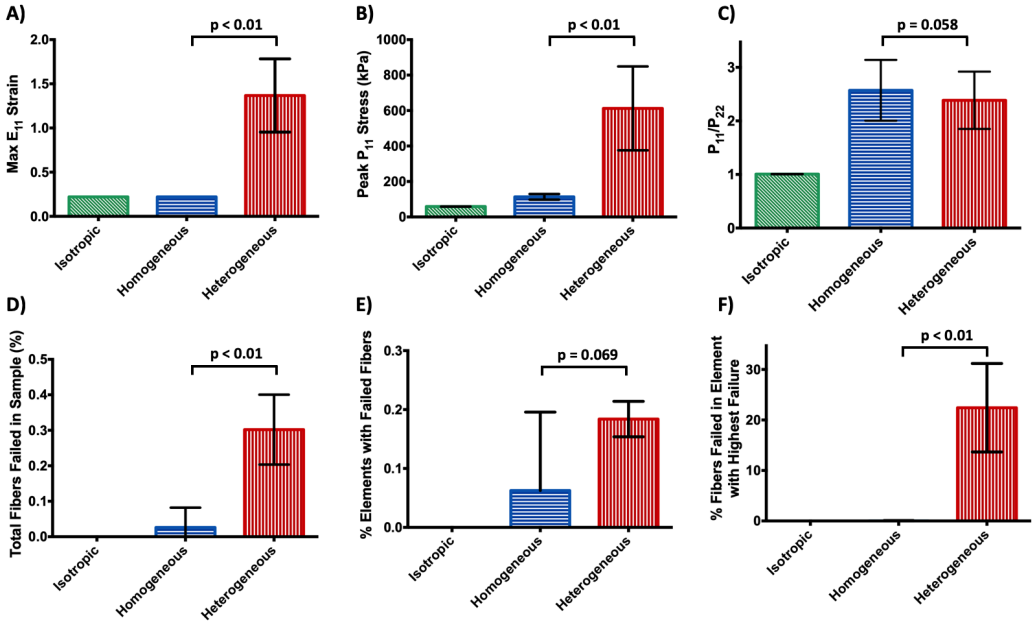

Figure 3.6: Bar plots containing the mean ± 95% CI for each of the 3 network cases at 20% strain, with p-values shown for the comparison between the homogeneous and heterogeneous case. **A,B)** The maximum E_{11} strain and P_{11} stress experienced in a single element for the samples was much higher in the heterogeneous case compared to the homogeneous and isotropic case. **C)** The degree of anisotropy in the homogeneous and heterogeneous case was much higher than the isotropic case. The homogeneous case displayed a slightly higher degree of anisotropy overall compared to the heterogeneous case. **D,E,F)** The amount of fiber failure and elements containing failed fibers was significantly higher for the heterogeneous case.

Chapter 4

Ex Vivo Mechanical Tests and Multiscale Computational Modeling Highlight the Importance of Intramural Shear Stress in Ascending Thoracic Aortic Aneurysms

The content of this chapter was submitted as a research article to the *Journal of Biomechanical Engineering* by Korenczuk, Dhume, Liao, and Barocas [Korenczuk, Christopher et al., 2019], and is currently under review. My contribution to the work was performing experimental testing, data processing, computational modeling, and writing.

4.1 Introduction

Ascending thoracic aortic aneurysms (ATAAs) are characterized by abnormal dilation of the ascending aorta, where the vessel exceeds its normal diameter of 2-3 cm [Iaizzo, 2009]. ATAA is a high-risk pathology, with aneurysm rupture or dissection likely to occur in untreated patients (21%-74%) [Davies et al., 2002], and with rupture in particular having high mortality rates (94%-100%) [Olsson et al., 2006]. Evaluating the failure risk of ATAAs is exceptionally difficult due to the nonuniform microstructural, geometric, and mechanical changes that occur in the vessel during disease progression. Aneurysms are often affected by wall thinning, structural disorganization, loss of vascular smooth muscle cells, and extracellular matrix components such as elastin, collagen and fibrillin [Humphrey, 2013]. The complex remodeling during aneurysm formation and growth undoubtedly gives rise to several underlying risk contributors, many of which may still be largely unidentified, making it difficult to determine accurately the likelihood of aneurysm failure.

Current risk assessment and patient diagnosis are based primarily on vessel diameter. If the ATAA diameter exceeds a threshold of approximately 5-6 cm [Davies et al., 2002,Elefteriades, 2002,Coady et al., 1999] or a growth rate of 0.5 cm/year [Saliba and Sia, 2015], surgical intervention is recommended. When ATAA risk is assessed solely with measurement-based techniques, however, mechanical and structural changes, which are well-known to occur in the ATAA pathology [Isselbacher, 2005, García-Herrera et al., 2012, Vorp et al., 2003, Okamoto et al., 2002], cannot be considered. The inefficiency of measurement-based diagnosis was shown by Vorp *et al.* [Vorp et al., 2003], who reported a 5-year mortality rate of 39% for ATAAs below the 6 cm diameter threshold and 62% for those above the 6 cm diameter threshold. Furthermore, Vorp *et al.* found no correlation between aneurysm diameter and tensile

strength [Vorp et al., 2003]. Clearly, failure contributors in the ATAA pathology must be better understood to help inform physician decisions and improve patient outcomes.

Morphological detail, typically obtained from CT, is invaluable and constantly improving as imaging science advances. The critical question, then, is *how can we use our understanding of vascular mechanics to improve on a diameter-based guideline?* Since dissection and rupture are mechanical events, a mechanical approach is justified, which requires exploring both the strength of the tissue and the stresses generated by the blood pressure. Regarding ATAA mechanics, recent studies have quantified non-aneurysmal and aneurysmal aortic tissue mechanical response through various loading configurations including bulge inflation [Trabelsi et al., 2015, Romo et al., 2014], uniaxial extension [García-Herrera et al., 2012, Vorp et al., 2003, Okamoto et al., 2002, Iliopoulos et al., 2009a, Duprey et al., 2010, Khanafer et al., 2011], biaxial extension [Okamoto et al., 2002, Choudhury et al., 2009, Matsumoto et al., 2009, Azadani et al., 2013, Geest et al., 2004, Duprey et al., 2016], peel [Pasta et al., 2012, Noble et al., 2016], and shear [Sommer et al., 2016] testing regimes. As a general rule, those studies found significant anisotropy, with the tissue stronger in the circumferential than in the axial direction [Humphrey, 2013, Okamoto et al., 2002, Duprey et al., 2010]. Aneurysm tissue is generally stiffer [Vorp et al., 2003, Phillippi et al., 2011a] but weaker [Vorp et al., 2003, Duprey et al., 2010, Phillippi et al., 2011a] than healthy tissue, perhaps due to elastin degradation in the aneurysm pathology [Campa et al., 1987]. Regional heterogeneity has also been observed, with differences between the lesser and greater curvature wall mechanics [Duprey et al., 2010, Khanafer et al., 2011, Gao et al., 2006, Thubrikar et al., 1999, Poullis et al., 2008]. Although none of these trends was absolute, they provide extensive insight on aneurysm mechanics.

For stress estimation, finite-element modeling has been the most popular approach

[Trabelsi et al., 2015,Liang et al., 2017,Kim et al., 2012,Nathan et al., 2011,Pal et al., 2014]. These models, taken collectively, describe a complex, heterogeneous stress field in the tissue. Bulk constitutive equations, such as the HGO model [Liang et al., 2017,Gasser et al., 2006], 2-fiber family model [Kim et al., 2012,Holzapfel et al., 2005], and Demiray model [Trabelsi et al., 2015], have become commonly used to describe the material behavior of the tissue. While these constitutive models have advantages such as reducing computational energy, they fail to incorporate fully the underlying tissue composition and structure, which is essential to macroscale tissue behavior, especially in the ATAA pathology, where microstructural changes are undoubtedly present. Furthermore, parameter values are often fit to experimental data from only one or two loading conditions (i.e. uniaxial, biaxial), which may overlook the complex mechanical behavior given by the comprehensive multidirectional response of the tissue (i.e. incorporating radial and shear directions). Without the consideration of multiple loading conditions in parameter fitting, these models will lack the information needed to produce accurate predictive results for the complex behavior of ATAAs.

Despite much progress in understanding ATAA mechanics using both experimental testing and computational modelling, the comprehensive mechanical strength of ATAA tissue in all directions, all regions, and all loading configurations has not been well documented. Furthermore, the mechanisms of aneurysm rupture and dissection are still largely unknown. It has been proposed, however, that interlaminal strength (i.e. between wall layers) plays a significant role in the failure process [Pal et al., 2014]. Interlamellar strength has been studied in a peel [Pasta et al., 2012,Noble et al., 2016] and uniaxial [MacLean et al., 1999, Sommer et al., 2016] geometry, with significant lower strength found than in the in-plane circumferential or axial direction. The one previous study of ATAA tissue in interlamellar shear [Sommer et al., 2016], like our own work on the porcine ascending thoracic aorta [Witzenburg et al., 2017], showed a

similarly low strength. The potential role of interlamellar shear is further supported by (1) the mechanical observation that a curved tube, unlike a straight tube, generates intramural shear (not to be confused with wall shear stress from blood flow) when inflated, and (2) the clinical observation that ATAAs tend to dissect rather than outright rupture, a result consistent with shear failure in cylindrical laminates. Taken together, these observations suggest the hypothesis that **interlamellar forces created by intramural shear stress contribute to the dissection of ATAAs.** To evaluate this hypothesis, we used a combination of multidirectional mechanical experiments on ATAA tissue and multiscale computational modeling.

4.2 Methods

4.2.1 Experiments

This study was approved by the Institutional Review Board (IRB) at the University of Minnesota (Study #1312E46582). Resected human ATAA tissue was obtained from patient surgeries at the University of Minnesota Medical Center (Fig. 4.1A, 4.2A). Following surgery, tissue was stored in 1x PBS at 4°C. The lesser curvature region (Fig. 4.1B) was marked with a small suture stitch placed in the adventitial layer by the surgeon (Fig. 4.2B). Samples were cleaned of excess connective tissue and cut open axially along the line midway between the lesser and greater curvatures (Fig. 4.2C). Sample preparation followed the same protocol used previously for porcine ascending aortic tissue, described extensively in [Witzenburg et al., 2017]. Uniaxial, peel, and lap samples (Fig. 4.3) were prepared by initially cutting a rectangular full-thickness tissue piece, approximately 10mm x 5mm, where the 10 mm dimension indicates either the circumferential or axial direction. Uniaxial dogbone samples were created by cutting partial semicircles out of the center of the rectangle on both sides

with a biopsy punch (r = 2.5 mm), to produce a width in the neck region of 2.34 mm on average. Peel samples were prepared from the rectangles by making an incision on one end, in the center of the media, parallel to the vessel wall to initiate peel propagation. Lap samples were cut by making an incision in the media on both ends of the rectangle and removing roughly half of the thickness on each side of the sample, leaving an overlap region of 3.69 mm on average in the center. Biaxial samples (Fig. 4.3) were cut from a square (approximately 20 mm x 20 mm) into a cruciform shape using biopsy punches (r = 12 mm) on each of the corners. Samples were photographed to measure the undeformed sample geometry using ImageJ.

Uniaxial, peel, and lap samples were clamped with custom grips, placed in a 1x PBS bath at room temperature, and pulled at 3 mm/min in strain-to-failure experiments on a uniaxial testing machine (MTS, Eden Prairie, MN). A static 10N load cell recorded the forces, and grip stretch was calculated using the actuator displacement. Uniaxial samples that did not fail in the neck region were discarded, as well as lap or peel samples that did not fail in the medial layer. Biaxial samples were tested in displacement-controlled equibiaxial experiments (Instron 8800 Microtester) to 30% grip strain while 5N load cells recorded forces.

For uniaxial, biaxial, and lap tests, an average first Piola-Kirchoff stress (PK1) was calculated by dividing grip force by the relevant area, and grip stretch was calculated by dividing grip separation distance by the initial grip separation distance. For the peel test, peel tension was calculated as the grip force divided by the sample width. Results were analyzed with Tukey's multiple comparison test using GraphPad Prism 6.

4.2.2 Multiscale Model

A custom multiscale model that we previously used [Witzenburg et al., 2017] for porcine aortic tissue was implemented to simulate the ATAA tissue behavior. Specimen geometries were created and meshed in Abaqus based on the average dimensions of each experimental sample. Mesh sizes ranged from 600 to 1460 hexahedra elements for the geometries. The multiscale model incorporates three scales: tissue (mm), network (μm), and fiber (nm) levels. The model follows an iterative loop that satisfies the global Cauchy stress balance after displacements are applied on the tissue level (Fig. 4.4). Once applied, tissue-level displacements are passed to the Gauss points in each finite element, where representative volume elements (RVEs) consisting of fibrous networks in parallel with a nearly incompressible Neo-Hookean component are deformed. These fibrous networks resemble the arterial media, as they consist of a planar layer of collagen and elastin fibers, surrounded on both top and bottom by interlamellar connection (I.C.) fibers representing components such as VSMCs and fibrillin, which reside between the lamellar layers. All of the network nodes are connected to a Delaunay network of fibers with infinitesimal stiffness in order to stabilize the network. The same fibrous network was used for each element in all of the different geometries. On the microscale level, each fiber is defined by a constitutive equation of the form

$$F = \frac{E_f A_f}{B}(e^{(B*\epsilon_G)} - 1) \tag{4.1}$$

where F is the fiber force, E_f is the fiber modulus, A_f is the fiber cross-sectional area, B is the fiber nonlinearity, and ϵ_G is the fiber Green strain. Every fiber type had the same fiber radius (100 nm), and thus cross-sectional area (3.14 E+04 nm^2). A Neo-Hookean ground matrix accounts for nonfibrous material, governed by an equation of the form

$$\sigma_m = \frac{G}{J}(B - I) + \frac{2G\nu}{J(1-2\nu)}(I * ln(J)) \tag{4.2}$$

where σ_m is the Cauchy stress of the matrix, G is the shear modulus, J is the determinant of the deformation tensor, B is the left Cauchy-Green deformation tensor, I is the identity matrix, and ν is the Poisson's ratio. After deformation is applied to the network, the internal forces are equilibrated, and the volume averaged stress over the RVE is calculated using the boundary nodes. These stresses are then passed up to the macroscale, and this process iterates until the global Cauchy stress balance is satisfied. Failure is accounted for on the microscale level, where each fiber is given a critical stretch value, above which the fiber fails and is numerically removed from the network.

Network composition in the ATAA model was altered from our previous healthy porcine model to incorporate physiological changes present in the aneurysm case (Fig. 4.4). In the new ATAA networks,

- fewer elastin fibers were present to account for elastin degradation
- collagen fiber arrangement was more isotropic to represent collagen disorganization
- fewer I.C. fibers were present to simulate VSMC and interlamellar component loss.

Model parameters (Table 4.1) were manually adjusted from previous values [Witzenburg et al., 2017] to fit the experimental data for the uniaxial, lap, and biaxial loading conditions concurrently. Boundary conditions were based on the experimental setup for each loading condition. For uniaxial and lap geometries, one end was fixed in all directions, while the opposite end was displaced in the appropriate direction and fixed in the other two directions. For the biaxial geometry, each arm was displaced

in the appropriate direction and fixed in the other two directions. Each simulation was run on 256 cores at the Minnesota Supercomputing Institute.

4.2.3 Multiscale Inflation

The same multiscale modeling approach was used to inflate a patient-specific ATAA geometry. A patient CT scan was obtained for one patient (see Fig. 4.1A), and the geometry was manually segmented using the Vascular Modelling Toolkit (www.vmtk.org). The boundary of the inner lumen was clearly visible in the CT scan, but the outer boundary was not. The segmented shell of the ATAA lumen was meshed in Abaqus and uniformly extruded by 2.4 mm (the average thickness from all experimental samples) in Matlab. To apply an internal pressure on the ATAA mesh, nodes located on the surface of the inner lumen were identified. A force boundary condition was then applied to each of the nodes during the simulation, where nodal displacements were imposed to satisfy the pressure condition at each incremental step. The same iterative process of network equilibration, stress calculation based on network boundary nodes, and macroscale stress scaling was performed, as described previously.

A biphasic solute diffusion problem was then specified in FEBio to define a local cylindrical coordinate system for each of the elements, allowing proper network orientation and stress calculations in the multiscale model. To identify the axial direction, a large concentration of arbitrary solute was placed at the proximal end of the ATAA, contained within the vessel wall. The solute was then allowed to diffuse toward the distal end (driven by the concentration gradient), and the solute flux in each element defined the axial direction. The same process was used to determine the radial direction, except the initial solute concentration was placed on the inner lumen surface, and allowed to diffuse radially to the outer surface. The solute flux in each element

then defined the radial direction. Following the simulations, the cross product of the axial and radial directions was taken to define the circumferential direction for each element. In order to ensure an orthogonal coordinate system, the cross product of the circumferential and axial directions was performed to define the final radial direction. Networks of the same specifications used during optimization were then generated and rotated appropriately for each element, based on the calculated coordinate systems.

Fiber parameters were set as the values obtained from the optimization to the experimental data, specified above. Since the patient CT was captured with the tissue in a loaded configuration *in vivo*, the unloaded length of each fiber was set to be 80% of its initial length, to simulate fiber prestretch. The nodes residing on the lumen of the proximal end of the vessel were fixed in all directions to resemble anchoring at the aortic root, while the rest of the vessel was allowed to move freely in all other directions. The ATAA geometry was inflated to a pressure of 50 mmHg, a value well below the normal blood pressure but sufficient to produce significant expansion of the vessel in this adventitia-free model, and to allow us to focus on the initial stages of tissue damage, which could drive subsequent remodeling.

4.3 Results

4.3.1 Experiments

Strain-to-failure experiments for the uniaxial, lap, and peel loading conditions showed a few notable trends. First, ATAA tissue displayed similar nonlinear, anisotropic, prefailure behavior to healthy porcine tissue, but was weaker in most loading cases, failing at a lower stress and stretch. Second, ATAA tissue was strongest in the uniaxial loading condition, and weakest in the shear lap loading condition. There was no significant difference between tissue from the greater vs. lesser curvature

regions in any test (data in supplement), so results for the two regions were pooled in all subsequent analysis.

ATAA uniaxial samples exhibited significantly lower strength in the circumferential direction compared to porcine tissue (Fig. 4.5C, 4.5E), similar to previous studies [García-Herrera et al., 2012, Vorp et al., 2003, Witzenburg et al., 2017]. There was, however, no difference in tensile strength between ATAA and porcine tissue in the axial direction (Fig. 4.5D, 4.5E). In both ATAA directions, the failure stretch was lower than for porcine samples (Fig. 4.5F).

Lap samples were significantly stronger in the circumferential direction compared to the axial direction (Fig. 4.6C-E), similar to results seen by [Sommer et al., 2016]. ATAA samples showed a significantly lower failure strength (Fig. 4.6E) compared to porcine samples. All orientations and locations exhibited a lower failure stretch compared to porcine data.

ATAA peel samples exhibited a significantly higher peel tension in the axial direction compared to circumferential (Fig. 4.7B) in agreement with previous studies [Pasta et al., 2012]. Both the circumferential and axial directions showed a significantly lower peel tension compared to porcine samples (Fig. 4.7B).

Biaxial samples showed a slight increase in nonlinearity for both the circumferential and axial directions compared to porcine data (Fig. 4.8C, 4.8D). The similarity between ATAA and porcine aortic tissue in biaxial tests is consistent with the similar prefailure curves in Figures 4.5 and 4.6. The biaxial samples also displayed tissue anisotropy in favor of the circumferential direction, in the same fashion as the uniaxial and lap testing.

Overall, ATAA tissue showed the highest strength in uniaxial loading conditions and the lowest strength in shear for both circumferential and axial orientations. The prefailure data for uniaxial, lap, and biaxial samples were similar to porcine tissue, but

the uniaxial and lap samples exhibited lower failure stresses and stretches for ATAA tissue, with ATAA tensile strength and peel tension roughly half of the corresponding values for porcine aorta. The failure stretch for uniaxial tests was also considerably lower for the ATAA samples under uniaxial and shear loading. Taking the data collectively, we conclude that the ATAA tissue shows comparable mechanics to the healthy porcine tissue at subfailure loads, but fails at significantly lower stretch/load.

4.3.2 Modeling

One set of network parameters (Table 4.1) was determined to fit the experimental data from the uniaxial, lap, and biaxial loading configurations. For the uniaxial case (Fig. 4.9, top), the model captured the anisotropic behavior prior to failure quite well, but it showed some inaccuracy in the prediction of the failure stretch. For the lap tests (Fig. 4.9, middle), the model showed similar good performance prior to failure and matched the failure points more closely. The model, when properly parameterized, also captured the 10-fold difference in failure stress between the uniaxial and lap experiments. Finally, for the biaxial experiments (Fig. 4.9, bottom), the model overpredicted the stress, but correctly described the anisotropy of the tissue. We know of no other computational model that has been applied to such a wide range of experimental data.

Certain other features that are not measurable experimentally can be interrogated by the model. These include the stress field in each experiment, visualized in the middle column of Fig. 4.9. The regions of highest stress correspond to the locations of tissue failure, as investigated by us earlier [Korenczuk et al., 2017] in the context of a continuum anisotropic failure model. Perhaps most important is the ability of the model to examine micro-mechanics, as shown in the enlarged images of individual networks, and in the pie charts in the right hand column of Fig. 4.9. An important

difference between uniaxial and shear loading can be seen: in the uniaxial tests, between 55-60% of the failed fibers in the model are collagen and elastin, and only 40-45% of the failed fibers are interlamellar connections. In the shear lap case, in contrast, 49-78% of the failed fibers are interlamellar connections, suggesting that in the shear case, the lamellae may not fail at all, but rather they are allowed to slide relative to each other because of failed connections between them.

Inflation of the patient ATAA geometry yielded two major findings, (1) the sample exhibited a high amount of shear stress relative to its shear strength and (2) I.C. fibers were the primary fiber type to fail in the sample. During inflation, the sample exhibited the highest circumferential and shear strain near the greater curvature of the vessel (Fig. 4.10B, 4.10C), and a heterogeneous stress field throughout (Fig. 4.10D-F). The circumferential stress was higher than shear stress, with both stresses being highest in the regions of fiber failure (Fig. 4.10E-G). Although shear stress did not reach the same magnitude overall as stress in the circumferential direction, shear stress values were quite high, especially considering the tissue is much weaker in shear (c.f. experimental results). In certain locations, particularly near elements with high fiber failure, shear stress was even higher than circumferential stress (Fig. 4.10D). The importance of shear stress is particularly highlighted by the fact that I.C. fibers showed a much higher percentage of fiber failure compared to collagen and elastin fibers (Fig. 4.10H, 4.10I). In fact, the fraction of failed fibers that were interlamellar connections was greater in the inflation simulations (Fig. 4.10I) than in any of the simulated mechanical tests (Fig. 4.9). It is noted that the difference may be due to incomplete failure of the simulated vessel (i.e. the collagen and elastin would eventually fail). These results provide a comprehensive look into the mechanics and failure of ATAA tissue, and strongly suggest that shear loading plays a large role in the failure process.

4.4 Discussion

The three key results from this work are (1) that ATAA tissue shows similar prefailure behavior to porcine aorta, but has consistently lower strength, (2) that ATAA tissue is extremely weak in shear, to the point that even though shear stresses are not as large as tensile stresses in the vessel, shear failure may in fact be an important mechanism, and (3) a comprehensive approach considering multiple loading configurations must be used when assessing ATAA failure, as the vessel exhibits complex mechanical behavior.

Human ATAA tissue exhibited markedly different responses in all loading conditions and orientations compared to non-aneurysmal porcine tissue. The relative change of failure stress between ATAA and porcine samples however, showed no dependence on location or orientation. Rather, the ATAA failure stress (or peel tension) was roughly 50% of the corresponding value for porcine tissue in all cases. These results suggest that aneurysm disease progression may not favor any specific direction, but rather that it homogeneously compromises the structural integrity of the tissue, at least on average. Lap samples showed the lowest strength out of all loading conditions, suggesting that failure could most easily occur in the shear loading condition. This finding emphasizes the importance of interlaminar shear strength in the mechanical stability of the aneurysm pathology, and implicates its consideration as a possible risk factor. Shear may also be important in terms of tissue remodeling because of the load it places on the interlamellar connections, which represent, in part, the smooth muscle cells. Unlike circumferential and axial loads, which can be borne in significant part by the collagen and elastin in the aortic wall, shear stresses must be borne by the cells and thus could be a major driver for pathological remodeling of the tissue. Furthermore, the interlamellar failure in the inflation simulation is consistent

with dissection rather than outright rupture of ATAAs [Davies et al., 2002, Pal et al., 2014].

Human ATAA results for uniaxial and biaxial samples were in agreement with previous studies [Vorp et al., 2003, Okamoto et al., 2002]. Shear failure results showed the same trend in anisotropy (circumferential > axial) compared to [Sommer et al., 2016], but exhibited lower failure stresses, particularly in the axial direction. Peel samples exhibited lower average peel tension ($\sim$ 65 N/m) for both the circumferential and axial directions compared to [Pasta et al., 2012], but showed a similar trend in anisotropy (axial > circumferential). Here, we have presented a comprehensive resource for understanding experimental prefailure and failure behavior of ATAA tissue, particularly documenting the strength of the tissue in loading conditions previously less studied (i.e. shear).

Considering the stark differences in mechanical response and failure between experimental loading conditions, the multiscale model captured the overall behavior well. Using multiple loading configurations to optimize model parameters and incorporating the anatomical structure when creating network architecture allowed our multiscale model to provide unique insight on the comprehensive mechanical response of ATAA tissue to subfailure and failure loads across multiple length scales. The uniaxial loading condition exhibited high fiber failure in the planar layer of collagen and elastin, while the lap loading condition experienced high levels of I.C. failure, suggesting that the I.C.s bear a significant amount of the mechanical responsibility in the shear loading configuration. Furthermore, multiscale inflation simulations showed high shear stresses and I.C. failure, suggesting that shear is an important factor to consider when analyzing ATAA modes of failure. More work must clearly be done to quantify the importance of shear in predicting vessel failure, but these results suggest a new possible mode of failure and risk factor when considering ATAAs.

Though useful, our multiscale model still presented a variety of limitations. Microscale networks were constructed as simplified representations of the ATAA microenvironment, and oversimplified aspects such as vascular smooth muscle cells and fibrillin by only using one fiber type to describe the interlamellar space. Only passive mechanics were studied and modeled, neglecting the clearly present role of active contractility within the vessel wall, which may significantly affect the simulated tissue behavior, and thus our conclusions. Furthermore, the medial layer of the vessel wall was the only layer modeled, even though the adventitial layer is known to contribute mechanical stability [Holzapfel et al., 2000], and carries more than 50% of the pressure load at higher pressures [Schulze-Bauer et al., 2002]. The combination of modeling only passive mechanics and excluding the adventitial layer explains the large deformation observed during simulated inflation at a relatively low maximum pressure (50 mmHg).

Overall, several noteworthy differences were observed between human ATAA and porcine tissue, most of which suggest that the disease remodeling and weakening may involve multiple components. Tissue composition is clearly affected in different ways, meriting further exploration of the constituents' orientation and composition. Our findings also suggest that shear plays an important role in the failure of ATAAs, and must not be overlooked. These results emphasize the importance of fully understanding the structural and mechanical changes that occur in ATAAs, especially in terms of multidirectional failure, as the tissue is constantly under complex loading conditions *in vivo* where risk is not fully captured by current diameter-based methods.

4.5 Acknowledgment

The authors acknowledge the Minnesota Supercomputing Institute (MSI) and Bionet at the University of Minnesota Hospital for providing high-performance computing resources and tissue, respectively, that contributed to the research results reported within this paper. The authors also recognize and appreciate the technical assistance of Colleen Witzenburg, Ryan Mahutga, Celeste Blum, and Kenzie Trewartha. This work was supported by NIH grants R01 EB005813 and U01 HL139471, and by the National Science Foundation Graduate Research Fellowship Program under Grant No. 00039202 (CEK). Any opinions, findings, and conclusions or recommendations expressed in this material are those of the author(s) and do not necessarily reflect the views of the National Science Foundation. CEK is a recipient of the Richard Pyle Scholar Award from the ARCS Foundation.

Parameters	Value
Collagen Fibers	
Network orientation tensor, $[\Omega_{zz}\ \Omega_{\theta\theta}\ \Omega_{rr}]$	[0.42 0.58 0]
Fiber modulus (MPa), E_c	1.76
Fiber nonlinearity, B_c	1.1
Failure stretch, λ_c	2.0
Elastin Fibers	
Network orientation tensor, $[\Omega_{zz}\ \Omega_{\theta\theta}\ \Omega_{rr}]$	[0.52 0.48 0]
Fiber modulus (MPa), E_e	1.54
Fiber nonlinearity, B_e	0.9
Failure stretch, λ_e	2.2
Interlamellar Connections	
Network orientation tensor, $[\Omega_{zz}\ \Omega_{\theta\theta}\ \Omega_{rr}]$	[0.3 0.46 0.24]
Fiber modulus (MPa), E_{IC}	3.0
Fiber nonlinearity, B_{IC}	1.9
Failure stretch, λ_{IC}	1.7
Matrix	
Poisson's ratio, ν	0.495
Shear Modulus (MPa), G	3.76E-04
Proportions	
Total network volume fraction, ϕ	0.5
Elastin-to-collagen ratio	17:20

Table 4.1: The manually adjusted parameters for the multiscale model fit to all loading conditions (uniaxial, lap, biaxial). Initial guesses for parameters were based off of previous work with healthy porcine tissue [Witzenburg et al., 2017].

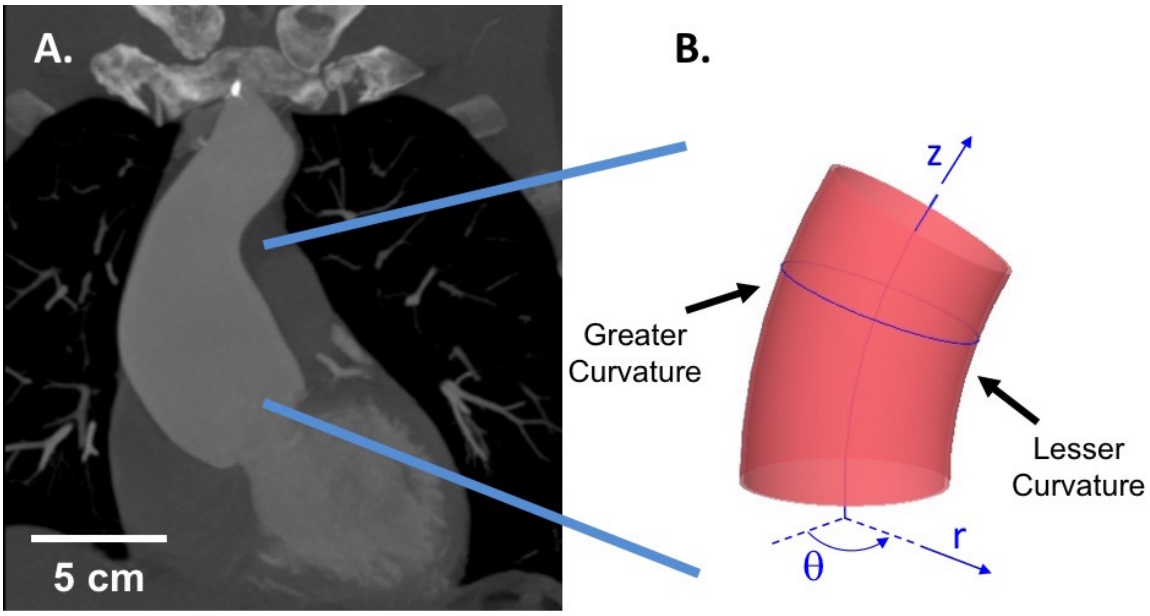

Figure 4.1: **A)** A coronal view of a patient ATAA from a CT scan. Scale bar shown in white. **B)** Conventions used for circumerential (θ), axial (z), and radial (r) directions. Greater and lesser curvatures also indicated.

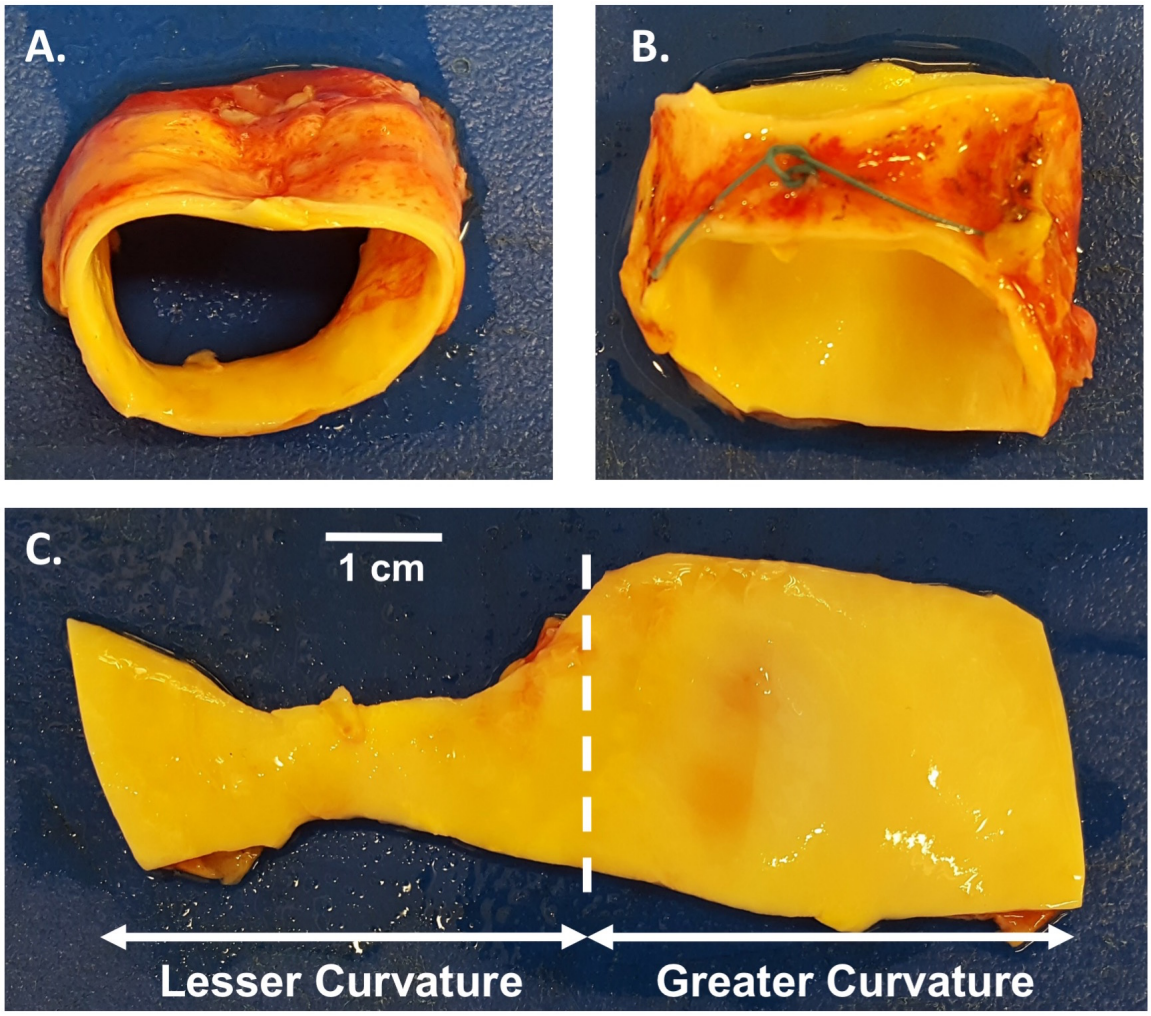

Figure 4.2: ATAA sample shown from **A)** transverse and **B)** sagittal directions. Lesser curvature indicated by the blue suture stitch. **C)** Intimal view of the ATAA tissue after opened. Greater and lesser curvatures indicated by arrows.

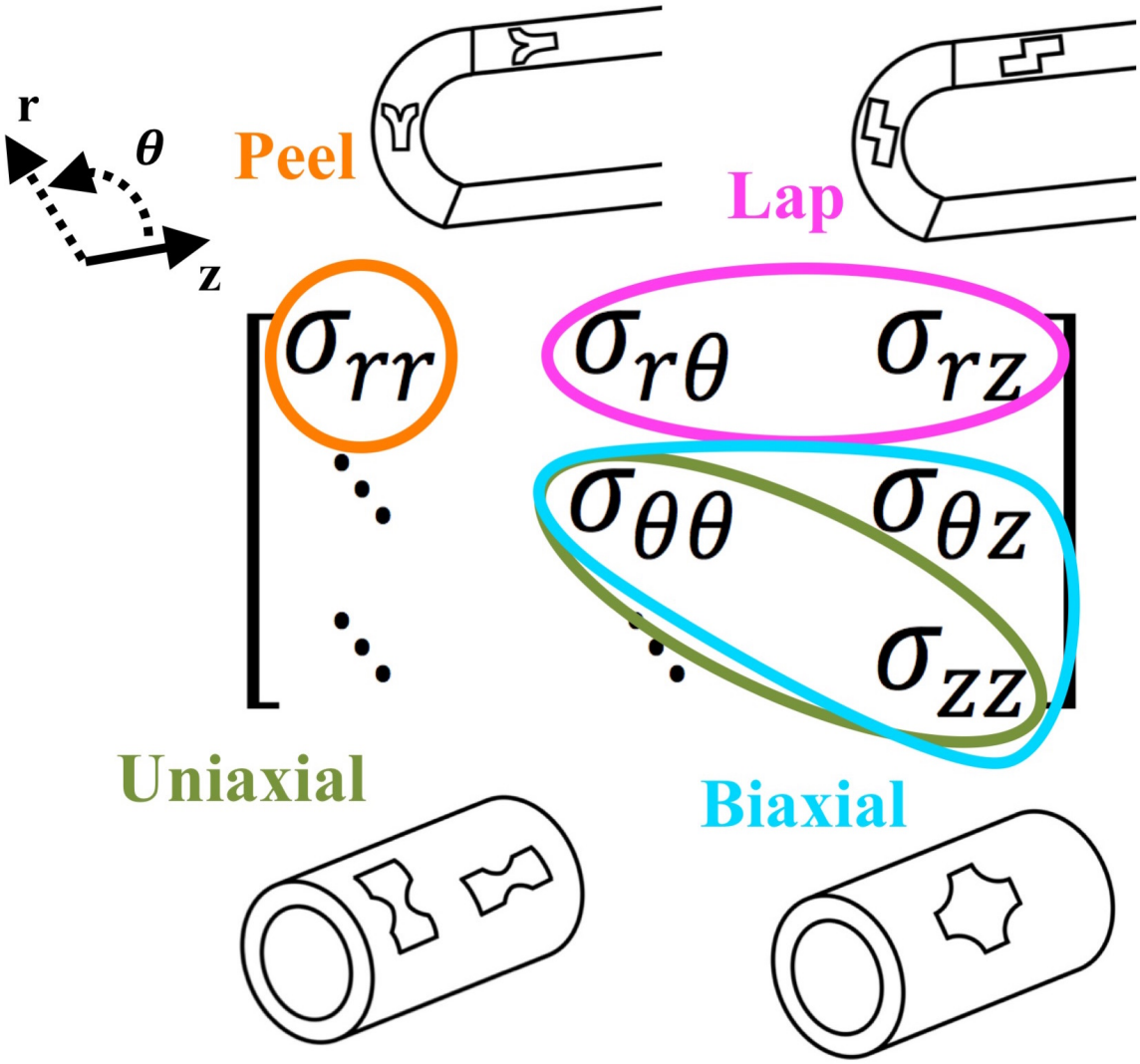

Figure 4.3: Stress tensor showing each of the loading conditions (uniaxial, peel, lap, and biaxial), and the stresses they produce (in-plane, in-plane shear, interlamellar shear).

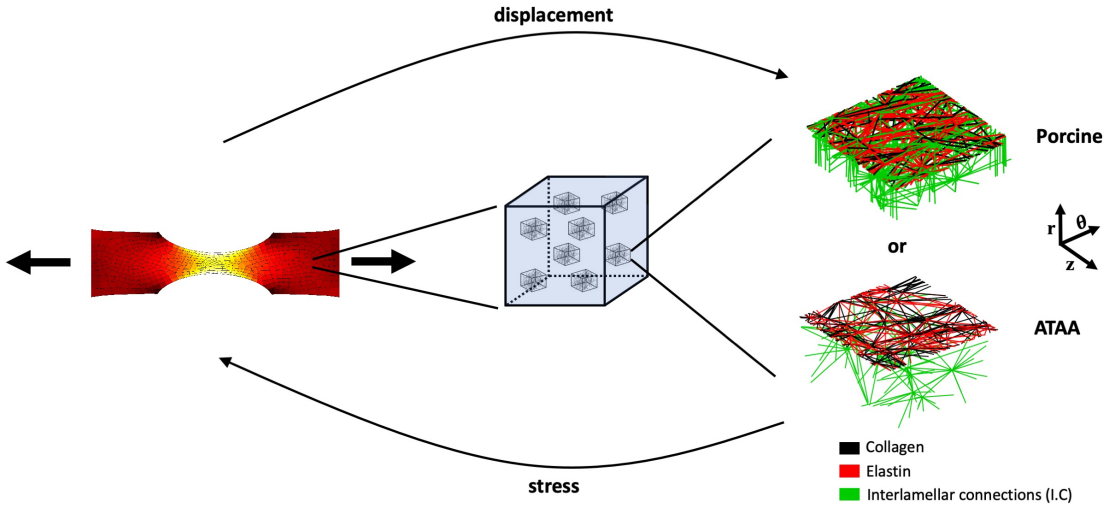

Figure 4.4: Graphic describing the overall multiscale computational modeling process. First, boundary conditions are applied to the macroscale finite element mesh (uniaxial geometry, left). RVEs located at each of the Gauss points within each element (middle) deform based on the element deformation, and are allowed to equilibrate, where all forces are balanced (right). The volume-averaged stress is then calculated for each RVE, and scaled up to the macroscale. This overall process iterates until force equilibrium is achieved on the macroscale.

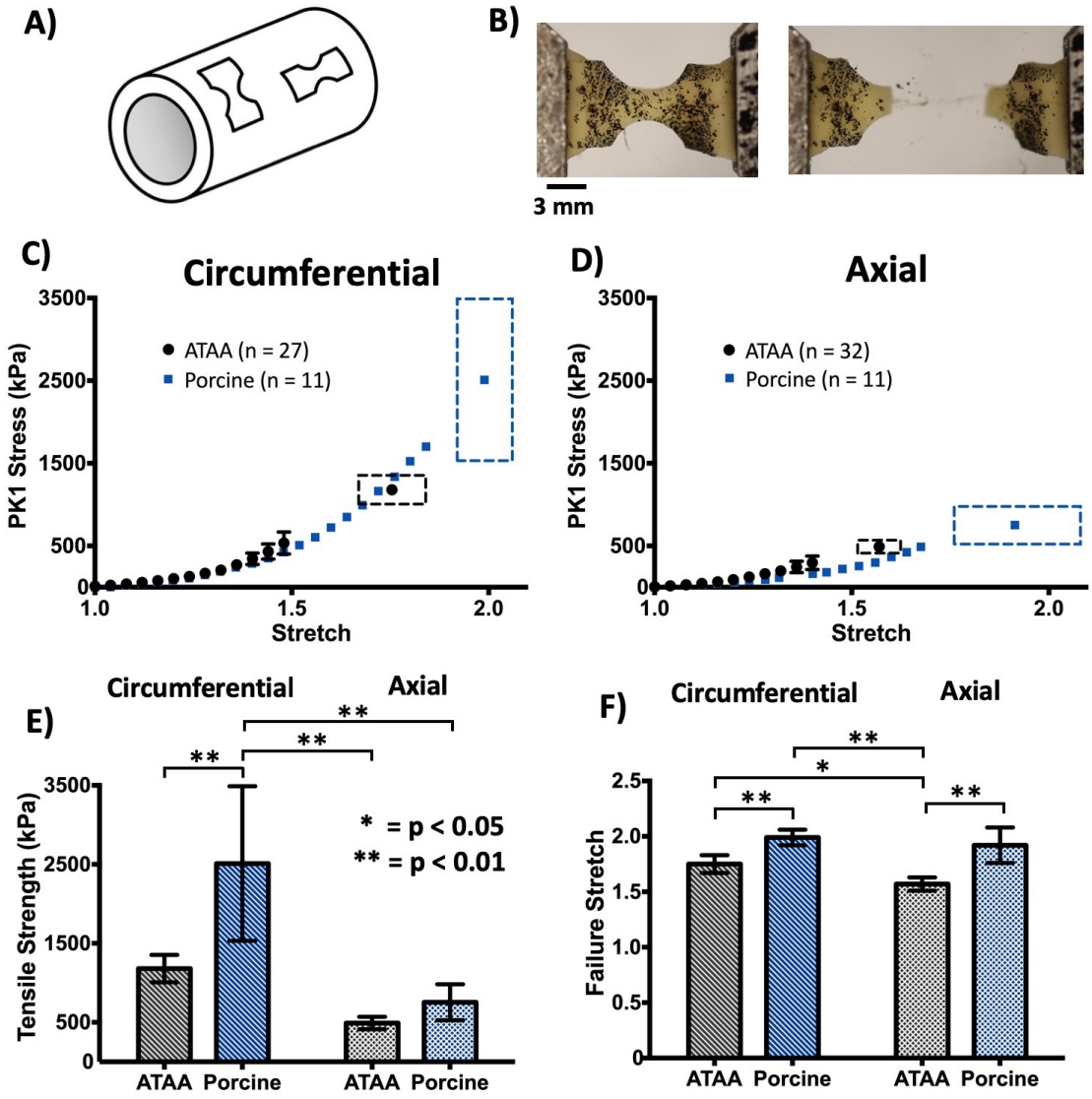

Figure 4.5: Results for uniaxial experiments. **A)** Schematic of uniaxial dogbone geometries on the vessel. **B)** One representative sample being pulled to failure. **C, D)** Circumferential and axial data shown for ATAA (black circles) and porcine tissue(blue squares). Average points with 95% CI are shown for ATAA, with a 95% CI box on the final failure point. Confidence intervals are not shown for porcine data for clarity. **E, F)** Circumferential and axial tensile strength and failure stretch shown for ATAA (black) and porcine (blue) data (mean $\pm$ 95% CI) with statistical significance between groups.

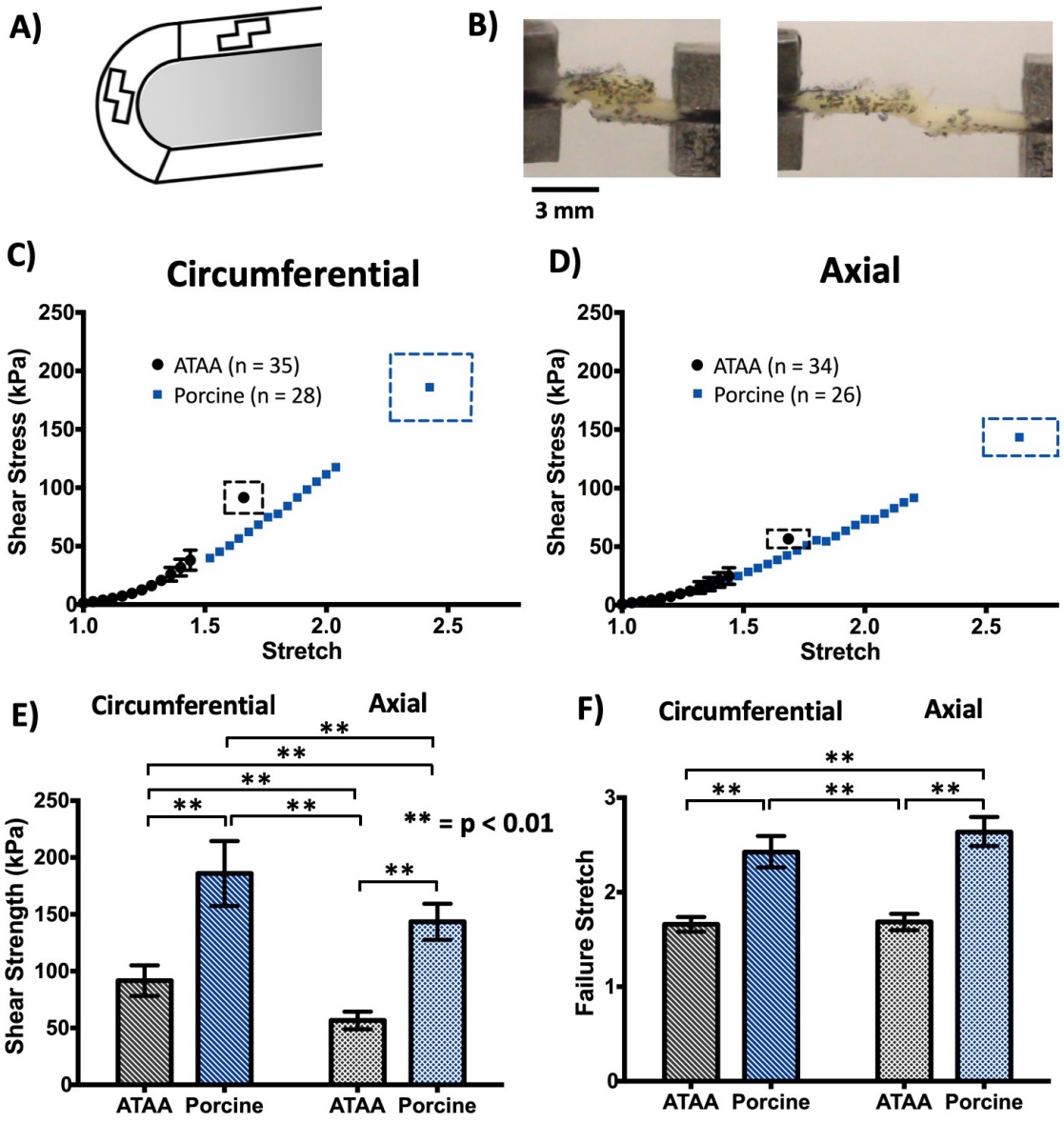

Figure 4.6: Results for lap experiments. **A)** Schematic of lap geometries on the vessel. **B)** One representative sample being pulled to failure. **C, D)** Circumferential and axial data shown for ATAA (black circles) and porcine tissue(blue squares). Average points with 95% CI are shown for ATAA, with a 95% CI box on the final failure point. Confidence intervals are not shown for porcine data for clarity. **E, F)** Circumferential and axial shear strength and failure stretch shown for ATAA (black) and porcine (blue) data (mean ± 95% CI).

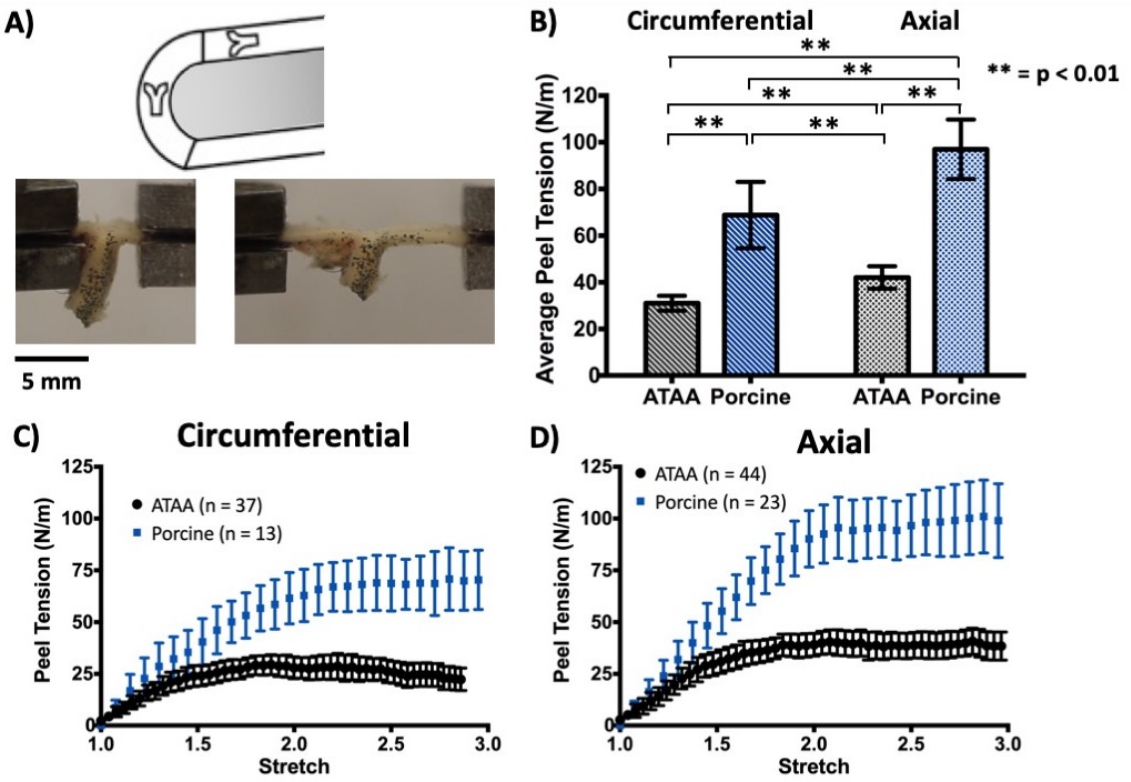

Figure 4.7: Results for peel experiments. **A)** A schematic showing the peel geometries on the vessel, and one representative sample being pulled to failure. **B)** Circumferential and axial average peel tension shown for ATAA (black) and porcine (blue) data (mean ± 95% CI). **C, D)** Circumferential and axial data shown for ATAA (black circles) and porcine tissue(blue squares). Average points are shown, with 95% CI.

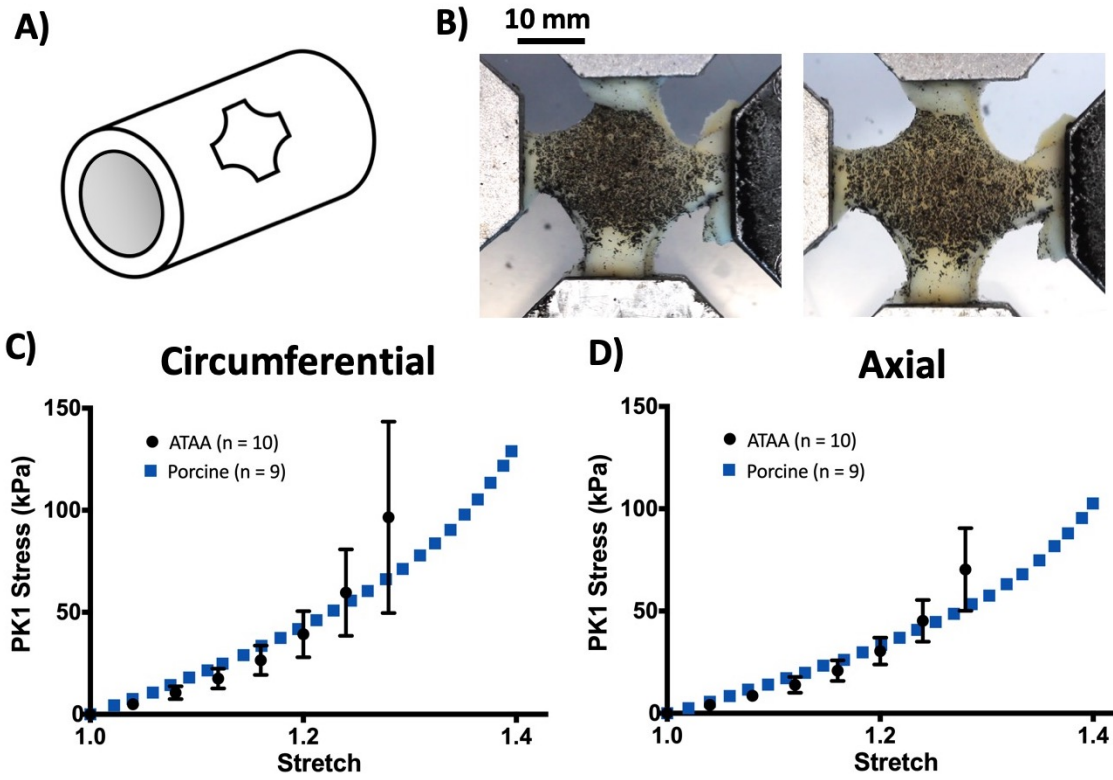

Figure 4.8: Results for biaxial experiments. **A)** Schematic of biaxail geometry on vessel. **B)** One representative sample being pulled in equibiaxial stretch. **C, D)** Circumferential and axial data shown for ATAA (black circles) and porcine tissue (blue squares). Average points with with 95% CI are shown for ATAA. Confidence intervals are not shown on porcine data for clarity.

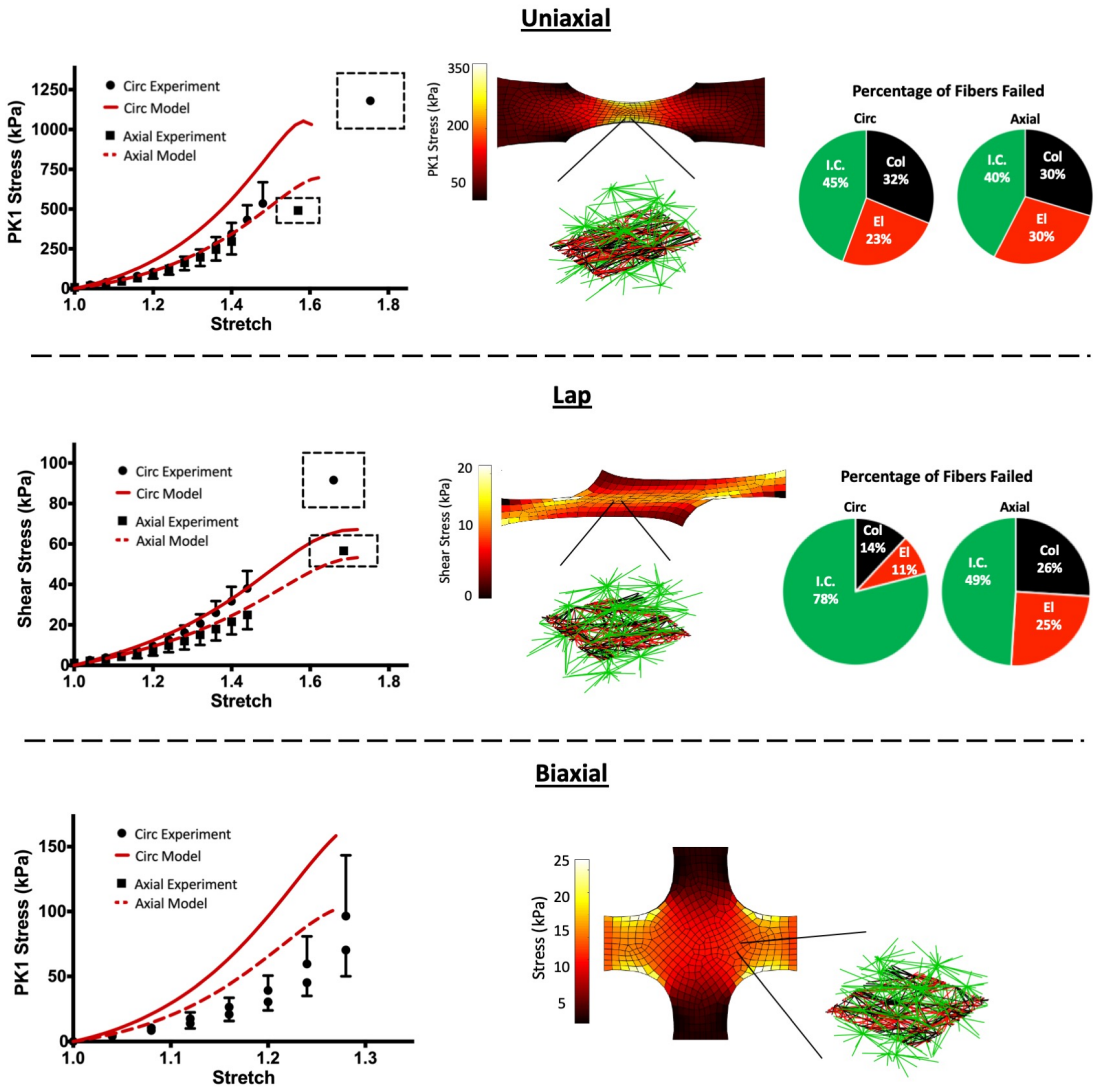

Figure 4.9: Multiscale modeling results for the uniaxial (top), lap (middle) and biaxial (bottom) loading cases. Model comparisons to experimental data are shown on the left for each loading condition. Model (red lines) shows similar behavior compared to ATAA experimental values for circumferential (black circles) and axial (black squares) directions. Error bars for experimental data are shown on either the top (circ) or bottom (axial) for clarity. Deformed macroscale geometries and networks are shown midway through the simulation (center). Percentages of failed fibers (right) are shown for both directions in the uniaxial and lap cases.

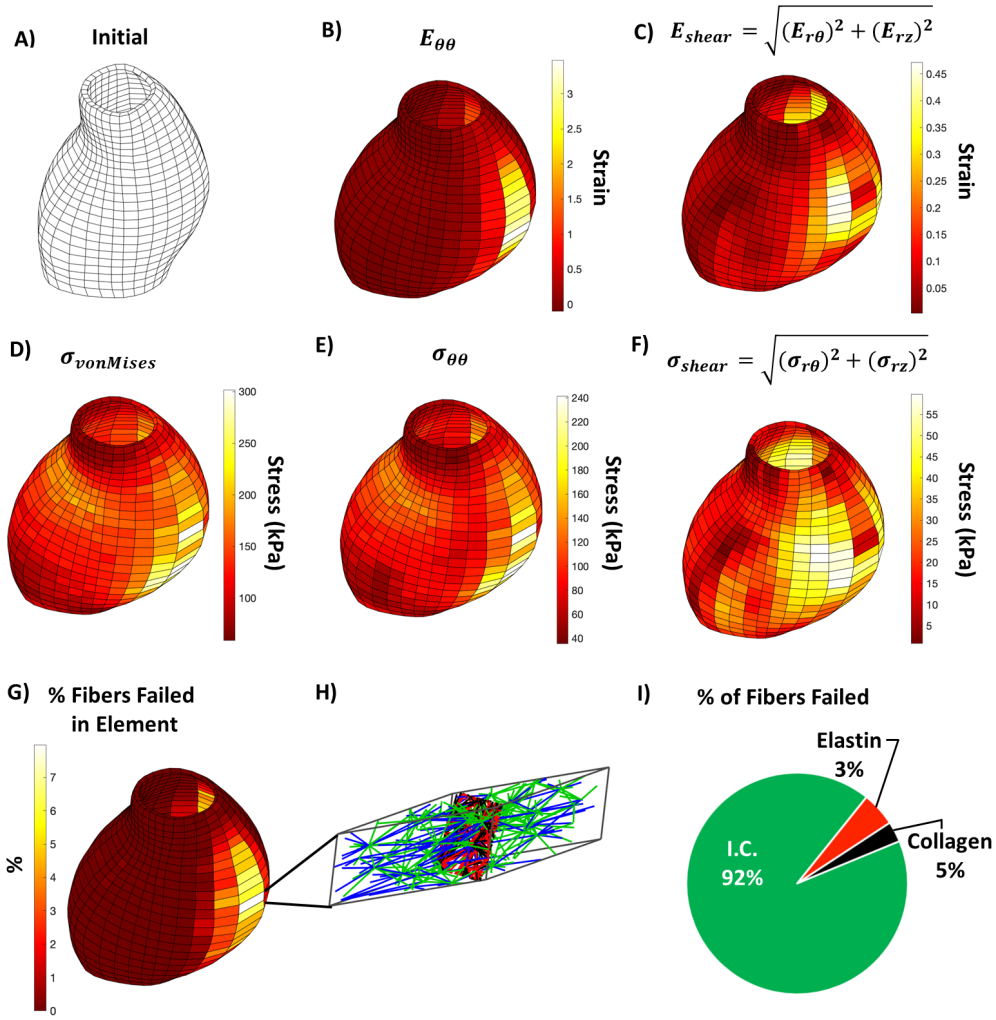

Figure 4.10: Multiscale results for patient ATAA inflation. **A)** The initial, undeformed state of the vessel prior to inflation, oriented such that the greater curvature is on the right. **B-G)** The deformed vessel at 50 mmHg, showing circumferential strain, shear strain, the ratio of shear to circumferential stress, circumferential stress, shear stress, and % of fiber failed in each element, respectively. **H)** A deformed network from the element with the most fiber failure. Black fibers represent collagen, red fibers represent elastin, green fibers represent I.C.s, and blue fibers indicate fibers that have failed in the network. High I.C. fiber failure ($\sim$17%) was present in the element with the most failed fibers compared to collagen ($\sim$1%) and elastin ($\sim$0.5%). **I)** The percentages of failed fibers throughout the entire vessel, showing significantly higher I.C. fiber failure throughout. The sample exhibited a heterogeneous response for all metrics, exhibiting fiber failure in locations of high circumferential and shear stress.

4.6 Supplemental Results

4.6.1 Experimental

Uniaxial samples showed a significant difference ($p < 0.01$) in tensile strength between the circumferential and axial directions (Fig. 4.11A), $\sigma_{\theta\theta} = 1308.6 \pm 226.5$ kPa, $\sigma_{zz} = 527.8 \pm 117.5$ kPa (mean $\pm$ 95%CI) for the greater curvature and $\sigma_{\theta\theta} = 1044.2 \pm 307.6$ kPa, $\sigma_{zz} = 449.4 \pm 113.3$ kPa for the lesser curvature).

ATAA peel samples showed no significant difference in peel tension between the circumferential and axial direction on the greater curvature (Fig. 4.11B, $T_{\theta\theta}^{peel} = 31.96 \pm 4.93$ N/m, $T_{zz}^{peel} = 39.86 \pm 5.82$ N/m), but did show a statistically significant ($p < 0.01$) difference in favor of the axial direction on the lesser curvature ($T_{\theta\theta}^{peel} = 30.0 \pm 4.45$ N/m, $T_{zz}^{peel} = 45.0 \pm 8.7$ N/m). No significant difference was found between the greater and lesser curvatures for either orientation.

When ATAA failure stresses and peel tension were normalized by respective porcine values for the uniaxial, peel, and lap tests, there were no significant differences between any of the orientations or loading conditions. Each sample exhibited roughly half of the porcine tissue strength in every testing geometry and location (Fig. 4.12).

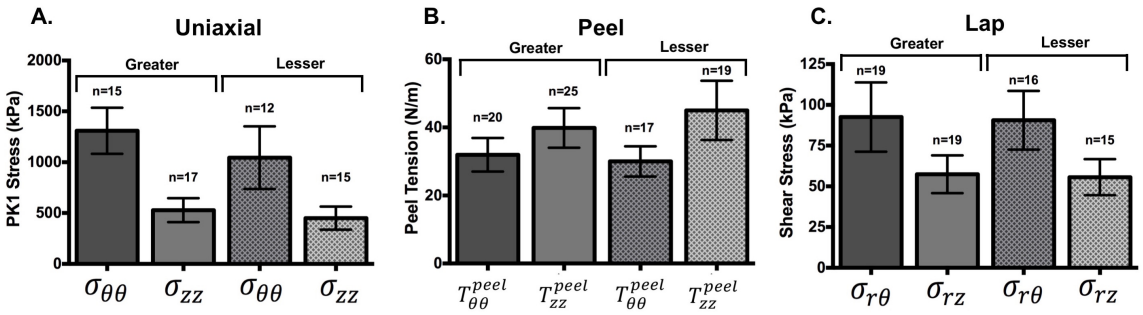

Figure 4.11: Comparison of greater and lesser curvature for uniaxial, peel, and lap loading configurations. No significant differences were seen between the greater and lesser curvature for any loading conditions or directions.

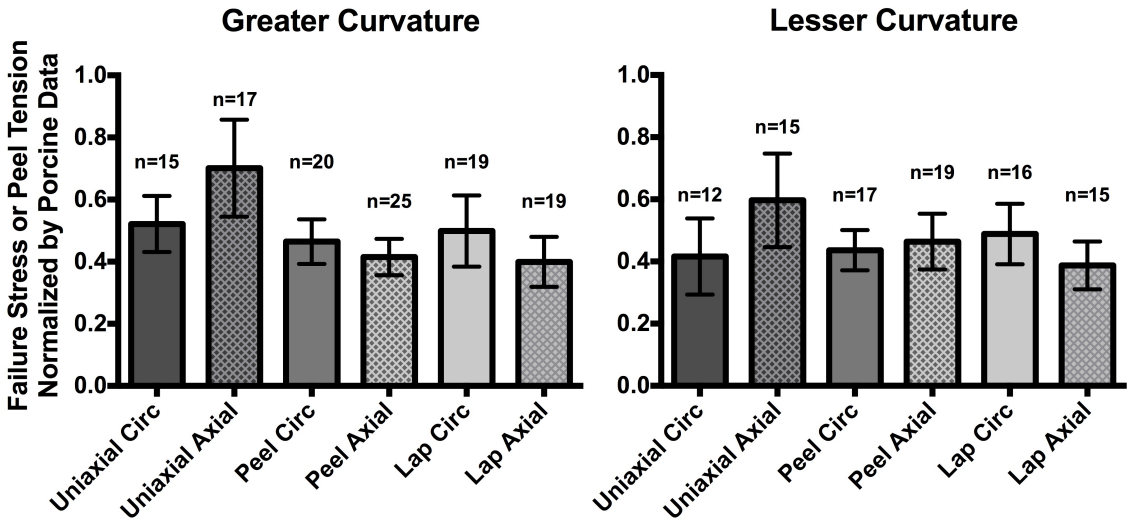

Figure 4.12: Greater and lesser curvature values normalized by porcine values for each given loading condition and direction. All ATAA samples exhibited roughly half the strength of porcine tissue.

Chapter 5

The Contribution of Individual Microstructural Components in Arterial Mechanics and Failure

The content of this chapter is in preparation for a manuscript to submit by Korenczuk, Blum, and Barocas. My contribution to the work was aiding in experimental testing and data processing, along with preparing computational models.

5.1 Introduction

Elastin, collagen, and vascular smooth muscle cells (VSMCs) are the primary components that comprise the microstructure of the arterial medial layer, playing a significant role in the vessel's mechanical response [Wagenseil and Mecham, 2009]. During the course of the cardiac cycle, varying loading configurations are imposed on the vessel wall, causing each microstructural component to experience different amounts of combined loading. While macroscopic mechanical behavior, such as nonlinearity

and anisotropy, has been observed in vessel studies [Ferruzzi et al., 2011, Vorp et al., 2003, Okamoto et al., 2002], the contribution of each individual constituent to the overall vessel mechanics is still relatively unclear. Furthermore, it is unknown how the responsibility of loading between these constituents shifts during aberrant remodeling, as in ascending thoracic aortic aneurysms (ATAAs), and how this changes the overall failure mechanics of the vessel.

In the native aortic media, collagen and elastin comprise planar lamellar layers that span the vessel thickness. Collagen exhibits a preferred orientation in the circumferential direction, giving rise to vessel anisotropy, while elastin is relatively isotropic. In cylindrical vessels, the planar layers bear a significant amount of loading during expansion and contraction, as the vessel does not experience high amounts of shear. In curved geometries, however, such as the ascending aorta, the loading imposed on the vessel wall changes, introducing intramural shear (chapter 4, [Korenczuk et al., 2019]). Intramural shear mechanically engages the interlamellar components, namely VSMCs and fibrillin-1, and introduces them to the complex mechanical response of the vessel. As these components do not typically bear mechanical load, the vessel exhibits a much weaker response in shear loading conditions compared to tensile loading [Witzenburg et al., 2017, Korenczuk et al., 2019].

In the pathological case of ATAAs, remodeling of the microstructural components occurs. Typically, along with diameter enlargement and wall thinning, the pathology is accompanied by disorganization or loss of elastin, collagen, VSMCs, and fibrillin [Campa et al., 1987, Humphrey, 2013]. Due to the complex nature of the ATAA pathology, it is difficult to understand how mechanical loading changes on the tissue, and thus its underlying components. Previous work (chapter 4, [Korenczuk et al., 2019]) has shown that the vessel is strongest in uniaxial loading, but weakest in shear lap loading. Furthermore, during simulations of inflation, ATAAs experience a high

amount of shear loading, and exhibit high interlamellar fiber failure. These results demand further interrogation of the mechanical contribution each constituent within the vessel wall, to help understanding mechanical loading in cases such as ATAAs.

Selectively removing components via enzymatic digestion allows demarcation between constituent contributions to various loading configurations. Previous digestion studies have removed collagen and/or elastin from aortic tissue [Gundiah et al., 2007, Weisbecker et al., 2013, Schriefl et al., 2015] or carotid tissue [Fonck et al., 2007], followed by uniaxial testing or pressurization. These studies found that elastin bore more mechanical loading at low-stretch regimes, transitioning to collagen load bearing at higher stretches. Furthermore, collagen was identified as the primary component in tissue softening/damage [Weisbecker et al., 2013, Schriefl et al., 2015]. Though these studies provide insight on the contribution of individual components in the arterial wall, only one loading condition and 1-2 digestion groups were studied. This trend is also seen in non-digestion studies on arterial mechanics, often exploring uniaxial testing [Macrae et al., 2016, García-Herrera et al., 2012, Vorp et al., 2003, Okamoto et al., 2002, Iliopoulos et al., 2009a, Duprey et al., 2010, Khanafer et al., 2011], but showing a deficiency in shear testing [Sommer et al., 2016]. Testing shear loading configurations is highly important, as the vessel may experience shear during inflation, and many disease etiologies begin between the artery layers [Mazurek et al., 2017]. Despite much progress in understanding vessel mechanics, there remains a need to explore the role of each arterial component, in order to grasp the underlying mechanisms behind important vascular diseases. Here, we use enzymatic digestion to explore the role of collagen, elastin, and VSMCs on the mechanical composition of porcine abdominal aortas in uniaxial and shear lap loading configurations. These two test protocols were chosen to evaluate both normal and shear stress effects on the tissue.

5.2 Methods

5.2.1 Experiments

Sample Preparation

Porcine abdominal aorta samples were sourced from the University of Minnesota's Visible Heart Lab and stored in 1x PBS solution for no longer than 24 hours post-dissection. A total of (n=11) pigs were utilized over the course of this study, and sample locations were randomized to account for animal variability.

Tissue thickness was measured using calipers by taking six measurements at different positions along the artery and calculating an average thickness. Uniaxial and lap samples were prepared in a similar fashion to previous studies [Witzenburg et al., 2017, Korenczuk et al., 2019]. All arteries were cut open along their axial lengths to produce planar sections, allowing for uniaxial and lap samples to be cut in the circumferential (θ) and axial (z) directions (Fig. 5.1).

Digestion Techniques

Different incubation times of collagenase, elastase, and SDS were chosen as independent variables to observe the degradation rate of vessels under a single solution concentration, attempting to isolate digestion of collagen, elastin, and VSMCs, respectively.

Collagenase and elastase solutions were prepared (500 U ml-1, Type IV, Worthington Biochemicals, NJ, USA, and 10 U ml-1, porcine pancreatic elastase, Worthington Biochemicals, NJ, USA, respectively) in 1X Dulbecco's phosphate-buffered saline solution (Quality Biological, MD, USA). Samples were thoroughly cleaned and incubated at 37° C for either 1, 3, 5, 7, or 9 hours [Mazurek et al., 2017]. All tissue was

completely submerged in buffered-media and thoroughly washed in 1X PBS following treatments. SDS solutions were prepared in 1X phosphate-buffered saline solution (PBS, Quality Biological, MD, USA). Samples were subjected to 2 cycles of 1 hour in solution followed by a 5-minute rinse with PBS, then for a third cycle of 2 hours in solution and a 5-minute rinse in PBS at room temperature on a rocker. Samples were subsequently incubated at 4° C for either 24, 48, 72, or 96 hours. All samples were imaged in their undeformed configuration and reserved for later analysis. Small portions from each artery segment were collected after each digestion for histological review.

Uniaxial Strain-to-Failure

Uniaxial and lap data was collected using a Microbionix Uniaxial Tester (University of Minnesota, Tissue Mechanics Lab) and a 10 N load cell (MTS) attached to a stationary backing. Samples were clamped into machined grips lined with sandpaper to prevent slippage of the tissue. After the samples had been placed into the uniaxial grips, the load cell was zeroed, and the actuator arm was moved so a 0.2 N pre-load was measured. Once the preload was applied, each sample was imaged, and the initial grip gauge length was measured via ImageJ. Samples were then pulled to failure at a constant rate of 0.045 mm/s. To maintain tissue hydration during the experiments, samples were placed in a 1X PBS bath at room temperature. Mechanical testing of untreated tissue was conducted as a control. The Microbionix Uniaxial Tester recorded the force and position from the 10N MTS load cell and the actuator arm.

The First Piola-Kirchhoff stress of uniaxial samples was calculated by dividing the grip force by the original cross-sectional area of the neck. For lap samples, the average shear stress was calculated as the force divided by the original overlap area of the sample. Grip stretch was calculated for both samples by dividing the deformed

grip length by the original length.

5.3 Results

5.3.1 Experiments

Histology is shown for collagenase (Fig. 5.2), elastase (Fig. 5.3), and SDS (Fig. 5.4) groups. Control data (Fig. 5.5A, 5.6A, n = 4-5 for each) were used to establish baseline stress and strain values in the absence of matrix degradation enzymes and validate the testing methods. As expected, the circumferential direction showed greater stiffness in both the uniaxial and the lap tests. Individual data curves for each of the digestion cases in uniaxial (Fig. 5.5) and lap (Fig. 5.6) configurations showed a trend of decreasing mechanical strength with increasing digestion time, as expected (n = 1-4 for each digestion case). In the subsequent examination of the digested samples, we focused on the failure point, defined as the maximum stress, and we calculated the average failure stress and failure stretch.

The average failure stresses and stretches are shown in Figs. 5.7 and 5.8. For the collagenase and elastase groups (Figs. 5.7A,B and 5.8A,B), after an initial rise in failure stress at the 1-hour time point, especially in the uniaxial tests, further digestion led to a gradual decline in failure stress indicative of a degraded collagen matrix. The early strengthening can be attributed to a preliminary cross-linking of amino acids located near the enzyme binding sites in the collagen [Snedeker and Gautieri, 2014]. This effect was most notable in the circumferential direction. Collagen and elastin digestion showed little effect on failure stretch for either the uniaxial or the lap geometry. Besides a slight drop in the axial failure stretch for the collagenase case (Fig. 5.7A), the only notable trend is in the lap collagenase case. Here, the circumferential direction saw an initial increase in failure stretch, followed by a declining trend, and

finally a sharp increase. The axial direction also experienced the same trend, only with a longer initial increase, and quicker decrease in failure stretch with exceeding digestion time. Whether these can be attributed to actual behavior, or noise due to sample and test method variability, is unknown.

SDS treatment did not make any significant impact on the uniaxial loading case for either failure stress or stretch (Fig. 5.7C). In the lap loading case (Fig. 5.8C), however, the circumferential failure stress caused a declining trend (similar to the lap collagenase and elastase groups), while the axial failure stress remained constant until 96 hrs, where there was a sharp increase. Failure stretch was also affected, with both circumferential and axial direction experiences upward trends with increasing digestion time.

An additional observation, whose significance is not clear, is that while control lap samples (circ and axial) and digested (collagenase and elastase) lap samples in the circumferential direction failed in the overlap region, axial digested samples failed in the sample arms. Since the arms of a lap sample are in extension during the test, this shift in the location of the failure point may be driven by weakening of the tissue in uniaxial extension as seen in Figure 5.5. Similarly, the drop-in failure stress during lap testing (Fig. 5.6) is not necessarily an indication of weakening in shear but rather a consequence of extreme weakening of the arms.

5.4 Discussion

Much is understood about the biological and biomechanical mechanisms that contribute to vascular disease progression, but many aspects of mechanical contribution remain unknown. The lack of available tissue from the onset of vascular disease to its end stages makes ex-vivo digestion experiments a critical substitute. This study

examined the contributions of collagen, elastin, and VSMCs to the failure behavior of the tissue in both shear and uniaxial extension.

When treating with collagenase, uniaxial testing showed a failure stress of half for both directions compared to when treating with elastase. This trend highlights the mechanical importance of collagen as a primary load-bearer within the vessel wall. As collagen is degraded, the mechanical strength of the vessel decreases much more compared to when elastin is degraded, similar to other studies [Schriefl et al., 2015]. Failure stretches for the two cases remained similar. Lap samples did not exhibit as stark of a trend, with both collagenase and elastase groups showing very similar failure stresses. Some trends may be present in the failure stretches of lap collagenase samples (as mentioned previously), but overall there seems to be minimal effect on the lap failure stretch with either collagenase or elastase treament.

SDS treatments seem to have minimal effect on the uniaxial strength of the vessel, which affirms the primary mechanical role of the lamellar layer. As VSMCs were digested, the uniaxial failure stress and stretch remained relatively constant. In the lap loading case, however, some interesting trends did present themselves. Axial failure stress remained constant, followed by a significant increase at 96 hrs of digestion. The reason for this increase is unknown, but could be due to significant digestion effects at long time points, where more than just VSMCs are digested after long periods of exposure, causing unknown reorganization. Lap samples in the circumferential direction, on the other hand, exhibited decreased failure stress with increased SDS treatment. Though the amplitude of decline was about half as strong as the collagenase and elastase treatments, the decline is still present. This result confirms previous results (chapter 4, [Korenczuk et al., 2019]) that suggest VSMCs (and other interlamellar components) play a larger role in the mechanical response of the vessel in shear than tensile loading. Furthermore, the failure stretch for both circumferential

and axial directions increased in the lap case with increasing digestion time, suggesting that the failure of VSMCs in shear happens first, and may drive subsequent (and thus catastrophic) failure in the vessel overall by placing more stress on lamellar components after failure. The failure stretch is nearly twice that in both directions for the 96 hr case when comparing SDS groups to collagenase and elastase. These results align with previous work (chapter 4, [Korenczuk et al., 2019]), and highlight the importance of understanding remodeling and thus mechanical reorganization of load-bearing in pathological cases such as ATAAs, particularly as it relates to shear loading configurations.

5.5 Future Work

In order to better understand the contribution of each component to arterial failure, these experiments are being paired with a multiscale finite-element model used previously [Witzenburg et al., 2017, Korenczuk et al., 2019]. The model, described extensively in [Witzenburg et al., 2017], simulates both the uniaxial and lap testing geometries, containing networks comprised of collagen, elastin, and interlamellar connection fibers. The parameters for each of these fibers will be specified to match the control group of experimental data presented here, ensuring an appropriate material description. Each of the digestion cases will be modeled by decreasing the concentration of the different components individually, allowing a comprehensive look at the effect digestion has on failure for both loading conditions. The model will help provide further insight to the mechanical response and failure of the abdominal aorta as it relates to its microstructural components.

5.6 Acknowledgment

We gratefully acknowledge the Visible Heart Lab at the University of Minnesota for providing porcine aortic tissue. This work was supported by the National Science Foundation Graduate Research Fellowship Program under Grant No. 00039202 (CEK). Any opinions, findings, and conclusions or recommendations expressed in this material are those of the author(s) and do not necessarily reflect the views of the National Science Foundation. CEK is a recipient of the Richard Pyle Scholar Award from the ARCS Foundation.

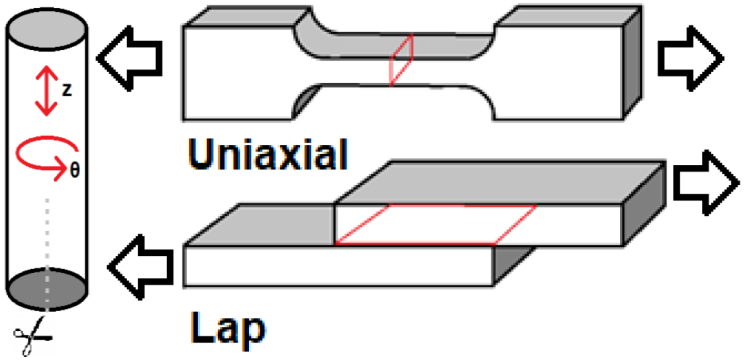

Figure 5.1: Uniaxial and lap testing geometries. Arrows indication the direction of loading, and red outlines indicate the cross-sectional area used for the calculation of stress.

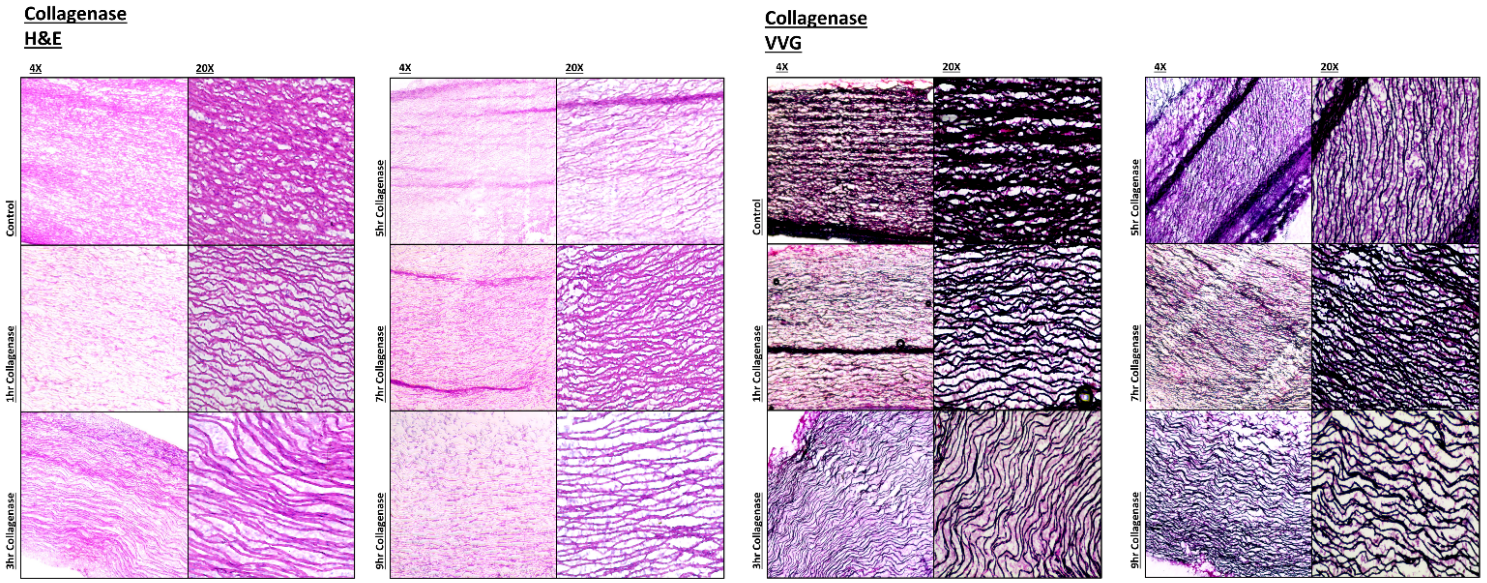

Figure 5.2: Histological staining for collagenase groups.

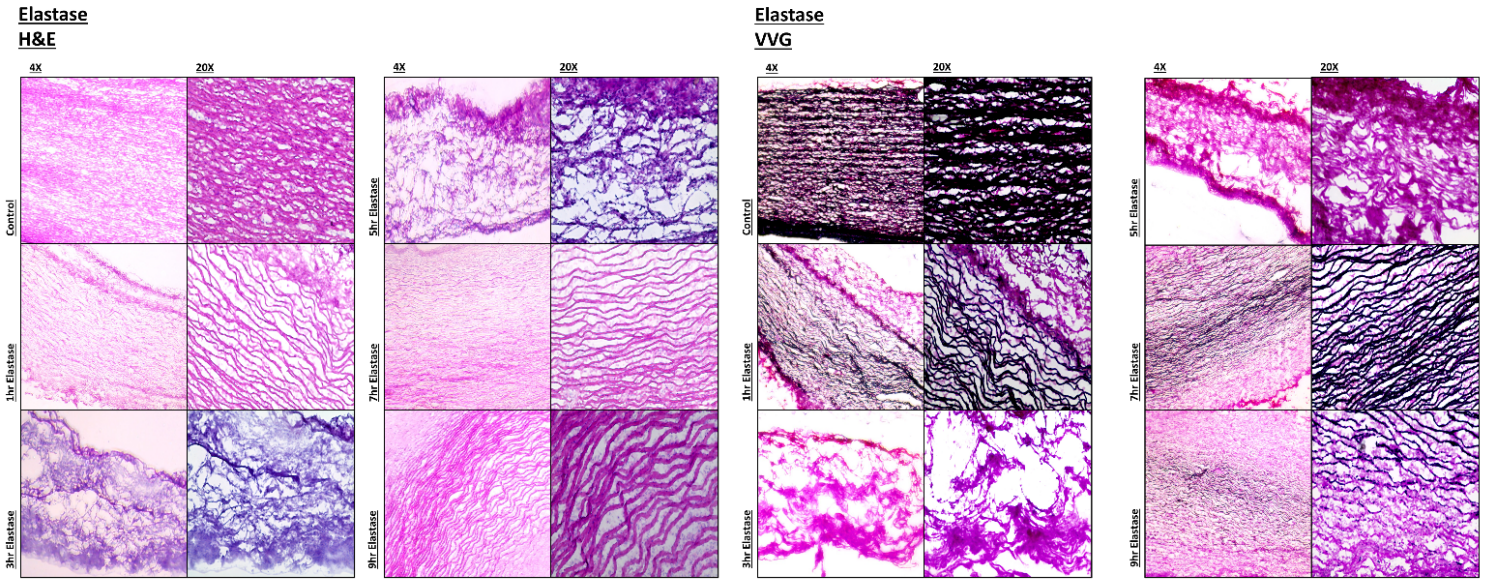

Figure 5.3: Histological staining for elastase groups.

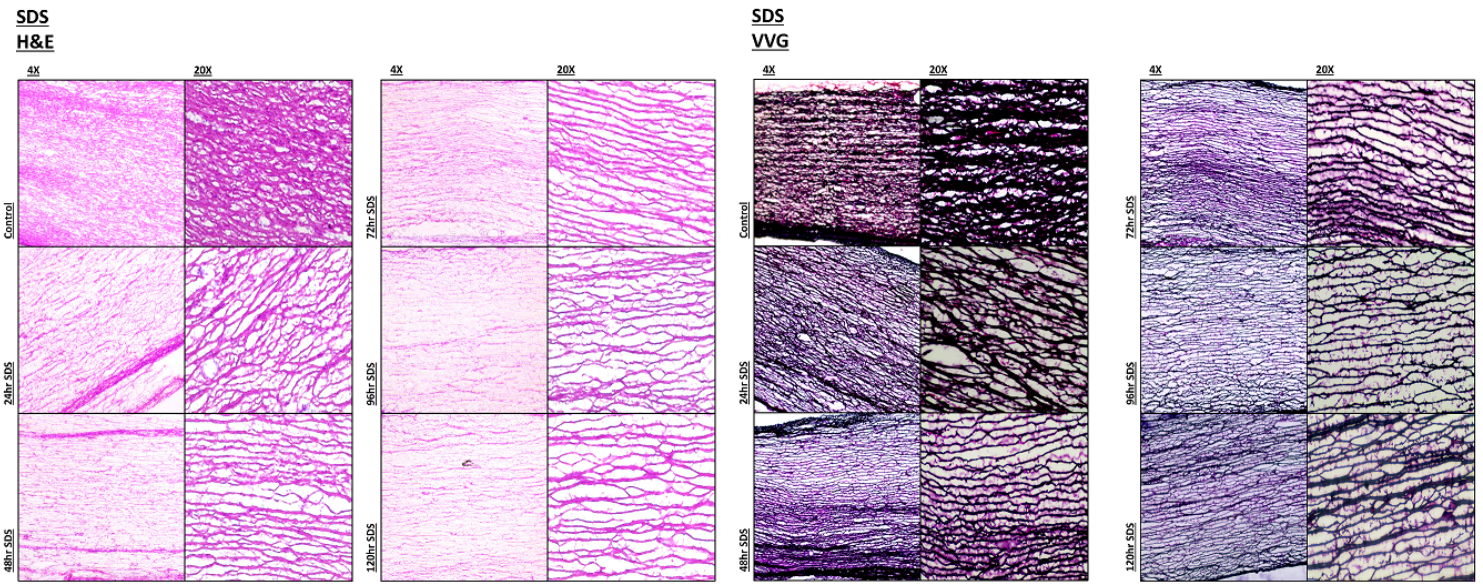

Figure 5.4: Histological staining for SDS groups.

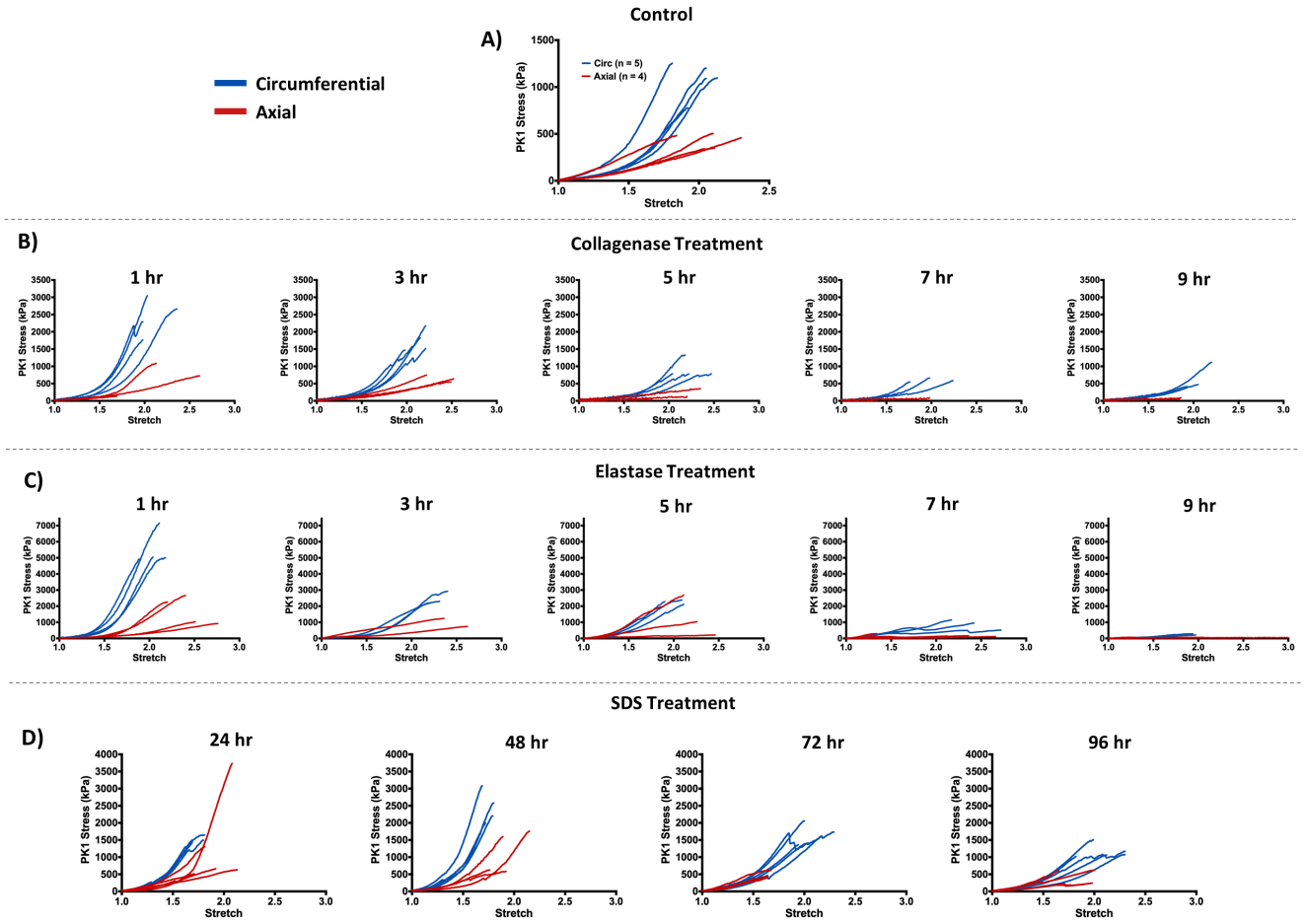

Figure 5.5: A) Stress/stretch plots shown for uniaxial controls. Blue = circumferential, red = axial. B) Uniaxial collagenase, treatment time indicated by figure title. C) Uniaxial elastase, treatment time indicated by figure title. D) Uniaxial SDS, treatment time indicated by figure title.

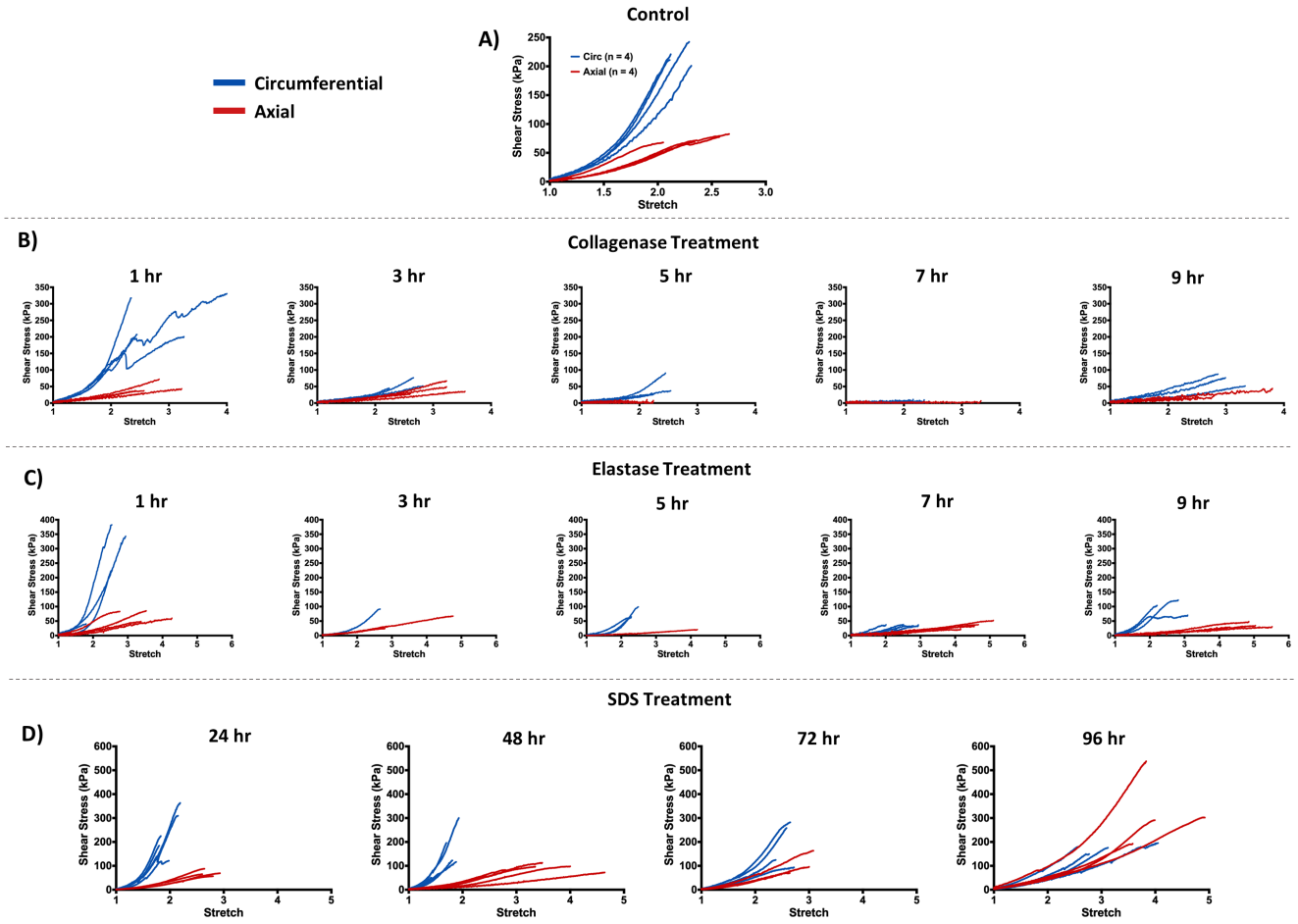

Figure 5.6: A) Stress/stretch plots shown for lap controls. Blue = circumferential, red = axial. B) Lap collagenase, treatment time indicated by figure title. C) Lap elastase, treatment time indicated by figure title. D) Lap SDS, treatment time indicated by figure title.

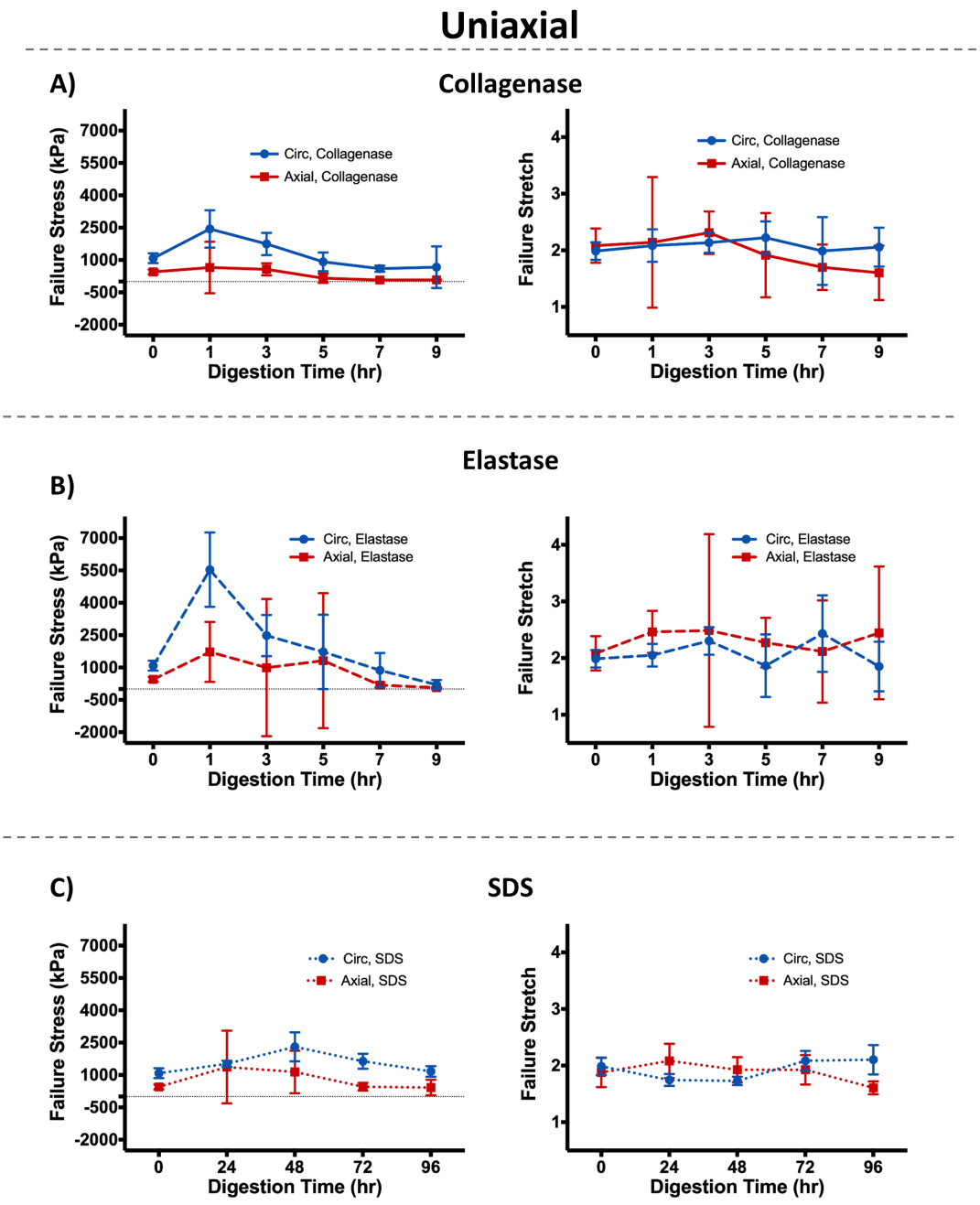

Figure 5.7: Average results for uniaxial samples. A) Average failure stress (left) and stretch (right) shown for each of the time points in the collagenase group. Error bars indicated 95% Confidence Intervals. B) Average failure stress and stretch for the elastase groups. C) Average failure stress and stretch for the SDS groups.

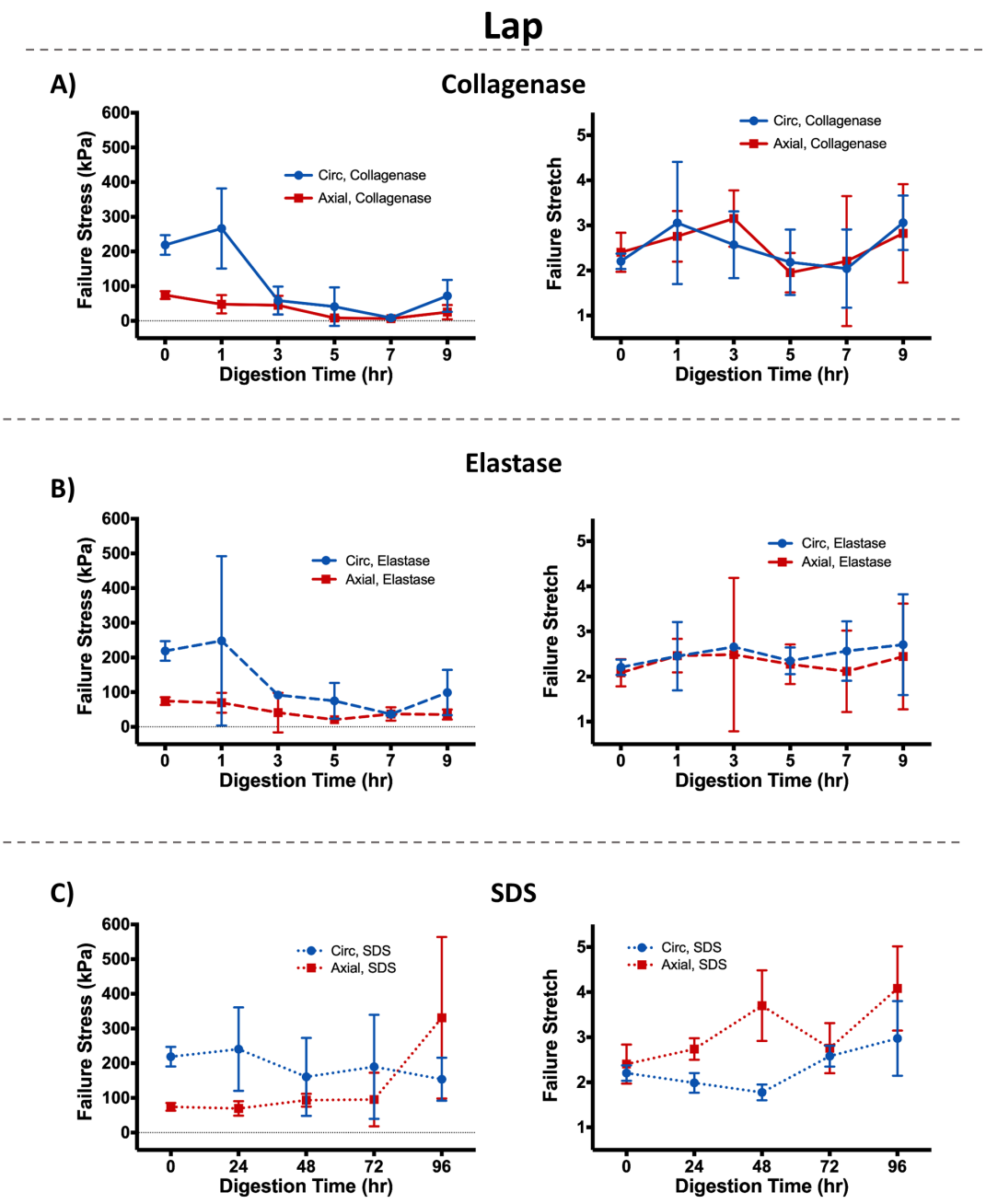

Figure 5.8: Average results for lap samples. A) Average failure stress (left) and stretch (right) shown for each of the time points in the collagenase group. Error bars indicated 95% Confidence Intervals. B) Average failure stress and stretch for the elastase groups. C) Average failure stress and stretch for the SDS groups.

Chapter 6

Conclusions and Future Work

6.1 Major Findings and Conclusions

The field of soft tissue mechanics, specifically the area of failure prediction, has made significant strides over the past few decades as modeling capabilities continue to increase. Predictive tools are becoming more accurate, and computational models more readily available. The work presented here adds to a continuously growing field, taking a systematic approach to analyze failure of cardiovascular tissues.

First, the practice of using isotropic failure criteria for anisotropic tissues was challenged in chapter 2, by exploring the Tsai-Hill failure criterion. We found that the Tsai-Hill failure criterion, though relatively simplistic by definition, was able to predict failure in porcine abdominal aortic tissue more accurately than other commonly used isotropic failure criteria. The Tsai-Hill failure criterion had better prediction in the particular case of complex tissue loading, where shear stresses and strength play a larger role.

Next, we explored the role of microstructural fiber alignment and density by interrogating failure of myocardial infarcted tissue through a multiscale modeling ap-

proach in chapter 3. As cardiovascular tissues such as the heart and aorta rely heavily on their microstructural components and organization, understanding how fiber orientation affects failure in myocardial tissue is crucial. Our results showed that heterogeneous fiber networks have a significant effect on the overall tissue response, producing locations of high stress and strain within the tissue. Furthermore, tissue simulations that incorporated heterogeneous networks saw drastically higher rates of failure, highlighting the important role that fiber orientation plays in tissue response and subsequent failure. Even when tissue samples with homogeneous and heterogeneous fiber networks shared the same average fiber direction and degree of alignment for the overall sample, characteristics such as anisotropy, peak strain, peak stress, and fiber failure differ greatly between the two cases.

In chapter 4, we expanded upon this modeling work, focusing on the complex pathology of ATAAs. Our model considered several crucial factors which contribute to ATAA failure, incorporating complex loading situations to specify accurate model parameters, and simulating patient-specific ATAA failure. Our results highlighted the lack of innate intramural shear strength in the tissue, and significant impact shear stress may have on tissue failure. The tissue exhibited the lowest strength in shear loading conditions, and also experienced high shear stresses during inflation simulations, suggesting that shear strength and stress play a role in the delamination and failure of ATAAs. Interlamellar connections also experienced the highest amount of failure during inflation simulations, revealing that vessel response relies heavily on the interlamellar components to bear mechanical load.

Lastly, in chapter 5, we explored the mechanical responsibility of each microstructural component within the aortic wall. Our preliminary results show that collagen and elastin bear a large responsibility of the load in uniaxial loading conditions, while VSMCs play a much larger role in shear loading conditions. These results,

taken collectively, exemplify the importance of accurate material descriptions and failure criteria when predicting failure in complex tissues such as ATAAs. With the understanding that both myocardial infarctions and ATAA tissue experience severe microstructural remodeling, predictive tools should consider these aspects during mechanical assessment, as they play a significant role in the tissue response.

6.2 Future Directions

Though novel and important, the work here is certainly not exhaustive. The potential for future studies to further develop and expand upon these results remains endless. As a majority of my research has been spent studying the ATAA pathology, I will provide some thoughts on possible next steps.

In chapter 4, we were able to produce one of the first multiscale computational models of a patient ATAA geometry. The results provided extensive insight to the behavior of ATAA tissue under inflation, but only one geometry was observed. In order to better understand how shear plays a role, and whether the risk of failure can be capture via modeling, more inflation simulations need to be performed. By growing a larger database of inflation simulations, other potential risk factors may also be observed, such as curvature, wall thickness, and tissue heterogeneity (i.e. calcifications or other tissue defects). Furthermore, our model specified fiber parameters based on an average of data collected from a variety of patients, and every network in the model was similar in fiber density and orientation (i.e. spatial heterogeneity was not considered). Future models could specify parameters to fit different patient demographics and tissue conditions, creating a more patient-specific approach.

Additionally, inflation simulations can be performed on patients with longitudinal CT scans. Due to the often slow-progressing failure or delamination of ATAAs, there

are times when the location of failure initiation can be observed via CT. By simulating the geometry in a state prior to failure, risk factors, such as shear stress, can be examined to see if they can predict locations of actual patient tissue failure. The ability to observe failure progression and initiation is often unavailable when analyzing soft tissue failure, making the ATAA pathology a unique case of failure development. Furthermore, the multiscale model could be expanded to incorporate other aspects, such as fiber remodeling (i.e. deposition and removal) and active cell contraction, which both play a role in the progression and response of ATAAs.

While the multiscale model presents an in-depth look into tissue failure by incorporating fibrous components, the ultimate goal is to provide better predictive tools to inform physician risk assessment. Large mesh geometries paired with extensive fibrous networks yields a rather computational expensive tool that requires substantial user input. Once key risk contributors are identified, the implications can be distilled into a simpler model that allows for more clinical impact. The potential of using a simplified hyper-elastic model through automated segmentation and inflation would be tangibly beneficial to the medical field, given that risk contributors can be easily assessed, and a comprehensive risk assessment compiled.

It is clear that measurements of aneurysm size do not fully capture the risk of failure, nor the role of each mechanical contributor during the complex remodeling of the pathology. It is also clear that the ATAA condition imposes a severely detrimental impact on the quality and survival of human life. It remains my hope that one day, the work compiled here can contribute to the creation of better predictive tools for assessing the risk of ATAA failure, ultimately improving patient outcomes.

Bibliography

[Abdelmohsen et al., 2012] Abdelmohsen, K., Tominaga-Yamanaka, K., Srikantan, S., Yoon, J. H., Kang, M. J., and Gorospe, M. (2012). RNA-binding protein AUF1 represses Dicer expression. *Nucleic Acids Research*.

[Agarwal et al., 2006] Agarwal, B., Broutman, L., and Chandrashekhara, K. (2006). *Analysis and performance of fiber composites.* John Wiley & Sons.

[Aktas and Karakuzu, 1999] Aktas, A. and Karakuzu, R. (1999). Failure Analysis of Two-Dimensional Carbon-Epoxy Composite Plate Pinned Joint. *Mechanics of Composite Materials and Structures*, 6:347–361.

[Alford et al., 2008] Alford, P. W., Humphrey, J. D., and Taber, L. A. (2008). Growth and remodeling in a thick-walled artery model: Effects of spatial variations in wall constituents. *Biomechanics and Modeling in Mechanobiology*.

[Alford and Taber, 2008] Alford, P. W. and Taber, L. A. (2008). Computational study of growth and remodelling in the aortic arch. *Computer Methods in Biomechanics and Biomedical Engineering*.

[Arola and Ramulu, 1997] Arola, D. and Ramulu, M. (1997). Orthogonal cutting of fiber-reinforced composites: A finite element analysis. *International Journal of Mechanical Sciences*, 39(5):597–613.

[ASTM, 2001] ASTM (2001). Standard Test Method for Lap Shear Adhesion for Fiber Reinforced Plastic (FRP) Bonding. *Standards*.

[Avanzini et al., 2014] Avanzini, A., Battini, D., Bagozzi, L., and Bisleri, G. (2014). Biomechanical Evaluation of Ascending Aortic Aneurysms. *BioMed Research International*.

[Azadani et al., 2013] Azadani, A. N., Chitsaz, S., Mannion, A., Mookhoek, A., Wisneski, A., Guccione, J. M., Hope, M. D., Ge, L., and Tseng, E. E. (2013). Biomechanical Properties of Human Ascending Thoracic Aortic Aneurysms. *Annals of Thoracic Surgery*, 96(1):50–58.

[Babu et al., 2015] Babu, A. R., Byju, A. G., and Gundiah, N. (2015). Biomechanical Properties of Human Ascending Thoracic Aortic Dissections. *Journal of Biomechanical Engineering*.

[Baek et al., 2007] Baek, S., Gleason, R. L., Rajagopal, K. R., and Humphrey, J. D. (2007). Theory of small on large: Potential utility in computations of fluid-solid interactions in arteries. *Computer Methods in Applied Mechanics and Engineering*, 196(31-32):3070–3078.

[Balakhovsky et al., 2014] Balakhovsky, K., Jabareen, M., and Volokh, K. Y. (2014). Modeling rupture of growing aneurysms. *Journal of Biomechanics*, 47(3):653–658.

[Ban et al., 2017] Ban, E., Zhang, S., Zarei, V., Barocas, V., Winkelstein, B., and Picu, C. (2017). Collagen organization in facet capsular ligaments varies with spinal region and with ligament deformation. *Journal of Biomechanical Engineering*, 139(7):071009.

[Beisang et al., 2012] Beisang, D., Rattenbacher, B., Vlasova-St Louis, I. A., and Bohjanens, P. R. (2012). Regulation of CUG-Binding Protein 1 (CUGBP1) binding to target transcripts upon T cell activation. *Journal of Biological Chemistry*.

[Beller et al., 2004] Beller, C. J., Labrosse, M. R., Thubrikar, M. J., and Robicsek, F. (2004). Role of aortic root motion in the pathogenesis of aortic dissection. *Circulation*, 109(6):763–769.

[Benjamin et al., 2018] Benjamin, E., Virani, S., Callaway, C., Chamberlain, A., Chang, A., Cheng, S., Chiuve, S., Cushman, M., Delling, F., Deo, R., de Ferranti, S., Ferguson, J., Fornage, M., Gillespie, C., Isasi, C., Jimenez, M., Jordan, L., Judd, S., Lackland, D., Lichtman, J., Lisabeth, L., Liu, S., Longnecker, C., Lutsey, P., Mackey, J., Matchar, D., Matsushita, K., Mussolino, M., Nasir, K., O'Flaherty, M., Palaniappan, L., Pandey, A., Pandey, D., Reeves, M., Ritchey, M., Rodrigues, C., Roth, G., Rosamond, W., Sampson, U., Satou, G., Shah, S., Spartano, N., Tirschwell, D., Tsao, C., Jenifer, V., Willey, J., Wilkins, J., Wu, J., Alger, H., Wong, S., and Muntner, P. (2018). Heart disease and stroke statistics - 2018 update: A report from the American Heart Association. *Circulation*, 137(12):e67–e492.

[Benyumov et al., 2012] Benyumov, A. O., Hergert, P., Herrera, J., Peterson, M., Henke, C., and Bitterman, P. B. (2012). A Novel Zebrafish Embryo Xenotransplantation Model to Study Primary Human Fibroblast Motility in Health and Disease. *Zebrafish*.

[Berger and Elefteriades, 2012] Berger, J. A. and Elefteriades, J. A. (2012). Toward uniformity in reporting of thoracic aortic diameter.

[Booth et al., 2012] Booth, A. J., Hadley, R., Cornett, A. M., Dreffs, A. A., Matthes, S. A., Tsui, J. L., Weiss, K., Horowitz, J. C., Fiore, V. F., Barker, T. H., Moore, B. B., Martinez, F. J., Niklason, L. E., and White, E. S. (2012). Acellular normal and fibrotic human lung matrices as a culture system for in vitro investigation. *American Journal of Respiratory and Critical Care Medicine*.

[Caliari et al., 2016] Caliari, S. R., Vega, S. L., Kwon, M., Soulas, E. M., and Burdick, J. A. (2016). Dimensionality and spreading influence MSC YAP/TAZ signaling in hydrogel environments. *Biomaterials*.

[Campa et al., 1987] Campa, J. S., Greenhalgh, R. M., and Powell, J. T. (1987). Elastin degradation in abdominal aortic aneurysms. *Atherosclerosis*, 65(1):13–21.

[Cezayirlioglu et al., 1985] Cezayirlioglu, H., Bahniuk, E., Davy, D. T., and Heiple, K. G. (1985). Anisotropic yield behavior of bone under combined axial force and torque. *Journal of Biomechanics*, 18(1):61–69.

[Chandran et al., 2008] Chandran, P. L., Stylianopoulos, T., and Barocas, V. H. (2008). Microstructure-Based, Multiscale Modeling for the Mechanical Behavior of Hydrated Fiber Networks. *Multiscale Modeling & Simulation*.

[Chaudhuri et al., 2015] Chaudhuri, O., Gu, L., Darnell, M., Klumpers, D., Bencherif, S. A., Weaver, J. C., Huebsch, N., and Mooney, D. J. (2015). Substrate stress relaxation regulates cell spreading. *Nature Communications*.

[Chaudhuri et al., 2016] Chaudhuri, O., Gu, L., Klumpers, D., Darnell, M., Bencherif, S. A., Weaver, J. C., Huebsch, N., Lee, H. P., Lippens, E., Duda, G. N., and Mooney, D. J. (2016). Hydrogels with tunable stress relaxation regulate stem cell fate and activity. *Nature Materials*.

[Chaulk et al., 2014] Chaulk, S. G., Lattanzi, V. J., Hiemer, S. E., Fahlman, R. P., and Varelas, X. (2014). The hippo pathway effectors TAZ/YAP regulate dicer expression and MicroRNA biogenesis through Let-7. *Journal of Biological Chemistry*.

[Chen et al., 2015] Chen, Y., Mohammed, A., Oubaidin, M., Evans, C. A., Zhou, X., Luan, X., Diekwisch, T. G., and Atsawasuwan, P. (2015). Cyclic stretch and compression forces alter microRNA-29 expression of human periodontal ligament cells. *Gene*.

[Choudhury et al., 2009] Choudhury, N., Bouchot, O., Rouleau, L., Tremblay, D., Cartier, R., Butany, J., Mongrain, R., and Leask, R. L. (2009). Local mechanical and structural properties of healthy and diseased human ascending aorta tissue. *Cardiovascular Pathology*, 18(2):83–91.

[Chuong and Fung, 1983] Chuong, C. J. and Fung, Y. C. (1983). Three-dimensional stress distribution in arteries. *Journal of Biomechanical Engineering*, 105(3):268–274.

[Claeson and Barocas, 2017] Claeson, A. A. and Barocas, V. H. (2017). Planar biaxial extension of the lumbar facet capsular ligament reveals significant in-plane shear forces. *Journal of the Mechanical Behavior of Biomedical Materials*, 65:127–136.

[Clark and Glagov, 1985] Clark, J. M. and Glagov, S. (1985). Transmural organization of the arterial media. The lamellar unit revisited. *Arteriosclerosis: An Official Journal of the American Heart Association, Inc.*, 5(1):19–34.

[Clarke et al., 2016] Clarke, S. A., Richardson, W. J., and Holmes, J. W. (2016). Modifying the mechanics of healing infarcts: Is better the enemy of good? *Journal of Molecular and Cellular Cardiology*, 93:115–124.

[Cleveland Clinic, 2014] Cleveland Clinic (2014). Thoracic Aortic Aneurysm.

[Clouthier et al., 2015] Clouthier, A. L., Hosseini, H. S., Maquer, G., and Zysset, P. K. (2015). Finite element analysis predicts experimental failure patterns in vertebral bodies loaded via intervertebral discs up to large deformation. *Medical Engineering and Physics*, 37(6):599–604.

[Coady et al., 1999] Coady, M. A., Rizzo, J. A., Hammond, G. L., Kopf, G. S., and Elefteriades, J. A. (1999). Surgical intervention criteria for thoracic aortic aneurysms: a study of growth rates and complications. *The Annals of Thoracic Surgery*, 67(6):1922–1926.

[Codelia et al., 2014] Codelia, V. A., Sun, G., and Irvine, K. D. (2014). Regulation of YAP by mechanical strain through Jnk and Hippo signaling. *Current Biology*.

[Conrad et al., 2014] Conrad, T., Marsico, A., Gehre, M., and Ørom, U. A. (2014). Microprocessor activity controls differential miRNA biogenesis in vivo. *Cell Reports*.

[Cortes et al., 2010] Cortes, D. H., Lake, S. P., Kadlowec, J. A., Soslowsky, L. J., and Elliott, D. M. (2010). Characterizing the mechanical contribution of fiber angular distribution in connective tissue: Comparison of two modeling approaches. *Biomechanics and Modeling in Mechanobiology*, 9(5):651–658.

[Cosgrove et al., 2016] Cosgrove, B. D., Mui, K. L., Driscoll, T. P., Caliari, S. R., Mehta, K. D., Assoian, R. K., Burdick, J. A., and Mauck, R. L. (2016). N-cadherin adhesive interactions modulate matrix mechanosensing and fate commitment of mesenchymal stem cells. *Nature Materials*.

[Cowin, 1986] Cowin, S. C. (1986). Fabric Dependence of an Anistropic Strength Criterion. *Mechanics of Materials*, 5:251–260.

[Cretu et al., 2010] Cretu, A., Castagnino, P., and Assoian, R. (2010). Studying the Effects of Matrix Stiffness on Cellular Function using Acrylamide-based Hydrogels. *Journal of Visualized Experiments*.

[Cruz et al., 2007] Cruz, C., Sousa, A. R., Madureira, A. J., Pinho, T., Ramos, I., Pinho, P., Silva Cardoso, J., and Maciel, M. J. (2007). Number 13-07: An Important Tool Before A Tetralogy of Fallot Reoperation.

[Davies et al., 2006] Davies, R. R., Gallo, A., Coady, M. A., Tellides, G., Botta, D. M., Burke, B., Coe, M. P., Kopf, G. S., and Elefteriades, J. A. (2006). Novel measurement of relative aortic size predicts rupture of thoracic aortic aneurysms. *Annals of Thoracic Surgery*.

[Davies et al., 2002] Davies, R. R., Goldstein, L. J., Coady, M. A., Tittle, S. L., Rizzo, J. A., Kopf, G. S., and Elefteriades, J. A. (2002). Yearly rupture or dissection rates for thoracic aortic aneurysms: simple prediction based on size. *The Annals of Thoracic Surgery*, 73(1):17–28.

[Derrien et al., 2000] Derrien, K., Fitoussi, J., Guo, G., and Baptiste, D. (2000). Prediction of the effective damage properties and failure properties of nonlinear anisotropic discontinuous reinforced composites. *Computer Methods in Applied Mechanics and Engineering*, 185(2-4):93–107.

[Dewald et al., 2004] Dewald, O., Ren, G., Duerr, G. D., Zoerlein, M., Klemm, C., Gersch, C., Tincey, S., Michael, L. H., Entman, M. L., and Frangogiannis, N. G. (2004). Of mice and dogs: species-specific differences in the inflammatory response following myocardial infarction. *The American journal of pathology*, 162(4):665–677.

[Dhume et al., 2018] Dhume, R. Y., Shih, E. D., and Barocas, V. H. (2018). Multiscale model of fatigue of collagen gels. *Biomechanics and Modeling in Mechanobiology*, 18(1):175–187.

[Dingemans et al., 2000] Dingemans, K. P., Teeling, P., Lagendijk, J. H., and Becker, A. E. (2000). Extracellular matrix of the human aortic media: An ultrastructural histochemical and immunohistochemical study of the adult aortic media. *Anatomical Record*.

[Dobrin, 1978] Dobrin, P. B. (1978). Mechanical Properties of Arteries. *Physiological Reviews*, 58(2):397–460.

[Dotter et al., 1950] Dotter, C. T., Roberts, D. J., and Steinberg, I. (1950). Aortic length: angiocardiographic measurements. *Circulation*.

[Doyle et al., 2009] Doyle, B. J., Callanan, A., Burke, P. E., Grace, P. A., Walsh, M. T., Vorp, D. A., and McGloughlin, T. M. (2009). Vessel asymmetry as an additional diagnostic tool in the assessment of abdominal aortic aneurysms. *Journal of Vascular Surgery*, 49(2):443–454.

[Doyle et al., 2010] Doyle, B. J., Cloonan, A. J., Walsh, M. T., Vorp, D. A., and McGloughlin, T. M. (2010). Identification of rupture locations in patient-specific abdominal aortic aneurysms using experimental and computational techniques. *Journal of Biomechanics*, 43(7):1408–1416.

[Dufort et al., 2011] Dufort, C. C., Paszek, M. J., and Weaver, V. M. (2011). Balancing forces: Architectural control of mechanotransduction.

[Duprey et al., 2010] Duprey, A., Khanafer, K., Schlicht, M., Avril, S., Williams, D., and Berguer, R. (2010). In vitro characterisation of physiological and maximum elastic modulus of ascending thoracic aortic aneurysms using uniaxial tensile testing. *European Journal of Vascular and Endovascular Surgery*, 39(6):700–707.

[Duprey et al., 2016] Duprey, A., Trabelsi, O., Vola, M., Favre, J. P., and Avril, S. S. (2016). Biaxial rupture properties of ascending thoracic aortic aneurysms. *Acta Biomaterialia*, 42:273–285.

[Duthon et al., 2006] Duthon, V. B., Barea, C., Abrassart, S., Fasel, J. H., Fritschy, D., and Ménétrey, J. (2006). Anatomy of the anterior cruciate ligament. *Knee Surgery, Sports Traumatology, Arthroscopy*, 14(3):204–213.

[Elefteriades, 2002] Elefteriades, J. A. (2002). Natural history of thoracic aortic aneurysms: indications for surgery, and surgical versus nonsurgical risks. *The Annals of Thoracic Surgery*, 74(5):S1877–S1880.

[Elefteriades, 2010] Elefteriades, J. A. (2010). Indications for aortic replacement. In *Journal of Thoracic and Cardiovascular Surgery*.

[Etz et al., 2012] Etz, C. D., Misfeld, M., Borger, M. A., Luehr, M., Strotdrees, E., and Mohr, F. W. (2012). Current indications for surgical repair in patients with bicuspid aortic valve and ascending Aortic Ectasia.

[Feerick et al., 2013] Feerick, E. M., Liu, X. C., and McGarry, P. (2013). Anisotropic mode-dependent damage of cortical bone using the extended finite element method (XFEM). *Journal of the Mechanical Behavior of Biomedical Materials*, 20:77–89.

[Ferrara and Pandolfi, 2008] Ferrara, A. and Pandolfi, A. (2008). Numerical modelling of fracture in human arteries. *Computer Methods in Biomechanics and Biomedical Engineering*.

[Ferruzzi et al., 2011] Ferruzzi, J., Vorp, D. A., and Humphrey, J. D. (2011). On constitutive descriptors of the biaxial mechanical behaviour of human abdominal aorta and aneurysms. *Journal of the Royal Society Interface*.

[Fomovsky et al., 2012a] Fomovsky, G. M., Clark, S. A., Parker, K. M., Ailawadi, G., and Holmes, J. W. (2012a). Anisotropic reinforcement of acute anteroapical infarcts improves pump function. *Circulation: Heart Failure*, 5(4):515–522.

[Fomovsky and Holmes, 2009] Fomovsky, G. M. and Holmes, J. W. (2009). Evolution of scar structure, mechanics, and ventricular function after myocardial infarction in the rat. *American Journal of Physiology-Heart and Circulatory Physiology*, 298(1):H221–H228.

[Fomovsky et al., 2011] Fomovsky, G. M., MacAdangdang, J. R., Ailawadi, G., and Holmes, J. W. (2011). Model-based design of mechanical therapies for myocardial infarction. *Journal of Cardiovascular Translational Research*, 4(1):82–91.

[Fomovsky et al., 2012b] Fomovsky, G. M., Rouillard, A. D., and Holmes, J. W. (2012b). Regional mechanics determine collagen fiber structure in healing myocardial infarcts. *Journal of Molecular and Cellular Cardiology*, 52(5):1083–1090.

[Fonck et al., 2007] Fonck, E., Prod'hom, G., Roy, S., Augsburger, L., Rüfenacht, D. A., and Stergiopulos, N. (2007). Effect of elastin degradation on carotid wall mechanics as assessed by a constituent-based biomechanical model. *American Journal of Physiology-Heart and Circulatory Physiology*, 292(6):H2754–H2763.

[Francia et al., 2012] Francia, S., Michelini, F., Saxena, A., Tang, D., De Hoon, M., Anelli, V., Mione, M., Carninci, P., and D'adda Di Fagagna, F. (2012). Site-specific DICER and DROSHA RNA products control the DNA-damage response. *Nature*.

[Fuchs et al., 2006] Fuchs, C., Bhattacharyya, D., and Fakirov, S. (2006). Microfibril reinforced polymer-polymer composites: Application of Tsai-Hill equation to PP/PET composites. *Composites Science and Technology*, 66(16):3161–3171.

[Gao et al., 2006] Gao, F., Watanabe, M., and Matsuzawa, T. (2006). Stress analysis in a layered aortic arch model under pulsatile blood flow. *Biomed Eng Online*, 5(25):1–11.

[Gao et al., 2012] Gao, X. M., White, D. A., Dart, A. M., and Du, X. J. (2012). Post-infarct cardiac rupture: Recent insights on pathogenesis and therapeutic interventions. *Pharmacology and Therapeutics*, 134(2):156–179.

[García-Herrera et al., 2012] García-Herrera, C. M., Atienza, J. M., Rojo, F. J., Claes, E., Guinea, G. V., Celentano, D. J., García-Montero, C., and Burgos, R. L. (2012). Mechanical behaviour and rupture of normal and pathological human ascending aortic wall. *Medical & biological engineering & computing*, 50(6):559–566.

[Gasser and Holzapfel, 2006] Gasser, T. C. and Holzapfel, G. A. (2006). Modeling the propagation of arterial dissection. *European Journal of Mechanics, A/Solids*.

[Gasser et al., 2006] Gasser, T. C., Ogden, R. W., and Holzapfel, G. A. (2006). Hyperelastic modelling of arterial layers with distributed collagen fibre orientations. *Journal of the Royal Society, Interface / the Royal Society*, 3(6):15–35.

[Geest et al., 2004] Geest, J. P. V., Sacks, M. S., and Vorp, D. A. (2004). Age Dependency of the Biaxial Biomechanical Behavior of Human Abdominal Aorta. *Journal of Biomechanical Engineering*, 126(6):815.

[Gennisson et al., 2010] Gennisson, J. L., Deffieux, T., Macé, E., Montaldo, G., Fink, M., and Tanter, M. (2010). Viscoelastic and anisotropic mechanical properties of in vivo muscle tissue assessed by supersonic shear imaging. *Ultrasound in Medicine and Biology*, 36(5):789–801.

[Gilling-Smith et al., 2005] Gilling-Smith, G. L., Vallabhaneni, S. R., How, T. V., Brennan, J. A., Harris, P. L., and Carter, S. D. (2005). Heterogeneity of Tensile Strength and Matrix Metalloproteinase Activity in the Wall of Abdominal Aortic Aneurysms. *Journal of Endovascular Therapy*, 11(4):494–502.

[Gleason et al., 2004] Gleason, R. L., Taber, L. A., and Humphrey, J. D. (2004). A 2-D Model of Flow-Induced Alterations in the Geometry, Structure, and Properties of Carotid Arteries. *Journal of Biomechanical Engineering*, 126(3):371–381.

[Gómez-Benito et al., 2005] Gómez-Benito, M. J., García-Aznar, J. M., and Doblaré, M. (2005). Finite element prediction of proximal femoral fracture patterns under different loads. *Journal of biomechanical engineering*, 127(1):9–14.

[Gray, 1918] Gray, H. (1918). *Anatomy of the Human Body*. Lea and Febiger, Philadelphia.

[Gregory et al., 2011] Gregory, D. E., Veldhuis, J. H., Horst, C., Wayne Brodland, G., and Callaghan, J. P. (2011). Novel lap test determines the mechanics of delamination between annular lamellae of the intervertebral disc. *Journal of Biomechanics*, 44(1):97–102.

[Groenink et al., 1999] Groenink, M., Langerak, S. E., Vanbavel, E., van der Wall, E. E., Mulder, B. J., van der Wal, A. C., and Spaan, J. A. (1999). The influence of aging and aortic stiffness on permanent dilation and breaking stress of the thoracic descending aorta. *Cardiovascular research*, 43(2):471–480.

[Grosse et al., 2014] Grosse, I., Huang, L., Davis, J., and Cullinane, D. (2014). A Multi-Level Hierarchical Finite Element Model for Capillary Failure in Soft Tissue. *Journal of biomechanical engineering*, 136(August):1–8.

[Gundiah et al., 2007] Gundiah, N., B Ratcliffe, M., and A Pruitt, L. (2007). Determination of strain energy function for arterial elastin: Experiments using histology and mechanical tests. *Journal of Biomechanics*, 40(3):586–594.

[Hadi and Barocas, 2013] Hadi, M. F. and Barocas, V. H. (2013). Microscale Fiber Network Alignment Affects Macroscale Failure Behavior in Simulated Collagen Tissue Analogs. *Journal of Biomechanical Engineering*.

[Hadi et al., 2012] Hadi, M. F., Sander, E. A., and Barocas, V. H. (2012). Multiscale Model Predicts Tissue-Level Failure From Collagen Fiber-Level Damage. *Journal of Biomechanical Engineering*.

[Haskett et al., 2012] Haskett, D., Speicher, E., Fouts, M., Larson, D., Azhar, M., Utzinger, U., and Vande Geest, J. (2012). The effects of angiotensin II on the coupled microstructural and biomechanical response of C57BL/6 mouse aorta. *Journal of Biomechanics*.

[Hatami-Marbini and Picu, 2009] Hatami-Marbini, H. and Picu, R. C. (2009). Heterogeneous long-range correlated deformation of semiflexible random fiber networks. *Physical Review E - Statistical, Nonlinear, and Soft Matter Physics*, 80(4):046703.

[He et al., 2013] He, Y., Huang, C., Lin, X., and Li, J. (2013). MicroRNA-29 family, a crucial therapeutic target for fibrosis diseases.

[Herrera et al., 2018a] Herrera, J., Beisang, D. J., Peterson, M., Forster, C., Gilbertsen, A., Benyumov, A., Smith, K., Korenczuk, C. E., Barocas, V. H., Guenther, K., Hite, R., Zhang, L., Henke, C. A., and Bitterman, P. B. (2018a). Dicer1 deficiency in the idiopathic pulmonary fibrosis fibroblastic focus promotes fibrosis by suppressing MicroRNA biogenesis. *American Journal of Respiratory and Critical Care Medicine*.

[Herrera et al., 2018b] Herrera, J., Henke, C. A., and Bitterman, P. B. (2018b). Extracellular matrix as a driver of progressive fibrosis.

[Herrera et al., 2015] Herrera, J., Peterson, M., Parker, M., Smith, K., Henke, C., and Bitterman, P. (2015). Hippo signaling pathway deregulation in IPF controls microRNA-29 expression [abstract]. *Am J Respir Crit Care Med*, 191:A5337.

[Hill, 1950] Hill, R. (1950). *The Mathematical Theory of Plasticity*.

[Holmes et al., 1997] Holmes, J. W., Nuñez, J. A., and Covell, J. W. (1997). Functional implications of myocardial scar structure. *The American journal of physiology*, 272(5):H2123–H2130.

[Holmes et al., 2013] Holmes, K. W., Maslen, C. L., Kindem, M., Kroner, B. L., Song, H. K., Ravekes, W., Dietz, H. C., Weinsaft, J. W., Roman, M. J., Devereux, R. B., Pyeritz, R. E., Bavaria, J., Milewski, K., Milewicz, D., Lemaire, S. A., Hendershot, T., Eagle, K. A., Tolunay, H. E., Desvigne-Nickens, P., and Silberbach, M. (2013). GenTAC registry report: Gender differences among individuals with genetically triggered thoracic aortic aneurysm and dissection. *American Journal of Medical Genetics, Part A*.

[Holzapfel et al., 2000] Holzapfel, G. A., Schulze-Bauer, C. A. J., and Stadler, M. (2000). Mechanics of angioplasty: Wall, balloon and stent. *Mechanics in Biology*, 30:141–156.

[Holzapfel et al., 2005] Holzapfel, G. A., Sommer, G., Gasser, C. T., and Regitnig, P. (2005). Determination of layer-specific mechanical properties of human coronary arteries with nonatherosclerotic intimal thickening and related constitutive modeling. *American Journal of Physiology Heart and Circulatory Physiology*, 289(5):2048–2058.

[Huang et al., 2012] Huang, X., Yang, N., Fiore, V. F., Barker, T. H., Sun, Y., Morris, S. W., Ding, Q., Thannickal, V. J., and Zhou, Y. (2012). Matrix stiffness-induced myofibroblast differentiation is mediated by intrinsic mechanotransduction. *American Journal of Respiratory Cell and Molecular Biology*.

[Humphrey and Yin, 1987] Humphrey, J. and Yin, F. (1987). On constitutive relations and finite deformations of passive cardiac tissue - I. A pseudostrain-energy function. *Journal of Biomechanical Engineering*, 109(4):298–304.

[Humphrey, 1995] Humphrey, J. D. (1995). Mechanics of the arterial wall: review and directions. *Critical reviews in biomedical engineering*.

[Humphrey, 2002] Humphrey, J. D. (2002). *Cardiovascular solid mechanics: cells, tissues, and organs*. Springer Science & Business Media, New York.

[Humphrey, 2013] Humphrey, J. D. (2013). *Cardiovascular solid mechanics: cells, tissues, and organs*. Springer Science & Business Media.

[Humphrey and Holzapfel, 2012] Humphrey, J. D. and Holzapfel, G. A. (2012). Mechanics, mechanobiology, and modeling of human abdominal aorta and aneurysms. *Journal of Biomechanics*, 45(5):805–814.

[Humphrey and Rajagopal, 2003] Humphrey, J. D. and Rajagopal, K. R. (2003). A constrained mixture model for arterial adaptations to a sustained step change in blood flow. *Biomechanics and modeling in mechanobiology*.

[Hurks et al., 2012] Hurks, R., Pasterkamp, G., Vink, A., Hoefer, I. E., Bots, M. L., Van De Pavoordt, H. D., De Vries, J. P. P., and Moll, F. L. (2012). Circumferential heterogeneity in the abdominal aortic aneurysm wall composition suggests lateral sides to be more rupture prone. *Journal of Vascular Surgery*, 55(1):203–209.

[Hwang et al., 2015] Hwang, E., Hughes, R. E., Palmer, M. L., and Carpenter, J. E. (2015). Effects of biceps tension on the torn superior glenoid labrum. *Journal of Orthopaedic Research*, 33(10):1545–1551.

[Iaizzo, 2009] Iaizzo, P. A. (2009). *Handbook of cardiac anatomy, physiology, and devices*. Springer Science & Business Media.

[Iliopoulos et al., 2009a] Iliopoulos, D. C., Deveja, R. P., Kritharis, E. P., Perrea, D., Sionis, G. D., Toutouzas, K., Stefanadis, C., and Sokolis, D. P. (2009a). Regional and directional variations in the mechanical properties of ascending thoracic aortic aneurysms. *Medical engineering & physics*, 31(1):1–9.

[Iliopoulos et al., 2009b] Iliopoulos, D. C., Kritharis, E. P., Giagini, A. T., Papadodima, S. A., and Sokolis, D. P. (2009b). Ascending thoracic aortic aneurysms are associated with compositional remodeling and vessel stiffening but not weakening in age-matched subjects. *Journal of Thoracic and Cardiovascular Surgery*.

[Isselbacher, 2005] Isselbacher, E. M. (2005). Thoracic and abdominal aortic aneurysms. *Circulation*, 111(6):816–828.

[Joyce et al., 2009] Joyce, E. M., Liao, J., Schoen, F. J., Mayer, J. E., and Sacks, M. S. (2009). Functional Collagen Fiber Architecture of the Pulmonary Heart Valve Cusp. *Annals of Thoracic Surgery*, 87(4):1240–1249.

[Jugdutt, 2003] Jugdutt, B. I. (2003). Ventricular remodeling after infarction and the extracellular collagen matrix: When is enough enough? *Circulation*, 108(11):1395–1403.

[Jugdutt et al., 1996] Jugdutt, B. I., Joljart, M. J., and Khan, M. I. (1996). Rate of Collagen Deposition during Healing and Ventricular Remodeling after Myocardial Infarction in Rat and Dog Models. *Circulation*, 94(1):94–101.

[Kaiser et al., 2008] Kaiser, T., Kellenberger, C. J., Albisetti, M., Bergsträsser, E., and Buechel, E. R. (2008). Normal values for aortic diameters in children and adolescents - Assessment in vivo by contrast-enhanced CMR-angiography. *Journal of Cardiovascular Magnetic Resonance*.

[Karimi et al., 2014] Karimi, A., Navidbakhsh, M., and Razaghi, R. (2014). Plaque and arterial vulnerability investigation in a three-layer atherosclerotic human coronary artery using computational fluid-structure interaction method. *Journal of Applied Physics*, 116(6).

[Khanafer et al., 2011] Khanafer, K., Duprey, A., Zainal, M., Schlicht, M., Williams, D., and Berguer, R. (2011). Determination of the elastic modulus of ascending thoracic aortic aneurysm at different ranges of pressure using uniaxial tensile testing. *Journal of Thoracic and Cardiovascular Surgery*, 142(3):682–686.

[Kim et al., 2012] Kim, J.-H., Avril, S., Duprey, A., and Favre, J.-P. (2012). Experimental characterization of rupture in human aortic aneurysms using a full-field measurement technique. *Biomechanics and Modeling in Mechanobiology*, 11(6):841–853.

[Kim et al., 2016] Kim, Y.-K., Kim, B., and Kim, V. N. (2016). Re-evaluation of the roles of DROSHA, Export in 5, and DICER in microRNA biogenesis. *Proceedings of the National Academy of Sciences of the United States of America*.

[Koch et al., 2014] Koch, R. G., Tsamis, A., D'Amore, A., Wagner, W. R., Watkins, S. C., Gleason, T. G., and Vorp, D. A. (2014). A custom image-based analysis tool for quantifying elastin and collagen micro-architecture in the wall of the human aorta from multi-photon microscopy. *Journal of Biomechanics*.

[Korenczuk et al., 2017] Korenczuk, C., Votava, L., Dhume, R., Kizilski, S., Brown, G., Narain, R., and Barocas, V. (2017). Isotropic failure criteria are not appropriate for anisotropic fibrous biological tissues. *Journal of Biomechanical Engineering*, 139(7).

[Korenczuk et al., 2019] Korenczuk, C. E., Dhume, R. Y., Liao, K. K., and Barocas, V. H. (2019). Ex Vivo Mechanical Tests and Multiscale Computational Modeling Highlight the Importance of Intramural Shear Stress in Ascending Thoracic Aortic Aneurysms. *Journal of Biomechanical Engineering*, Under Revi.

[Korenczuk, Christopher et al., 2019] Korenczuk, Christopher, E., Barocas, V. H., and Richardson, W. J. (2019). Effects of Collagen Heterogeneity on Myocardial Infarct Mechanics in a Multiscale Fiber Network Model. *Journal of Biomechanical Engineering*, (Under Review).

[Kozuń, 2016] Kozuń, M. (2016). Delamination properties of the human thoracic arterial wall with early stage of atherosclerosis lesions. *Journal of Theoretical and Applied Mechanics*.

[Krishnan et al., 2015] Krishnan, K., Ge, L., Haraldsson, H., Hope, M. D., Saloner, D. A., Guccione, J. M., and Tseng, E. E. (2015). Ascending thoracic aortic aneurysm wall stress analysis using patient-specific finite element modeling of in vivo magnetic resonance imaging. In *Interactive Cardiovascular and Thoracic Surgery*.

[Kumar et al., 2009] Kumar, M. S., Pester, R. E., Chen, C. Y., Lane, K., Chin, C., Lu, J., Kirsch, D. G., Golub, T. R., and Jacks, T. (2009). Dicer1 functions as a haploinsufficient tumor suppressor. *Genes and Development*.

[Kurzynska-Kokorniak et al., 2015] Kurzynska-Kokorniak, A., Koralewska, N., Pokornowska, M., Urbanowicz, A., Tworak, A., Mickiewicz, A., and Figlerowicz, M. (2015). The many faces of Dicer: The complexity of the mechanisms regulating Dicer gene expression and enzyme activities. *Nucleic Acids Research*.

[Lai et al., 2012] Lai, V. K., Lake, S. P., Frey, S. P., Tranquillo, R. T., and Barocas, V. H. (2012). Mechanical Behavior of Collagen-Fibrin Co-Gels Reflects Transition

From Series to Parallel Interactions With Increasing Collagen Content. *Journal of Biomechanical Engineering*, 134(1):011004.

[Lake et al., 2012] Lake, S. P., Hadi, M. F., Lai, V. K., and Barocas, V. H. (2012). Mechanics of a fiber network within a non-fibrillar matrix: Model and comparison with collagen-agarose co-gels. *Annals of Biomedical Engineering*.

[Lake et al., 2010] Lake, S. P., Miller, K. S., Elliott, D. M., and Soslowsky, L. J. (2010). Tensile properties and fiber alignment of human supraspinatus tendon in the transverse direction demonstrate inhomogeneity, nonlinearity, and regional isotropy. *Journal of Biomechanics*.

[Liang et al., 2017] Liang, L., Liu, M., Martin, C., Elefteriades, J. A., and Sun, W. (2017). A machine learning approach to investigate the relationship between shape features and numerically predicted risk of ascending aortic aneurysm. *Biomechanics and Modeling in Mechanobiology*, 16(5):1519–1533.

[Lin and Gregory, 2015] Lin, S. and Gregory, R. I. (2015). MicroRNA biogenesis pathways in cancer.

[Little and Khalsa, 2005] Little, J. S. and Khalsa, P. S. (2005). Material properties of the human lumbar facet joint capsule. *J Biomech Eng*, 127(1):15–24.

[Liu et al., 2015] Liu, F., Lagares, D., Choi, K. M., Stopfer, L., Marinković, A., Vrbanac, V., Probst, C. K., Hiemer, S. E., Sisson, T. H., Horowitz, J. C., Rosas, I. O., Fredenburgh, L. E., Feghali-Bostwick, C., Varelas, X., Tager, A. M., and Tschumperlin, D. J. (2015). Mechanosignaling through YAP and TAZ drives fibroblast activation and fibrosis. *American Journal of Physiology-Lung Cellular and Molecular Physiology*.

[Liu, 2007] Liu, J. Y. (2007). Analysis of off-axis tension test of wood specimens. *Wood and Fiber Science*, 34(2):205–211.

[Luo et al., 2016] Luo, Y., Duprey, A., Avril, S., and Lu, J. (2016). Characteristics of thoracic aortic aneurysm rupture in vitro. *Acta Biomaterialia*, 42:286–295.

[Lv et al., 2013] Lv, L.-L., Cao, Y.-H., Ni, H.-F., Xu, M., Liu, D., Liu, H., Chen, P.-S., and Liu, B.-C. (2013). MicroRNA-29c in urinary exosome/microvesicle as a biomarker of renal fibrosis. *American Journal of Physiology-Renal Physiology*.

[Maas et al., 2012] Maas, S. A., Ellis, B. J., Ateshian, G. A., and Weiss, J. A. (2012). FEBio: Finite Elements for Biomechanics. *Journal of Biomechanical Engineering*, 134(1):011005.

[MacLean et al., 1999] MacLean, N. F., Dudek, N. L., and Roach, M. R. (1999). The role of radial elastic properties in the development of aortic dissections. *Journal of Vascular Surgery*, 29(4):703–710.

[Macrae et al., 2016] Macrae, R. A., Miller, K., and Doyle, B. J. (2016). Methods in Mechanical Testing of Arterial Tissue: A Review.

[Maier et al., 2010] Maier, A., Gee, M. W., Reeps, C., Pongratz, J., Eckstein, H.-H., and Wall, W. A. (2010). A comparison of diameter, wall stress, and rupture potential index for abdominal aortic aneurysm rupture risk prediction. *Annals of Biomedical Engineering*, 38(10):3124–3134.

[Mao et al., 2008] Mao, S. S., Ahmadi, N., Shah, B., Beckmann, D., Chen, A., Ngo, L., Flores, F. R., lin Gao, Y., and Budoff, M. J. (2008). Normal Thoracic Aorta Diameter on Cardiac Computed Tomography in Healthy Asymptomatic Adults. Impact of Age and Gender. *Academic Radiology*.

[Marinković et al., 2013] Marinković, A., Liu, F., and Tschumperlin, D. J. (2013). Matrices of physiologic stiffness potently inactivate idiopathic pulmonary fibrosis fibroblasts. *American Journal of Respiratory Cell and Molecular Biology*.

[Martin et al., 2015] Martin, C., Sun, W., and Elefteriades, J. (2015). Patient-specific finite element analysis of ascending aorta aneurysms. *American Journal of Physiology-Heart and Circulatory Physiology*.

[Martufi et al., 2014] Martufi, G., Gasser, T. C., Appoo, J. J., and Di Martino, E. S. (2014). Mechano-biology in the thoracic aortic aneurysm: a review and case study.

[Matsumoto et al., 2009] Matsumoto, T., Fukui, T., Tanaka, T., Ikuta, N., Ohashi, T., Kumagai, K., Akimoto, H., Tabayashi, K., and Sato, M. (2009). Biaxial tensile properties of thoracic aortic aneurysm tissues. *Journal of Biomechanical Science and Engineering*, 4(4):518–529.

[Matura et al., 2007] Matura, L. A., Ho, V. B., Rosing, D. R., and Bondy, C. A. (2007). Aortic dilatation and dissection in Turner syndrome. *Circulation*.

[Matzenmiller et al., 1995] Matzenmiller, A., Lubliner, J., and Taylor, R. L. (1995). A constitutive model for anisotropic damage in fiber-composites. *Mechanics of Materials*, 20(2):125–152.

[Mazurek et al., 2017] Mazurek, R., Dave, J. M., Chandran, R. R., Misra, A., Sheikh, A. Q., and Greif, D. M. (2017). Vascular Cells in Blood Vessel Wall Development and Disease. In *Advances in Pharmacology*.

[McCloy et al., 2014] McCloy, R. A., Rogers, S., Caldon, C. E., Lorca, T., Castro, A., and Burgess, A. (2014). Partial inhibition of Cdk1 in G2 phase overrides the SAC and decouples mitotic events. *Cell Cycle*.

[McCormick et al., 2017] McCormick, R. J., Musch, T. I., Bergman, B. C., and Thomas, D. P. (2017). Regional differences in LV collagen accumulation and mature

cross-linking after myocardial infarction in rats. *American Journal of Physiology-Heart and Circulatory Physiology*, 266(1):H354–H359.

[Melo et al., 2014] Melo, E., Garreta, E., Luque, T., Cortiella, J., Nichols, J., Navajas, D., and Farré, R. (2014). Effects of the Decellularization Method on the Local Stiffness of Acellular Lungs. *Tissue Engineering Part C: Methods*.

[Mohan and Melvin, 1983] Mohan, D. and Melvin, J. W. (1983). Failure properties of passive human aortic tissue. II—Biaxial tension tests. *Journal of Biomechanics*, 16(1):31–44.

[Mori et al., 2014] Mori, M., Triboulet, R., Mohseni, M., Schlegelmilch, K., Shrestha, K., Camargo, F. D., and Gregory, R. I. (2014). Hippo signaling regulates microprocessor and links cell-density-dependent mirna biogenesis to cancer. *Cell*.

[Mott et al., 2010] Mott, J. L., Kurita, S., Cazanave, S. C., Bronk, S. F., Werneburg, N. W., and Fernandez-Zapico, M. E. (2010). Transcriptional suppression of mir-29b-1/mir-29a promoter by c-Myc, hedgehog, and NF-kappaB. *Journal of Cellular Biochemistry*.

[Nagel et al., 2014] Nagel, T. M., Hadi, M. F., Claeson, A. a., Nuckley, D. J., and Barocas, V. H. (2014). Combining displacement field and grip force information to determine mechanical properties of planar tissue with complicated geometry. *Journal of biomechanical engineering*, 136(11):1–5.

[Nakatani, 2011] Nakatani, S. (2011). Left Ventricular Rotation and Twist: Why Should We Learn? *Journal of Cardiovascular Ultrasound*.

[Narain et al., 2012] Narain, R., Samii, A., and O'Brien, J. F. (2012). Adaptive anisotropic remeshing for cloth simulation. *ACM Transactions on Graphics*, 31(6):1.

[Narain et al., 2014] Narain, R., Samii, A., Pfaff, T., and O'Brien, J. (2014). ARCSim: Adaptive Refining and Coarsening Simulator.

[Nataatmadja et al., 2003] Nataatmadja, M., West, M., West, J., Summers, K., Walker, P., Nagata, M., and Watanabe, T. (2003). Abnormal extracellular matrix protein transport associated with increased apoptosis of vascular smooth muscle cells in marfan syndrome and bicuspid aortic valve thoracic aortic aneurysm. *Circulation*, 108 Suppl:II329–34.

[Natali et al., 2005] Natali, A. N., Pavan, P. G., Carniel, E. L., Lucisano, M. E., and Taglialavoro, G. (2005). Anisotropic elasto-damage constitutive model for the biomechanical analysis of tendons. *Medical Engineering and Physics*, 27(3):209–214.

[Nathan et al., 2011] Nathan, D. P., Xu, C., Gorman, J. H., Fairman, R. M., Bavaria, J. E., Gorman, R. C., Chandran, K. B., and Jackson, B. M. (2011). Pathogenesis of acute aortic dissection: a finite element stress analysis. *The Annals of Thoracic Surgery*, 91(2):458–463.

[Nicholls et al., 1983] Nicholls, S. P., Gathereole, L. J., Keller, A., and Shah, J. S. (1983). Crimping in rat tail tendon collagen: morphology and transverse mechanical anisotropy. *International Journal of Biological Macromolecules*, 5(5):283–288.

[Nijs et al., 2014] Nijs, J., Gelsomino, S., Lucà, F., Parise, O., Maessen, J. G., and Meir, M. L. (2014). Unreliability of aortic size index to predict risk of aortic dissection in a patient with Turner syndrome. *World journal of cardiology*.

[Noble et al., 2016] Noble, C., Smulders, N., Lewis, R., Carré, M. J., Franklin, S. E., MacNeil, S., and Taylor, Z. A. (2016). Controlled peel testing of a model tissue for diseased aorta. *Journal of Biomechanics*, 49(15):3667–3675.

[Nuismer and Whitney, 1975] Nuismer, R. J. and Whitney, J. M. (1975). Uniaxial failure of composite laminates containing stress concentrations. *Fracture mechanics of composites*, ASTM Inter.

[Oak et al., 2011] Oak, S. R., Murray, L., Herath, A., Sleeman, M., Anderson, I., Joshi, A. D., Coelho, A. L., Flaherty, K. R., Toews, G. B., Knight, D., Martinez, F. J., and Hogaboam, C. M. (2011). A micro RNA processing defect in rapidly progressing idiopathic pulmonary fibrosis. *PLoS ONE*.

[Okamoto et al., 2002] Okamoto, R. J., Wagenseil, J. E., DeLong, W. R., Peterson, S. J., Kouchoukos, N. T., and Sundt III, T. M. (2002). Mechanical properties of dilated human ascending aorta. *Annals of Biomedical Engineering*, 30(5):624–635.

[Olsson et al., 2006] Olsson, C., Thelin, S., Stahle, E., Ekbom, A., and Granath, F. (2006). Thoracic aortic aneurysm and dissection: increasing prevalence and improved outcomes reported in a nationwide population-based study of more than 14,000 cases from 1987 to 2002. *Circulation*, 114(24):2611–2618.

[Omar et al., 2015] Omar, A. M. S., Vallabhajosyula, S., and Sengupta, P. P. (2015). Left Ventricular Twist and Torsion. *Circulation: Cardiovascular Imaging*.

[Pal et al., 2014] Pal, S., Tsamis, A., Pasta, S., D'Amore, A., Gleason, T. G., Vorp, D. A., and Maiti, S. (2014). A mechanistic model on the role of "radially-running" collagen fibers on dissection properties of human ascending thoracic aorta. *Journal of Biomechanics*, 47(5):981–988.

[Pandit et al., 2010] Pandit, K. V., Corcoran, D., Yousef, H., Yarlagadda, M., Tzouvelekis, A., Gibson, K. F., Konishi, K., Yousem, S. A., Singh, M., Handley, D., Richards, T., Selman, M., Watkins, S. C., Pardo, A., Ben-Yehudah, A., Bouros,

D., Eickelberg, O., Ray, P., Benos, P. V., and Kaminski, N. (2010). Inhibition and role of let-7d in idiopathic pulmonary fibrosis. *American Journal of Respiratory and Critical Care Medicine*.

[Pandit et al., 2011] Pandit, K. V., Milosevic, J., and Kaminski, N. (2011). MicroRNAs in idiopathic pulmonary fibrosis.

[Pape et al., 2007] Pape, L. A., Tsai, T. T., Isselbacher, E. M., Oh, J. K., O'gara, P. T., Evangelista, A., Fattori, R., Meinhardt, G., Trimarchi, S., Bossone, E., Suzuki, T., Cooper, J. V., Froehlich, J. B., Nienaber, C. A., Eagle, K. A., and Investigators, I. R. o. A. A. D. I. (2007). Aortic diameter >or = 5.5 cm is not a good predictor of type A aortic dissection: observations from the International Registry of Acute Aortic Dissection (IRAD). *Circulation*, 116(10):1120–1127.

[Parker et al., 2014] Parker, M. W., Rossi, D., Peterson, M., Smith, K., Sikstrom, K., White, E. S., Connett, J. E., Henke, C. A., Larsson, O., and Bitterman, P. B. (2014). Fibrotic extracellular matrix activates a profibrotic positive feedback loop. *Journal of Clinical Investigation*.

[Pasta et al., 2012] Pasta, S., Phillippi, J. A., Gleason, T. G., and Vorp, D. A. (2012). Effect of aneurysm on the mechanical dissection properties of the human ascending thoracic aorta. *The Journal of thoracic and cardiovascular surgery*, 143(2):460–467.

[Pfaff et al., 2014] Pfaff, T., Narain, R., De Joya, J. M., and O'Brien, J. F. (2014). Adaptive Tearing and Cracking of Thin Sheets. *ACM Transactions on Graphics*, 33(4):1–9.

[Phillippi et al., 2011a] Phillippi, J. A., Pasta, S., and Vorp, D. A. (2011a). Biomechanics and pathobiology of aortic aneurysms. In *Biomechanics and Mechanobiology of Aneurysms*, pages 67–118. Springer.

[Phillippi et al., 2011b] Phillippi, J. A., Pasta, S., and Vorp, D. A. (2011b). Biomechanics and pathobiology of aortic aneurysms. In *Biomechanics and Mechanobiology of Aneurysms*, pages 67–118. Springer.

[Pichamuthu et al., 2013] Pichamuthu, J. E., Phillippi, J. A., Cleary, D. A., Chew, D. W., Hempel, J., Vorp, D. A., and Gleason, T. G. (2013). Differential tensile strength and collagen composition in ascending aortic aneurysms by aortic valve phenotype. *Annals of Thoracic Surgery*.

[Picu, 2011] Picu, R. C. (2011). Mechanics of random fiber networks - A review. *Soft Matter*, 7(15):6768–6785.

[Pierce et al., 2007] Pierce, E. M., Carpenter, K., Jakubzick, C., Kunkel, S. L., Flaherty, K. R., Martinez, F. J., and Hogaboam, C. M. (2007). Therapeutic targeting of CC ligand 21 or CC chemokine receptor 7 abrogates pulmonary fibrosis induced

by the adoptive transfer of human pulmonary fibroblasts to immunodeficient mice. *American Journal of Pathology*.

[Pietruszczak et al., 1999] Pietruszczak, S., Inglis, D., and Pande, G. N. (1999). A fabric-dependent fracture criterion for bone. *Journal of Biomechanics*, 32(10):1071–1079.

[Poullis et al., 2008] Poullis, M. P., Warwick, R., Oo, A., and Poole, R. J. (2008). Ascending aortic curvature as an independent risk factor for type A dissection, and ascending aortic aneurysm formation: a mathematical model. *European journal of cardio-thoracic surgery : official journal of the European Association for Cardio-thoracic Surgery*, 33(6):995–1001.

[Quental et al., 2016] Quental, C., Folgado, J., Monteiro, J., and Sarmento, M. (2016). Full-thickness tears of the supraspinatus tendon: A three-dimensional finite element analysis. *Journal of Biomechanics*, 49(16):3962–3970.

[Quindlen et al., 2015] Quindlen, J. C., Lai, V. K., and Barocas, V. H. (2015). Multiscale Mechanical Model of the Pacinian Corpuscle Shows Depth and Anisotropy Contribute to the Receptor's Characteristic Response to Indentation. *PLoS Computational Biology*.

[Raghavan et al., 2000] Raghavan, M. L., Vorp, D. A., Federle, M. P., Makaroun, M. S., and Webster, M. W. (2000). Wall stress distribution on three-dimensionally reconstructed models of human abdominal aortic aneurysm. *Journal of vascular surgery*, 31(4):760–769.

[Raghupathy et al., 2011] Raghupathy, R., Witzenburg, C., Lake, S. P., Sander, E. a., and Barocas, V. H. (2011). Identification of Regional Mechanical Anisotropy in Soft Tissue Analogs. *Journal of Biomechanical Engineering*, 133(September 2011):091011.

[Rahaman et al., 2014] Rahaman, S. O., Grove, L. M., Paruchuri, S., Southern, B. D., Abraham, S., Niese, K. A., Scheraga, R. G., Ghosh, S., Thodeti, C. K., Zhang, D. X., Moran, M. M., Schilling, W. P., Tschumperlin, D. J., and Olman, M. A. (2014). TRPV4 mediates myofibroblast differentiation and pulmonary fibrosis in mice. *Journal of Clinical Investigation*.

[Rangarajan and Weinberg, 2003] Rangarajan, A. and Weinberg, R. A. (2003). Comparative biology of mouse versus human cells: Modelling human cancer in mice.

[Rattenbacher et al., 2010] Rattenbacher, B., Beisang, D., Wiesner, D. L., Jeschke, J. C., von Hohenberg, M., St. Louis-Vlasova, I. A., and Bohjanen, P. R. (2010). Analysis of CUGBP1 Targets Identifies GU-Repeat Sequences That Mediate Rapid mRNA Decay. *Molecular and Cellular Biology*.

[Richardson et al., 2015] Richardson, W. J., Clarke, S. A., Alexander Quinn, T., and Holmes, J. W. (2015). Physiological implications of myocardial scar structure. *Comprehensive Physiology*, 5(4):1877–1909.

[Richardson and Holmes, 2016] Richardson, W. J. and Holmes, J. W. (2016). Emergence of Collagen Orientation Heterogeneity in Healing Infarcts and an Agent-Based Model. *Biophysical Journal*, 110(10):2266–2277.

[Roccabianca et al., 2014] Roccabianca, S., Figueroa, C. A., Tellides, G., and Humphrey, J. D. (2014). Quantification of regional differences in aortic stiffness in the aging human. *Journal of the mechanical behavior of biomedical materials*, 29:618–634.

[Roderburg et al., 2011] Roderburg, C., Urban, G. W., Bettermann, K., Vucur, M., Zimmermann, H., Schmidt, S., Janssen, J., Koppe, C., Knolle, P., Castoldi, M., Tacke, F., Trautwein, C., and Luedde, T. (2011). Micro-RNA profiling reveals a role for miR-29 in human and murine liver fibrosis. *Hepatology*.

[Romo et al., 2014] Romo, A., Badel, P., Duprey, A., Favre, J. P., and Avril, S. (2014). In vitro analysis of localized aneurysm rupture. *Journal of Biomechanics*, 47(3).

[Rouillard and Holmes, 2012] Rouillard, A. D. and Holmes, J. W. (2012). Mechanical regulation of fibroblast migration and collagen remodelling in healing myocardial infarcts. *Journal of Physiology*, 590(18):4585–4602.

[Sacks, 2003] Sacks, M. S. (2003). Incorporation of experimentally-derived fiber orientation into a structural constitutive model for planar collagenous tissues. *Journal of biomechanical engineering*, 125(2):280–7.

[Saliba and Sia, 2015] Saliba, E. and Sia, Y. (2015). The ascending aortic aneurysm: When to intervene? *IJC Heart and Vasculature*, 6:91–100.

[Sander et al., 2009a] Sander, E., Stylianopoulos, T., Tranquillo, R., and Barocas, V. (2009a). Image-based biomechanics of collagen-based tissue equivalents. *IEEE Engineering in Medicine and Biology Magazine*.

[Sander et al., 2009b] Sander, E. A., Stylianopoulos, T., Tranquillo, R. T., and Barocas, V. H. (2009b). Image-based multiscale modeling predicts tissue-level and network-level fiber reorganization in stretched cell-compacted collagen gels. *Proceedings of the National Academy of Sciences*.

[Sanyal et al., 2014] Sanyal, A., Scheffelin, J., and Keaveny, T. M. (2014). The Quartic Piecewise-Linear Criterion for the Multiaxial Yield Behavior of Human Trabecular Bone. *Journal of Biomechanical Engineering*, 137(1):011009.

[Schafer et al., 2017] Schafer, M. J., White, T. A., Iijima, K., Haak, A. J., Ligresti, G., Atkinson, E. J., Oberg, A. L., Birch, J., Salmonowicz, H., Zhu, Y., Mazula, D. L., Brooks, R. W., Fuhrmann-Stroissnigg, H., Pirtskhalava, T., Prakash, Y. S., Tchkonia, T., Robbins, P. D., Aubry, M. C., Passos, J. F., Kirkland, J. L., Tschumperlin, D. J., Kita, H., and LeBrasseur, N. K. (2017). Cellular senescence mediates fibrotic pulmonary disease. *Nature Communications*.

[Schriefl et al., 2015] Schriefl, A. J., Schmidt, T., Balzani, D., Sommer, G., and Holzapfel, G. A. (2015). Selective enzymatic removal of elastin and collagen from human abdominal aortas: Uniaxial mechanical response and constitutive modeling. *Acta Biomaterialia*, 17:125–136.

[Schulze-Bauer et al., 2002] Schulze-Bauer, C. A. J., Regitnig, P., and Holzapfel, G. A. (2002). Mechanics of the human femoral adventitia including the high-pressure response. *American Journal of Physiology - Heart and Circulatory Physiology*, 282(6):H2427–H2440.

[Shah et al., 2014] Shah, S., Witzenburg, C., Hadi, M. F., Wagner, H., Goodrich, J., Alford, P., and Barocas, V. H. (2014). Prefailure and Failure Mechanics of the Porcine Ascending Thoracic Aorta: Experiments and a Multiscale Model. *Journal of biomechanical engineering*, 136(February):4–10.

[Snedeker and Gautieri, 2014] Snedeker, J. G. and Gautieri, A. (2014). The role of collagen crosslinks in ageing and diabetes - the good, the bad, and the ugly. *Muscles, ligaments and tendons journal*.

[Snowhill et al., 2004] Snowhill, P. B., Foran, D. J., and Silver, F. H. (2004). A mechanical model of porcine vascular tissues - Part I: Determination of macromolecular component arrangement and volume fractions. *Cardiovascular Engineering*.

[Sokolis et al., 2008] Sokolis, D. P., Boudoulas, H., and Karayannacos, P. E. (2008). Segmental differences of aortic function and composition: clinical implications. *Hellenic journal of cardiology : HJC = Hellenike kardiologike epitheorese*.

[Sokolis et al., 2012] Sokolis, D. P., Kritharis, E. P., and Iliopoulos, D. C. (2012). Effect of layer heterogeneity on the biomechanical properties of ascending thoracic aortic aneurysms. *Medical and Biological Engineering and Computing*, 50(12):1227–1237.

[Sommer et al., 2008] Sommer, G., Gasser, T. C., Regitnig, P., Auer, M., and Holzapfel, G. A. (2008). Dissection properties of the human aortic media: an experimental study. *Journal of biomechanical engineering*, 130(2):021007.

[Sommer et al., 2016] Sommer, G., Sherifova, S., Oberwalder, P. J., Dapunt, O. E., Ursomanno, P. A., DeAnda, A., Griffith, B. E., and Holzapfel, G. A. (2016). Me-

chanical strength of aneurysmatic and dissected human thoracic aortas at different shear loading modes. *Journal of Biomechanics*, 49:2374–2382.

[Stylianopoulos and Barocas, 2007a] Stylianopoulos, T. and Barocas, V. H. (2007a). Multiscale, Structure-Based Modeling for the Elastic Mechanical Behavior of Arterial Walls. *Journal of Biomechanical Engineering*, 129(4):611–618.

[Stylianopoulos and Barocas, 2007b] Stylianopoulos, T. and Barocas, V. H. (2007b). Volume-averaging theory for the study of the mechanics of collagen networks. *Computer Methods in Applied Mechanics and Engineering*.

[Sulli et al., 2012] Sulli, G., Di Micco, R., and Di Fagagna, F. D. A. (2012). Crosstalk between chromatin state and DNA damage response in cellular senescence and cancer.

[Svensson et al., 2003] Svensson, L. G., Kim, K. H., Lytle, B. W., and Cosgrove, D. M. (2003). Relationship of aortic cross-sectional area to height ratio and the risk of aortic dissection in patients with bicuspid aortic valves. *Journal of Thoracic and Cardiovascular Surgery*.

[Swahari et al., 2016] Swahari, V., Nakamura, A., Baran-Gale, J., Garcia, I., Crowther, A. J., Sons, R., Gershon, T. R., Hammond, S., Sethupathy, P., and Deshmukh, M. (2016). Essential Function of Dicer in Resolving DNA Damage in the Rapidly Dividing Cells of the Developing and Malignant Cerebellum. *Cell Reports*.

[Takaza et al., 2012] Takaza, M., Moerman, K. M., Gindre, J., Lyons, G., and Simms, C. K. (2012). The anisotropic mechanical behaviour of passive skeletal muscle tissue subjected to large tensile strain. *Journal of the Mechanical Behavior of Biomedical Materials*, 17:209–220.

[Teng et al., 2015] Teng, Z., Feng, J., Zhang, Y., Huang, Y., Sutcliffe, M. P. F., Brown, A. J., Jing, Z., Gillard, J. H., and Lu, Q. (2015). Layer- and Direction-Specific Material Properties, Extreme Extensibility and Ultimate Material Strength of Human Abdominal Aorta and Aneurysm: A Uniaxial Extension Study. *Annals of Biomedical Engineering*, 43(11):2745–2759.

[Thomopoulos et al., 2003] Thomopoulos, S., Williams, G. R., Gimbel, J. A., Favata, M., and Soslowsky, L. J. (2003). Variation of biomechanical, structural, and compositional properties along the tendon to bone insertion site. *Journal of Orthopaedic Research*, 21(3):413–419.

[Thubrikar et al., 1999] Thubrikar, M. J., Agali, P., and Robicsek, F. (1999). Wall stress as a possible mechanism for the development of transverse intimal tears in aortic dissections. *Journal of medical engineering & technology*, 23(4):127–134.

[Tiessen and Roach, 1993] Tiessen, I. M. and Roach, M. R. (1993). Factors in the initiation and propagation of aortic dissections in human autopsy aortas. *Journal of Biomechanical Engineering*, 115(1):123–125.

[Timmins et al., 2010] Timmins, L. H., Moore, J. E., Wu, Q., Yeh, A. T., and Greenwald, S. E. (2010). Structural inhomogeneity and fiber orientation in the inner arterial media. *American Journal of Physiology-Heart and Circulatory Physiology*.

[Todorovich-Hunter et al., 1988] Todorovich-Hunter, L., Johnson, D. J., Ranger, P., Keeley, F. W., and Rabinovitch, M. (1988). Altered elastin and collagen synthesis associated with progressive pulmonary hypertension induced by monocrotaline. A biochemical and ultrastructural study. *Lab Invest*.

[Tonar et al., 2015] Tonar, Z., Kubíková, T., Prior, C., Demjén, E., Liška, V., Králíčková, M., and Witter, K. (2015). Segmental and age differences in the elastin network, collagen, and smooth muscle phenotype in the tunica media of the porcine aorta. *Annals of Anatomy*.

[Tong et al., 2016] Tong, J., Cheng, Y., and Holzapfel, G. A. (2016). Mechanical assessment of arterial dissection in health and disease: Advancements and challenges. *Journal of Biomechanics*, 49(12):2366–2373.

[Tong et al., 2011] Tong, J., Sommer, G., Regitnig, P., and Holzapfel, G. A. (2011). Dissection properties and mechanical strength of tissue components in human carotid bifurcations. *Annals of Biomedical Engineering*.

[Trabelsi et al., 2015] Trabelsi, O., Davis, F. M., Rodriguez-Matas, J. F., Duprey, A., and Avril, S. (2015). Patient specific stress and rupture analysis of ascending thoracic aneurysms. *Journal of Biomechanics*, 48(10):1836–1843.

[Tsai, 1968] Tsai, S. W. (1968). *Fundamental aspects of fiber reinforced plastic composites*. Interscience, N.Y.

[Tsai and Wu, 1971] Tsai, S. W. and Wu, E. M. (1971). A General Theory of Strength for Anisotropic Materials. *Journal of Composite Materials*, 5(1):58–80.

[Tsamis et al., 2014] Tsamis, A., Pal, S., Phillippi, J. A., Gleason, T. G., Maiti, S., and Vorp, D. A. (2014). Effect of aneurysm on biomechanical properties of "radially-oriented" collagen fibers in human ascending thoracic aortic media. *Journal of Biomechanics*.

[Tsamis et al., 2013] Tsamis, A., Phillippi, J. A., Koch, R. G., Pasta, S., D'Amore, A., Watkins, S. C., Wagner, W. R., Gleason, T. G., and Vorp, D. A. (2013). Fiber micro-architecture in the longitudinal-radial and circumferential-radial planes of ascending thoracic aortic aneurysm media. *Journal of Biomechanics*.

[Tumaneng et al., 2012] Tumaneng, K., Schlegelmilch, K., Russell, R. C., Yimlamai, D., Basnet, H., Mahadevan, N., Fitamant, J., Bardeesy, N., Camargo, F. D., and Guan, K. L. (2012). YAP mediates crosstalk between the Hippo and PI(3)K-TOR pathways by suppressing PTEN via miR-29. *Nature Cell Biology*.

[van Baardwijk and Roach, 1987] van Baardwijk, C. and Roach, M. R. (1987). Factors in the propagation of aortic dissections in canine thoracic aortas. *Journal of Biomechanics*.

[van Rooij et al., 2008] van Rooij, E., Sutherland, L. B., Thatcher, J. E., DiMaio, J. M., Naseem, R. H., Marshall, W. S., Hill, J. A., and Olson, E. N. (2008). Dysregulation of microRNAs after myocardial infarction reveals a role of miR-29 in cardiac fibrosis. *Proceedings of the National Academy of Sciences*.

[Vande Geest et al., 2006] Vande Geest, J. P., Sacks, M. S., and Vorp, D. A. (2006). The effects of aneurysm on the biaxial mechanical behavior of human abdominal aorta. *Journal of Biomechanics*, 39(7):1324–1334.

[Volokh, 2008] Volokh, K. Y. (2008). Prediction of arterial failure based on a microstructural bi-layer fiber-matrix model with softening. *Journal of Biomechanics*.

[Volokh, 2011] Volokh, K. Y. (2011). Modeling failure of soft anisotropic materials with application to arteries. *Journal of the mechanical behavior of biomedical materials*, 4(8):1582–1594.

[Vorp et al., 1996] Vorp, D. A., Raghavan, M. L., Muluk, S. C., Makaroun, M. S., Steed, D. L., Shapiro, R., and Webster, M. W. (1996). Wall strength and stiffness of aneurysmal and nonaneurysmal abdominal aorta. *Annals of the New York Academy of Sciences*, 800(1):274–276.

[Vorp et al., 2003] Vorp, D. A., Schiro, B. J., Ehrlich, M. P., Juvonen, T. S., Ergin, M. A., and Griffith, B. P. (2003). Effect of aneurysm on the tensile strength and biomechanical behavior of the ascending thoracic aorta. *The Annals of Thoracic Surgery*, 75(4):1210–1214.

[Wagenseil and Mecham, 2009] Wagenseil, J. and Mecham, R. (2009). Vascular Extracellular Matrix and Arterial Mechanics. *American Physiological Society*, 89(3):957–989.

[Wang et al., 2001] Wang, D. H. J., Makaroun, M. S., and Vorp, D. A. (2001). Noninvasive estimation of wall strength distribution in human abdominal aortic aneurysm. *ASME-PUBLICATIONS-BED*, 51:35–36.

[Wang et al., 2015] Wang, L., Roper, S. M., Luo, X. Y., and Hill, N. A. (2015). Modelling of tear propagation and arrest in fibre-reinforced soft tissue subject to internal pressure. *Journal of Engineering Mathematics*.

[Watton et al., 2004] Watton, P. N., Hill, N. A., and Heil, M. (2004). A mathematical model for the growth of the abdominal aortic aneurysm. *Biomechanics and modeling in mechanobiology*, 3(2):98–113.

[Weaver, 2017] Weaver, V. M. (2017). Cell and tissue mechanics: the new cell biology frontier. *Molecular Biology of the Cell*.

[Weisbecker et al., 2013] Weisbecker, H., Viertler, C., Pierce, D. M., and Holzapfel, G. A. (2013). The role of elastin and collagen in the softening behavior of the human thoracic aortic media. *Journal of Biomechanics*, 46(11).

[White et al., 2017] White, E. J., Matsangos, A. E., and Wilson, G. M. (2017). AUF1 regulation of coding and noncoding RNA.

[Wisneski et al., 2014] Wisneski, A. D., Mookhoek, A., Chitsaz, S., Hope, M. D., Guccione, J. M., Ge, L., and Tseng, E. E. (2014). Patient-specific finite element analysis of ascending thoracic aortic aneurysm. *The Journal of heart valve disease*.

[Witzenburg et al., 2012] Witzenburg, C., Raghupathy, R., Kren, S. M., Taylor, D. A., and Barocas, V. H. (2012). Mechanical changes in the rat right ventricle with decellularization. *Journal of Biomechanics*.

[Witzenburg et al., 2017] Witzenburg, C. M., Dhume, R. Y., Shah, S. B., Korenczuk, C. E., Wagner, H. P., Alford, P. W., and Barocas, V. H. (2017). Failure of the Porcine Ascending Aorta: Multidirectional Experiments and a Unifying Model. *Journal of Biomechanical Engineering*, 139(3):031005.

[Woo and Whitcomb, 1996] Woo, K. and Whitcomb, J. (1996). Three-Dimensional Failure Analysis of Plain Weave Textile Composites Using a Global/Local Finite Element Method. *Journal of Composite Materials*, 30(9):984–1003.

[Woo et al., 1983] Woo, S. L., Gomez, M. a., Seguchi, Y., Endo, C. M., and Akeson, W. H. (1983). Measurement of mechanical properties of ligament substance from a bone-ligament-bone preparation. *Journal of orthopaedic research : official publication of the Orthopaedic Research Society*, 1(1):22–29.

[Woo et al., 1991] Woo, S. L., Hollis, J. M., Adams, D. J., Lyon, R. M., and Takai, S. (1991). Tensile properties of the human femur-anterior cruciate ligament-tibia complex. The effects of specimen age and orientation. *The American journal of sports medicine*, 19(3):217–225.

[Wood et al., 2011] Wood, S. A., Strait, D. S., Dumont, E. R., Ross, C. F., and Grosse, I. R. (2011). The effects of modeling simplifications on craniofacial finite element models: The alveoli (tooth sockets) and periodontal ligaments. *Journal of Biomechanics*, 44(10):1831–1838.

[Xia et al., 2014] Xia, H., Bodempudi, V., Benyumov, A., Hergert, P., Tank, D., Herrera, J., Braziunas, J., Larsson, O., Parker, M., Rossi, D., Smith, K., Peterson, M., Limper, A., Jessurun, J., Connett, J., Ingbar, D., Phan, S., Bitterman, P. B., and Henke, C. A. (2014). Identification of a cell-of-origin for fibroblasts comprising the fibrotic reticulum in idiopathic pulmonary fibrosis. *American Journal of Pathology*.

[Xia et al., 2017] Xia, H., Gilbertsen, A., Herrera, J., Racila, E., Smith, K., Peterson, M., Griffin, T., Benyumov, A., Yang, L., Bitterman, P. B., and Henke, C. A. (2017). Calcium-binding protein S100A4 confers mesenchymal progenitor cell fibrogenicity in idiopathic pulmonary fibrosis. *Journal of Clinical Investigation*.

[Zarei et al., 2017a] Zarei, V., Liu, C. J., Claeson, A. A., Akkin, T., and Barocas, V. H. (2017a). Image-based multiscale mechanical modeling shows the importance of structural heterogeneity in the human lumbar facet capsular ligament. *Biomechanics and Modeling in Mechanobiology*.

[Zarei et al., 2017b] Zarei, V., Zhang, S., Winkelstein, B. A., and Barocas, V. H. (2017b). Tissue loading and microstructure regulate the deformation of embedded nerve fibres: Predictions from single-scale and multiscale simulations. *Journal of the Royal Society Interface*.

[Zhao et al., 2010] Zhao, B., Li, L., Tumaneng, K., Wang, C. Y., and Guan, K. L. (2010). A coordinated phosphorylation by Lats and CK1 regulates YAP stability through SCFβ-TRCP. *Genes and Development*.

[Zimmerman et al., 2001] Zimmerman, S. D., Thomas, D. P., Velleman, S. G., Li, X., Hansen, T. R., and McCormick, R. J. (2001). Time course of collagen and decorin changes in rat cardiac and skeletal muscle post-MI. *Am J Physiol Heart Circ Physiol*, 281(4):H1816–H1822.

[Zulliger et al., 2004] Zulliger, M. A., Fridez, P., Hayashi, K., and Stergiopulos, N. (2004). A strain energy function for arteries accounting for wall composition and structure. *Journal of Biomechanics*.

[Zwahlen et al., 2015] Zwahlen, A., Christen, D., Ruffoni, D., Schneider, P., Schmölz, W., and Müller, R. (2015). Inverse Finite Element Modeling for Characterization of Local Elastic Properties in Image-Guided Failure Assessment of Human Trabecular Bone. *Journal of biomechanical engineering*, 137(1):011012.

Appendix A

Failure of the Porcine Ascending Aorta: Multidirectional Experiments and a Unifying Microstructural Model

The content of this chapter was published as a research article in the *Journal of Biomechanical Engineering* by Witzenburg, Dhume, Shah, Korenczuk, Wagner, Alford, and Barocas [Witzenburg et al., 2017]. My contribution was aiding in experimental testing and data processing, along with analyzing and processing simulation results.

A.1 Background

The ascending thoracic aorta (Figure A.1(a)) supports tremendous hemodynamic loading, expanding (∼11% area change [Mao et al., 2008]) during systole and elas-

tically recoiling during diastole to augment the forward flow of blood and coronary perfusion [Humphrey, 2002]. Although it is only about 5 cm long [Gray, 1918, Dotter et al., 1950] (15% of the total length of the thoracic aorta), the ascending aorta is involved in 60% of all thoracic aortic aneurysms [Isselbacher, 2005]. Aneurysm dissection and rupture (resulting in imminent death) are the primary risks associated with ascending thoracic aortic aneurysm (ATAA), occurring when the remodeled tissue is no longer able to withstand the stresses generated by the arterial pressure. Unfortunately, surgical repair of an ATAA also involves considerable risk. Statistically, death from rupture becomes more likely than death during surgery at an ATAA diameter over 5.5 cm, setting the current interventional guidelines [Isselbacher, 2005, Davies et al., 2002, Davies et al., 2006, Elefteriades, 2010]. Aortic dissection and rupture remain difficult to predict, however, occurring in a significant number of patients with smaller aneurysms [Isselbacher, 2005, Davies et al., 2006, Pape et al., 2007] while many patients with ATAA diameters above 5.5 cm do not experience aortic dissection or rupture. New surgical guidelines have been proposed based on aneurysm growth rate [Davies et al., 2002, Elefteriades, 2010] and normalized aneurysm size [Davies et al., 2006, Svensson et al., 2003, Kaiser et al., 2008], but growth rates can be difficult to determine and require sequential imaging studies [Berger and Elefteriades, 2012], and normalizing aneurysm size is still a controversial strategy [Matura et al., 2007, Nijs et al., 2014, Holmes et al., 2013, Etz et al., 2012]. A better understanding of aortic wall mechanics, especially failure mechanics, is imperative.

Because of the complex geometry of the aortic arch (aggravated in the case of aneurysm) and the complex mechanical environment surrounding an intimal tear, the stress field in a dissecting aorta involves many different shear and tensile stresses. It is therefore necessary to study tissue failure under as many loading conditions as possible. Tissue from the ascending aorta has been tested in a variety of configurations

(reviewed by Avanzini et al. [Avanzini et al., 2014]), with uniaxial and equibiaxial stretch tensile tests being the most common. In-plane uniaxial [Vorp et al., 2003, Iliopoulos et al., 2009b, Pichamuthu et al., 2013] and biaxial tension tests [Shah et al., 2014, Okamoto et al., 2002, Azadani et al., 2013, Babu et al., 2015] provide information on tensile failure in the plane of the medial lamella ($\sigma_{\theta\theta}$, σ_{zz}), and the biaxial tests can provide some additional information on in-plane shear ($\sigma_{\theta z}$). Although the dominant stresses in these tests may be the primary stresses during vessel rupture, they are not those driving dissection. Stresses near an advancing dissection include a combination of radial tension (σ_{rr}) and transmural shear ($\sigma_{r\theta}$, σ_{rz}) [van Baardwijk and Roach, 1987], which are more difficult to test experimentally. Peel tests on pieces of artery [Sommer et al., 2008, Tong et al., 2011, Tsamis et al., 2014, Kozuń, 2016] or aneurysm [Pasta et al., 2012] provide insight into the failure behavior of the tissue in radial tension (σ_{rr}), loading perpendicular to the medial lamella, as does direct extension to failure in the radial direction [Sommer et al., 2008]. To examine transmural shear stresses ($\sigma_{r\theta}$, σ_{rz}), the shear lap test, well established in the field of adhesives [ASTM, 2001] and used by Gregory et al. [Gregory et al., 2011] to study interlamellar mechanics of the annulus fibrosus of the intervertebral disk, is an attractive option. In the present work, our first objective was to obtain a more complete picture of artery failure mechanics by using a combination of in- plane uniaxial and equibiaxial, shear lap, and peel tests to cover all three-dimensional loading modalities (Figs. A.1(b) and A.1(c)). To the best of our knowledge, this study was the first to generate data on the interlamellar shear strength of aortic tissue in this manner.

The need for better experiments is complemented by the need for better computational models of tissue failure. Many theoretical models have been utilized to describe ATAAs, but only a few have addressed failure and dissection [Volokh, 2008, Gasser and Holzapfel, 2006, Ferrara and Pandolfi, 2008, Wang et al., 2015]. Volokh [Volokh,

2008] used a softening hyperelastic material model and a two-fiber family strain energy density function within the context of a bilayer arterial model to examine the failure of arteries during inflation. This model yields valuable results concerning rupture but does not address dissection. An impressive model of dissection mechanics was put forward by Gasser and Holzapfel [Gasser and Holzapfel, 2006], employing a finite-element (FE) model with independent continuous and cohesive zones. The Gasser-Holzapfel model combines a nonlinear continuum mechanical framework with a cohesive zone model to investigate the propagation of arterial dissection, and it agreed well with experimental peel test results [Sommer et al., 2008]. However, the reliance on the *a priori* definition of the location and size of the cohesive zone, the zone in which microcrack initialization and coalescence are confined, limits the model. In addition, the model does not address microscale failure; that is, it does not capture the complex fiber–fiber and fiber–matrix interactions during dissection and does not account for the lamellar structure of the vessel wall. Similar results to those of Gasser and Holzapfel were found by Ferrara and Pandolfi [Ferrara and Pandolfi, 2008], who investigated the impacts of mesh refinement and cohesive strength on dissection. Alternatively, Wang et al. [Wang et al., 2015] used an energy approach, rather than a cohesive zone, to simulate dissection in two dimensions. In addition to tear propagation, Wang's model was capable of simulating tear arrest, reflecting the clinical observation that dissection often occurs in stages. The energy approach presented, however, requires *a priori* definition of crack direction, does not allow changes in propagation direction, and does not address microscale failure. Advantages of a multiscale model include its ability to link observed macroscale properties to changes in microscale structure and its allowance of spontaneous failure initiation location and growth.

Recently, we utilized a multiscale model to describe *ex vivo* testing results of

porcine ascending aorta in both uniaxial and equibiaxial extension [Shah et al., 2014]. The tissue microstructure was idealized as a single network of uniform-diameter fibers functioning in parallel with a neo-Hookean component that accounted for all nonfibrillar contributions. Although that model worked well for in-plane behavior, the lack of an accurate representation of the lamellar structure rendered it inaccurate for out-of-plane data and failed to take advantage of the full capabilities of the multiscale computational framework. It was clearly necessary to modify the simplified microstructural organization of our earlier work and consider the layered structure of the medial lamellae, including in particular the interlamellar connections, in order to capture the tissue's biomechanics in all loading conditions more relevant to dissection. Therefore, the second and third objectives of this study were to generate a tissue-specific microstructure based on the layered structure of the aorta and to utilize the new microstructure to build a multiscale model capable of replicating experimental results from all the mechanical tests (uniaxial extension to failure, equibiaxial extension, peel to failure, and shear lap failure) performed.

A.2 Methods

A.2.1 Experiments

Ascending aortic tissue was obtained from healthy adolescent male swine ($\sim$6 months; 87.4 $\pm$ 9.6 kg, mean $\pm$ SD) following an unrelated *in vivo* study on right atrial radio frequency ablation and stored in 1% phosphate-buffered saline (PBS) solution at 4° C. Tissue specimens were tested within 48 h of harvest while immersed in 1% PBS at room temperature. Per our previous study [Shah et al., 2014], a ring of tissue was dissected from the ascending aorta and cut open along its superior edge (Figs. A.2(a) and A.2(b)). The tissue specimen was cut into small samples, both axially

and circumferentially aligned, for mechanical testing. Several samples were obtained from each aorta (a typical dissection and testing plan is shown in Figure A.2(c)).

Four different loading modalities were utilized to characterize the tissue mechanically: uniaxial, equibiaxial, peel, and lap tests (Figure A.3). Planar uniaxial and equibiaxial tests, which characterized the tissue in tension along the medial lamella ($\sigma_{\theta\theta}$, σ_{zz}, $\sigma_{\theta z}$), were performed and described previously [Shah et al., 2014]. The intima, adipose tissue, and adventitia were removed from samples tested uniaxially and biaxially. While these testing modalities are relevant to the rupture of the vessel, dissection of the ascending aorta occurs when the medial lamellae separates into two layers and thus is highly dependent on the behavior of the tissue across lamellae. Thus, two additional mechanical testing modes were utilized. Peel tests (cf. [Sommer et al., 2008, Tong et al., 2011, Pasta et al., 2012]) were performed to quantify the tissues' tensile response perpendicular to the medial lamellae (σ_{rr}) and subsequent dissection of the media into two layers. Shear lap tests were performed to quantify the tissues' response when exposed to shear along the medial lamella (σ_{rz}, $\sigma_{r\theta}$). The two protocols are described in detail below.

Peel Tests. The peel test (Figure A.3(c)) measures the adhesive force between two layers as they are pulled apart. For each rectangular sample designated for peel testing, a $\sim$4 mm incision was made parallel to the plane of the aortic wall to initiate delamination. The incision was made such that the delamination plane was approximately centered within the medial layer, thus separating the sample into two flaps of approximately equal thickness. Images of the sample were taken to determine its initial unloaded dimensions. There was a moderate variation in the exact location of the incision with respect to the center of the media due to sample size and cutting technique. If the delamination plane was outside the middle third of the sample thickness, the sample was discarded. Lines were drawn on the side of the sample with

Verhoeff's stain in order to track the progress of failure.

The two flaps of the delaminated section of the tissue sample were then mounted in a custom gripping system with sandpaper on either side to prevent slipping and secured to a uniaxial tester. Samples were cut and mounted on a uniaxial testing machine (MTS, Eden Prairie, MN) such that the vertical direction, as shown in Figure A.3(c), was either axial or circumferential with respect to the vessel. The two flaps were peeled apart, causing the tissue sample to delaminate, at a constant displacement rate of 3 mm/min, and force was measured with a 5 N load cell. Preliminary tests showed no significant dependence on grip speed in the range of 1-10 mm/min, so a single velocity was used for all the subsequent experiments. Images of the side of the sample were recorded every 5 s throughout testing to capture the progression of failure. Peel tension was computed as force divided by undeformed sample width for both axially and circumferentially oriented samples.

Shear Lap Failure. The shear lap test (Figure A.3(d)) produces large shear stresses in the overlap region. Rectangular samples designated for shear lap testing were specially shaped to test their shear strength. A $\sim$3.5 mm incision was made on each end of the sample centered within the medial layer and separating each end of the sample into two flaps of approximately equal thickness. The flap containing the intimal surface was removed from one end, and the flap containing the adventitial surface was removed from the other, resulting in the shear lap sample shape with an overlap length (black-dotted line in Figure A.3(d)) of 3.0 mm. Images of the sample were taken to determine its initial unloaded dimensions. Again, there was moderate variation in incision location with respect to the center of the media due to sample size and cutting technique; therefore, if either incision surface was measured to be outside, the middle third of the sample thickness the sample was discarded. Verhoeff's stain was used to texture the side of the sample for optical displacement tracking.

The specially cut sample was then mounted in a custom gripping system with sandpaper on either side to prevent slipping and secured to a uniaxial tester (MTS, Eden Prairie, MN). The height of the grips was adjusted such that the overlap surface was along the horizontal, and an image of the sample was taken to determine its initial unloaded dimensions. Each sample was extended to failure at a constant displacement rate of 3 mm/min, and force was measured with a 5 N load cell. During testing, digital video of the side of the sample was obtained at 24 fps, 1080p HD resolution, and spatial resolution of $\sim$103 pixels/mm. Image analysis and dis- placement tracking were performed per our previous studies [Raghupathy et al., 2011, Witzenburg et al., 2012].

Shear stress was computed as force divided by the undeformed overlap area (sample width multiplied by overlap length). Unlike the peel test, which has been used previously to investigate aortic tissue [Sommer et al., 2008, Pasta et al., 2012], to the best of our knowledge the shear lap test has never been used to investigate aorta or other cardiovascular soft tissues (though Gregory et al. used a similar test to investigate the shear properties of the annulus fibrosus [Gregory et al., 2011]). Therefore, displacement tracking was performed to verify that the shear lap test, as applied to the ascending thoracic aorta, produced large shear strains in the overlap region.

A.2.2 Statistical analysis and presentation

Unless otherwise stated, the p-values are based on unpaired two-tailed t-tests, and p-values less than 0.05 were deemed significant. Values are reported as mean $\pm$ 95% confidence interval (CI).

A.2.3 Model

The multiscale model employed was an extension of the previously presented model of collagen gel mechanics [Chandran et al., 2008, Hadi et al., 2012] applied recently to porcine aortic failure during in-plane tests [Shah et al., 2014]. It consisted of three scales: the FE domain at the millimeter (mm) scale, representative volume elements (RVEs) at the micrometer (μm) scale, and fibers with radii at the 100 nanometer (nm) scale. Each finite element contained eight Gauss points, and each Gauss point was associated with an RVE. Each RVE was comprised of a discrete fiber network in parallel with a nearly incompressible neo-Hookean component (to represent the nonfibrous material). The governing equations are given in Table A.1. The major advance to the model was the implementation of a new tissue-specific network, specifically designed to capture the different components of the aortic wall.

The aorta is organized into thick concentric medial fibrocellular layers which can be represented by discrete structural and functional units. The lamellar unit, detailed by Clark and Glagov [Clark and Glagov, 1985], consists of an elastic lamina sandwiched between two sheets of smooth muscle cells. The small-scale network in our computational model was designed to simulate the architecture of this discrete lamellar unit (Figure A.4), as visualized by histological analysis. Portions of unloaded porcine ascending aorta were cut such that the transmural structure was aligned in the circumferential, i.e., horizontal, direction and fixed in 10% buffered neutral formalin solution overnight, embedded in paraffin, and prepared for histological investigation per standard techniques. Sections were stained consecutively with hematoxylin and eosin (HE) stain (Figure A.4(a)) to visualize smooth-muscle cell nuclei, Masson's trichrome stain (Figure A.4(b)) to visualize collagen, and Verhoeff's Van Gieson stain (Figure A.4(c)) to visualize elastin. The final network structure is shown in Figure A.4(d), and the network parameters are given in Table A.2. The

Equation	Description	Scale
$\sigma_{ij,j} = \frac{1}{V} \oint \partial V \left(\sigma_{ij}^{L} - \sigma_{ij}\right) u_{k,j} n_k \mathrm{d}S$ σ:macroscale averaged Cauchy stress V: RVE volume σ^L: microscale stress u: RVE boundary displacement n: normal vector to RVE boundary	Macroscale volume-averaged stress balance	Tissue
$\sigma_{ij} = \frac{1}{V} \int \sigma_{ij}^{L} \mathrm{d}V = \frac{1}{V} \sum_b f_i x_j$ b: RVE boundary cross links x: boundary coordinate f: force acting on boundary	Volume-averaged RVE stress	Network
$F_f = \frac{EA}{\beta} \left(e^{\beta \frac{\lambda^2 - 1}{2}} - 1\right)$ F_f: fiber force E: fiber stiffness A: fiber cross-sectional area β: fiber non-linearity λ: fiber stretch	Fiber constitutive equation	Fiber
$\sigma_{ij}^{M} = \frac{G}{J} \left(B_{ij} - \delta_{ij}\right) + \frac{2G\nu}{J(1-2\nu)} \delta_{ij} ln(J)$ σ^M: matrix Cauchy stress G: matrix shear modulus J: deformation tensor determinant B: left Cauchy-Green tensor ν: Poisson's ratio	neo-Hookean matrix constitutive equation	Tissue

Table A.1: Governing equations applied within the multiscale model, as well as the length scale at which each equation was applied.

volume fraction for the tissue-specific network was set to 5% per the porcine aorta volume fraction measurements of Snowhill et al. [Snowhill et al., 2004]. The elastic lamina was represented by a 2-D sheet of elastin and collagen fibers. Collagen fibers within the elastin–collagen sheet were generated such that they exhibited strong circumferential orientation, based on the known tissue structure [Clark and Glagov, 1985, Tonar et al., 2015, Snowhill et al., 2004, Timmins et al., 2010, Sokolis et al., 2008]. Histological and compositional studies show more elastin than collagen within each lamina of the ascending aortic wall. Based on the histological observations of Sokolis et al. [Sokolis et al., 2008], the overall ratio of elastin-to-collagen within the 2-D sheet was set to 1.6. Elastin fibers were generated such that orientation was approximately isotropic within the plane. The radial properties of the aorta are less well established [Dobrin, 1978, MacLean et al., 1999] but are extremely important because failure of the interlamellar connections dictates delamination and thus aortic dissection. Within the model network, the interlamellar connections were designed to encompass the combined effect of all structural components (smooth muscle cells, fine collagen fibers, and fine elastin fibers) contributing to radial strength.

Smooth-muscle cells within the media exhibit preferential circumferential alignment [Clark and Glagov, 1985, Timmins et al., 2010, Dingemans et al., 2000], so interlamellar connections were aligned with circumferential preference. Since the interlamellar connections encompass the combined effect of all the structural components contributing to radial strength (smooth muscle cells, fine collagen fibers, and fine elastin fibers), it is somewhat unclear how to define the proportion of interlamellar connections-to-elastic lamina fibers. Snowhill et al. [Snowhill et al., 2004] determined the volume ratio of collagen to smooth muscle to be 1:1 in porcine vessels. While clearly the interlamellar connections encompass some collagen, and the elastic lamina contains large amounts of elastin, we utilized this 1:1 ratio.

Parameter	Value	References
Collagen fibers		
Network orientation, $[\Omega_{zz}, \Omega_{\theta\theta}, \Omega_{rr}]$	[0.1 0.9 0] ± [0.05 0.05 0] Mean ± 95% CI	[Clark and Glagov, 1985], [Tonar et al., 2015], [Snowhill et al., 2004], [Timmins et al., 2010]
Fiber stiffness ($E \times A$)	340 nN	[Lai et al., 2012]
Fiber non-linearity (β)	2.5	[Lai et al., 2012]
Failure stretch ($\lambda_{critical}$)	1.42	[Lai et al., 2012]
Elastin fibers		
Network orientation, $[\Omega_{zz}, \Omega_{\theta\theta}, \Omega_{rr}]$	[0.5 0.5 0] ± [0.05 0.05 0] Mean ± 95% CI	
Fiber stiffness ($E \times A$)	79 nN	[Shah et al., 2014]
Fiber non-linearity (β)	2.17	[Shah et al., 2014]
Failure stretch ($\lambda_{critical}$)	2.35	[Shah et al., 2014]
Interlamellar connections		
Network orientation, $[\Omega_{zz}, \Omega_{\theta\theta}, \Omega_{rr}]$	[0.2 0.6 0.2] ± [0.05 0.05 0.05] Mean ± 95% CI	[Clark and Glagov, 1985], [Tonar et al., 2015], [Snowhill et al., 2004], [Timmins et al., 2010]
Fiber stiffness ($E \times A$)	36.4 nN	[MacLean et al., 1999]
Fiber non-linearity (β)	0.01	[MacLean et al., 1999]
Failure stretch ($\lambda_{critical}$)	2	[MacLean et al., 1999]
neo-Hookean matrix		
Poisson's ratio (ν)	0.49	
Shear modulus (G)	1.7 kPa	[Shah et al., 2014]
Proportions		
Network volume fraction (ϕ)	0.05	[Snowhill et al., 2004] [Humphrey, 1995]
Elastin to collagen ratio (R)	8:5	[Tonar et al., 2015] [Sokolis et al., 2008]
Ratio of interlamellar connections to elastic lamina fibers (r)	1:1	[Snowhill et al., 2004]

Table A.2: Model parameter values and sources

Initial estimates of the fiber parameters (fiber stiffness, nonlinearity, and failure stretch) for collagen and elastin were based on our previous works [Shah et al., 2014, Lai et al., 2012], and those for the interlamellar connections were specified based on MacLean's experimental stress–strain behavior of the upper thoracic aorta subjected to radial failure [MacLean et al., 1999]. Properties were subsequently adjusted such that a single set of model parameters matched results from the suite of experiments performed herein; the final parameter values are given in Table A.2.

In addition to the smooth-muscle cells and connective tissue present within the lamellar unit, there is also fluid, primarily extracellular water [Humphrey, 1995], that combines with the smooth-muscle cells' cytoplasm to make tissue deformation nearly isochoric. A nonfibrous, neo-Hookean matrix was added to the network to make it nearly incompressible ($\nu = 0.49$). The fiber network and nonfibrous matrix operated as functionally independent until failure, at which point network failure dictated simultaneous matrix failure. Stresses developed by the new tissue-specific network and matrix were treated as additive, as in other constrained mixture models [Humphrey and Rajagopal, 2003, Alford and Taber, 2008, Alford et al., 2008, Gleason et al., 2004]. The matrix material was considered homogeneous throughout the global sample geometry; each element, however, was assigned a unique set of fiber networks. New networks were generated for each of the five model simulation replicates for the uniaxial test; the uniaxial simulations showed almost no variability in repeated runs (SD $< 1\%$ of value), so no replicates were performed for the other tests.

Macroscale and microscale stress and strain were coupled as described previously [Chandran et al., 2008, Hadi et al., 2012, Hadi and Barocas, 2013, Stylianopoulos and Barocas, 2007a]. Briefly, displacements applied to the macroscale model were passed down to the individual RVEs. The tissue-specific network within the RVE responded by stretching and rotating, generating net forces on the RVE boundary. A

volume-averaged stress was determined for each Gauss point within the element from the net forces on the network boundary and the nonfibrous resistance to volumetric deformation. The macroscopic displacement field was updated until the global Cauchy stress balance was satisfied. Grip boundaries were enforced using rigid boundary conditions and the remaining sample surfaces were stress-free. All model simulations were run using 256-core parallel processors at the Minnesota Supercomputing Institute, Minneapolis, MN; clock times averaged 10 h per simulation.

Finally, we ran a brief simulation of uniaxial extension in the radial direction to compare with the experimental results of MacLean et al. [MacLean et al., 1999], who performed uniaxial extension to failure of porcine aorta samples in the radial direction as noted earlier. The MacLean study represented an important test for our approach since the experiments were performed on the same tissue (healthy porcine thoracic ascending aorta) but in a mode that we did not use to generate and fit the model (radial extension to failure). Although MacLean did not report the tensile stress at failure, they reported the average tangent modulus at failure as well as the status of different samples at specific values of stretch; these data provided a basis for comparison with the model.

A.3 Results

Experiments were performed in four different geometries: uniaxial, biaxial, peel, and lap. In the uniaxial, peel, and lap tests, samples were prepared and pulled in two different directions, with some samples being tested in the axial direction and others in the circumferential direction. The multiscale model was used to describe all of the different experiments; the same set of model parameters was used for all of the experiments, including both prefailure and failure behavior.

A.3.1 Uniaxial extension to failure

Uniaxial samples (Figure A.5(a)) aligned both circumferentially (n = 11) and axially (n = 11) were loaded to failure. In Figure A.5(b), the first Piola-Kirchhoff (PK1) stress, defined as the grip force divided by the undeformed crosssectional area of the neck of the dogbone, was plotted as a function of grip stretch along with the best-fit tissue-specific model curves for samples aligned circumferentially and axially, respectively. The specified and regressed model parameters of Table A.2 allowed the model to match the experimental prefailure and failure results to within the 95% confidence intervals for both orientations, matching the roughly threefold difference in failure stress (2510 ± 979 kPa for samples aligned circumferentially as compared to 753 ± 228 kPa for those aligned axially) and similar to stretch to failure (1.99 ± 0.07 for samples aligned circumferentially as compared to 1.91 ± 0.16 for those aligned axially) in the circumferential case vis-á-vis the longitudinal case. The neck region of the simulated uniaxial samples (both circumferential and axial) experienced the largest stresses (as expected) and also a large degree of fiber reorientation, as can be seen in Figure A.5(b). For the simulated experiments oriented circumferentially, the collagen fibers, which were already preferentially aligned in the circumferential direction, became more strongly aligned and were stretched, leading to the relatively high stresses observed. In contrast, for the simulated experiments oriented axially, the collagen fibers tended to pull apart by stretching the surrounding elastin, leading to a significantly lower stress and more failure of the elastin fibers. In both simulations, the collagen fibers were most likely to fail due to the extremely large extensibility of the elastin fibers, but the tendency of the collagen fibers to break was much higher in the circumferentially aligned simulated experiments (Figure A.5(c)). This shift is attributed to the collagen fibers being aligned in the direction of the pull and thus being forced to stretch more during circumferential extension, whereas there is more

elastin and interlamellar connection stretch in the axial extension.

A.3.2 Equibiaxial extension

The averaged experimental PK1 stress was plotted as a function of grip stretch (n = 9; also used in our previous analysis [Shah et al., 2014]) along with the best-fit tissue-specific model curves in Figure A.6(a). The equibiaxial extension test was not performed to failure but instead was stopped at a stretch of 1.4 to ensure that the sample did not fail during testing (based on initial experiments to estimate the safe stretch limit). Thus, the peak circumferential (139 $\pm$ 43 kPa) and axial (102 $\pm$ 30 kPa) stresses were not failure stresses. The equibiaxial model results (lines) were in good agreement with the experiments in both directions but slightly overpredicted the degree of anisotropy, i.e., the separation between the two lines. In particular, stresses in the circumferential direction were slightly overpredicted but remained within the 95% confidence interval for the experiment. The arms of the sample showed behavior similar to the uniaxial experiments, as can be seen in the stress plots of Figure A.6(b), but our primary interest is in the central region that was stretched equibiaxially. As expected for equibiaxial extension, in-plane fiber orientation of the elements in this region showed little change (Figure A.6(c)); there was, however, a deviation from affinity because the stiffer collagen fibers did not stretch nearly as much as the more compliant elastin fibers. At the final stretch step, for example, the collagen fibers were extended to an average of 13% stretch, but the elastin fibers had an average of 118% stretch.

A.3.3 Peel to failure

Peel samples from both the circumferential (n = 13) and axial (n = 23) orientations were loaded to failure. Peel tension, defined as the grip force divided by the sample width, was used to quantify delamination strength. When plotted as a function of grip displacement, the peel tension rose to an initial peak and then plateaued until total sample failure (Figure A.7(a)); importantly, the rise in each individual experiment was quite steep, but since the rise occurred at different grip stretches in different experiments (because of variation in sample size and initial notch depth), the average data of Figure A.7(a) appear to rise smoothly. The simulation results were thus similar to individual experiments, but we did not introduce the sample-to-sample variation necessary to smooth out initial rise.

The initial point and end point of the plateau region were computed by splining the data into 20 sections and determining where the slope of a linear fit of the points in a section was not significantly different from zero. The value of peel tension in the plateau region was averaged in order to determine the peel strength of each sample. The standard deviation of peel tension within the plateau region was evaluated to assess the degree of fluctuation during the peeling process. The average peel tension was significantly higher ($p < 0.01$) for samples aligned axially versus circumferentially (97.0 ± 12.7 versus 68.8 ± 14.2 mN/mm, respectively) with an anisotropy ratio of 1.4, similar to the results reported by others [Kozuń, 2016, Pasta et al., 2012]. The standard deviation of peel tension showed similar anisotropy ($p < 0.001$) for samples aligned axially versus circumferentially (12.66 ± 2.22 versus 5.78 ± 1.04 mN/mm, respectively). The anisotropic response was present even when the standard deviation was normalized by average peel tension ($p < 0.05$, 0.145 ± 0.037 versus 0.088 ± 0.017, respectively, for a ratio of 1.65). Simulation results showed similar but less pronounced anisotropy (80.35 versus 67.01 mN/mm, ratio = 1.20). For both the

circumferentially and axially oriented simulated experiments, the first Piola-Kirchhoff stress was concentrated around the peel front (Figure A.7(b)), and there was extensive stretching of the interlamellar connections. In sharp contrast to the simulated uniaxial failure experiments (Figure A.5), the vast majority of failed fibers in the simulated peel failure experiments were interlamellar connections; this result highlights the need for a detailed anisotropic model because different physiologically relevant loading configurations impose very different mechanical demands on the tissue's components.

Regional analysis was performed to determine whether sample location, i.e., location along the aortic arch, had an effect on mean average or mean standard deviation of peel tension. First, samples, taken from both the axial and circumferential directions from multiple specimens, were grouped according to their distance from the inner and outer curvature of the aortic arch. No significant difference (all the p-values > 0.10, $n > 4$ for all groups) was observed. Then, axially oriented samples taken from a single specimen were grouped by where peel failure was initiated (proximal or distal to the heart, $n = 4$ for both groups). No significant difference was seen in mean average peel tension (paired t-test, p-value $= 0.26$) or mean standard deviation of peel tension (p-value $= 0.84$) between the two groups. Pairing was done based on sample location within the specimen.

A.3.4 Shear lap failure

As expected, the displacements were primarily in the pull direction, and shear strain was largest in the overlap region (Figs. A.8(a) and A.8(b)). In order to investigate the strain behavior of the tissue more fully, a line was drawn at the edge of the overlap surface, and strains tangential and normal to the overlap edge were calculated ($n = 15$ and $n = 19$ for axial and circumferential samples, respectively; some samples were not analyzed due to poor speckling). The maximum strain in each direction was

determined (Figs. A.8(c) and A.8(d)). For both the axially and circumferentially aligned samples, the shear strain, E_{nt}, was large in the overlap region, as desired. For the axially oriented samples, the shear strain was higher than both the normal ($p < 0.1$) and tangential strains ($p < 0.01$). For the circumferentially oriented samples it was significantly higher than the tangential strain ($p < 0.05$) and comparable to the normal strain ($p = 0.26$).

Shear lap samples from both the circumferential ($n = 28$) and axial ($n = 26$) orientations were loaded to failure. The nominal (average first Piola-Kirchhoff) shear stress, the force per overlap area (Figure A.9(a)), exhibited catastrophic failure similar to that seen in the uniaxial tests and unlike the steady failure of a peel test. Circumferentially oriented samples exhibited significantly higher ($p = 0.013$) peak shear stresses than axially aligned samples (185.4 ± 28.4 versus 143.7 ± 16.0 kPa, respectively). In both the axial and circumferential directions, the shear lap failure stress was less than 20% of the failure stress necessary for uniaxial failure, indicating that the tissue is far weaker in shear than in uniaxial tension. The grip strain at failure was used to quantify further the compliance of the tissue. Greater grip strain ($p = 0.07$) was necessary to fail samples aligned in the axial direction compared with those in the circumferential direction (1.63 ± 0.16 versus 1.43 ± 0.17, respectively). As can be seen in Figure A.9(a), the multiscale model predicted the shear lap behavior of circumferentially oriented samples well (within the 95% CI). It was less successful at predicting the shear lap behavior of axially oriented samples (below the 95% CI), thus overestimating tissue anisotropy. The overlap region edges of the simulated uniaxial samples (both circumferential and axial) experienced the largest stresses and also the largest degree of fiber reorientation (Figure A.9(b)). Interlamellar fibers within the lap region were rotated and stretched strongly by the shearing; the collagen and elastin fibers were stretched more than in the peel test but considerably less than in

the uniaxial and biaxial tests. As a result (Figure A.9(c)), the distribution of failed fibers was split more between the different fiber types than during peel or uniaxial failure. Even though the interlamellar connections, being much weaker than the others, were the most common to fail, there was also significant damage to the collagen and elastin fibers, perhaps due to the tangential component of the strain during the test (Figure A.8(d)).

A.3.5 Summary comparison of model and experiment

Since a stated goal of this work was construct a multiscale model of aortic tissue mechanics that predicts failure in many different physiologically relevant loading modalities, we present a brief summary of the experimental and model failure results. Figure A.10 shows the failure PK1 stress in uniaxial tests, failure tension in peel tests, and failure shear stress in shear lap tests for both the experiments and simulations for samples aligned in both the circumferential and axial directions. A single model with one set of parameters matches all of the experimental results well. It captures both the anisotropy exhibited in the different tests as well as the magnitude of stress or tension. In particular, the model predicts the considerably lower tissue strength observed in shear lap tests than that seen in uniaxial extension.

A.3.6 Uniaxial extension to failure in the radial direction

MacLean et al. [MacLean et al., 1999] reported that the average tangent modulus before failure was 61.4 $\pm$ 43 kPa. For our simulations, we found that the tangent modulus before failure was 58 kPa, in obvious good agreement with MacLean's experimental result. The stretch ratio at failure in the model was 3.1, and MacLean reported that "there was noticeable elastin layer separation" at a stretch ratio of 2,

and that a stretch ratio of 3.5 was "past the value at which the wall can maintain stress." Although the report of MacLean is obviously vague, the model results all appear to be consistent with MacLean's observations. The ability to make a reasonable prediction of an experiment performed using loading modality different from those used in the creation and specification of the model is a necessary feature for broader application in the future.

A.4 Discussion

Two important results came from the current work. First, a more complete picture of the failure behavior of aortic tissue was generated, demonstrating and quantifying the pronounced difference between the relatively high tissue strength in the lamellar plane (longitudinal and especially circumferential directions) and the low strength of the interlamellar connections (radial direction, demonstrated by peel and lap tests). Second, a novel multiscale, microstructural model was presented that, with proper adjustment of the model parameters, was able to reproduce the wide range of experimental observations accurately. This section focuses first on the experiments and then on the model, addressing them in the context of previous work by ourselves and others.

The current study used two novel test methods, the peel test and the shear lap test, to measure material failure in radial tension and transmural shear, respectively. The peel test is relatively new but has been used by others [Sommer et al., 2008, Tong et al., 2011, Pasta et al., 2012], and our results are consistent with their findings in terms of peel tension as well as the observation that the anisotropy typically expected of arteries in in-plane tests (higher circumferential versus axial stiffness) is reversed in peeling. Sommer et al. [Sommer et al., 2008] suggested that the anisotropic behavior

may be a protective mechanism since dissection in the axial direction is often associated with failure across elastic laminae, whereas dissection in the circumferential direction typically prop- agates between adjacent laminae. Pal et al. [Pal et al., 2014] suggested based on histology of peeled samples that the anisotropy may be due to stitching of the fibers, with failure in circumferential peeling occurring via a pull-out mechanism, whereas failure in axial peeling occurs via a tearing mechanism. This interesting conceptual description cannot be captured in our current model but clearly merits further investigation.

Although the shear lap test has been used on annulus fibrosus [Gregory et al., 2011], to the best of our knowledge it has not been applied to cardiovascular soft tissues. The loading curve for the shear lap test of ascending aorta showed catastrophic failure similar to that of a uniaxial test rather than the sliding behavior seen by Gregory et al., perhaps attributable to differences in the structure and properties between the annulus fibrosus and the ascending aorta. The failure behavior observed for the shear lap test retained the typical anisotropy expected of arteries, but required a much lower stress than that of uniaxial failure, presumably because the failure did not require as much breaking of collagen and elastin fibers. The shear lap and peel test results directly test the connections between lamellar units, and they are therefore critical in the case of a dissecting ascending aortic aneurysm. As our community moves forward to more patient-based geometries and simulations involving realistic geometries that necessarily lead to complex stress fields, validation of models in multidimensional loading is crucial. For example, it is common [Wisneski et al., 2014, Krishnan et al., 2015, Trabelsi et al., 2015, Martin et al., 2015, Martufi et al., 2014] to report results in terms of principal stresses, which are informative but do not address the fact that a stress acting radially or in shear is more likely to lead to tissue failure than one acting circumferentially. Martin et al. [Martin et al.,

2015] used a potentially generalizable energy-based failure threshold, but they based the failure criterion on uniaxial circumferential tests. Although Martin's work represents a significant advance and demonstrates the potential of the patient-specific FE approach, there is clear need for a more accurate failure model, which could be informed by the current work. Another major challenge is that the tissue properties surely change during aneurysm formation, growth, and remodeling. The current work used only healthy porcine tissue, so our results are useful in guiding thought but should not be considered representative of human aneurysm tissue. There is also great need to develop better tools to estimate tissue mechanical properties *in vivo*, which would allow the construction of patient-specific constitutive models to match the patient-specific geometries currently in use.

Another goal of this study was to generate a tissue-specific microstructural description based on the layered structure of the aorta. Such a description, when incorporated into our multiscale modeling framework, could replicate mechanical behavior of arteries in lamellar tension, radial tension, and transmural shear, thereby linking microscale failure to the macroscale response. The simplified microstructural organization of our previous work [Shah et al., 2014] was replaced with a new lamellar model to capture the microstructure more faithfully. The lamella's structure is an essential component in modeling dissection of ATAA since radial and shear loading involve failure of the interlamellar connections rather than the lamina itself. The microstructure design of Figure A.4 mimics the lamellar unit, detailed by Clark and Glagov [Clark and Glagov, 1985], and visualized here histologically. The unit is represented by a 2-D sheet of elastin and collagen fibers (which forms an elastic lamina) attached radially by interlamellar connections (which collectively encompass smooth-muscle cells and fine elastin and collagen fibers). Network parameters were selected to reflect the biological roles of each component and were adjusted to match the experimental results.

This approach was successful in matching a wide range of tissue mechanical tests, including one – radial extension to failure – that was not used during the fitting process, and it has the potential to be extended to the more disorganized (and thus more complex) architecture of the aneurysm, especially as better imaging and image-based modeling methods emerge [Koch et al., 2014, Tsamis et al., 2013]. The work of Pal et al. [Pal et al., 2014] represents an excellent example of this approach, developing a theoretical model of peel failure based on known structure. Pal's approach could be extended to a more general stress field using a strategy similar to ours. Finally, it is important to note that abnormal loading and damage can change tissue structure. For example, Todorovich-Hunter et al. [Todorovich-Hunter et al., 1988] observed the formation of islands of elastin within the pulmonary arteries of rats in which they induced pulmonary hypertension. Thus, moving forward imaging-based alterations to the network design may be necessary to capture the structure of a damaged or diseased aorta.

There are, of course, further opportunities to construct a more realistic micromechanical model of the healthy and the aneurysmal ascending thoracic aorta. As already noted, the work of Pal et al. [Pal et al., 2014] provides a different and intriguing view of interlamellar failure by tearing versus pull-out effects. Additionally, our current model used collagen orientation tensor with eigenvalues of 0.9 and 1.0, corresponding roughly to collagen aligned within 18° of the circumferential axis ($\sin^2(18°) = 0.1$). That number was based on the observed circumferential alignment of collagen fibers in the vessel wall but is an estimate and could be modified to provide a better match to the experimental data. In fact, the collagen and elastin fiber orientations within the $z\theta$ plane could also be treated as fitting parameters, which would likely improve the model fit, but we chose to use the best estimate from structural data rather than introduce further flexibility to an already highly parameterized

model. Finally, the Fung-type model of fiber mechanics (Table A.1, Equation (3)) could be replaced with a recruitment model, e.g., [Zulliger et al., 2004], which would provide an alternative mechanism to capture the nonlinear behavior associated with fiber waviness [Haskett et al., 2012] and might provide a better fit of the experimental data. All of these modifications are possible and could be implemented as additional data emerge about the arrangement and properties of the components of the arterial wall.

In summary, a microstructurally based multiscale model of prefailure and failure behaviors was able to match the experimentally measured properties of the healthy porcine ascending aorta in four different loading configurations and two different directions, and it was successful when applied to experiments in the literature that were not used during the fitting and specification project. This model could provide new insight into the failure mechanisms involved in aortic dissection and could be incorporated into patient-specific anatomical models, especially if model parameters associated with specific patients or patient groups can be obtained.

A.5 Acknowledgment

This work was supported by NIH Grant R01-EB005813. CMW was supported by a University of Minnesota (UMN) Doctoral Dissertation Fellowship, and CEK is the recipient of an ARCS Scholar Award. Tissue specimens were generously provided by the Visible Heart Lab at UMN. The authors gratefully acknowledge the Minnesota Supercomputing Institute (MSI) at UMN for providing resources that contributed to the research results reported within this paper.

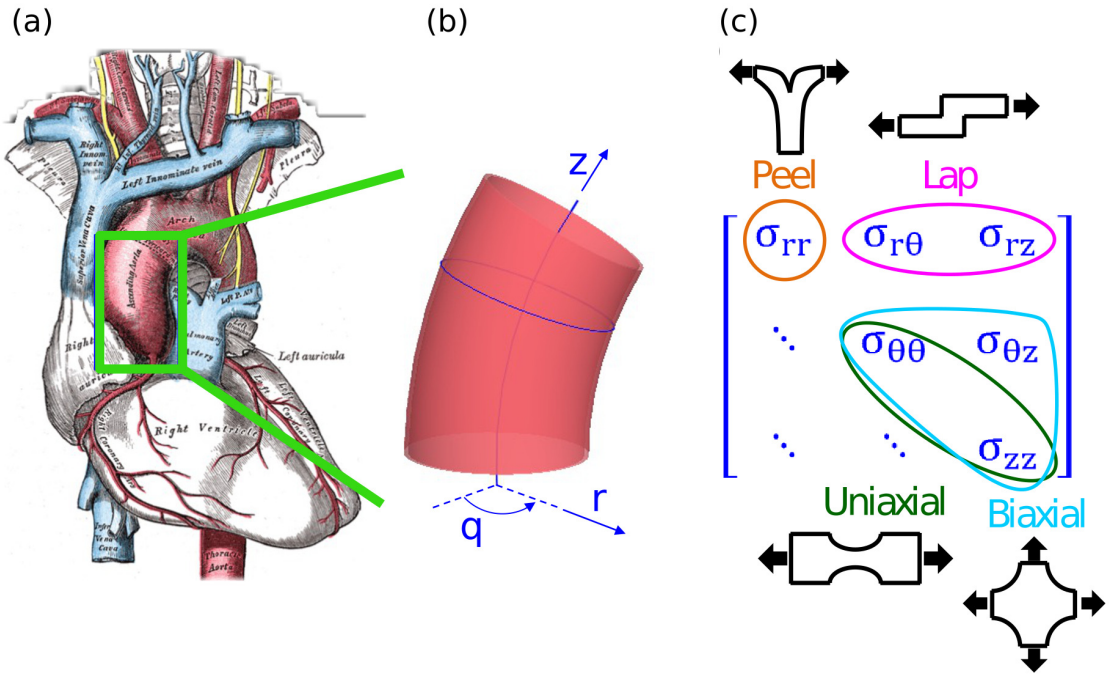

Figure A.1: The ascending thoracic aorta. (a) Illustration of the heart with the ascending aorta highlighted [Gray, 1918], (b) Geometry and coordinate system describing the ascending aorta, and (c) The three-dimensional stress tensor for the aorta, marked to show how different testing modes were used to target specific stress components.

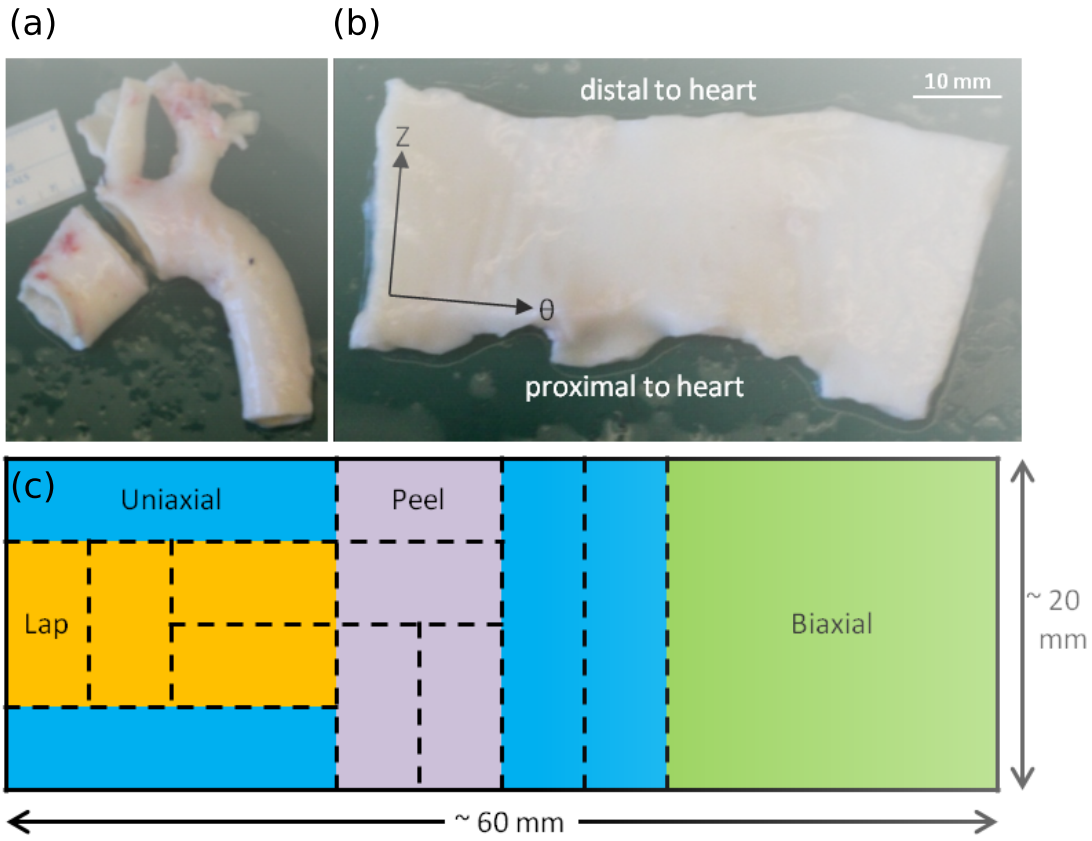

Figure A.2: Specimen dissection. (a) Porcine aortic arch with ascending aortic ring removed. The white star represents a marker used to keep track of tissue sample orientation. (b) The ring was cut open along its superior edge and laid flat with the intimal surface up and the axial, Z, and circumferential, θ, directions along the vertical and horizontal directions, respectively. Axial and circumferential directions are shown with black arrows. (c) Schematic showing a typical sectioning and testing plan for an ascending aortic specimen.

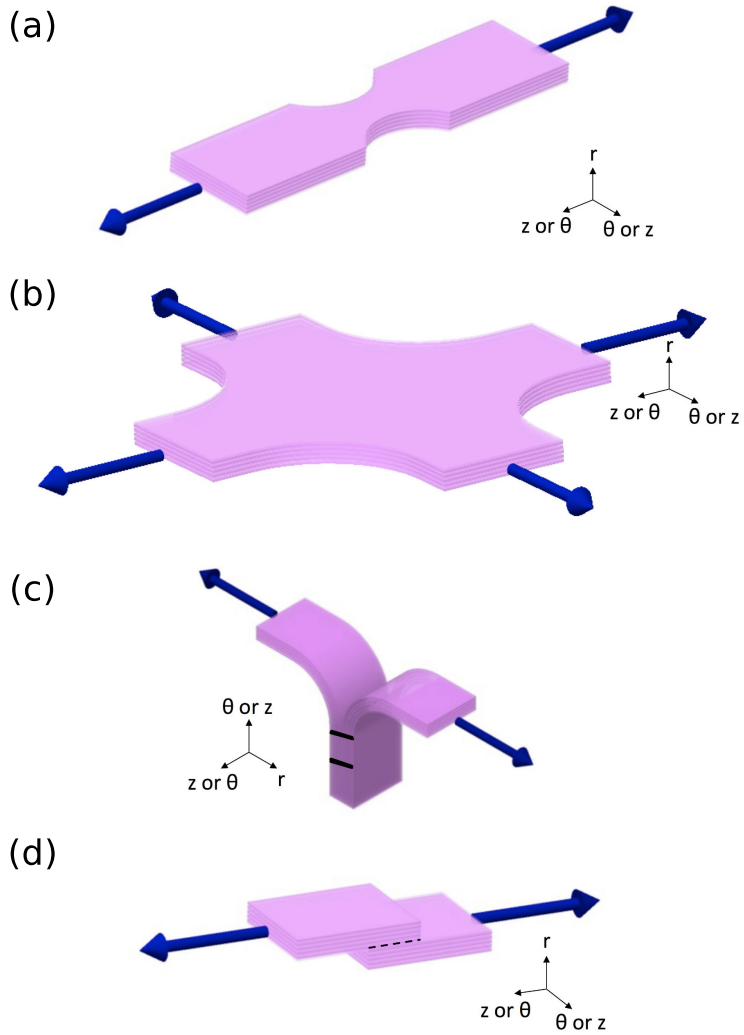

Figure A.3: Schematics of all mechanical tests. (a) Uniaxial test: samples were cut and mounted such that the direction of pull corresponded with either the axial or circumferential orientation of the vessel. (b) Equibiaxial test: samples were cut and mounted such that the directions of pull corresponded with the axial and circumferential orientations of the vessel. (c) Peel test: samples were cut and mounted such that the vertical direction corresponded with either the axial or circumferential orientation of the vessel. (d) Lap test: samples were cut and mounted such that the direction of pull corresponded with either the axial or circumferential orientation of the vessel; dotted black line indicates overlap length.

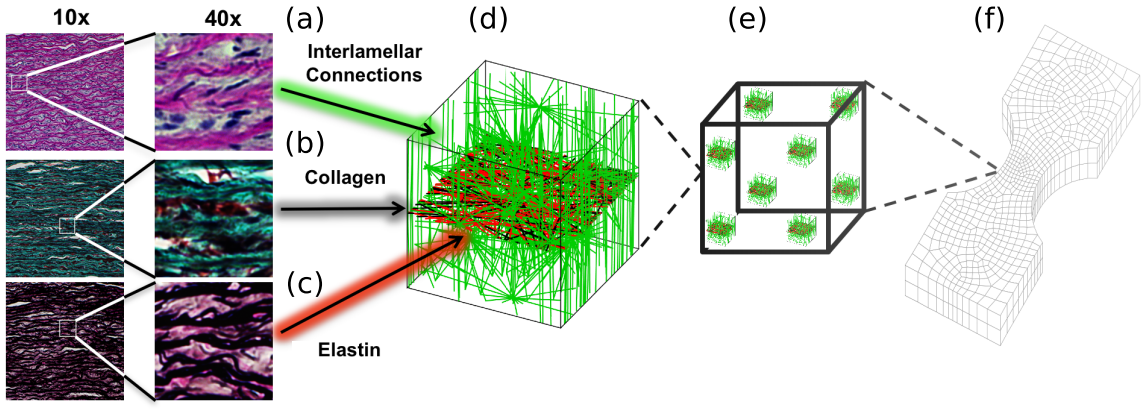

Figure A.4: Multiscale model based on aortic media structure. (a) Hematoxylin and eosin stain shows smooth muscle cell nuclei (dark purple) and elastic lamina (pink). (b) Masson's trichrome stain shows collagen (blue) within the lamina and smooth muscle (red). (c) Verhoeff–Van Gieson shows elastin (black/purple). (d) A microstructural model based on the histology contains a layer of elastin (red) reinforced by collagen fibers (black). The collagen fibers are aligned preferentially in the circumferential direction, and the elastin sheet is isotropic. Lamellae are connected by interlamellar connections (green) representing the combined contribution of fibrillin and smooth muscle. The interlamellar connections are aligned primarily in the radial direction but also have some preference for circumferential alignment to match smooth muscle alignment *in vivo*. (e) An RVE with eight gauss points. (f) FE geometry showing a uniaxial shaped sample (equibiaxial, lap, and peel geometries were also used).

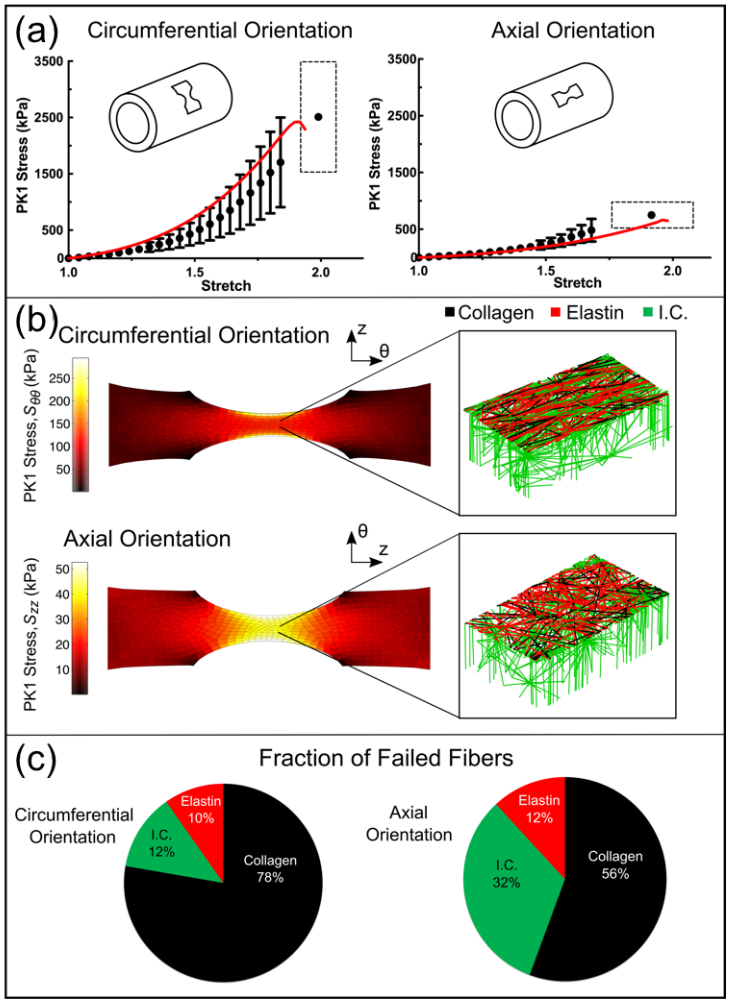

Figure A.5: Uniaxial extension to failure. (a) First Piola-Kirchhoff (PK1) stress versus grip stretch for circumferentially (n = 11) and axially (n = 11) orientated samples (dots, mean ± 95% CI). Error bars are only shown for stretch levels up to the point at which the first sample failed. The final dot shows the average stretch and stress at tissue failure, and the dashed rectangle indicates the 95% confidence intervals of stretch and stress at failure. The red lines show the model results for PK1 stress as a function of grip stretch. (b) PK1 stress distributions along the axis of applied deformation for both the circumferentially ($S_{\theta\theta}$) and axially (S_{zz}) aligned simulations, accompanied by an enlarged view of a network with the upper interlamellar connections removed to make the collagen and elastin visible. (c) Fraction of failed fibers of each type in the simulated experiment. Because the collagen fibers are preferentially aligned in the circumferential direction, more of the failed fibers were collagen for the circumferentially aligned simulation, whereas for the axially aligned simulation more of the failed fibers were interlamellar connections (I.C. = interlamellar connections).

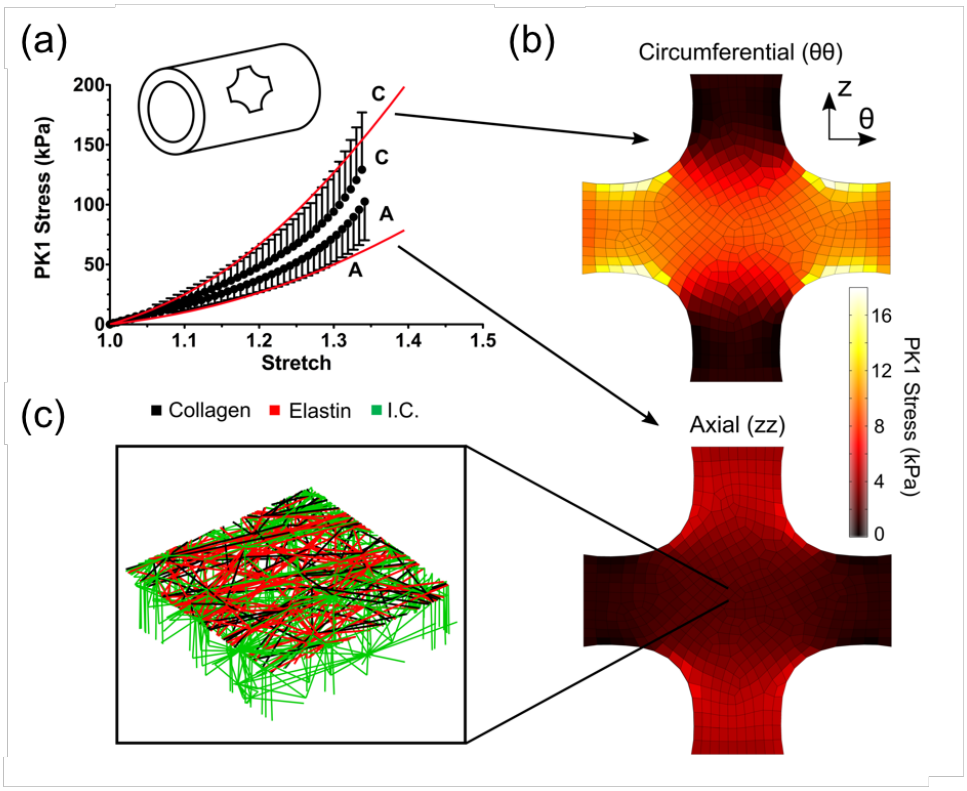

Figure A.6: Equibiaxial extension. (a) Mean PK1 stress as a function of grip stretch (dots) for equibiaxial extension. The 95% CI was 30–35% of the measured value but was omitted from the figure to improve visual clarity. The red lines show the model results for PK1 stress versus grip stretch. (b) Circumferential ($S_{\theta\theta}$) and axial (S_{zz}) PK1 stress distributions predicted by the model. (c) Enlarged view of a micronetwork with the upper interlamellar connections removed to make the collagen and elastin visible.

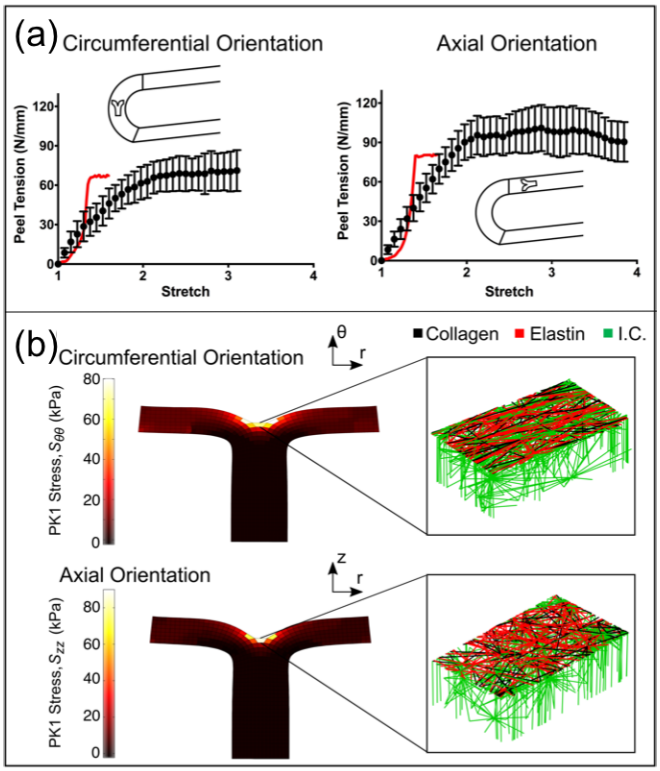

Figure A.7: Peel to failure. (a) Peel tension versus grip stretch for both circumferentially and axially oriented samples (dots, mean ± 95% CI). The red lines indicate the model results. (b) PK1 stress (S_{rr}) distributions along the axis of applied deformation for both the circumferentially and axially aligned simulations, accompanied by an enlarged view of a network with the upper interlamellar connections removed to make the collagen and elastin visible.

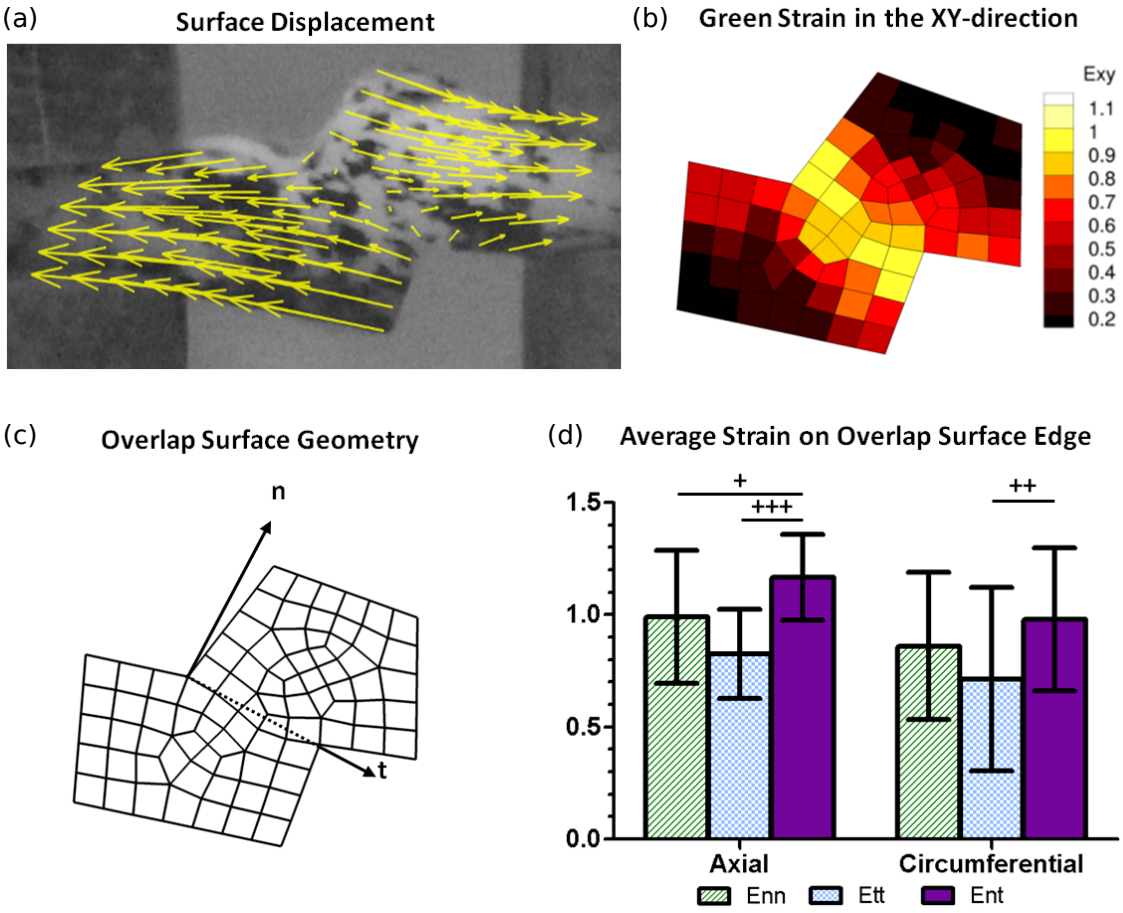

Figure A.8: Kinematics of the shear lap test. (a) Displacement of a representative shear lap sample, adjusted to zero displacement at the center. (b) Strain of the representative sample in the XY-direction. (c) Dotted line showing overlap surface edge and vectors with normal and tangential directions. (d) Average strain on the overlap surface edge for both axially (n = 15) and circumferentially (n = 19) oriented samples. Error bars indicate 95% confidence intervals. $^{+}p < 0.10$, $^{++}p < 0.05$, and $^{+++}p < 0.01$.

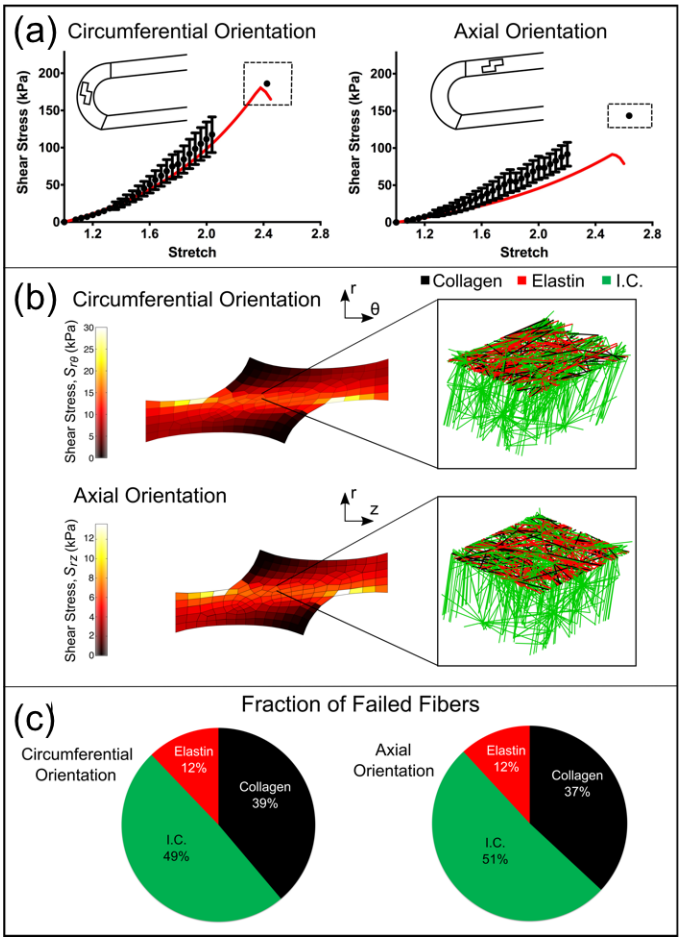

Figure A.9: Shear lap failure. (a) PK1 stress versus grip stretch for circumferentially (n = 28) and axially (n = 26) orientated samples (dots, mean ± 95% CI). Error bars are only shown for stretch levels up to the point at which the first sample failed. The final dot shows the average stretch and stress at tissue failure and the dashed rectangle indicates the 95% confidence intervals of stretch and stress at failure. The red lines show the model results. (b) Shear stress distributions along the axis of applied deformation for both the circumferentially ($S_{r\theta}$) and axially (S_{rz}) aligned simulations, accompanied by an enlarged view of a network with the upper interlamellar connections removed to make the collagen and elastin visible. (c) Fraction of failed fibers of each type in the simulated experiment (I.C. = interlamellar connections).

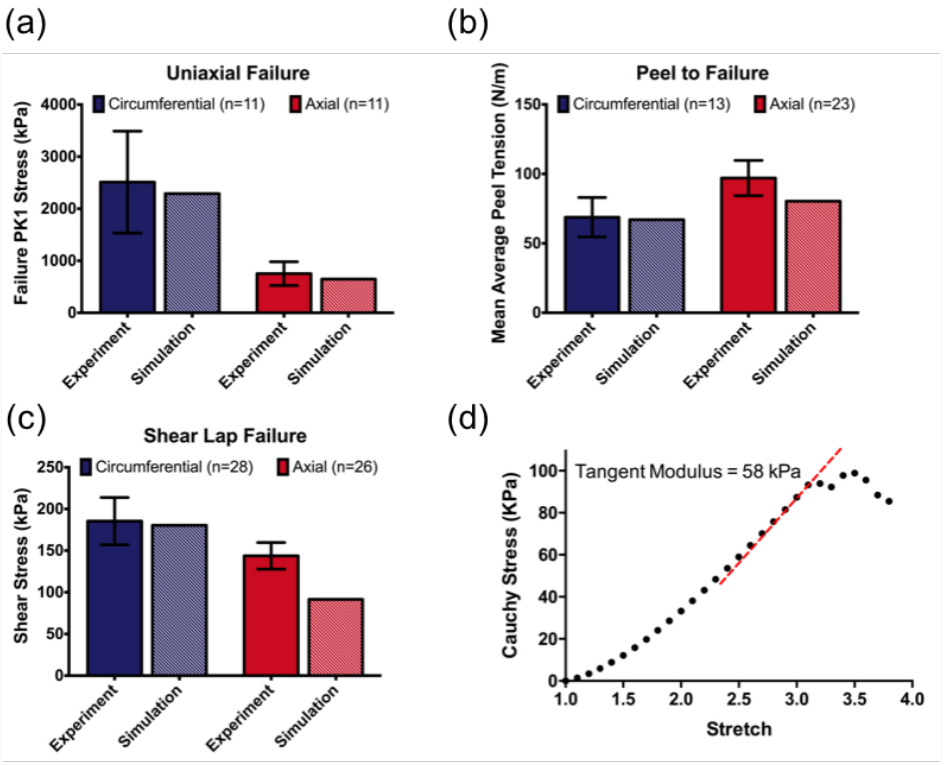

Figure A.10: Summary of experimental and model results. (a) Experimental and model failure PK1 stress ($S_{\theta\theta}$ and S_{zz}) in uniaxial tension tests for samples oriented circumferentially and axially. (b) Experimental and model failure tension in peel tests for samples oriented circumferentially and axially. (c) Experimental and model failure shear stress ($S_{r\theta}$ and S_{rz}) in shear lap tests for samples oriented circumferentially and axially. All the experimental data show mean $\pm$ 95% CI. (d) The model showed failure at a stretch ratio of 3.1 with a tangent modulus of 58 kPa in the region prior to failure, comparing well to MacLean's [MacLean et al., 1999] reported tangent modulus of 61 kPa.

Appendix B

Dicer1 Deficiency in the Idiopathic Pulmonary Fibrosis Fibroblastic Focus Promotes Fibrosis by Suppressing MicroRNA Biogenesis

The content of this chapter was submitted as a research article to the *American Journal of Respiratory and Critical Care Medicine* by Herrera, Beisang, Peterson, Forster, Gillbersten, Benyumov, Smith, Korenczuk, Barocas, Guenther, Hite, Zhang, Henke, and Bitterman [Herrera et al., 2018a]. My contribution to the work was performing uniaxial testing on lung tissue and processing results for mechanical comparisons.

Cite: Herrera, J., Beisang, D.J., Peterson, M., Forster, C., Gilbertsen, A., Benyumov, A., Smith, K., Korenczuk, C.E., Barocas, V.H., Guenther, K. and Hite, R., 2018. Dicer1 deficiency in the idiopathic pulmonary fibrosis fibroblastic focus pro-

motes fibrosis by suppressing microRNA biogenesis. American journal of respiratory and critical care medicine, 198(4), pp.486-496.

The American Journal of Respiratory and Critical Care Medicine is an official journal of the American Thoracic Society

B.1 Introduction

Idiopathic pulmonary fibrosis (IPF) is a relentlessly progressive form of lung scarring. Available data indicate that IPF lung extracellular matrix (ECM) itself is fibrogenic [Booth et al., 2012, Herrera et al., 2018b, Parker et al., 2014]. Fibroblasts cultured on decellularized IPF lung ECM (IPFECM) suppresses expression of miR-29 (microRNA-29) (a master negative regulator of stromal genes), leading to increased ribosome recruitment to hundreds of stromal genes, including: collagens, fibronectin, and their cognate integrins; matrix metalloproteinases; and proteins controlling proliferation and motility. Restoration of fibroblast miR-29 expression returns translation of miR-29 target genes back to baseline [Parker et al., 2014]. Although miR-29 suppression has been established in IPF [Pandit et al., 2010] and other fibrotic disorders [Roderburg et al., 2011, Lv et al., 2013, He et al., 2013, van Rooij et al., 2008] for several years; the underlying mechanisms remain unknown. Here we set out to unveil the molecular mechanism by which IPF-ECM decreases fibroblast miR-29 expression.

Identifying the ECM properties sensed by fibroblasts to suppress miR-29 has the potential to unveil new targets that can be exploited to develop therapies that interrupt fibrosis progression. One signature property of IPF lung ECM that distinguishes it from normal is its elastic modulus (stiffness). IPF lung ECM is up to an order of magnitude stiffer than normal, with steep stiffness gradients between fibrotic and morphologically uninvolved regions of the lung [Booth et al., 2012, Liu et al.,

2015]. Mechanotransduction of ECM stiffness has prominent roles in pathological processes, including cancer progression and fibrosis [Liu et al., 2015, Rahaman et al., 2014, Marinković et al., 2013, Dufort et al., 2011]. Expression of the mechanosensitive Hippo pathway constituent YAP (yes-associated protein) is increased in the IPF lung, and ectopic expression of activated YAP confers fibroblasts with fibrogenic properties, including increased ECM production [Liu et al., 2015]. YAP has dual functions with diametric effects on miR-29 expression. At the singlegene level, YAP serves as a transcriptional coactivator of miR-29b-1/a [Tumaneng et al., 2012], the gene encoding miR-29a and miR-29b-1; two of the three molecular species of miR-29 (a separate gene on chromosome 1 encodes miR-29b-2 [identical to miR-29b-1, together designated miR-29b] and miR-29c). In contrast, on a genome-wide level, YAP functions as a negative regulator of microRNA expression by sequestering p72, an integral component of the microRNA processing machinery [Mori et al., 2014]. Thus, mechanotransduction of ECM stiffness leading to activation of YAP provides a plausible molecular mechanism by which IPF-ECM regulates miR-29.

To explore this possibility, we combined in situ analysis of IPF lung tissue with experiments using primary human lung fibroblasts studied on decellularized human lung ECM, ECM functionalized hydrogels of tunable stiffness, and two xenograft models. Although stiff hydrogels triggered fibroblast YAP activation and increased miR-29 expression, decellularized IPF-ECM did exactly the opposite, excluding mechanotransduction of stiffness through YAP as the primary mechanism. Instead, we discovered that IPF-ECM suppresses microRNA biogenesis at the processing step by downregulating Dicer1 (an integral microRNA processing component) in the myofibroblast core of the fibroblastic focus, where active ECM synthesis is taking place. Dicer1 deficiency in primary lung fibroblasts decreased mature miR-29 levels and increased collagen expression on control-ECM (enforced Dicer1 expression was toxic, precluding

gain-of-function studies on IPF-ECM). We established a definitive mechanistic link to Dicer1 deficiency by showing that in both zebrafish and mouse xenografts, Dicer1 deficiency conferred human lung fibroblasts with cell-autonomous fibrogenicity. Our data show for the first time that ECM-mediated suppression of fibroblast Dicer1 in the myofibroblast core of the fibroblastic focus is a central step in IPF disease progression by decreasing the processing of precursor miR-29 into its mature antifibrotic forms. This finding provides foundational new knowledge that paves the way for developing novel precision therapeutics targeting fibrosis progression. Some of the results presented here have been previously reported in abstract form [Herrera et al., 2015].

B.2 Methods

Detailed methods can be found in the supplemental material.

B.2.1 Statistical Analysis

For analyses of data with sample sizes greater than six, one-sample or two-sample t tests were used for hypothesis testing on the means of the distributions. For analyses of data with sample sizes less than six, nonparametric tests such as the Wilcoxon rank sum test were used to test the medians of distributions. For miR-29 abundance data under conditions of YAP overexpression, a Kruskal-Wallis test was used for a nonparametric one-way ANOVA test followed by a Tukey test for pairwise comparisons with the P values adjusted for the multiple comparisons. For analysis of AUF-1 pull-down data, a one-sided Mann-Whitney U test was used. All analyses and plots were conducted in Prism.

B.3 Results

B.3.1 IPF-ECM Suppresses miR-29 Expression and Upregulates Collagen Production

Prior work using atomic force microscopy indicates that regions of the IPF-ECM are up to an order of magnitude stiffer than control-ECM (Ctrl-ECM) [Booth et al., 2012]. To interrogate the ECM at a scale approximating the size of the human lung acinus (3 mm x 10 mm 5 mm), we quantified uniaxial tensile strain in lung tissue strips and found IPF-ECM to be significantly stiffer than Ctrl-ECM at this scale of resolution (see Figure B.10 in the online supplement). Our prior studies indicate that IPF-ECM suppresses miR-29 family member expression in human lung fibroblasts [Parker et al., 2014]. We reexamined this effect with methodological refinements designed to minimize the effect of serum growth factors (low-serum survival medium) and controlled for patient-to-patient and lung ECM heterogeneity (Ctrl-ECM preparations from three patients or IPF-ECM preparations from three patients in each reaction). Under these more stringent conditions, IPF-ECM significantly decreased all miR-29 species (Figure B.1A). We next sought to determine whether relevant outside-in signaling pathways mediated this response. Pharmacologic agents inhibiting Notch (DAPT), PI3 kinase (LY294002), Rock/Rho (Y27632), Erk (SCH772984), focal adhesion kinase (PF562271), ALK5 (A83-01), or MTRF (CCG-100602) did not consistently restore fibroblast miR-29 levels on IPF-ECM (Figure B.11.

As a positive control, we examined previously verified miR-29 stromal targets (type IV collagen and type VI collagen mRNA [Parker et al., 2014]; and type I collagen protein secretion) in fibroblasts on IPF-ECM. As expected, suppression of miR-29 by IPFECM increased expression of these miR-29 target genes (Figures B.1B and B.1C; Figure B.12.

B.3.2 Stiffness Increases miR-29 Expression on Two-Dimensional Hydrogels

To determine whether stiffness and/or composition could account for the suppression of miR-29 expression on IPF-ECM, we cultured lung fibroblasts on synthetic two-dimensional (2D) polyacrylamide hydrogels (PA gels) of physiological stiffness (soft PA gels z3 kPa) or IPF stiffness (stiff PA gels z20 kPa). To validate our model system, we analyzed the impact of stiffness on a-smooth muscle actin expression. In accord with published data [Liu et al., 2015, Huang et al., 2012], lung fibroblasts displayed increased a-smooth muscle actin on stiff PA gels functionalized with type I collagen (Figure B.13. We next examined the effect of stiffness on miR-29 expression and were surprised to find that fibroblast miR-29 expression was increased by stiff PA gels functionalized with type I collagen, pointing away from stiffness *per se* as the property of IPF-ECM downregulating miR-29 (Figure B.2A). The PA gel system is versatile, as it allows the gels to be functionalized by coating with any ECM protein [Cretu et al., 2010]. To test the relative importance of stiffness versus composition in regulating miR-29, we supplemented the collagen I data by coating PA gels with collagen III alone, fibronectin alone, or an equal ratio of collagen I, collagen III, and fibronectin. Independent of substratum composition, stiffness consistently upregulated mature miR-29 abundance (Figures B.2B–B.2D), revealing the primacy of stiffness over composition in the 2D hydrogel model.

B.3.3 IPF-ECM Negatively Regulates YAP and Suppresses miR-29 Transcription

We next sought to determine whether there was a causal role for YAP in the regulation of miR-29 by IPF-ECM. In accord with prior work [Liu et al., 2015], when

fibroblasts resided on stiff 2D hydrogels, YAP nuclear localization (active YAP) and two canonical YAP transcriptional targets, which serve as readouts of YAP function, all increased (Figure B.14. Contrary to expectation, when lung fibroblasts were cultured on IPF-ECM, YAP nuclear localization was reduced (inactive YAP) (Figure B.3A), along with reduced expression of YAP transcriptional targets (Figure B.3B). Although YAP mRNA abundance is not influenced by ECM type [Parker et al., 2014], IPF-ECM significantly decreased YAP protein levels (Figure B.3C). YAP downregulation by IPF-ECM is in accord with a possible mechanistic relationship between YAP and one of its transcriptional targets, the gene encoding miR-29b-1/a [Tumaneng et al., 2012]. To examine this possibility, we introduced an miR-29b-1/a luciferase reporter [Mott et al., 2010] into lung fibroblasts and found that IPF-ECM caused a modest but significant suppression of miR-29b-1/a transcriptional activity (Figure B.3D). This raised the possibility that fibroblast YAP deficiency on IPF-ECM might lead to decreased transcription of *miR-29b-1/a*.

B.3.4 Enforced YAP Expression in Fibroblasts Does Not Restore Mature miR-29 Expression on IPF-ECM

To determine whether restoring YAP would rescue miR-29 expression on IPF-ECM, we transduced lung fibroblasts with one of two active YAP expression constructs. The first encoded a stably active YAP mutant—resistant to proteosomal degradation (YAP S127/381A [FLAG tagged]); and the second encoded a constitutively active and stable YAP mutant (5SA–S61/109/127/164/381A [Myc tagged]) [Zhao et al., 2010] (Figure B.4A). As evidence that we achieved YAP gain of function in both cases, YAP transcriptional targets, including primary–precursor (Pri-Pre) miR-29a, were all upregulated on IPF-ECM (Figures B.4B and B.4C). As a control, we exam-

ined the impact of YAP gain of function on miR-29b-2/c, which does not contain a YAP-responsive regulatory element [Mott et al., 2010], and found its transcript abundance to be decreased—an effect that may represent an indirect effect of YAP gain of function. Despite increases in Pri-Pre miR-29a, mature miR-29 species remained unchanged after YAP gain of function (Figure B.4D). YAP knockdown in lung fibroblasts on Ctrl-ECM had no effect (Figure B.15. Thus, the inability of YAP gain of function to rescue mature miR-29 expression in fibroblasts on IPF-ECM, despite increasing the levels of its primary/precursor forms, pointed downstream to deregulation of miR-29 processing as a candidate mechanism by which IPF-ECM suppresses miR-29.

B.3.5 IPF-ECM Suppresses the MicroRNA Processing Machinery

Processing of microRNA occurs cotranscriptionally, and processing of primary microRNA into precursor microRNA is a better predictor of mature microRNA abundance than transcriptional regulation alone [Conrad et al., 2014]. Prior work using mouse fibroblasts indicates that miR-29 expression depends on Drosha, Exportin-5, and Dicer1 [Kim et al., 2016], key components of the canonical microRNA processing machinery (Figure B.5A). Of note, Ago2 (Argonaute-2), another component of the microRNA processing pathway, is reduced in IPF [Oak et al., 2011]. To determine whether IPF-ECM altered microRNA processing, we measured Pri-Pre and mature miR-29a and 29c abundance (representing the two miR-29 genes) on ECM (Figure B.5B). Pri-Pre miR-29 abundance increased on IPFECM, strongly implicating a downstream block in microRNA processing, particularly in view of the decreased transcription observed for miR29b-1/a on IPF-ECM. We therefore sought to deter-

mine whether IPF-ECM regulated Dicer1, Ago2, Drosha, or Exportin-5. IPF-ECM suppressed steady-state levels of Ago2, Drosha, and Dicer1, whereas Exportin-5 levels did not consistently change (Figure B.5C, Figure B.16. As a control, we examined the expression of three noncanonically processed microRNAs on IPF-ECM. Among the three (miR-320a, -451, and -484) [Kim et al., 2016], two of the three noncanonically processed microRNAs were unaltered by ECM type (Figure B.17. As a control for internal consistency, we found that fibroblast expression of Dicer1 and other components of the microRNA processing machinery did not differ between soft and stiff polyacrylamide gels (Figure B.18. Taken together, our experiments identified a microRNA processing defect as central to the suppression of fibroblast miR-29 expression by IPF-ECM.

B.3.6 Dicer1 Expression Is Reduced in Cells Comprising the Myofibroblast-Rich Core of the Fibroblastic Focus

Our experiments show that deregulation of lung fibroblast miR-29 expression on IPF-ECM results from defects in microRNA processing. However, the microRNA processing machinery is a complex multicomponent apparatus, precluding efficient gain- and loss-of-function experiments involving each component singly or in combination. To direct our search for the microRNA processing step underlying the in vivo biology in IPF, we analyzed expression of microRNA processing components in the myofibroblast-rich core of the fibroblastic focus in IPF specimens [Xia et al., 2017]. We analyzed serial sections for: histology (hematoxylin and eosin), procollagen I (a nascent form of collagen I and an miR-29 target), Ago2, Dicer1, Exportin-5, and Drosha. We consistently found that the myofibroblast-rich core of fibroblastic foci (defined by procollagen I reactivity) was deficient in Dicer1 compared with the

focus perimeter and surrounding adjacent regions, whereas we found no consistent differences in Ago2, Exportin-5, or Drosha (n = 7 IPF specimens; Figure B.19.

Guided by this initial analysis, we serially sectioned IPF specimens to further explore Dicer1 expression at both the protein and RNA level. Serial sections (four tissue sections from one patient, 4 mm each) were analyzed for morphology (Figure B.6A), procollagen I (Figure B.6B), Dicer1 protein (Figure B.6C), and Dicer1 mRNA (*in situ* hybridization by RNAscope; Figure B.6D). We examined a region of active collagen synthesis within the myofibroblast-rich focus core (dashed outlined box) and the focus perimeter (solid outlined box) with higher magnification (Figures B.6B-B.6D, middle and right panels). The cells within the myofibroblast-rich core of the fibroblastic focus showed lower expression of both Dicer1 protein and mRNA (visualized as discrete brown dots) than cells at the focus perimeter. We quantified Dicer1 mRNA expression in six IPF lung specimens by enumerating the number of dots per cell within the myofibroblast-rich core compared with the focus perimeter (Figure B.15. Cells within the myofibroblastrich core had significantly lower levels of Dicer1 mRNA expression than cells at the focus perimeter (Poisson regression, $P<0.0001$). Taken together, our data implicate a deficiency of Dicer1 in the myofibroblastrich core region of the fibroblastic focus where active collagen synthesis is taking place (on the basis of procollagen I expression) in the *in vivo* mechanism of the IPF-ECM-mediated microRNA processing defect.

B.3.7 IPF-ECM Increases the Association of the Dicer1 Transcript with the RNABinding Protein AUF1

Available published literature points to control of Dicer1 mRNA levels by the RNAbinding protein AUF1 (AU-binding factor 1) [Abdelmohsen et al., 2012]. AUF1

binds to AU-rich elements in the Dicer1 transcript and recruits the mRNA degradation machinery, leading to decreased steady-state levels of the transcript. If this mechanism is operating in IPF, then the association of AUF1 with the Dicer1 transcript should increase on IPFECM. To test this possibility, we cultured primary human lung fibroblasts on IPFand control-ECM and quantified AUF1 binding to Dicer1 mRNA through RNA immunoprecipitation (Figure B.7). Consistent with this hypothesis, IPF-ECM increased the association of AUF1 with Dicer1 mRNA more than fivefold compared with control-ECM ($P<0.05$ one-sided Mann-Whitney U test).

B.3.8 Dicer1 Knockdown Decreases Mature miR-29 Abundance and Increases Expression of miR-29 Target Genes on Ctrl-ECM

If Dicer1 deficiency is central to the mechanism leading to reduced miR-29 levels in IPF, then decreasing Dicer1 levels in lung fibroblasts on Ctrl-ECM should replicate the biology observed on IPF-ECM. Stable Dicer1 knockdown in lung fibroblasts was achieved by transducing cells with a lentiviral-based shRNA (Figure B.8A). In accord with a causal role, Dicer1 suppression decreased miR-29 abundance in lung fibroblasts on Ctrl-ECM (normalized to miR-451, which is processed independently of Dicer1) [Kim et al., 2016] (Figure B.8B), leading to increased secretion of miR-29 target genes (Figure B.8C). We independently replicated this result in a second lung fibroblast line (Figure B.20. To test whether restoring Dicer1 would rescue fibroblast miR-29 expression on IPF-ECM, we attempted to overexpress Dicer1 in two primary fibroblast lines (and in a lung cancer line A549 as a nonfibroblast control); however, in each case, all cells detached from the substratum and showed morphological evidence of toxicity within 48 hours after gene delivery. This precluded analysis of fibroblast Dicer1 gain

of function on IPF-ECM. These data identify decreased Dicer1 processing of precursor forms of miR-29 in the mechanism by which IPF-ECM decreases fibroblast miR-29 expression.

B.3.9 Dicer1 Knockdown Imparts Fibroblasts with Fibrogenicity *In Vivo*

Having shown that Dicer1 deficiency in primary human lung fibroblasts is sufficient to decrease all three species of miR-29 and increase ECM synthesis in vitro, we next sought to determine whether these same Dicer1-deficient fibroblasts would display increased ECM production *in vivo* in the absence of any other cues. We considered using a lung fibroblast–specific conditional Dicer1 knockout (KO) mouse model for this purpose but chose not to use this model on the basis of two considerations. First, the effect of Dicer1 KO in mouse lung fibroblasts may not be comparable to Dicer1 deficiency in primary human lung fibroblasts, which could differ profoundly from those in mouse cells when modeling cell-autonomous functions [Rangarajan and Weinberg, 2003]. Second, studies in cancer using Dicer1 KO mice show that the Dicer1-null state inhibits tumor formation, a cell-autonomous function, whereas Dicer1 haploinsufficiency is permissive [Swahari et al., 2016, Kumar et al., 2009]. Therefore, we took a direct approach to test whether Dicer1-deficient primary human lung fibroblasts would display cell intrinsic/autonomous fibrogenicity using two in vivo xenograft model systems specifically designed for this purpose.

We previously described the use of zebrafish embryos as a simple and rapid *in vivo* xenograft system for assessing lung fibroblast fibrogenicity [Xia et al., 2014, Benyumov et al., 2012]. In control xenografts injected with fibroblasts transduced with nonsilencing scrambled shRNA, there were scattered procollagen I–expressing cells

at the periphery of the graft, with only sparse procollagen I expression in the graft core (Figure B.9A). In contrast, xenografts injected with fibroblasts transduced with Dicer1 shRNA (Dicer1-KD) displayed prominent procollagen I expression throughout (Figure B.9B). Quantification by image analysis indicated a significant increase in human procollagen I expression in xenografts containing Dicer1-KD fibroblasts compared with those with nonsilencing scrambled shRNA control (Figure B.9C). As an independent assessment of *in vivo* fibrogenicity, we tested Dicer1-KD fibroblasts in a mouse tail vein injection xenograft model. In this model, IPF lung fibroblasts produce prominent angiocentric fibrotic lesions, whereas control lung fibroblasts do not [Xia et al., 2014,Pierce et al., 2007]. The lungs of mice receiving fibroblasts transduced with nonsilencing scrambled shRNA (n = 8) produced no morphological lesions (Figure B.9D, left panels), a result consistent with our prior report using unaltered primary lung fibroblasts [Xia et al., 2014]. In sharp contrast, the lungs from four out of eight mice injected with Dicer1-KD fibroblasts developed fibrotic lesions ($P<0.04$), similar in morphology to those formed by IPF lung fibroblasts [Xia et al., 2014] (Figure B.8D, middle and right panels). The largest of these fibrotic lesions spanned 300 mm at the 13- day time point (Figure B.21. Thus, Dicer1 deficiency—even in the absence of cues from a fibrotic ECM—is sufficient to confer human lung fibroblasts with cellautonomous fibrogenicity in two *in vivo* xenograft models.

B.4 Discussion

Here we show that IPF-ECM inhibits lung fibroblast miR-29 expression upstream at the level of transcription and downstream at the processing step by suppressing Dicer1. Dicer1 deficiency suppresses lung fibroblast miR-29 expression on control ECM and confers lung fibroblasts with cell-autonomous fibrogenicity in vivo. We pro-

vide strong validation for our findings by showing that the cells in the myofibroblast-rich core of the IPF fibroblastic focus, where active collagen synthesis is taking place, display reduced levels of Dicer1 compared with cells comprising the focus perimeter. These data identify Dicer1 deficiency as a critical missing step in the mechanism of the IPF-ECM–driven profibrotic feedback loop, providing a new pathway to exploit for stopping fibrosis progression.

Several pathways can regulate miR-29 expression [He et al., 2013]; however, we began our studies on the basis of the prevailing hypothesis in the field that ECM stiffness transduced through YAP could explain miR-29 deficiency in IPF. This concept derived from studies showing that stiffness drives lung fibroblast ECM production in a YAP-dependent manner on hydrogels [Liu et al., 2015], that stiff IPF-ECM drives fibroblast ECM production by deregulation of miR-29 [Parker et al., 2014], and that YAP regulates miR-29 expression [Tumaneng et al., 2012] and microRNA processing [Mori et al., 2014], establishing a mechanistic link. When we compared fibroblast YAP and miR-29 expression on soft versus stiff hydrogels (a 2D system) to YAP and miR-29 expression on Ctrl-ECM versus IPFECM (a 3D system), stiff 2D hydrogels activated YAP and increased miR-29 levels, whereas IPF-ECM inactivated YAP and decreased miR-29 levels. This excluded stiffness as the primary property of IPFECM transduced by fibroblasts to deregulate YAP and miR-29.

Although these results were unexpected, they point to other ECM and cell surface properties that might play a role. These include dimensionality, viscoelasticity, cell–cell interactions, and cyclic stretch. In experiments examining mesenchymal stromal cell (MSC) YAP expression in response to substratum dimensionality [Caliari et al., 2016], stiffness drove YAP activation in a 2D system; whereas stiffness inactivated YAP in a 3D system. This result is in accord with our data, which showed fibroblast YAP activation on stiff 2D gels but YAP inactivation on IPF-ECM. In ad-

dition, independent of substratum stiffness or dimensionality, MSC YAP activation is driven by increased viscoelasticity [Chaudhuri et al., 2016, Chaudhuri et al., 2015], a parameter not yet assessed in the IPF lung. As an additional consideration, the YAP response to MSC mechanosensing of matrix stiffness is dampened by an order of magnitude when MSC N-cadherin (mimicking cell–cell interactions) is ligated [Cosgrove et al., 2016]. It is also worth noting that the constant strain and relaxation of the lungs during respiration represent a potentially important set of forces. Mammary epithelial cells activate YAP in response to cyclic stretch [Codelia et al., 2014], and cyclic stretch and compression in periodontal ligament cells regulate miR-29 and downstream gene expression [Chen et al., 2015]. Together, these studies illustrate the complexity of the mechanosensing–mechanotransduction axis, highlighting a critical gap in our understanding of fibrosis progression in IPF.

Dicer1 can act as both a tumor suppressor and oncogene [Kurzynska-Kokorniak et al., 2015]. Global microRNA deregulation due to a microRNA processing defect is an established theme in cancer [Lin and Gregory, 2015] and has been implicated in IPF [Oak et al., 2011, Pandit et al., 2011]. In accord with Dicer1 haploinsufficiency supporting cell autonomy in cancer, we found that experimentally induced Dicer1 deficiency in human lung fibroblasts decreased miR-29 abundance, increased collagen production, and supported cell-autonomous fibrogenicity in zebrafish and mouse xenografts. Thus, both cancer and IPF exploit decreases but not ablation of the terminal steps in microRNA processing to stabilize cell-autonomous pathology. Another emerging function of Dicer1 is its role in DNA damage repair [Swahari et al., 2016, Francia et al., 2012], which we speculate might play a dual role in IPF progression. Recent data indicate that cellular senescence markers are expressed within the fibroblastic focus [Schafer et al., 2017], and there is extensive crosstalk between DNA damage repair and cellular senescence [Sulli et al., 2012]. Thus, our study provides

strong support for the concept that the IPF fibroblastic focus is highly polarized, with Dicer1 deficiency restricted to the myofibroblast-rich core of the fibroblastic focus functioning as a driver of fibrosis progression.

The mechanisms regulating Dicer1 expression remain incompletely defined. Our data support a role for the RNA binding protein AUF1, which associates with the 3' untranslated region of RNA to recruit the RNA degradation machinery [Abdelmohsen et al., 2012]. We found that IPF-ECM increases binding of AUF1 to the Dicer1 transcript more than fivefold, providing an explanation for some of the decrease in Dicer1 transcript we observed. Another possible mechanism is suggested by studies relating cell density to microRNA processing; nuclear YAP was necessary for processing precursor microRNAs into their mature forms [Chaulk et al., 2014]. The microRNA Let-7, however, did not follow this trend. In the absence of nuclear YAP, Let-7 accumulates and targets Dicer1 mRNA (which contains Let-7 target sites), leading to a reduction in Dicer1 levels and defective microRNA processing. This is relevant because Let-7 levels are altered in IPF lung tissue [Pandit et al., 2011]. However, the focus of studies to date has been whole lung tissue, and it remains to be determined whether Let-7 is increased within the procollagen I rich focus core where Dicer1 levels are low.

Although the underlying ECM properties that generate and maintain the polarity of the fibroblastic focus are not defined, one approach to elucidating this information would be to develop a comprehensive tissue atlas that combines mechanical measurements with cell identity and cell biology region by region. Although on average the IPF lung is stiffer than control, and there are some regional data available using atomic force microscopy, there are no data in IPF in which ECM mechanical properties (static and dynamic), topography, and chemistry have been coregistered to cell type and cell biology. Such data have proved highly informative in cancer

biology [Weaver, 2017]. Given the spatial heterogeneity of the fibrotic process in IPF, the importance of mechanotransduction in regulating cellular functions relevant to fibrosis, and the striking polarity of the fibroblastic focus, we conclude that studies connecting mechanics to cell biology region by region will be important to understand the molecular basis for fibrosis progression in IPF.

B.5 Acknowledgment

The authors thank Daniel J. Tschumperlin and Delphine Sicard for assistance in characterizing ECM mechanical properties and Vitaly Polunovsky for helpful suggestions and critical review of the manuscript. Any opinions, findings, and conclusions or recommendations expressed in this material are those of the authors.

B.6 Supplemental Material

B.6.1 Methods

Patient derived cell lines and decellularized lung

All studies involving patient-derived materials were approved by the University of Minnesota Institutional Review Board for Human Subjects Research (IRB # 1504M68341). Human lung tissue was procured and de-identified by the University of Minnesota CTSI's Biological Materials Procurement Network (BioNet).

Primary human lung fibroblast lines and culture conditions All cell lines were derived from histologically uninvolved lung tissue adjacent to resected tumors. Tissue was minced and added to 35 mm plastic tissue culture dishes for 2-3 weeks in explant growth medium (DMEM + 20%FBS, 200 IU/mL Streptomycin, 200 IU/mL Penicillin). Outgrowth cells were sub-cultivated into 150 mm dishes in fibroblast growth media (DMEM + 10% FBS, 100 IU/mL Streptomycin, 100 IU/mL Penicillin) and designated passage 1. Cells were characterized as fibroblasts by their typical spindle shaped morphology, the expression of vimentin and alpha-smooth muscle actin, and no expression of factor VIII and surfactant C. Cells were cultured (37° C, 5% CO_2) in fibroblast growth medium and sub-cultivated at a 1:3 split ratio. All experiments were conducted with cells between passages 3 to 6. In total, 23 primary human lung cell lines were used.

Experiments utilizing decellularized human lung ECM The study was conducted using 2 types of patient-derived lung tissue: i) histologically uninvolved tissue adjacent to resected tumors (Control), or ii) pathologically confirmed IPF (usual interstitial pneumonia) obtained at the time of biopsy or lung transplantation. Freshly frozen tissue was sectioned at 200 μm and decellularized in a series of solutions (1% SDS,

1% Triton X-100, 1M NaCl) as described [Parker et al., 2014]. Each decellularized preparation was cut into strips approximating 1 cm^2. When choosing tissue regions for our preparations, we avoided major arteries/veins and airways for both lung types in our ECM preparations.

To minimize the effect of patient to patient and lung region to lung region variation, each experiment was conducted in 15 mL conical polypropylene tubes, with each tube containing decellularized ECM from 3 patient controls or 3 IPF patients. In total we used 11 patient samples for Ctrl-ECM preparations and 8 patient samples for IPF-ECM preparations; randomly selecting 3 for each experiment performed. Technical replicates used the same ECM preparations and the same cell lines; biological replicates (independent replication of an experiment) randomized both cell lines and ECM preparations (within the same class, IPF or Ctrl). To each tube we added 5 x 105 fibroblasts in 2 mL survival medium (DMEM + 1% FBS, 100 IU/mL Streptomycin, 100 IU/mL Penicillin) and incubated the cell-ECM mixture at 37° C in an atmosphere containing 5% CO_2, 95% air while oscillating each tube at 6 revolutions per minute. Prior reports indicate that the choice of detergents (SDS vs CHAPS) in the decellularization protocol can affect cell biology [Melo et al., 2014]. We therefore tested both detergents in parallel and quantified mature miR-29 expression by qPCR as a biologically relevant readout (Figure B.22. Mature miR-29 was suppressed by IPF-ECM independent of the detergent protocol used. For all experiments, we used SDS for decellularization as previously reported by our laboratory [Parker et al., 2014]. To further characterize the system, we quantified cell attachment and proliferation on each type of ECM. Of the 5 x 105 input fibroblasts, ∼2.1 x 105 cells attached to Ctrl-ECM and ∼1.1 x 105 attached to IPF-ECM (Figure B.23. Recovery of attached cells on the 2 types of ECM was comparable. Among attached cells, BrdU incorporation was similar on the 2 ECM types reaching a steady state value of ∼20%

in survival medium and ∼40% in growth medium (Figure B.24.

Polyacrylamide Gels

Polyacrylamide gels of 3 kPa or 20 kPa were cast following an established protocol [Cretu et al., 2010]. Gels were functionalized with either 100 μg/mL Type I Collagen (Advanced BioMatrix 5005), 50 μg/mL Type III Collagen (Advanced BioMatrix 5021), 10μg/mL Fibronectin (Advanced BioMatrix 5050), or a combination of all three using 10μg/mL of each. 2 x105 fibroblasts were seeded on each gel and incubated in survival medium for 24 hours. For lysate preparations, hydrogels were washed twice in PBS, blotted dry, and placed cell side down into 150 μL lysis buffer (Cell Signal # 9803) with protease inhibitors (Roche # 11873580001).

Vectors/Plasmids

For YAP gain-of-function experiments, plasmids pQCXIH-Flag-YAPS127\381A (Addgene # 33069) and pQCXIH-Myc-YAP-5SA (Addgene # 33093) were cloned into expression plasmid pSIN-EF1α-DEST-pMDG-psPX2 (Addgene # 12260). Cells were transduced and used for experimentation 48 hours after transduction. For YAP and Dicer1 loss-of-function, 3 constructs for pGIPZ Human YAP1 shRNA (Dharmacon # V2LHS 65508, V2LHS 65509, V2LHS 247011), 3 constructs for pGIPZ Human Dicer1 shRNA (Dharmacon # V2LHS 99123, V2LHS 201823, V3LMM 239140) and 1 construct pGIPZ Non-Silencing (Scrambled) Lentiviral shRNA Control (Dharmacon # RHS4346) were packaged into the pGIPZ lentivirus systems (GE Health) and a cocktail of all 3 silencing constructs were used to transduce fibroblasts for 48 hours (YAP) or 7 days (Dicer1) prior to initiating the experiment.

Western blot and antibodies

The protocol we developed to produce and analyze lysates from cells cultured on ECM minimizes protein contamination from the medium and ECM; and normalizes loading by accounting for unavoidable differences in the amount of these contaminating proteins from sample to sample. Cell-ECM preparations are washed twice in PBS. Excess PBS is blotted and preparations are submerged in 150 ∼L of Lysis Buffer (Cell Signal # 9803) with protease inhibitors (Roche # 11873580001) in a 1.5 mL tube. The cell-ECM\lysis buffer mixture was mechanically disrupted with a pipette, sonicated, centrifuged and the liquid phase was retained. To standardize loading in the presence of contaminating eluted ECM proteins and residual media proteins; in each assay, we loaded 10 ∼L of lysate, immunoblotted for GAPDH, and quantified GAPDH by densitometry. The densitometry values for GAPDH in each lysate was used to equalize lysate loading, enabling us to compare the abundance of proteins from sample to sample. Blots were incubated (4° C) overnight with primary antibodies (Table B.1. Blots were washed 3X in TBS-T and incubated (1 h, room temperature) with secondary antibodies (either goat anti-rabbit IgG HRP [Calbiochem 401393; 1:10,000] or Rat anti-mouse IgG HRP [Calbiochem 401253; 1:2,500]). Blots were developed using ECL western blotting detection (GE Healthcare W9488333) following the manufacturer's protocol.

Reverse Transcription and Quantitative PCR Analysis

RNA was isolated with TRI reagent (Sigma T9424) and chloroform extracted. Isolated RNA was reverse transcribed using miScript II RT Kit (Qiagen 218161) according to the manufacturer's recommendation. NE-PER Nuclear and Cytoplasmic Extraction Reagent (ThermoScientific # 78833; manufacturer's recommendation) was used to fractionate nuclear and cytoplasmic RNA. By using validated primers (Table

B.2) that share PCR conditions, we were able to probe for mature miR, Pri-Pre miR, and mRNA from the same reverse transcription reaction using SYBR – Green PCR Kit (Qiagen 218073; manufacturers recommendation) and analyzed by Roche Light Cycler 1.5 (Software Version 3.5).

Luciferase Promoter Assay

The miR29-b-1/a firefly luciferase promoter construct was a kind gift from Justin Mott, University of Nebraska [Mott et al., 2010]. Plasmids miR29-b-1/a and pRLTK (Promega E2241) were co-transfected into primary lung fibroblasts using Lipofectamine 3000 (Life Technologies L3000008) according to the manufacturer's recommendation. Using a dual luciferase reporter assay (Promega E1910), luminescence was quantified using a Lumat LB 9507 luminometer (Berthold Technologies).

AUF1-Dicer1 mRNA immunoprecipitation

RNA-immunoprecipitations were performed as we previously described [Rattenbacher et al., 2010, Beisang et al., 2012, White et al., 2017] with the following modifications. Primary human lung fibroblasts were cultured on tissue culture plastic in DMEM + 10% FBS to ∼50% confluence (mid-log phase) and shifted to DMEM + 1% FBS for 24 h. Cells were added to tubes containing Ctrl- or IPF- ECM and cultures were continued in DMEM + 1% FBS for 18h. Cells were chemically removed from the ECM with trypsin, and the cell pellet was collected by centrifugation. Cytoplasmic lysates were prepared by adding 1 cell pellet volume of NP-40 lysis buffer (10mM Hepes, 100 mM KCl, 5 mM MgCl2, 25 mM EDTA, 0.5% IGEPAL, 2mM DTT, 50U/ml RNase out and protease inhibitors). Lysates (50μl) of lysates were incubated (1h, 4° C) with protein A sepharose beads (Santa Cruz) blocked with bovine serum albumen and coated with antiAUF1 antibody (Millipore) or control rabbit IgG (Millipore) in NT2

buffer (50mM Tris–HCl pH 7.5, 150mM NaCl, 1mM MgCl2, 0.05% IGEPAL) with appropriate inhibitors. Beads were washed 6 times with NT2 buffer, and incubated with NT2 buffer containing SDS and proteinase K (30 min, 65° C). RNA was extracted using Trizol reagent and subjected to qPCR for Dicer1 and GAPDH mRNA.

Zebrafish Xenograft Assay

Zebrafish (Danio rerio) wild type embryos were obtained through the University of Minnesota Zebrafish Research Core Facility with approval from the Institutional Animal Care and Use Committee (IACUC Protocol 1502-32338A). Human cells, in addition to GFP labeling, were stained with a vital dye PKH26 (Sigma) and grafted into the central portion of the zebrafish embryo blastoderm at the oblong-sphere stages as previously described [Benyumov et al., 2012]. Host-embryos developed at 28.5° C. 46 hours post-grafting, embryos were immobilized with Tricane (Sigma) and fixed with 4% paraformaldehyde for 48 hours prior to paraffin-embedding (Due to the size of the fish, a one-hour processing cycle was performed to avoid over-processing and hardening of tissue).

Mouse Xenograft Assay

Female, age 8 weeks, NOD.Cg-Prkdc scid Il2rg tm1Wjl /SzJ mice (Jackson Laboratory, Farmington, CT, product number 005557) were divided into 2 groups and inoculated by tail vein injection with 106 primary human fibroblasts transduced with either Dicer1 shRNA or scrambled shRNA control following IACUC Protocol 1407-31641A. 4 mice from each group were sacrificed 6-days post inoculation. At the time of sacrifice, lungs were harvested, formalin-fixed and paraffin-embedded.

Immunohistochemistry/Immunofluorescence

Human lung samples or fibroblasts cultured on decellularized ECM and were formalin-fixed and paraffin-embedded (FFPE). De-paraffinized and rehydrated 4 μm sections were subjected to antigen-heat retrieval (BioCare RV1000) for 25 minutes at 100° C (then allowed to cool to room temperature for 20 minutes), followed by 10 minutes in 3% hydrogen peroxide and 1 hour in Background SNIPER (BioCare BS966) blocking reagent at room temperature. Fibroblasts cultured on 2-D hydrogels were formalin-fixed and subjected to antigen-heat retrieval followed by a Background SNIPER blocking reagent. For anti-procollagen I, we used proteinase K (Millipore 21627; working strength) for 10 minutes instead of antigen-heat retrieval. After blocking, sections or gels were exposed overnight (4° C) to primary antibodies (Table B.3) diluted in 10% Background SNIPER. For permanent staining, Novolink Polymer Detection Systems (Leica RE7270-RE; manufacturer's recommendation) was used and developed with DAB chromagen (Covance SIG-31042; manufacturer's recommendation). For procollagen type I, biotinylated anti-Rat (Vector Laboratories # BA-4001) was used at 1:500 in 10% Background Sniper followed by Streptavidin-HRP (Covance SIG-32254; working strength) and DAB chromagen. Slides were counterstained with hematoxylin and cover-slipped with Permount (FisherSci # SP15). For immunofluorescence, after overnight primary antibody incubation, anti-Rabbit Cy3 or anti-rat Alexa 594 (Jackson 711-165-152; Abcam ab150156) in 10% Background SNIPER was incubated for 2 hours at room temperature and cover-slipped with Prolong Gold Antifade Mountant w/ DAPI (ThermoFisher P36931).

To quantify procollagen I levels in zebrafish xenografts, a single plane image of the graft was acquired. Using ImageJ (v1.50i, NIH), an outline was drawn around each graft and area mean fluorescence measured, along with adjacent background readings. The total corrected cellular fluorescence (TCCF) = integrated density –

(area of selected cell × mean fluorescence of background readings), was calculated as described [McCloy et al., 2014].

RNAscope

Formalin-fixed paraffin-embedded 4 μm sections were used following the manufacturers guidelines (Advanced Cell Diagnostic, ACD). In situ hybridization was performed for human Dicer1 (ACD, # 403051) using RNAscope 2.5 HD Reagent Kit (ACD, # 322300). Tissue was counterstained with hematoxylin and coverslipped with permount.

Histological Stains

Formalin-fixed paraffin-embedded 4 μm sections were deparaffinized and rehydrated. Hematoxylin & Eosin (H&E) and Masson Trichrome histological stains were performed by the Bionet Core Facility at University of Minnesota.

Histological Imaging

Samples containing permanent stains (DAB substrate/H&E/trichrome counterstain) were imaged using a Leica EC3 microscope and Leica MME camera. Fluorescent images were collected using a Zeiss Axiovert 200 fluorescence microscope and analyzed using AxioVision (Release 4.7.2).

Pharmacological Inhibitors

10 μM CCG-100602 (Cayman Chemical: 1207113-889) [MRTF inhibitor], 20 nM A83-01 (Tocris, # 2939) [ALK5 inhibitor], 10 μM Ly293002 (Cell Signal, # 9901) [PI3K inhibitor], 5 μM DAPT (Sigma, # 5942) [Notch inhibitor], 10 μM SCH772984 (AbMole BioScience, # 942183-80-4) [Erk inhibitor], 10 μM PF562271 (AbMole BioScience,

717907-75-0) [Focal Adhesion Kinase inhibitor], and 10 μM Y27632 (Sigma, # Y0503) [Rock inhibitor] were diluted according to the manufacturer's instructions and administered to cells at time of ECM culturing.

Uniaxial Extension to Failure

Lung ECM was sectioned using a tissue mold (Electron Microscopy Sciences # 69012) into rectangular uniaxial strips (3 mm x 5 mm x 15 mm) approximating the dimensions of a human lung acinus. Samples were tested in uniaxial strain to failure experiments on a biaxial machine (Instron, Norwood, MA) in the uniaxial mode using either $\pm$5N or $\pm$500N load cells and custom grips. Using computer software (WaveMatrix version 1.8), we applied a strain rate of 1%/second until failure, and the force was recorded by the load cells at a sampling rate of 100Hz. Only samples that failed in the center were included in the analysis. Samples that failed near the testing grip were discarded.

The force from the static load cell was divided by the undeformed cross-sectional area to calculate the first Piola-Kirchhoff Stress. The same undeformed cross-sectional area was used for all samples (15 mm^2). Grip strain was calculated using the initial distance between the grips (10 mm for all samples) and grip displacement during testing. Each stress-strain curve was processed with a bilinear fitting code using a least squares method, courtesy of Dr. Spencer Lake (Washington University in St. Louis, full method described in [Lake et al., 2010], to provide a toe and linear region modulus.

BrdU labeling

Fibroblasts cultured on decellularized ECM were pulsed with BrdU (Life Technologies 00-0103; per the manufacturer's recommendation) for 24 hours prior to formalin-

fixation and paraffin-embedding.

Antibody	**Company**	**Cat #**
αSMA	Abcam	32575
Ago2	Abcam	32381
AKT	Cell Signal	9272
p-AKT-S473	Cell Signal	4060
Col1a2	Abcam	34710
Dicer1	Cell Signal	3363
Drosha	Cell Signal	3410
ERK	Cell Signal	9102
p-ERK-T202 \Y204	Cell Signal	9106
Exportin-5	Cell Signal	12565
FAK	Santa Cruz	SC-558
p-FAK-Y397	Cell Signal	3283
FLAG-tag	Miullipore	MABS1244
GAPDH	Santa Cruz	25778
Myc-Tag	Cell Signal	2278
MMP-2	Abcam	37150
YAP	Cell Signal	14074

Table B.1: List of primary antibodies used for immunoblot. Conditions as recommended by manufacturer.

Mature miR	**Cat #**	**Precursor miR**	**Cat #**	**mRNA**	**Cat #**
miR-29a	MS00003262	pre-miR-29a	MP00001736	Col1a2	QT00037793
miR-29b	MS00006566	pre-miR-29c	MP00001757	Col4a2	QT00231707
miR-29c	MS000003269			Col6a2	QT00067039
miR-320a	MS00014707			CTGF	QT00052899
miR-451	MS00004242			CYR61	QT00003451
miR-484	MS00004277			Dicer1	QT00015176
RNU6	MS00033740			GAPDH	QT00079247
				Hes1	QT00039648

Table B.2: List of validated qPCR primers from Qiagen.

Antibody	**Company**	**Cat #**	**Antigen Retrieval**	**Concentration**
Ago2	Abcam	32381	AHR	1:8,000
BrdU	Roche	11903800	AHR	1:800
Dicer1	Abcam	14601	AHR	1:16,000
Drosha	Abcam	ab183732	AHR	1:2,000
Exportin-5	Abcam	ab129006	AHR	1:500
human procollogan type I	Abcam	ab64409	prot-K	1:500
YAP	Cell Signal	14074	AHR	1:800

Table B.3: List of primary antibodies used for immunochemistry. Antigen-heat retrieval (AHR) or Protienase-K (Prot-K)

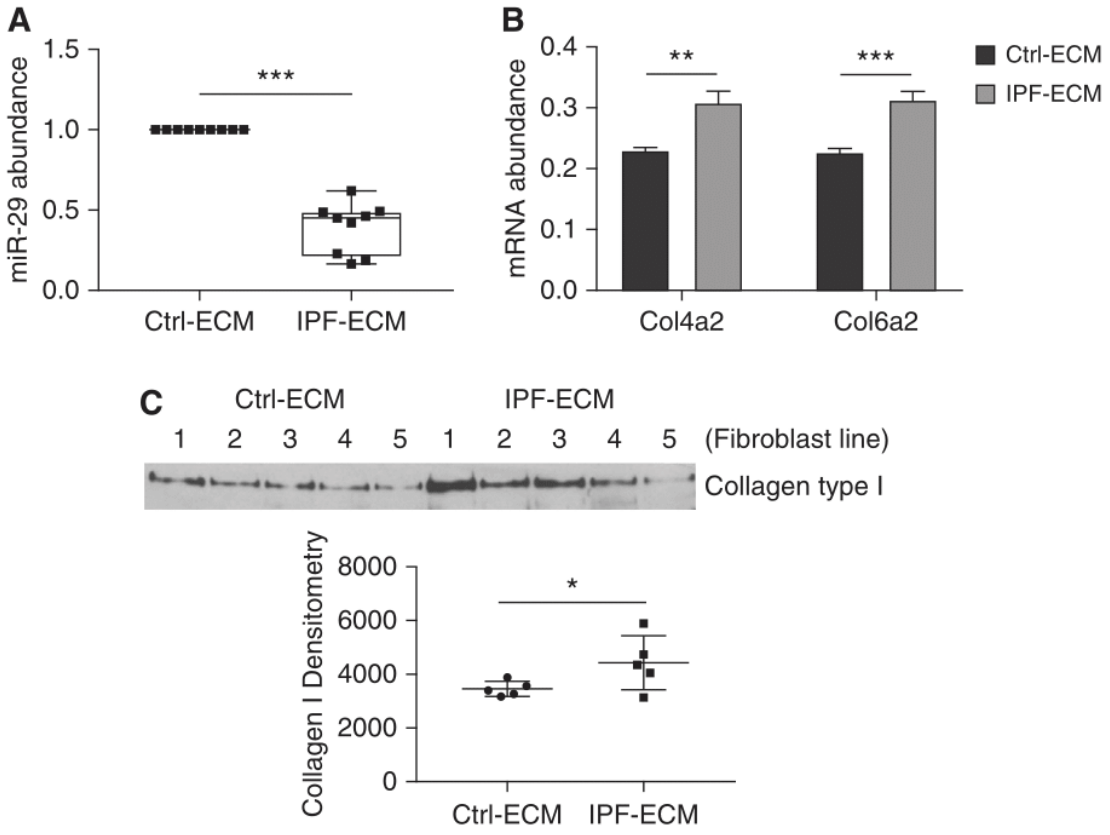

Figure B.1: Idiopathic pulmonary fibrosis (IPF)–extracellular matrix (ECM) suppresses miR-29 (microRNA-29) expression and upregulates collagen production. Lung fibroblasts were cultured on control or IPF-ECM for 18 hours. **A** Mature miR-29a, -29b, and -29c values were quantified by quantitative PCR (qPCR) and normalized to RNU6 (n = 1 cell line). Shown is a box-and-whisker plot representing the mean of three technical replicates for the three species of miR-29 with the values for control (Ctrl)-ECM set to 1. **B** qPCR for Col4a2 and Col6a2 normalized to GAPDH (n = 2, representative experiment shown), and P value was calculated using the Student's two-tailed t test. **C** Medium was removed and equal volumes of serum-free medium were added to each reaction. After 8 hours, the conditioned medium was collected and equal volumes analyzed by immunoblot for type I collagen (n = 5 cell lines, densitometry values shown in graph below). Error bars represent mean ± SD. P value was calculated using the Student's two-tailed t test for A and B, and paired two-tailed t test for C. *P<0.05, **P<0.01, ***P<0.005.

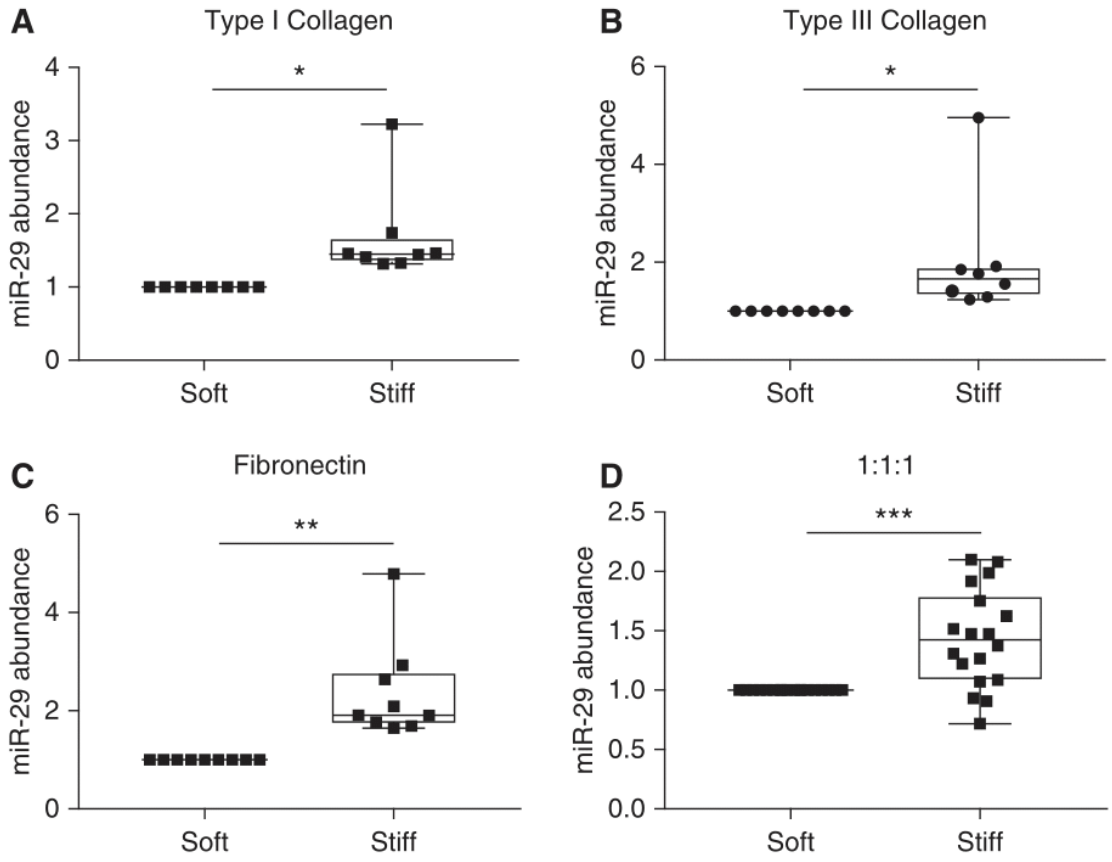

Figure B.2: Stiffness increases miR-29 (microRNA-29) expression in two-dimensional hydrogels. Primary lung fibroblasts were cultured for 24 hours in survival medium on gels mimicking physiological stiffness (3 kPa; soft polyacrylamide gels) or gels mimicking idiopathic pulmonary fibrosis stiffness (20 kPa; stiff polyacrylamide gels). Gels were functionalized with either: **A** type I collagen (n = 3 cell lines); **B** type III collagen (n = 3 cell lines); **C** fibronectin (n = 3 cell lines); or **D** an equal ratio of type I collagen, type III collagen, and fibronectin (n = 6 cell lines). Shown is a box-and-whisker plot of the mean quantitative PCR values on stiff hydrogels compared with soft (set to 1) for miR-29a, -29b, and -29c (normalized to RNU6 expression). P values were calculated using the Student's paired two-tailed t test. *P<0.05, **P<0.01, ***P<0.001.

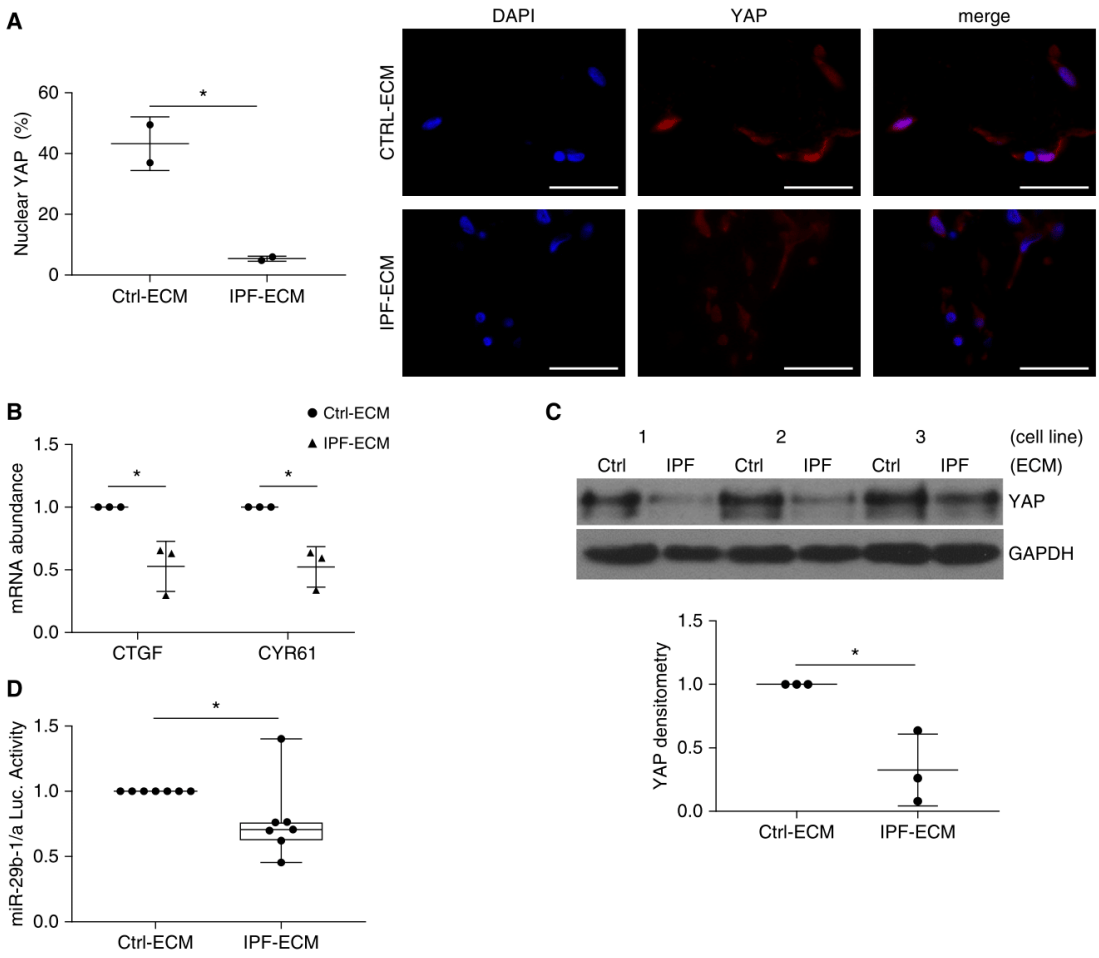

Figure B.3: Idiopathic pulmonary fibrosis (IPF)–extracellular matrix (ECM) negatively regulates YAP (yes-associated protein) and suppresses miR-29 (microRNA-29) transcription. **A**–**C** Fibroblasts were cultured for 24 hours on ECM and **A** (left panel) nuclear YAP (percentage positive cells) was quantified by immunofluorescence microscopy (n = 2 cell lines, mean values shown); (right panel) representative image shown with scale bars representing 50 mm. **B** Quantitative PCR for CTGF and CYR61 (normalized to GAPDH; n = 3 cell lines, mean values shown normalized to control [Ctrl]-ECM [set to 1]). **C** YAP expression was quantified by immunoblot (normalized to GAPDH; using three cell lines designated 1, 2, and 3; mean values shown normalized to Ctrl-ECM [set to 1]). Mean densitometry values are shown in lower panel. **D** Fibroblasts transfected with an miR-29b-1/a firefly luciferase reporter were cultured for 24 hours on ECM, and luciferase activity was quantified (normalized to Renilla luciferase; n = 7 cell lines shown as a box-and-whisker plot, mean value shown normalized to Ctrl-ECM [set to 1]). Error bars represent mean6SD. P values were calculated using the Student's paired two-tailed t test. *P<0.05.

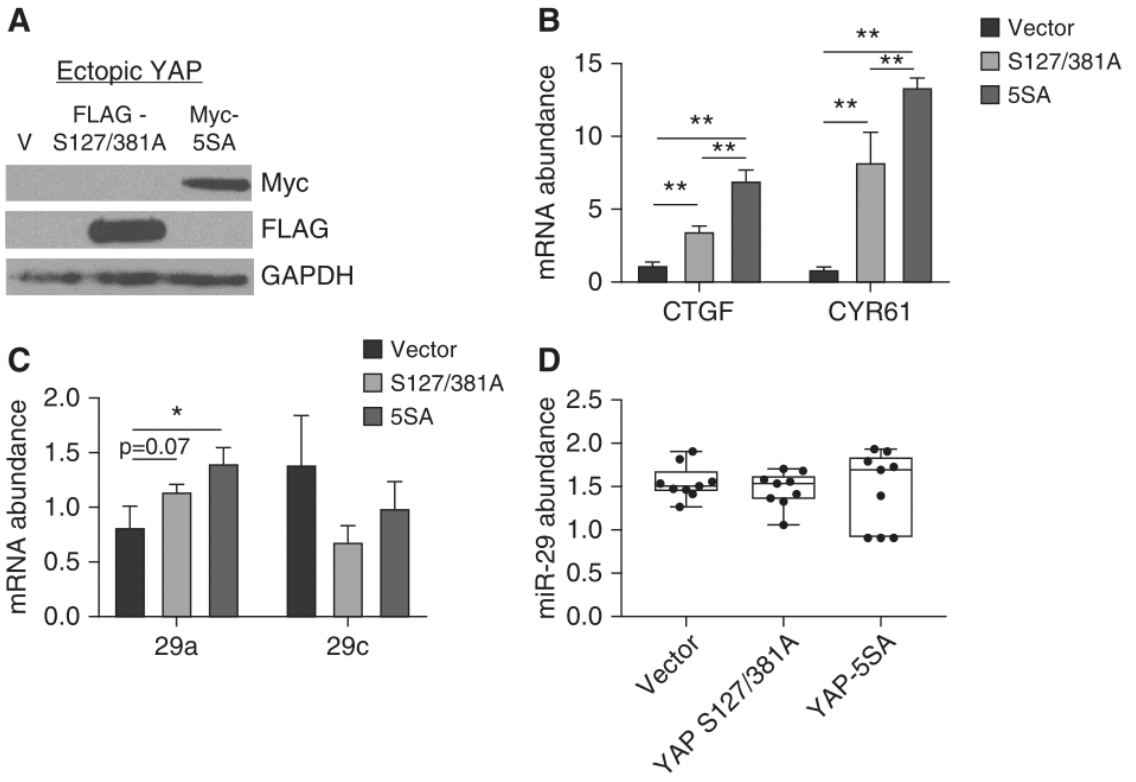

Figure B.4: Enforced YAP (yes-associated protein) expression does not restore maturemiR-29 (microRNA-29) expression on idiopathic pulmonary fibrosis (IPF)–extracellular matrix (ECM). **A**–**D** Fibroblasts were transduced with empty vector, YAP S127/381A–FLAG-tagged, or YAP 5SA–MYC-tagged and cultured on IPF-ECM for 18 hours. **A** Ectopic YAP expression was analyzed by immunoblot for anti-FLAG and anti-MYC. **B** YAP target genes CTGF and CYR61 were quantified by quantitative PCR (qPCR) normalized to GAPDH. **C** Primary–precursor miR-29a and -29c were quantified by qPCR normalized to GAPDH; **D** mature miR-29a, -29b, and -29c were quantified by qPCR normalized to RNU6 (n = 2, representative experiment shown). Error bars represent means ± SD for B and C, and a box-and-whisker plot is shown for D. P value was calculated using a one-way ANOVA test followed by a Tukey test. *P<0.001, **P<0.0001

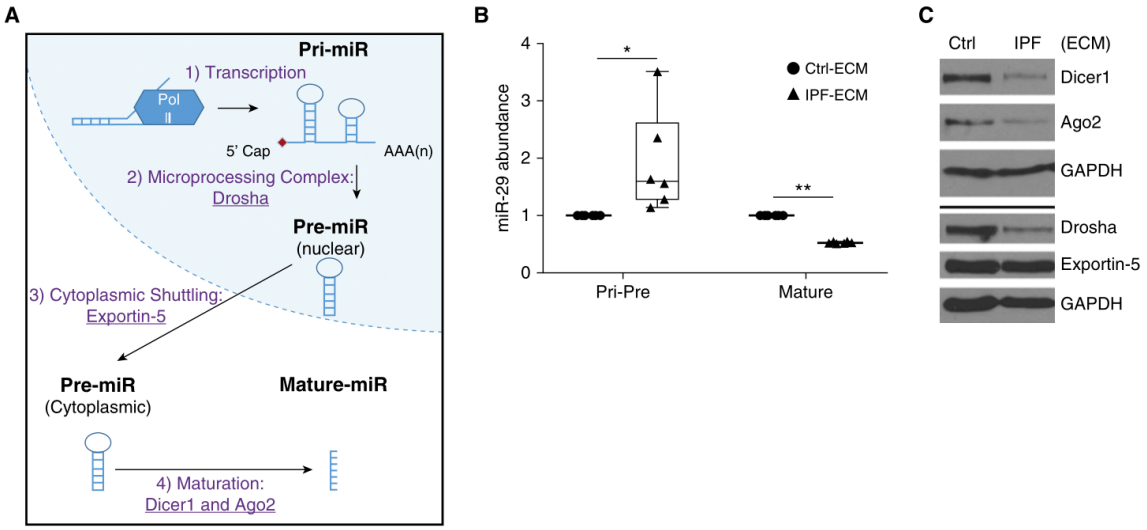

Figure B.5: Idiopathic pulmonary fibrosis (IPF)–extracellular matrix (ECM) suppresses the microRNA processing machinery. **A** MicroRNA biogenesis schematic: 1) microRNAs are transcribed into primary microRNA (Pri-miR), 2) processed into precursor microRNA (Pre-miR) by the microprocessor complex (including Drosha), 3) actively shuttled from the nucleus to the cytoplasm by Exportin-5, and 4) processed into mature microRNAs by Ago2 and Dicer1. **B** Fibroblasts were cultured on ECM for 18 hours and quantitative PCR was used to analyze the grouped values of Pri-Pre and mature microRNA-29a (miR-29a) and miR-29c normalized to GAPDH or RNU6, respectively (n = 3 cell lines, mean value shown normalized to control [Ctrl]-ECM [set to 1]). Data are shown as a box-and-whisker plot, and P value was calculated using the Student's paired t test. *P<0.05, **P<0.0001. **C** Fibroblasts were cultured on ECM for 24 hours. Shown are immunoblots for Dicer1, Ago2, Drosha, Exportin-5, and GAPDH (n = 1 cell line).

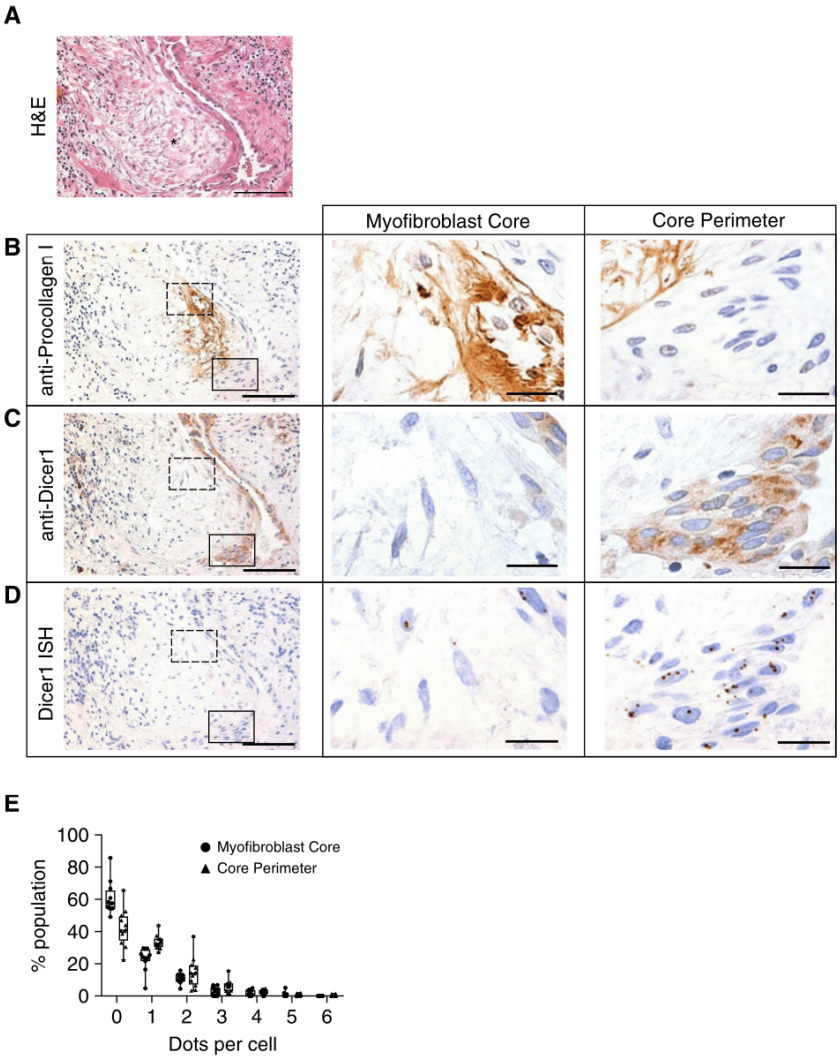

Figure B.6: Regions of the lung actively synthesizing collagen are deficient in Dicer1. An idiopathic pulmonary fibrosis (IPF) specimen was serially sectioned at 4 mm and processed for histology and immunohistochemistry. **A** Hematoxylin and eosin (H&E) image with an asterisk labeling a fibroblastic focus. (**B-D**, left panels) Immunostain for anti-procollagen I **B**, anti-Dicer1 **C**, and in situ hybridization by RNAscope for Dicer1 mRNA (D). **(B-D**, middle and right panels) The myofibroblast core (dashed outlined box in left panels) and focus perimeter (solid outlined box in left panels) were reimaged at higher-power magnification. Scale bars represent 100 mm (left panels) or 20 mm (middle and right panels). **E** Quantification of RNAscope data. We enumerated dots within cells in the myofibroblast core or core perimeter shown as a frequency distribution (percentage population). Poisson regression, $P<0.0001$ ($n = 6$ patients with IPF [12 fibroblastic foci total, 1-3 fibroblastic foci analyzed per patient]).

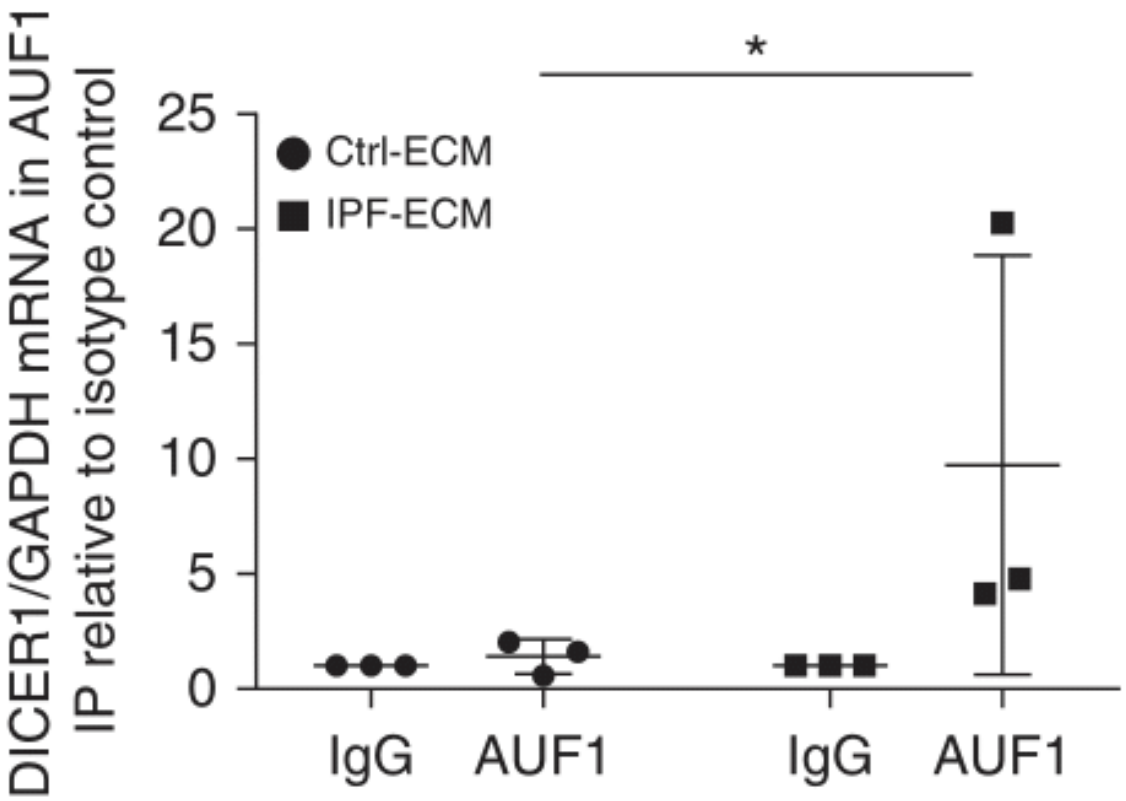

Figure B.7: Idiopathic pulmonary fibrosis (IPF)–extracellular matrix (ECM) increases the association of RNA binding protein AUF1 with Dicer1mRNA. RNA-immunoprecipitation (RNA-IP) was performed (n = 3 cell lines) against the RNA binding protein AUF1 (or isotype control, IgG) on lysates from cells cultured on control (Ctrl)- or IPFECM, and the amount of coprecipitated Dicer1 mRNA was quantified by quantitative PCR. Dicer1 mRNA was normalized to immunoprecipitated GAPDH mRNA levels (a highly abundant transcript to control for nonspecific associations). Dicer1/GAPDH expression levels are displayed relative to the isotype control (IgG) precipitation from the corresponding ECM type. Error bars represent SD, and P value was calculated using a one-sided Mann-Whitney U test. *P = 0.05.

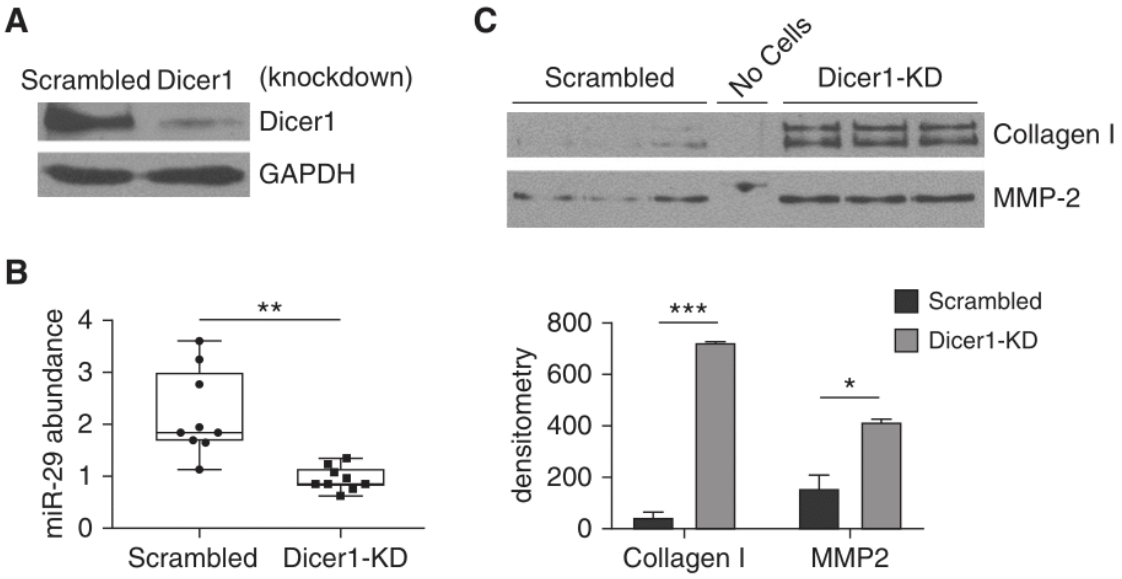

Figure B.8: Dicer1 knockdown in fibroblasts decreases mature miR-29 (microRNA-29) abundance on control extracellular matrix. Fibroblasts were transduced with Dicer1 shRNA or scrambled control to establish stable expression. **A** Shown is an immunoblot for Dicer1. (**B** and **C**) Equal numbers of transduced cells were cultured on control extracellular matrix for 18 hours. Medium was removed and equal volume of serum-free medium was added to each reaction for 8 additional hours. **B** Quantitative PCR for mature miR-29a, -29b, and -29c normalized to miR-451. Data are shown as a box-and-whisker plot, and P value was calculated using the Student's two-tailed t test. **C** Equal volumes of conditioned medium were analyzed by immunoblot for collagen I and MMP-2 (n = 2, representative experiment shown in triplicate). Densitometry values are shown in the lower panel, with error bars representing the SD, and P value was calculated using the Student's two-tailed t test. *P<0.01, **P<0.001, ***P<0.0001. KD = knockdown.

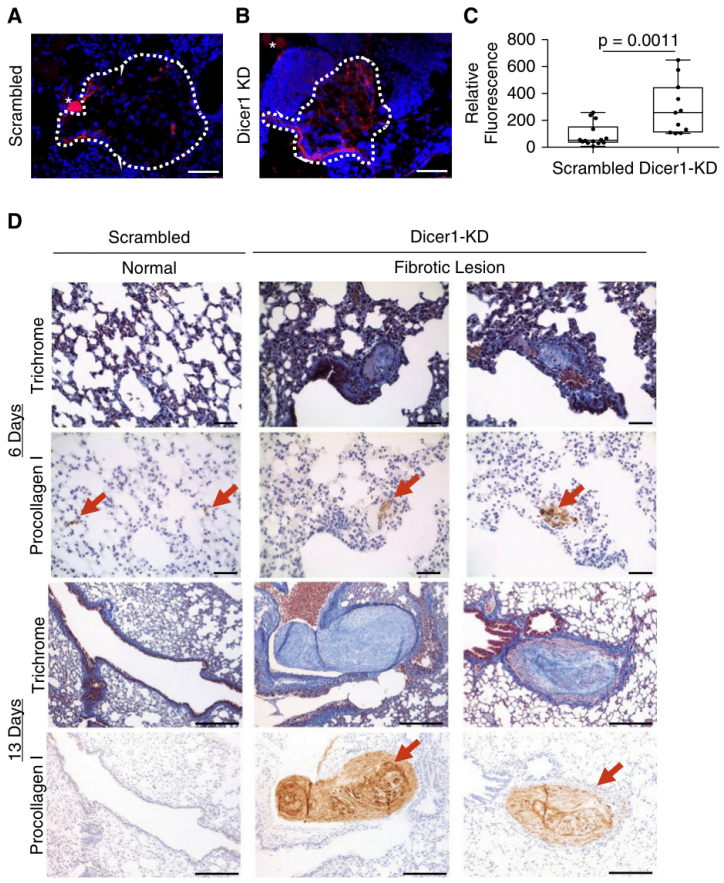

Figure B.9: Dicer1 knockdown imparts fibroblasts with fibrogenicity in vivo. **A-C** Zebrafish xenograft assay: 10^2 scrambled control or Dicer1-knockdown (KD) fibroblasts (cells from the same population of lung fibroblasts used in Figure B.8 were xenografted into each zebrafish embryo, which was incubated for 46 hours, anesthetized, and fixed before analysis. Representative xenograft images of **A** scrambled control or **B** Dicer1-KD fibroblasts immunostained for human procollagen I (red) counterstained with DAPI (graft DAPI-positive area outlined by dotted white line, scale bar represents 50 mm, asterisk indicates sectioning artifact: a yolk granule with autofluorescence). **C** A Fire LUT was applied using ImageJ to the unaltered images to quantify relative procollagen fluorescence, corrected to a background uninvolved area from the same image. Shown is a box-and-whisker plot of relative procollagen fluorescence with P values calculated using the Wilcoxon sum-rank test (n= 13 scrambled control and n = 11 Dicer1-KD zebrafish xenografts, P = 0.0011). **D** Mouse xenograft assay: 106 scrambled control or Dicer1-KD fibroblasts (cells from the same population of lung fibroblasts used in Figure B.8 were injected by tail vein into mice and lungs were harvested after 6 and 13 days (n = 4 scrambled control and n = 4 Dicer1-KD per time point for a total of 16 mice). P value was calculated using Fisher exact test (P = 0.04). Trichrome and procollagen I immunostain (red arrows mark human fibroblasts) identify fibrotic lesions (scale bar represents 50 mm for 6-day time point, or 200 mm for 13-day time point).

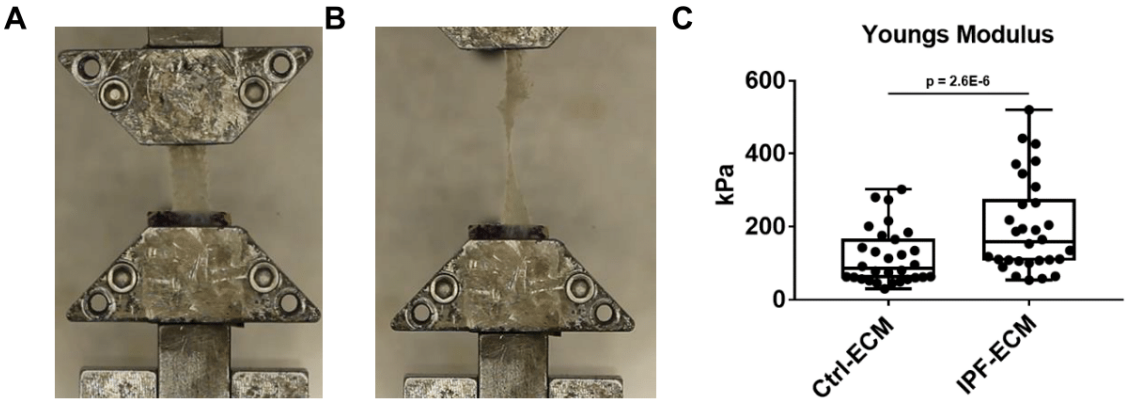

Supplemental Figure B.10: Uniaxial Tensile Mechanics of Lung ECM. **A** Decellularized ECM was loaded onto clamps. **B** The ECM was stressed until tissue failure ensued. **C** Young's elastic modulus measurements of generated force curves are represented as a box and whisker plot. P value was calculated using the Wilcoxon Rank-Sum test (n = 30 each group; 6 Ctrl-ECM and 6 IPF-ECM – 5 replicates each).

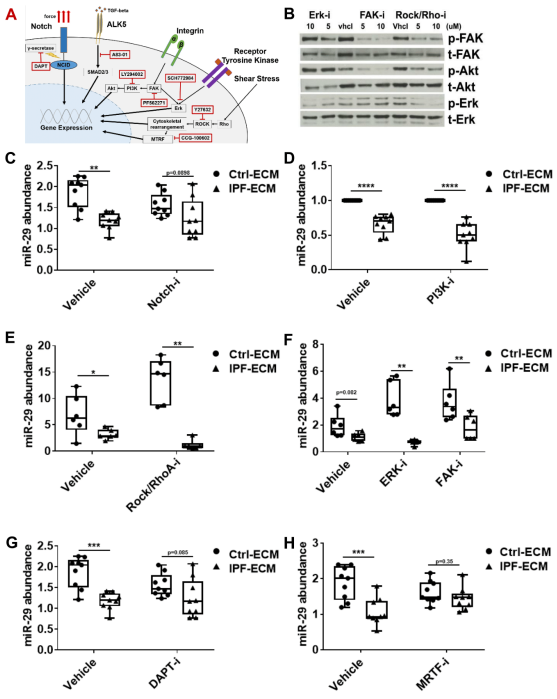

Supplemental Figure B.11: Pharmacological inhibition of Notch, PI3K, Rock/Rho, Erk, FAK, andALK5 do not prevent loss of miR-29 expression on IPF-ECM. **A** Schematic of the outside-in signaling pathways evaluated. **B** Primary lung fibroblasts were treated with inhibitor for 24 hours and immunoblotted for p-FAK (Y397)), total FAK, p-Akt (ser473), total Akt, p-Erk (T202 \Y204), and total Erk. **C-G** Primary lung fibroblasts were cultured on ECM for 18 hours with the indicated pharmacological agent and analyzed by qPCR for the grouped values of mature miR-29a, 29b, and 29c (normalized to RNU6). Shown as box and whisker plot. **C** Notch inhibitor: DAPT (5 μM which suppressed Notch downstream transcriptional targets in primary lung fibroblasts [data not shown], n = 1 cell line), **D** PI3 kinase inhibitor: LY294002 (10 μM previously shown to suppress p-Akt activation in primary lung fibroblasts, n = 3 cell lines; mean value shown normalized to Ctrl-ECM [set to 1]), **E** Rock and RhoA inhibitor: Y27632 (10 μM previously shown to suppress ROCK/RhoA in primary lung fibroblast [Huang et al., 2012] (n = 1 cell line), and **F** Erk inhibitor: SCH772984 (10 μM, n = 1 cell line) or FAK inhibitor: PF562271 (10 μM, n = 1 cell line). **G** ALK5 inhibitor: A83-01 (20 nM as previously used in primary lung fibroblasts [Booth et al., 2012] (n = 1 cell line). **H** MRTF inhibitor: CCG-100602 (10 μM, n = 1 cell line) normalized to miR-484 which we verified to be stably expressed in our system (RNU6 was unstable with CCG-100602 treatment and therefore not suitable for normalization). * p<0.05, ** p<0.01, *** p<0.001, **** p<0.0001

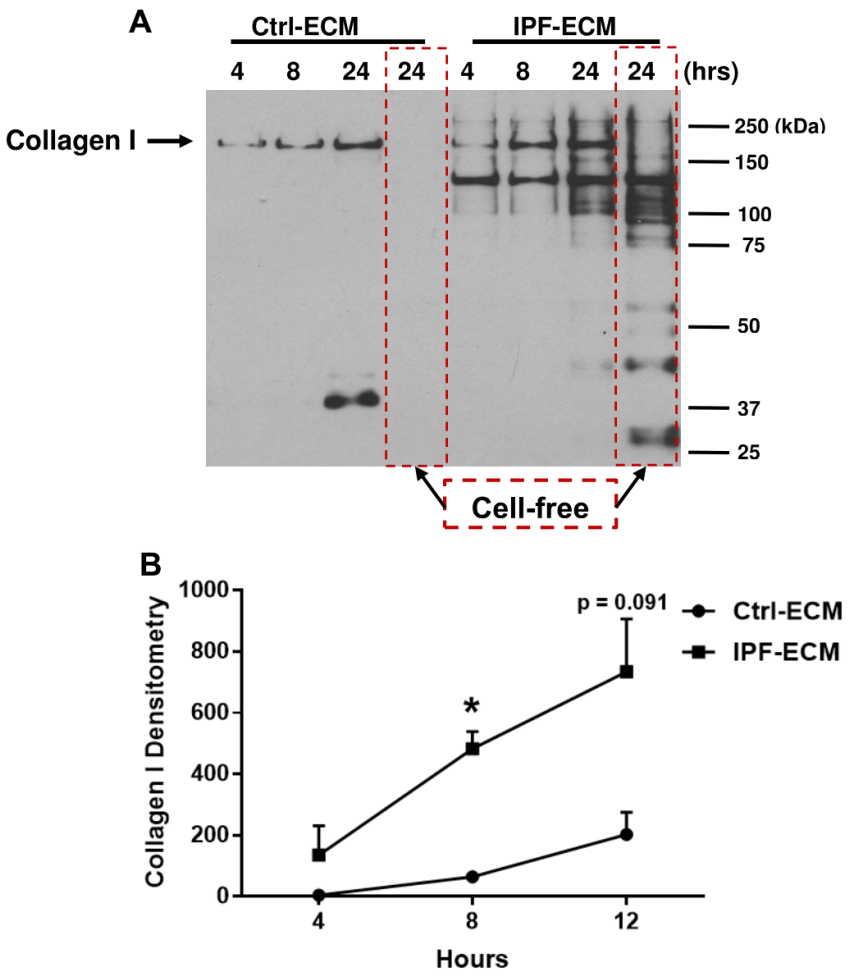

Supplemental Figure B.12: Kinetics of type I collagen expression by fibroblasts cultured on decellularized ECM. Fibroblasts were cultured on ECM for 18 hours and medium was replaced with equal amounts of serum-free medium for the indicated time. **A** Immunoblot for collagen I using equal amounts of conditioned media collected from fibroblasts cultured on Ctrl-ECM or IPF-ECM. 24-hour cell-free lanes (boxed in red dotted lines) were included to evaluate the contribution collagen I leaching out of the decellularized ECM (arrow). **B** Using equal volumes of conditioned medium for each time-point, the immunoblot was probed for type I collagen and signal was quantified by densitometry. (n = 1). Error bars represent means ± S.E.M. P value was calculated using the student two-tailed T-test. * $p<0.05$

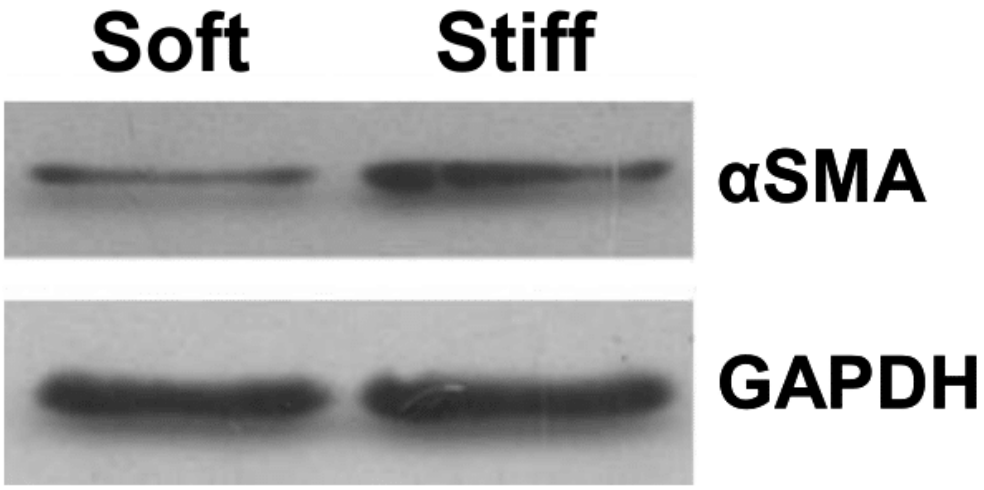

Supplemental Figure B.13: Stiffness upregulates αSMA expression in lung fibroblasts. Lung fibroblasts were cultured on soft or stiff PA gels functionalized with type I collagen for 24 hours and immunoblot was performed for αSMA and GAPDH. (n = 2, representative blot shown).

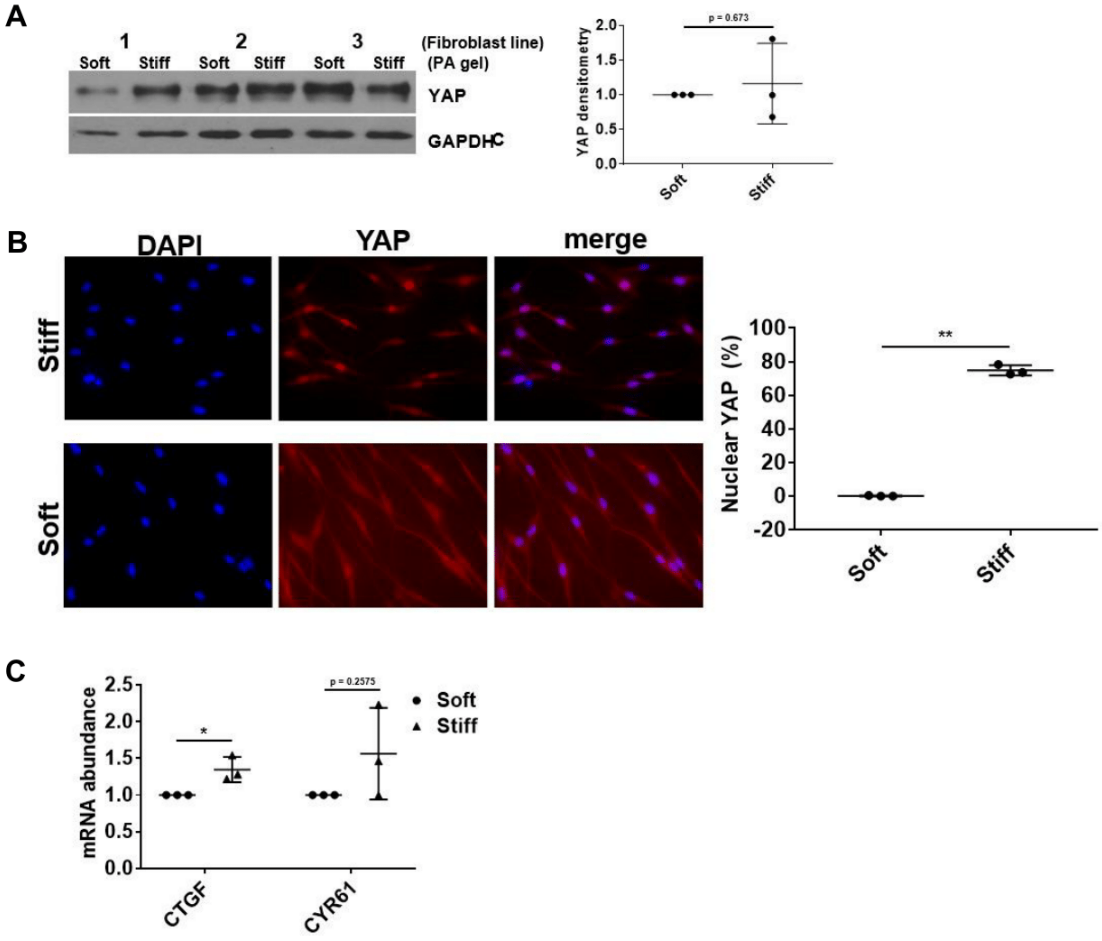

Supplemental Figure B.14: Stiffness drives YAP activation on polyacrylamide (PA) hydrogels. Primary lung fibroblasts were cultured on soft or stiff PA gels for 24 hours. **A** Immunoblots for YAP and GAPDH (n = 3 cell lines, densitometry on right panel normalized to soft gels set to a value of 1). **B** YAP immunofluorescence in fibroblasts on soft or stiff PA gels (n = 3 cell lines, quantification on right panel with mean values shown). **C** qPCR of CTGF and CYR61 (YAP transcriptional targets) normalized to GAPDH (n = 3 cell lines, mean values shown normalized to soft). Error bars represent means ± S.D. P value was calculated using the student paired two-tailed T-test. * $p<0.05$, ** $p<0.001$

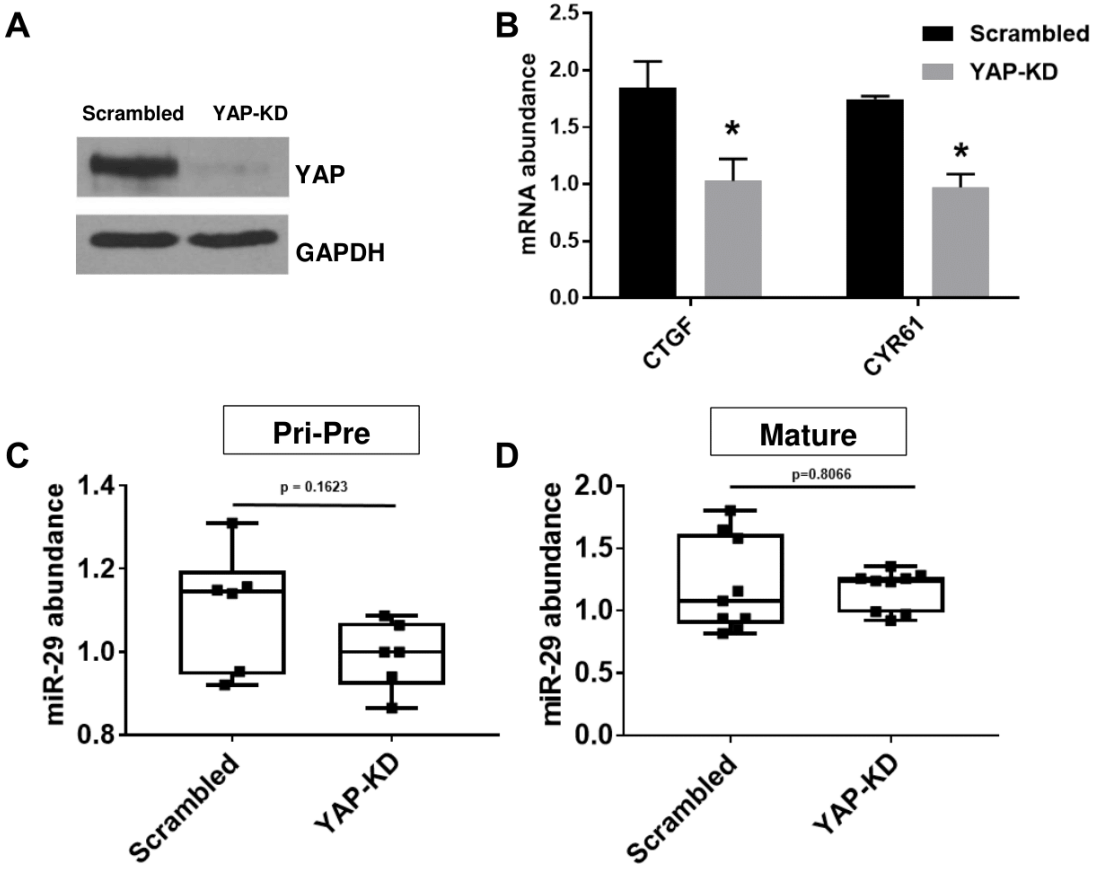

Supplemental Figure B.15: YAP loss-of-function does not alter miR-29 expression on Ctrl-ECM. Fibroblasts transduced with YAP shRNA or scrambled shRNA control were cultured on Ctrl-ECM for 18 hours. **A** Immunoblot for YAP and GAPDH **B** qPCR for CTGF and CYR61 (YAP transcriptional targets) normalized to GAPDH, **C** qPCR for the group values of Pri-Pre miR-29a and -29c normalized to GAPDH, and **D** qPCR for the group values of mature miR-29a, -29b, -29c normalized to RNU6 (n = 3, representative experiment shown). Error bars represent means ± S.D. for **B** and box and whisker plots for **C-D**. P value was calculated using the student two-tailed T-test for (B & D) and a Mann-Whitney Test for (C). * $p<0.05$

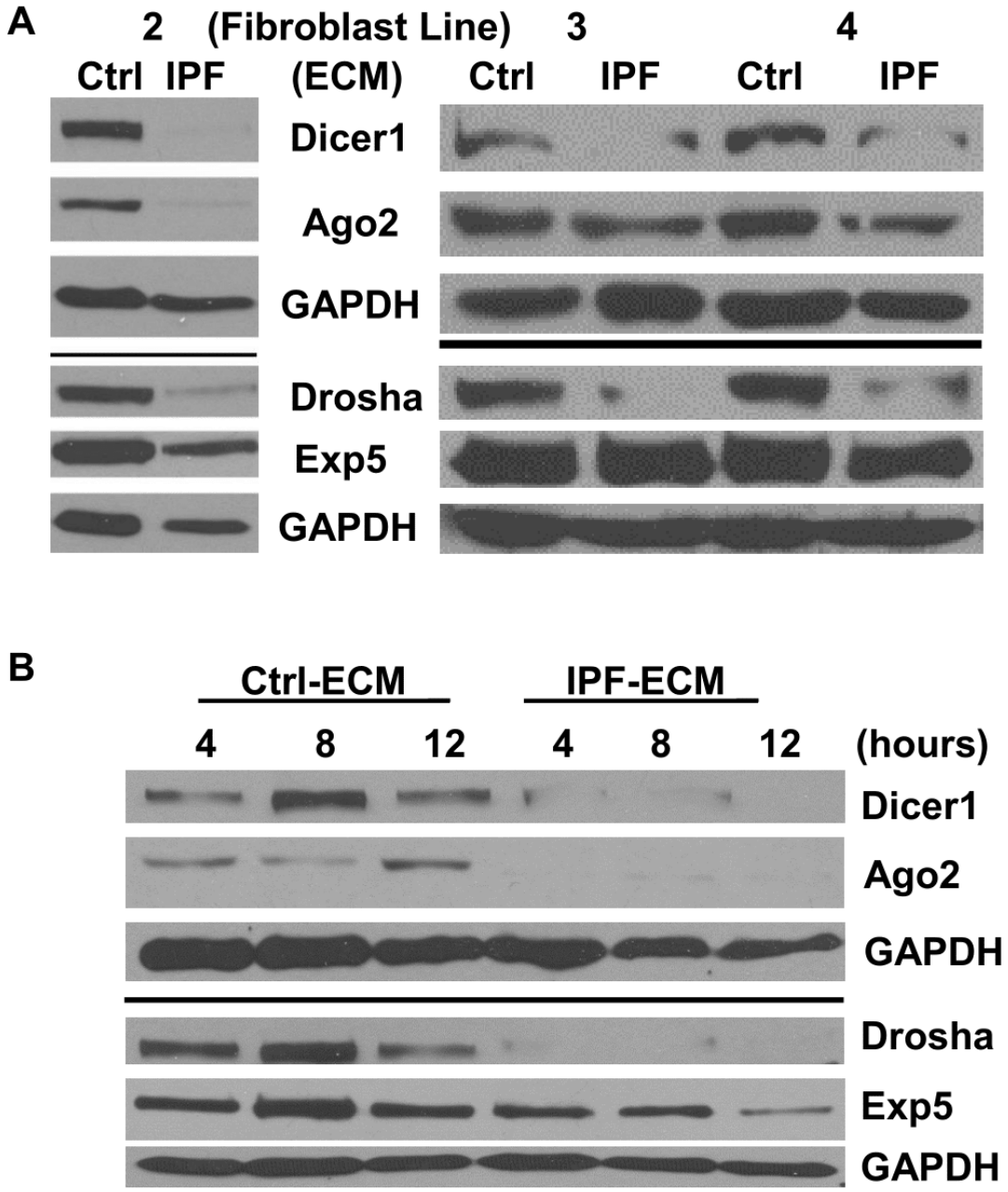

Supplemental Figure B.16: The microRNA processing machinery is suppressed by IPF-ECM. **A** Fibroblasts were cultured on decellularized ECM for 24 hours (n = 3 cell lines) or **B** 4, 8, and 12 hours. Shown are immunoblots for Dicer1, Ago2, Drosha, Exportin-5, and GAPDH (n = 1 cell line).

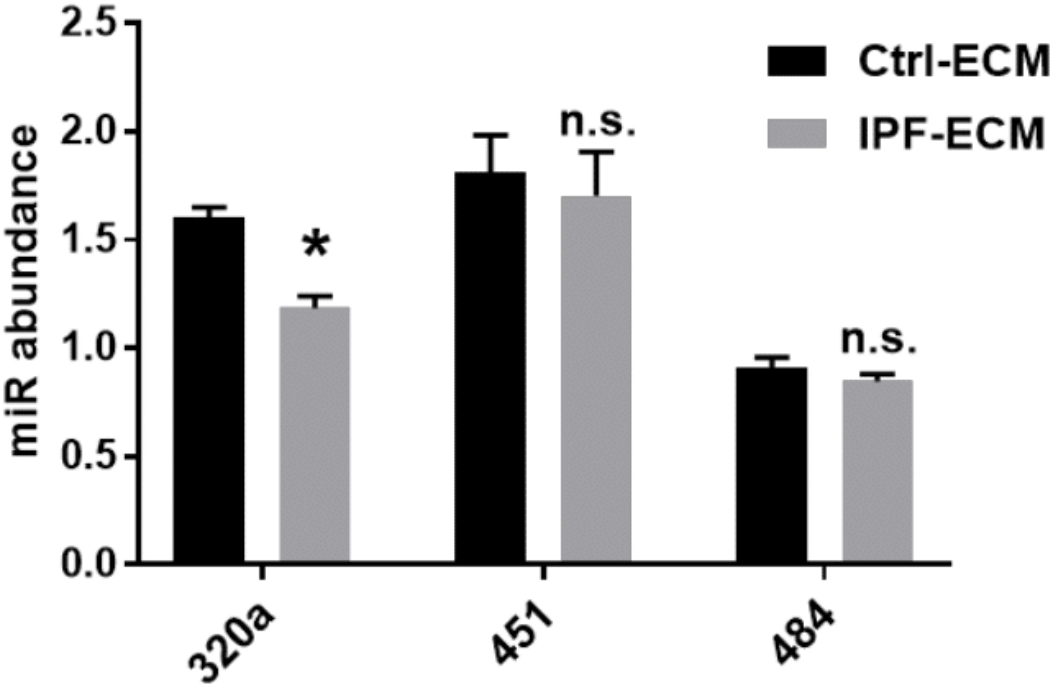

Supplemental Figure B.17: Non-canonical microRNA expression in fibroblasts cultured on ECM. Lung fibroblasts were cultured on ECM for 18 hours and qPCR performed for mature miR-320a, -451, and -484 normalized to RNU6 (n = 2 cell lines, representative experiment shown). Error bars represent means ± S.E.M. P value was calculated using the student two-tail T-test (n.s. = not significant). * $p<0.05$

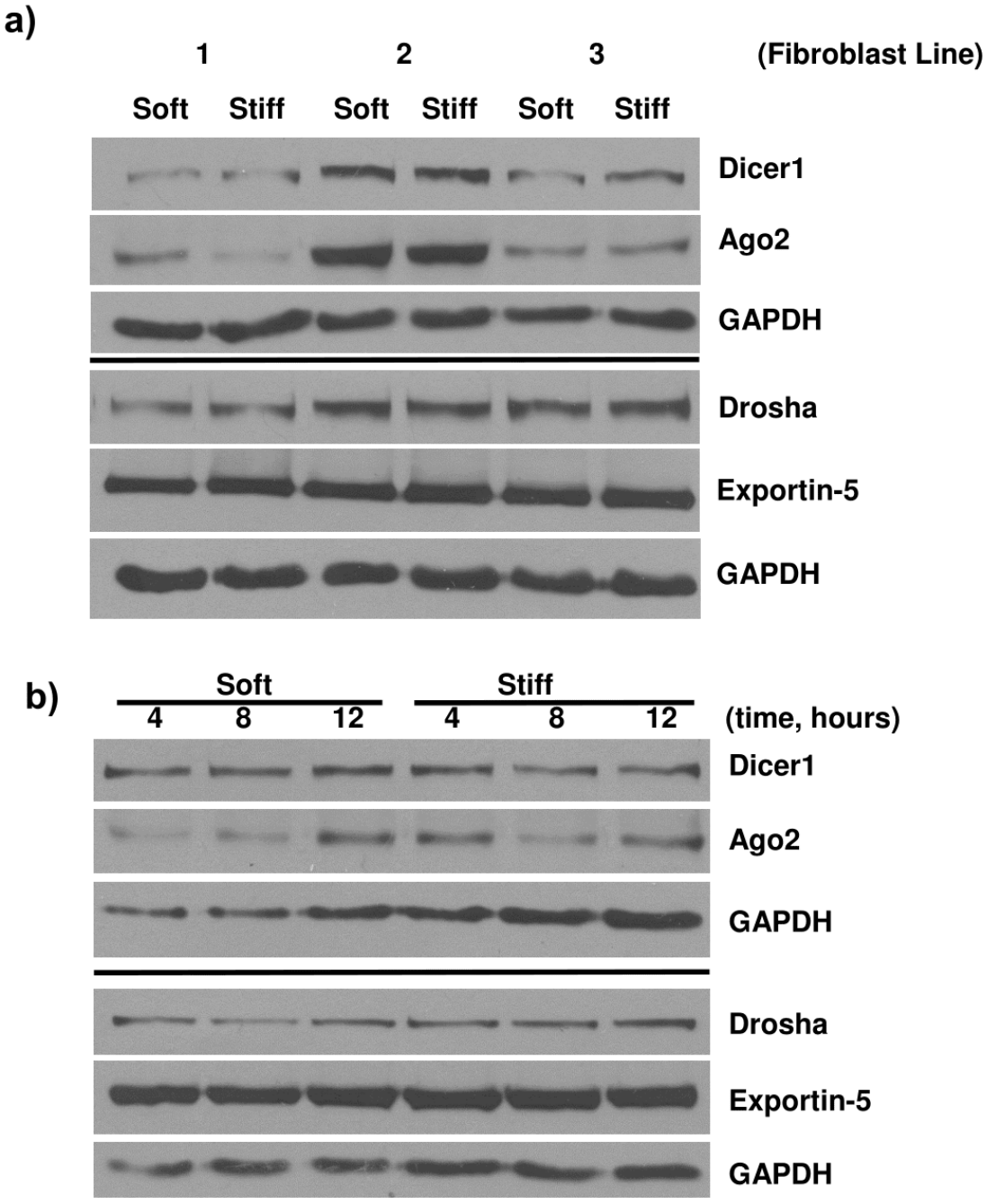

Supplemental Figure B.18: Stiffness does not alter the microRNA processing machinery. Primary lung fibroblasts were cultured on soft or stiff PA gels coated with type I collagen for 24 hours. (a) Immunoblot for Dicer1, Ago2, Drosha, Exportin-5, and GAPDH (n = 3 cell lines, indicated as 1, 2, or 3). (b) Primary lung fibroblasts were cultured on PA gels for the times indicated. Immunoblot for Dicer1, Ago2, Drosha, Exportin-5, and GAPDH (n = 1 cell line).

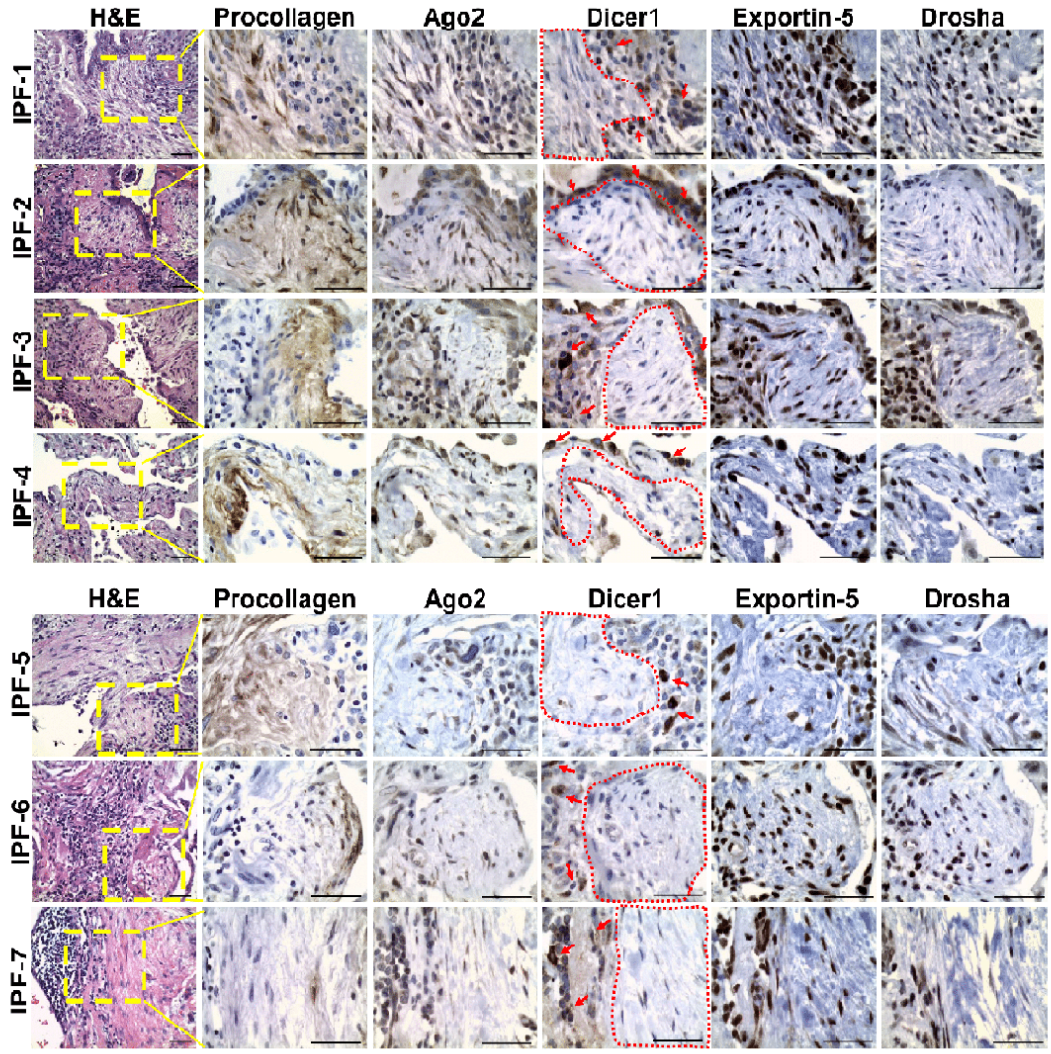

Supplemental Figure B.19: Dicer1 is reduced in cells comprising the myofibroblast-rich core. Formalin-fixed paraffin embedded IPF specimens were serially sectioned at 4 μm and processed for H & E, procollagen I, Ago2, Dicer1, Exportin-5, and Drosha. (scale bar represents 50 μm). The red dotted line on Dicer1 image outlines the myofibroblast-rich core and red arrows point to Dicer1 positive cells. (n = 7 IPF specimens).

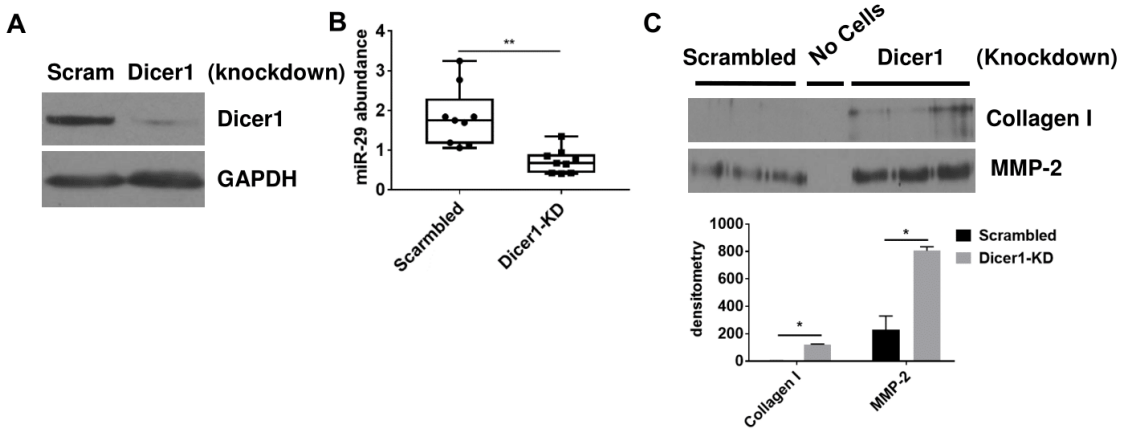

Supplemental Figure B.20: Dicer1 regulates miR-29 expression. A second primary lung fibroblast line was transduced with Dicer1 shRNA or scrambled shRNA control and cultured on Ctrl-ECM for 18 hours. After 18 hours, medium was replaced with equal volumes of serum-free medium for 8 additional hours. **A** Immunoblot for Dicer1 and GAPDH. **B** qPCR for the grouped values of mature miR-29a, -29b, and -29c normalized to miR-451 shown as a box and whiskers plot. **C** immunoblot for collagen I and MMP-2 (n = 1 cell line, done in triplicate). Densitometry quantifications shown in lower panel with error bars represent means ± S.D. P values were calculated using the student two-tailed T-test. * $p<0.05$.

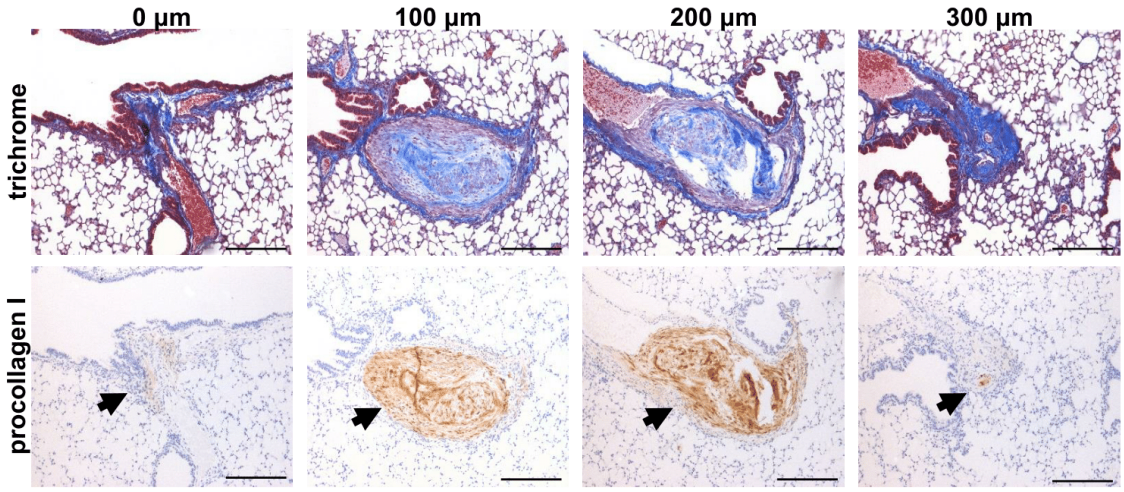

Supplemental Figure B.21: Fibroblasts deficient in Dicer1 form large lesions in the lungs of mice after 13 days post-injection. A mouse lung specimen from Figure 8 was sectioned at 100 μm intervals and stained for trichrome and human procollagen I. Shown is one fibrotic lesion marked by human procollagen I reactivity (black arrow) spanning 300 μm of tissue. Scale bar = 200 μm.

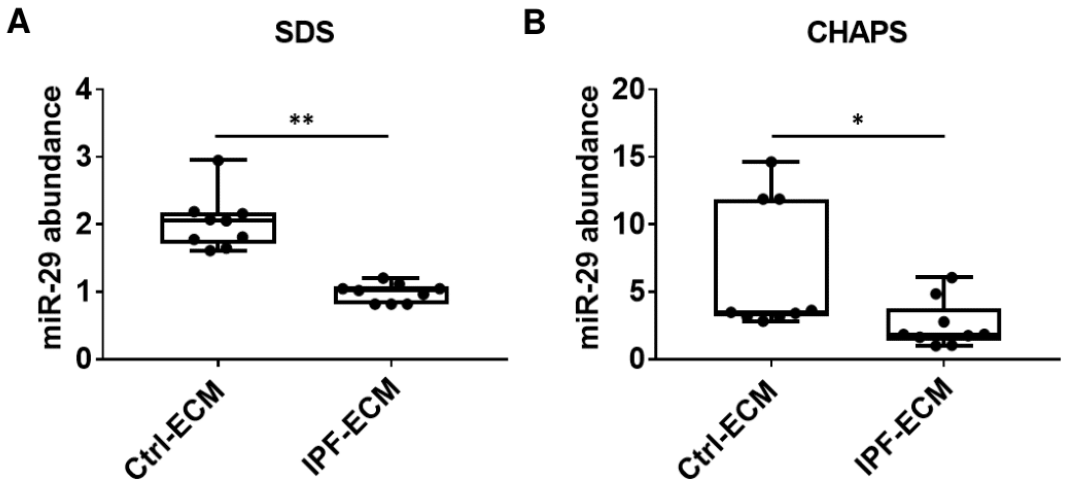

Supplemental Figure B.22: Decellularization methodology does not influence expression of mature miR-29 by ECM. ECM was decellularized with 1% SDS **A** or 8 mM CHAPS **B** followed by 1% Triton X-100 and 1M NaCl and cultured with primary lung fibroblasts for 18 hours. qPCR for the grouped values of mature miR-29a, -29b, and -29c are shown normalized to RNU6 (n = 2, representative experiment shown). Shown as a box and whiskers plot and P value was calculated using the student two-tailed T-test. * $p<0.05$ ** $p<0.0001$.

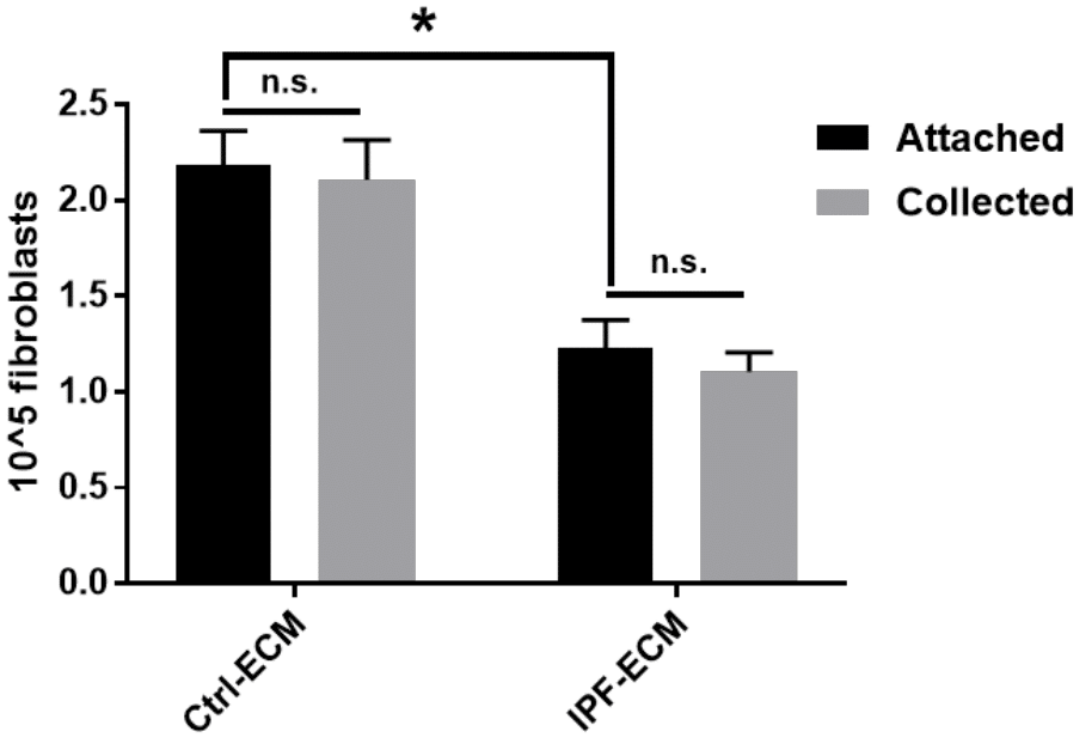

Supplemental Figure B.23: Recovery efficiency of fibroblasts from ECM is comparable; but IPFECM has a lower attachment efficiency. 5 x105 lung fibroblasts were cultured on control or IPF-ECM for 3 hours and unattached cells were quantified ("attached" = 5 x 105 – unattached). After 24 hours, cells were released from the fibroblast-ECM preparation with trypsin and the "collected" cells were quantified. (n = 1 cell line, 5 replicates). Error bars represent means ± S.E.M. and P value was calculated using the student two-tailed T-test (n.s. = not significant). * $p<0.05$

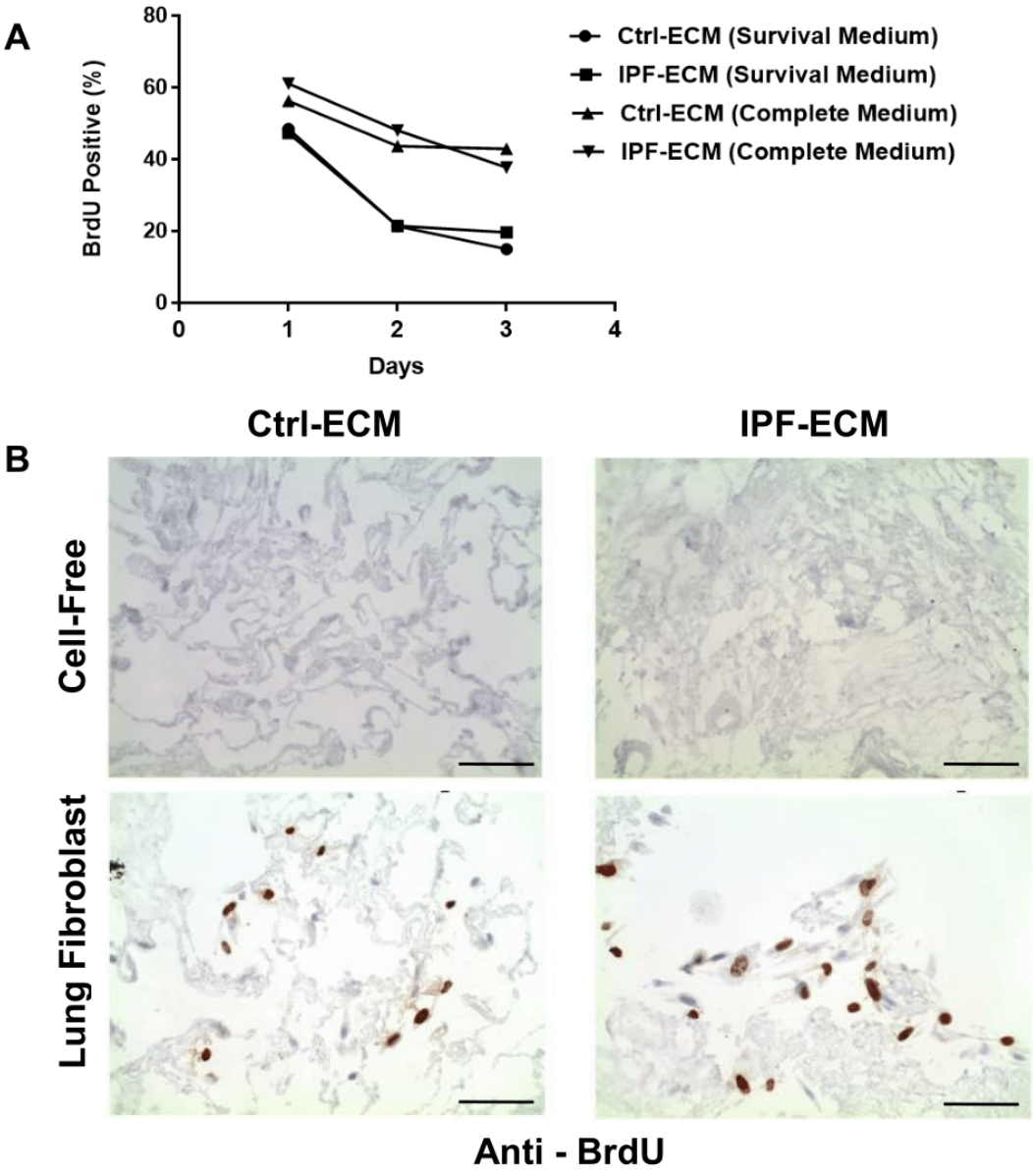

Supplemental Figure B.24: Lung fibroblasts proliferate on decellularized ECM. Lung fibroblasts cultured in either survival or growth medium were pulsed with BrdU for 24 hours, formalin-fixed and paraffin embedded. **A** 3-day time-course of percent BrdU positive cells, **B** representative images of ECM on day 3 with (lower panels) or without (upper panels) fibroblasts (n = 1; scale bars represent 50 μm).